

Hydrothermal circulation from very high to low  
temperatures in the lower oceanic crust - Evidence from  
layered gabbros from the Oman Ophiolite and from  
partial melting experiments on oceanic gabbros

Von der Naturwissenschaftlichen Fakultät  
der Gottfried Wilhelm Leibniz Universität Hannover

zur Erlangung des Grades

DOKTOR DER NATURWISSENSCHAFTEN

Dr. rer. nat.

genehmigte Dissertation

von

Dipl.-Geow. Paul Eric Wolff

geboren am 03.09.1983 in Königstein/Ts

2014

*Referent:* Prof. Dr. Jürgen Koepke

*Koreferent:* Prof. Dr. Wolfgang Bach

*Tag der Promotion:* 04/06/2014



# Table of content

Abstract.....	VII
Zusammenfassung .....	IX

## **Chapter A - Hydrothermal circulation in the lower oceanic crust at fast-spreading ridges..... 11**

A.1 Introduction .....	11
A.2 Accretion and structure of the oceanic crust at fast-spreading ridges and the need for hydrothermal cooling of the lower oceanic crust .....	13
A.3 The Semail ophiolite (Oman) as unique resource to study processes of the lower oceanic crust.....	15
A.4 The record of high temperature hydrothermal alteration of the deep oceanic crust .....	19
Determining high temperature hydrothermal circulation in the lower oceanic crust.....	20
A.4.1 The discovery of the fluid-triggered hydrous partial melting reaction in the deep oceanic crust.....	22
A.4.2 Using isotopic data as indicator for water/rock interactions .....	23
A.5 Outline and aims of this study.....	24

## **Chapter B - The record of hydrothermal imprint from magmatic to low temperature in a layered gabbro series from the Wadi Wariyah (Oman ophiolite)..... 25**

B.1 Geological setting and previous work.....	25
B.2 Field description of dikes and veins from the Wadi Wariyah.....	27
B.2.1 Field orientation, amount and spacing of dikes, veins, and halos within the layered gabbro of Wadi Wariyah .....	31
B.3 Analytical Techniques.....	32
B.3.1 Sample selection and preparation.....	33
B.3.2 X-ray fluorescence (XRF) .....	33
B.3.3 Inductively Coupled Plasma Mass Spectrometry (ICP-MS).....	34
B.3.4 Comparison between XRF and ICP-MS analysis.....	34
B.3.5 Electron microprobe analysis (EMPA).....	36
B.3.6 Laser Ablation ICP-MS .....	37
B.3.7 Multi Collector-ICP-MS.....	38

B.3.8 Laser Fluorination .....	38
B.4 Petrographic record of dikes/veins, altered gabbro, and layered gabbro .....	38
B.4.1 Layered gabbro .....	39
B.4.2 Gabbroic Dikes .....	40
B.4.3 Dark veins .....	44
B.4.4 Epidote veins .....	45
B.4.5 Prehnite veins .....	47
B.4.6 Halos, altered gabbro, and highly altered gabbro .....	47
B.4.7 An-bearing metagabbro .....	47
B.5 Bulk rock chemistry .....	48
B.5.1 Major elements .....	48
B.5.2 Trace elements .....	50
B.5.3 Rare earth elements (REE) .....	53
B.6 Mineral chemistry .....	55
B.6.1 Major elements .....	55
B.6.2 Trace elements including REE .....	62
B.7 Isotopic composition .....	66
B.8 Discussion .....	67
B.8.1 Formation conditions of the hydrothermal system .....	67
B.8.1.1 Estimations of formation temperature .....	67
B.8.1.2 Determination of water/rock ( <i>W/R</i> ) ratios and alteration temperatures .....	73
B.8.1.1 Synopsis of dike and vein formation .....	75
B.8.2 The hydrous partial melting reaction as indicator for water/rock interactions at very high temperatures .....	75
B.8.3 Formation and evolution of amphibole tracing very high and high temperature reaction at the transition between magmatic to hydrothermal conditions .....	79
B.8.3.1 Origin of magmatic pargasite and metamorphic evolution to hornblende /actinolite .....	79
B.8.3.2 Formation of Cl-rich amphiboles by a seawater-derived hydrothermal brine ...	81
B.8.4 Formation of epidote veins as indicator for fluid/rock interactions of the layered gabbro and gabbroic dikes .....	82
B.8.4.1 <sup>87</sup> Sr/ <sup>86</sup> Sr systematic between epidote veins and altered gabbros - complex element exchange with a transient fluid-vapour during hydrothermal alteration .....	83
B.8.5 Low-temperature seawater-rock interactions in the Wadi Wariyah .....	86
B.8.5.1 Anorthitization of gabbroic rocks as indicator for high temperature pervasive hydrothermal alteration .....	87
B.8.6 The use of the same pathways during multi-stage hydrothermal alteration of the lower gabbro section .....	88
B.9 Conclusions .....	89

**Chapter C - The reaction mechanism of fluid-induced partial melting of gabbros in the oceanic crust .....** **91**

C.1 Abstract .....	91
C.2 Introduction .....	92
C.3 Experimental and analytical techniques .....	94

C.3.1	Experimental techniques.....	94
C.3.2	Starting material .....	95
C.3.3	Electron microprobe analysis .....	96
C.4	Experimental results .....	98
C.4.1	Phase relation and textural features .....	98
C.4.2	Mineral composition.....	101
C.4.3	Melt composition.....	104
C.5	Discussion.....	106
C.5.1	State of equilibrium; comparison to equilibrium experiments .....	106
C.5.2	Formation of immiscible melts and implication for natural systems .....	108
C.5.3	Details of the hydrous partial melting reaction .....	109
C.5.4	Application to nature - implication for the late stage evolution of oceanic gabbros .....	111
C.5.4.1	Zone of An-rich plagioclase .....	111
C.5.4.2	Consistence in the observed textural details.....	113
C.5.5	Absence of percolating, highly differentiated melts as source for the precipitation of late-stage silicate minerals in natural gabbros .....	113
C.6	Conclusions .....	116

**Chapter D - Implications for the hydrothermal circulation in the lower oceanic crust at fast-spreading ridges..... 118**

References.....	123
Tables.....	130
Appendix.....	161
Acknowledgments .....	163
Curriculum vitae .....	164
List of Publications .....	165

# Abstract

Hydrothermal circulation within the oceanic crust at fast-spreading ridges is one of the key processes controlling the cooling of the oceanic crust. During hydrothermal circulation, the crust undergoes extensive chemical exchange with seawater. If during the accretion of the lower crust in-situ crystallization of deep gabbros plays a significant role (so-called "*sheeted sill model*"), thermal models suggest that extensive hydrothermal circulation within the lower section of the oceanic crust must exist.

However, the extent and temperature of hydrothermal circulation within the lower oceanic crust and related petrological record are still poorly constrained. This thesis presents a complementary approach of partial melting experiments on oceanic gabbros and petrological, geochemical and isotopic data from hydrothermal dikes and veins crosscutting a layered olivine gabbro from the Wadi Wariyah in the Southern Oman ophiolite, forming the deepest parts of the crustal series in the Oman ophiolite. The results show that hydrothermal activity within the lower crust starts at very high temperature and very low water/rock ratios (0.4-6) with the production of amphibole-bearing dikes and veins. Complementary experimental results, characteristic mineral assemblages, and trace element modelling suggest partial melting of the layered gabbro triggered by aqueous fluids at temperatures of about 1000°C (based on amphibole thermometry). Rims of amphibole extremely enriched in chlorine (up to 5 wt%) indicate the influence of very Cl-rich brines (vapour) at the transition between the magmatic and metamorphic regime (temperatures: 500-800°C). At lower temperatures, hydrothermal circulation produced veins consisting of greenschist facies minerals (epidote, chlorite, and actinolite). Isotopic data indicate an interaction between gabbro and hydrothermal fluid at temperatures between 300-500°C and water/rock ratios between 0.7-15.2. In a final stage, cm-thick monomineralic prehnite veins indicate low temperature hydrothermal circulation at temperatures around 250°C and the highest water/rock ratios of up to 18.8.

The results suggest that the hydrothermal alteration within the lower oceanic crust proceeds in multiple stages from "*magmatic*" to very low temperatures with increasing water/rock ratios and decreasing temperature. The study highlights that the same pathways were used at different temperatures for hydrothermal circulation. Conclusively, hydrothermal circulation at magmatic temperatures needs to be considered for thermal models regarding cooling of the deep oceanic crust via fluid circulation.

*Keywords: hydrothermal alteration, fast-spreading ridges, layered gabbro, Oman ophiolite, water-rock interactions, strontium isotopes, oxygen isotopes, experimental petrology, partial melting, oceanic gabbro, immiscible melts*





# Zusammenfassung

Hydrothermale Zirkulation innerhalb der ozeanischen Kruste an schnell spreizenden Rückensystemen ist ein bedeutender Prozess, der die Kühlung der ozeanischen Kruste kontrolliert. Die hydrothermale Zirkulation bewirkt für die Kruste einen intensiven chemischen Austausch mit Meerwasser. Sollte bei der Bildung von ozeanischer Kruste in-situ Kristallisation tiefer Gabbros wichtige Rolle spielen („*sheeted sill model*“), deuten thermische Modelle darauf hin, dass extensive hydrothermale Zirkulation in der unteren ozeanischen Kruste vorhanden sein muss.

Die Ausdehnung, maximale Temperaturen und der damit verbundene petrographische Nachweis von hydrothermalen Zirkulation innerhalb der unteren ozeanischen Kruste sind allerdings erst wenig erforscht. Die vorliegende Dissertation präsentiert komplementäre Untersuchungen von partiellen Schmelzexperimenten an natürlichen ozeanischen Gabbros sowie eine detaillierte petrographische und geochemische Studie hydrothermalen Gänge in einem lagigen Olivingabbro aus dem Wadi Wariyah im südlichen Oman Ophiolite, welcher den tiefsten Teil der Kruste im Oman Ophiolite bildet. Die Ergebnisse zeigen, dass innerhalb der unteren Kruste die hydrothermale Aktivität mit der Bildung von Amphibole-führenden Gängen bei sehr hohen Temperaturen und sehr geringen Wasser/Gesteins-Verhältnissen (0,4-6) beginnt. Die Ergebnisse der komplementären experimentellen Studie in Zusammenhang mit charakteristischen Paragenesen und Spurenelementmodellierung von partiellem Schmelzen weisen darauf hin, dass bei Temperaturen von ca. 1000°C (bestimmt durch Amphibol-Thermometrie) wasserreiche Fluide eine partielle Schmelzreaktion innerhalb des Olivingabbros auslösen. Amphibole, extrem angereichert an Chlor (bis zu 5 Gew%), zeigen den Einfluss von Cl-reichen wässrigen Fluiden im Übergang zwischen magmatischen zu metamorphen Bedingungen (500-800°C) an. Mit abnehmender Temperatur bilden sich Gänge mit typischen Mineralen der Grünschieferfazies (Epidote, Chlorit und Aktinolith). Isotopendaten deuten auf eine Wechselwirkung zwischen dem Olivingabbro und hydrothermalen Fluiden bei Temperaturen von 300-500°C und Wasser/Gesteins-Verhältnissen zwischen 0,7-15,2 hin. In der letzten Stufe der hydrothermalen Überprägung entstehen cm-dicke Gänge aus monomineralischem Prehnit, die hydrothermale Alteration bei sehr niedrigen Temperaturen um 250°C und sehr hohe Wasser/Gesteins-Verhältnissen von bis zu 18,8 anzeigen.

Die Ergebnisse deuten darauf hin, dass hydrothermale Alteration innerhalb der unteren ozeanischen Kruste in mehreren Schritten von „*magmatischen*“ bis hin zu sehr niedrigen Temperaturen verläuft. Dabei steigen die Wasser/Gesteins-Verhältnisse mit abnehmender Temperatur. Die Studie zeigt, dass die gleichen Pfade für die hydrothermal Überprägung

der unteren Kruste bei sehr hohen als auch bei sehr niedrigen Temperaturen durchflossen werden. Hydrothermale Alteration bei sehr hohen Temperaturen muss bei der Erstellung von thermischen Modellen für die Abkühlungsgeschichte der ozeanischen Kruste mit berücksichtigt werden.

*Schlagwörter: Hydrothermale Zirkulation, schnell-spreizenden Rücken, lagige Gabbros, Oman ophiolite, Wasser-Gestein Reaktionen, Strontium Isotope, Sauerstoff Isotope, experimentelle Petrologie, partielle Schmelzen, ozeanische Gabbros, nicht mischbare Schmelzen*

# Chapter A

## Hydrothermal circulation in the lower oceanic crust at fast-spreading ridges

### A.1 Introduction

Hydrothermal circulation of seawater below mid-ocean ridges is one of the key processes controlling the chemical exchange between two of the major reservoirs on Earth (ocean and oceanic crust) and it is regarded to provide sufficient cooling of newly formed oceanic crust. Consequently, it plays a fundamental role in the Earth's heat budget and it is regarded to explain heat flow anomalies. Hydrothermal alteration results in the metamorphism of oceanic crustal rocks at depth and in the formation of black smokers, associated with metalliferous deposits on the seafloor, and one of the most extraordinary ecological niches for life on Earth.

Since the first discovery of seafloor hydrothermal vents in the late 1970s [*Corliss et al.*, 1979], a large variety of hydrothermal vents were recognized at the seafloor of slow and fast-spreading oceanic ridges [*Hannington et al.*, 2011]. After many years of intensive studies on the processes related to hydrothermal circulation at mid-ocean ridges it is now widely accepted that hydrothermal circulation operates by seawater penetrating into fractures of the oceanic crust. The seawater is heated up, reaching temperatures that can exceed a maximum of 400°C, undergoes chemical and mass exchange with the surrounding rock, and then discharge as a chemical modified hydrothermal vents fluid at the seafloor (Figure 1) [*German and Van Damm*, 2008; *Alt and Bach*, 2008].

Models for hydrothermal convection cell generally consider that hydrothermal circulation is restricted to the upper parts of the oceanic crust: pillow basalts, sheeted dike complex, and the gabbro/dike transition. These rocks usually show hydrothermal alteration within the greenschist facies resulting in typical mineral assemblages [*Alt*, 1995; *Humphris and*

Thompson, 1978]. Underlying gabbroic rocks recovered from the seafloor as well as studies on deep crustal gabbroic rocks from old fragments of oceanic crust (Ophiolites), however, often displays evidence for extensive interaction with seawater with hot seawater-derived fluids. These rocks usually show typical metamorphism of hydrothermal reaction lower than about 500°C resulted from seawater penetrating down in cracks created as the response of thermal contraction of the cooling of the lithosphere, as it spread away from the ridge [Lister, 1974]. In the last decades, more and more studies indicate that many of the gabbroic rocks have experienced hydrothermal reactions, which occur at temperatures greater than 500°C. Petrological investigations imply that hydrothermal reactions starts at temperatures up to 1000°C [Bosch *et al.*, 2004; Nicolas and Mainprince, 2005], which may causes hydrous partial melting within gabbroic protolith near “magmatic” conditions. These findings suggest that early hydrothermal circulation, near the ridge, is not confined to the uppermost lavas and sheeted dike crustal unit, but may also operates into the lower sections of the oceanic crust (Figure 1). Furthermore, some thermal and accretion models of oceanic crust at fast-spreading ridges indicate that hydrothermal circulation within the lower oceanic crust is an essential requirement to provide sufficient cooling to the deep oceanic lithosphere (see below). Even though these are indicators for hydrothermal circulation operating at high temperature in the lower oceanic crust, it has not been directly observed so far in recent oceanic crust. Thus, the extent, maximum temperatures as well as the petrological record and the principal reactions related to the hydrothermal alteration of the lower oceanic crust are only insufficient investigated and still under debate.

This study focus on the petrological record and related reaction of hydrothermal circulation, with a special focus on the high temperature hydrothermal reactions, within the lower oceanic crust based on a complementary study of hydrothermal dikes and veins within a gabbro from the deep crust of the Semail ophiolite (Oman) combined with an experimental study to answer some of the major questions addressed to hydrothermal

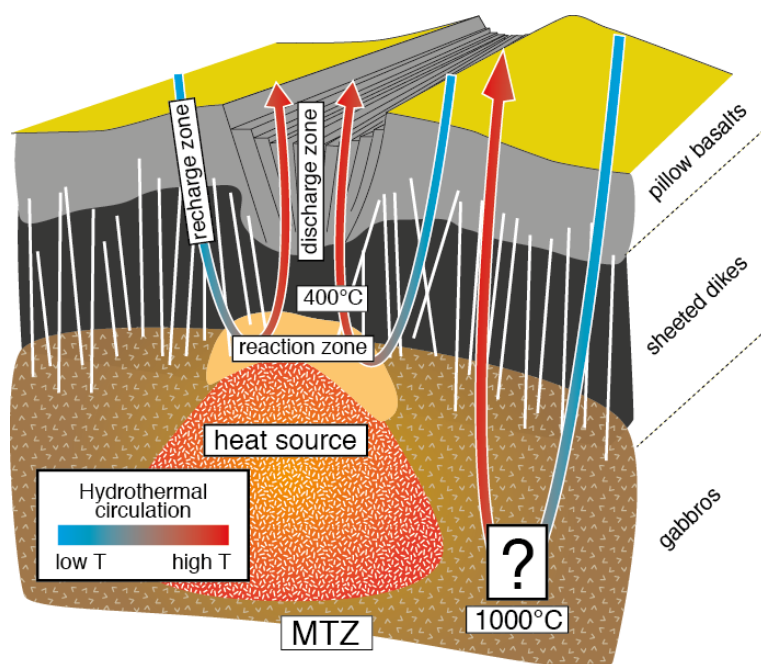


**Figure 1.** Schematic illustration of the mechanism of submarine hydrothermal systems below fast-spreading mid ocean ridges. The three main reaction stages of the hydrothermal circulation within the pillow basalts and sheeted dikes are shown [after German and Van Damm, 2006]. Beside the well-known hydrothermal circulation in the pillow basalts and sheeted dikes operating at about 400°C, some studies indicate that many gabbros from the lower crust experienced also a hydrothermal alteration of temperatures up to 1000°C (for details see text), leading to the hypothesis that hydrothermal circulation at fast-spreading ridges is also active in the lower crust. MTZ = Moho Transition Zone.

circulation in the lower oceanic crust: (1) What is the petrological record of high temperature hydrothermal alteration in the lower oceanic crust? (2) What are the reactions related to high temperature hydrothermal activity? (3) How is high temperature hydrothermal alteration related to the well-known lower temperature hydrothermal alteration?

## A.2 Accretion and structure of the oceanic crust at fast-spreading ridges and the need for hydrothermal cooling of the lower oceanic crust

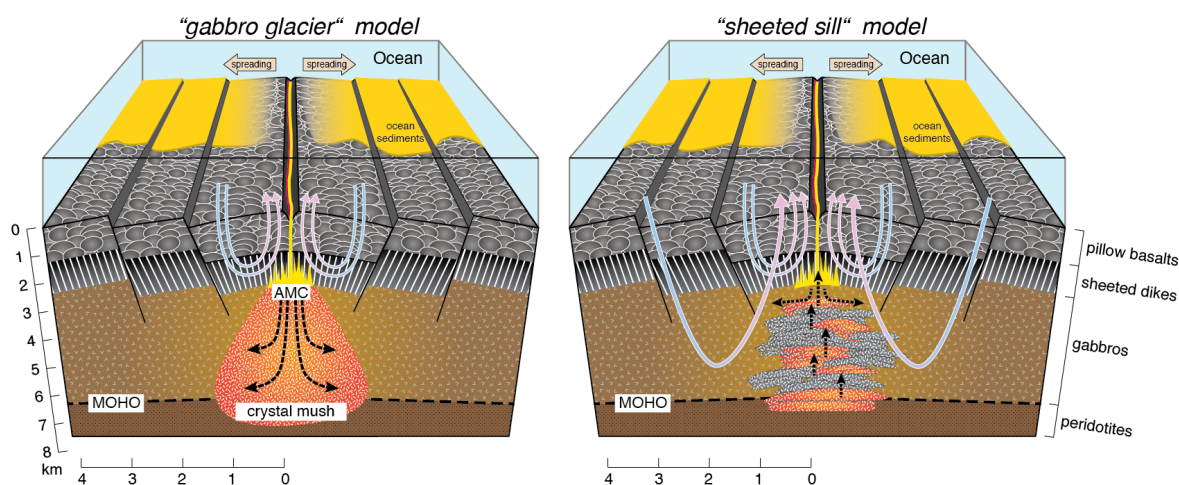


**Figure 2.** Two end member models for crustal accretion at fast-spreading ridges. Note, that for the “sheeted sill” model (right) a significant cooling of the lower oceanic crust is necessary. Most probably, a seawater derived hydrothermal circulation operating at high temperatures enables the cooling of the deep oceanic crust. This in contrast to the well-known hydrothermal circulation, which cools the sheeted dikes and pillow basalts in the “gabbro glacier” model. See text for more details.

Formation of oceanic crust at mid-ocean ridge systems plays a fundamental role in the plate-tectonic cycle of the Earth. Extending about 50-60,000 km across the ocean floor, about two thirds of the Earth’s surface is covered by oceanic crust producing a total amount of about 3 km<sup>2</sup> new oceanic crust per year. About one third of the oceanic crust is formed in a fast-spreading environment (spreading rate >40 mm/yr.). The general igneous structure of the oceanic crust created at fast-spreading ridges exhibits a relatively uniform seismic stratigraphy [e.g., Canales *et. al.*, 2003] and is regarded as layered and relatively homogeneous (Figure 2). Below oceanic sediments, the top two layers consist of lava flows and pillow basalts (~1-2 km thick) underlain by a sheeted dike complex (~1-2 km thick). A 3-5 km thick gabbroic unit of variable texture and lithologies underlies the volcanic sections. Finally, ultramafic rock of the lower crust and mantle, including harzburgites and dunites, characterize the transition between crust and the mantle. Seismic and tomographic imaging of the crust beneath the East Pacific Rise shows that a thin (~50 m) and narrow (0.5-1.5 km) melt lens occurs at 1-2 km depth [Sinton and Detrick, 1992]. Beneath the melt lens a wider region of low velocities indicates the presence of coexisting melt and crystals (so-called “mush zone”). It has been well established that the diversity of

lithologies in the lower oceanic crust derives as cumulates from crystallization of tholeiitic basalts at low pressure (100-200 MPa). These include mainly olivine gabbros and gabbros with subordinated gabbro-norites, oxide gabbros, and troctolites. Experimental studies and texture of basalts and plutonic rocks, as well as geochemical studies provide evidences for a general low-pressure crystallization order in mid-ocean ridge basalts: olivine  $\Rightarrow$  olivine + plagioclase  $\Rightarrow$  olivine + plagioclase + clinopyroxene [e.g., Grove *et al.*, 1992] resulting in an average mode for olivine gabbros from fast-spreading oceanic crust of 8% olivine, 57% plagioclase, and 33% clinopyroxene [Coogan, 2007].

One question still remains under debate is how the lower oceanic accrete and the way that the produced heat is removed in order to provide sufficient cooling of newly formed oceanic crust. Based on petrologic and geophysical observation two general accretion models are discussed (Figure 2): (1) the “*gabbro glacier*” model [Henstock, 1993; 2002; Phipps Morgan and Chen, 1993; Quick and Denlinger, 1993] and (2) the “*sheeted sills*” model [Bédard *et al.*, 1988; Boudier *et al.*, 1996; Kelemen *et al.*, 1997; Korenaga and Kelemen, 1998]. The “*gabbro glacier*” model assumes that most of the crystallization occurs within the shallow melt lens. The crystals subside down to form the entire lower oceanic crust. In this model the overlying hydrothermal circulation in the sheeted dikes and pillows basalts removes the latent heat of crystallization. In contrast, the “*sheeted sill*” model assumes that crystallization occurs in-situ in multiple sills. This model was developed on the basis of gabbroic sills within a mantle section of the Semail ophiolite, which were interpreted as in-situ crystallization products [Kelemen *et al.*, 1997]. Extrapolation leads to the conclusion that most or almost the entire deep oceanic crust may crystallize in-situ in a multiple sill complex. Moreover, a recent direct sampling of deep fast-spreading crust at Hess Deep in the equatorial East Pacific Rise (EPR) provides robust evidence against the “*gabbro glacier*” model implying that a significant part of the lower oceanic is indeed formed rather by sill-like intrusions than by a gabbroic suspension current originated from the axial melt lens [Gillis *et al.*, 2013].

Even if the precise structure of the lower oceanic crust still remains unclear and might be a hybrid of the two end member models [Coogan *et al.*, 2002c; Korenaga and Kelemen, 1998], at least for the “*sheeted sill*” model one strong requirement is a significant cooling through the lower crust, to discharge the latent heat of crystallization and to avoid large melting of the lower crust [Chen, 2001; Cherkaoui *et al.*, 2003; Maclennan *et al.*, 2004]. Thermal models on the accretion of fast-spreading oceanic crust imply that this cooling can only be facilitated by hydrothermal convection operating in the lower oceanic crust at high to very high temperatures [Chen, 2001; Maclennan *et al.*, 2004; 2005] leading to closely spaced, near vertical isotherms.

Furthermore, thermal models on the heat flow of the oceanic lithosphere provide the need of hydrothermal circulation by a strong discrepancy between the observed heat flow and the prediction of conductive cooling models (Figure 3), which can be only balanced by cooling as a result of hydrothermal circulation [Stein and Stein, 1994]. In these model about 34% of the predicted global heat flux ( $32 \times 10^{12}$  W) must result from hydrothermal

---

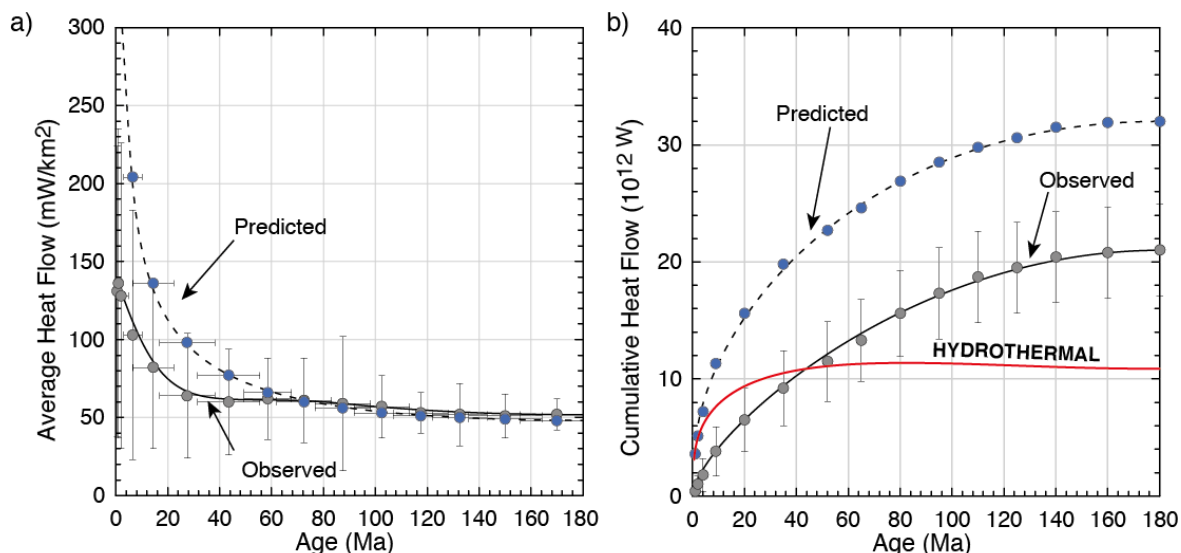


**Figure 3.** (a) Observed and predicted average conductive heat flow versus the age of the oceanic lithosphere. (b) Cumulative heat flux versus age of oceanic crust separated into observed (conductive). The predicted heat flux based on the lithospheric cooling model GDH1. Hydrothermal heat flux is the predicted minus observed heat flux. Both figures based on constraints from *Stein and Stein* [1994].

circulation. Thus, if hydrothermal circulation exists in the lower oceanic crust operating at high temperatures it may contribute to the hydrothermal circulation at fast-spreading ridges in order to remove the heat of crystallization and balance the heat flow. Since most of the models do not include high temperature hydrothermal circulation of the lower oceanic crust, because the related reactions and the petrological record are still not entirely understood, it is necessary to perform detailed studies on the petrological record of hydrothermal alteration in the lower oceanic crust.

### A.3 The Semail ophiolite (Oman) as unique resource to study processes of the lower oceanic crust

Due to the inaccessibility of the lower oceanic crust at modern fast-spreading ridges our knowledge of the petrology and structure of lower oceanic crust derives mainly from four sources: ophiolite complex, which represents old fragments of oceanic crust obducted on land; drilling of oceanic crust; exposures of the lower oceanic crust in oceanic core complexity, at fracture zones and at tectonic windows; and indirect observations derived geophysical studies, i.e. by seismic studies.

For the reason that only relative few samples of the lower oceanic crust are available and that till today no coherent section through the entire lower oceanic crust at fast-spreading ridges exists, the petrological structure of the lower oceanic crust and related processes are primary constrained from observation in ophiolites [*Coleman, 1977; Nicolas, 1989*]. The irrefutable similarity of ophiolites to modern mid-ocean ridges makes ophiolites to a unique and essential resource to study mid-ocean ridge processes. Especially, the Semail ophiolite in the Northern Oman and United Arabian Emirates (U.A.E.) is regarded to be

one of the best-preserved and best-studied ophiolites on Earth, and studies from this ophiolite lead to tremendous understanding of how modern mid-ocean ridge form.

The Semail ophiolite extends c. 550 km long and max. 150 km wide, which makes it the largest fragment of oceanic crust obducted on land. It was formed in the Neotethys during the Upper Cretaceous [e.g., *Searle and Cox*, 1999]. Plagiogranite bodies within the ophiolite have been dated at  $95.3 \pm 0.2$  Ma [*Rioux et al.*, 2013; *Warren et al.*, 2005], which marks the formation age of the rocks now exposed. The equivalent structure of the Semail ophiolite clearly indicates that the crust formed in a submarine spreading environment analogue to modern mid-ocean ridge systems at fast-spreading ridges (Figure 4). Nevertheless, many researches have pointed out the complex tectonic history of the ophiolite and demonstrated the important differences between the Semail ophiolite and recent mid-ocean ridge systems. These include geochemical differences between the volcanic rocks and mid-ocean ridge basalts [*Alabaster et al.*, 1982; *Ernewein et al.*, 1988; *MacLeod et al.*, 2013; *Pearce et al.*, 1981], and the presence of special plutonic sequences and lithologies [*Goodenough et al.*, 2010; *Koepke et al.*, 2009; *Rioux et al.*, 2013; *Tamura et al.*, 2008; *Tsuchiya et al.*, 2012] within the mantle and the crustal sections. For some authors, these differences are regarded to be due the ophiolite formed on top of a steeply NE-dipping subduction zone. This results in the detachment of cold oceanic crust steeply dipping to cause a high-pressure record in the underlying metamorphic sole [*Boudier and Nicolas*, 1985; *Searle and Cox*, 1999]. The contentious debate is on going since decades about whether the Semail ophiolite has been formed in a fast-spreading mid-ocean ridge system or a supra-subduction zone setting. Nowadays, some scientists regard the Semail ophiolite as subduction zone related [e.g., *Dilek and Furnes*, 2011; *Stern et al.*, 2012]. For other authors, the subduction zone-related processes are post-dated the ophiolite genesis (approximately 1 Ma) [*Rioux et al.*, 2013], or were very shallow dipping, initiated by “*hot intra-oceanic thrusting*” regarded to indicating the origin of the obduction process [e.g., *Boudier and Nicolas*, 2007; *Koepke et al.*, 2009; *Yamasaki et al.*, 2006]. However, due to the good accessibility and the evidently similarity to recent oceanic gabbros from fast-spreading ridge [e.g., *Gillis et al.*, 2013], the lower crust exposed in the Semail ophiolite is a unique resource to study mid-ocean ridge processes as well as the record of hydrothermal alteration of the lower oceanic crust, but petrological/geochemical models derived from gabbroic rocks from the of the Semail ophiolite must handled with care due to the unclear geotectonic setting of this ophiolite (subduction zone-related magmatism vs. mid-ocean ridge processes magmatism).

The lower crust of the Semail ophiolite is well exposed over the entire ophiolite and displays many coherent sections through the lower crust [e.g., *Browning*, 1980; *Hopson et al.*, 1981; *MacLeod and Yaouancq*, 2000; *Pallister and Hopson*, 1981; *Yaouancq and MacLeod*, 2000] resulting in the general crustal stratigraphy starting from the sheeted dike-gabbro transition zone: varitextured gabbro (0.1-1 km); foliated gabbro (0.3-2 km); layered gabbro (1-4 km); and ultramafic rocks from Moho transitional zone of variable thickness (Figure 4) [thicknesses after *Coogan et al.*, 2002a]. The upper section composed of the varitextured gabbros, consisting gabbro with variable grain size and textures, is considered as products derived directly from fractional crystallization of the shallow melt lens [*Yaouancq and MacLeod*, 2000; see also *Koepke et al.*, 2011 for recent oceanic crust from EPR]. In contrast, the lower sections of the lower crust are regarded to derived from crystal

---



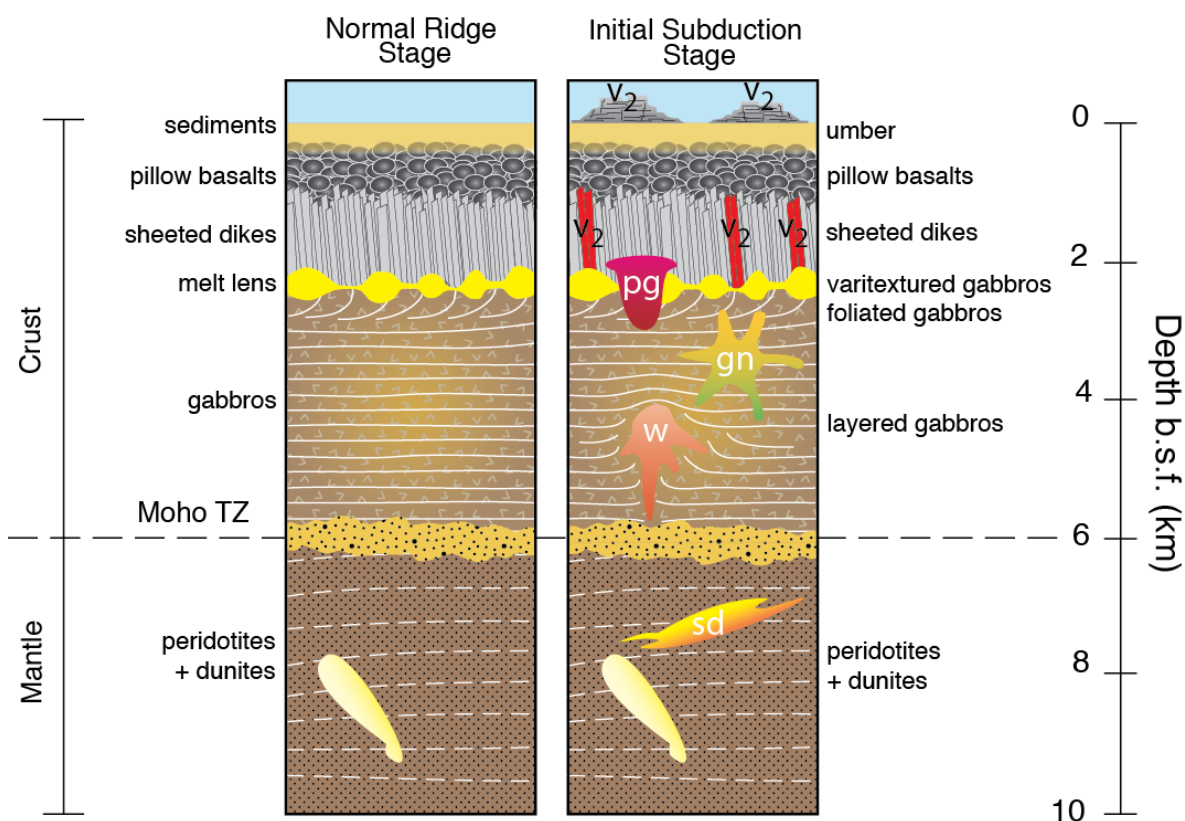


**Figure 4.** Petrological model for the Oman ophiolite compared to modern mid-ocean ridges at fast-spreading ridges. *Left:* Normal ridge stage representing the model for the stratigraphic structure of oceanic crust formed at fast-spreading ridges. Moho TZ represents the Moho Transition Zone, which can vary in thickness and composition. Yellow field in the mantle section marks crosscutting dunites of variable thickness. *Right:* Initial subduction stage of the Oman ophiolite. The beginning of subduction causes characteristic crosscutting lithologies: “secondary dunites” (sd), wehrlites (w), gabbroonorites (gn), large plagiogranitic bodies (pg) and secondary volcanics ( $v_2$ ) with typical arc-type signature as sheeted dikes and sheet flow.

precipitations left after the partial crystallization of a basaltic magma and then subsequently removed from remaining magma. It mainly composed of the constituent minerals olivine, plagioclase, and clinopyroxene forming medium-grained olivine gabbros with a cumulate texture and alternating layering. The layering is defined by variation in the modal proportions of the main mineral constituent on a cm to dm scale. It may be caused by tectonic transport of melt either as sinking from above as it crystallize from the melt lens or as flowing from beneath as it is extracted from the mantle. *Henstock et al.* [1993] originated the layering from cyclic melts rather than sedimentation at the bottom of an axial melt lens followed by a deformation process. Another possible explanation is that the layers are frozen, stacked sill intrusion, which show regular “graded” modal layering [Boudier et al., 1996; Kelemen et al., 1997; Lissenberg et al., 2004]. That gabbros from modern fast-spreading crust are also layered was recently confirmed by direct sampling of EPR deep gabbros [Gillis et al., 2013].

In principle, the layered gabbros show very primitive composition with Mg# ( $Mg\# = [Mg^{2+}/Mg^{2+}+Fe^{2+}] \times 100$  on a molar base) in excess of 70-80, very low incompatible element concentration (e.g.,  $K_2O$ ,  $TiO_2$ , Zr), and depleted rare earth element (REE) concentrations. A positive Eu anomaly indicates the accumulation of plagioclase within these rocks. Mineral compositions strongly reflects the crystallization products in parental

MORB and show primitive to slight evolved composition lead to high Mg# in olivine and clinopyroxene, and high An ( $An = [Ca^{2+}/Ca^{2+}+Na^{2+}+K^{2+}] \times 100$  on a molar base) content in plagioclase. Compositional variation of the minerals is relatively small over the entire crustal section, which varies in thickness from 2 to 4 km [Lippard *et al.*, 1986; MacLeod and Yaouancq, 2000; Nicolas, 1989; Pallister and Hopson, 1981; Yaouancq and MacLeod, 2000]. However, Browning [1980; 1982] showed based on electron microprobe analyses of a 600 m thick layered gabbro section from the Wadi Abyad that the layered gabbro shows a further cyclicity in phase composition on a scale of 5-100 m. He interpreted that as repeated feeding of the magma chamber by more primitive magma from the mantle. The textural and compositional features of the lower gabbro section of the Semail ophiolite are in good agreement with gabbroic rocks recovered from modern mid-ocean ridges at fast-spreading ridges making studies on gabbroic rocks from the Semail ophiolite an essential resource to determine the structure, formation, and composition of modern deep crustal section at fast-spreading ridges [e.g., Coogan, 2007].

Beside the igneous formation of the gabbroic rocks from the Semail ophiolite, many studies pointed out that the record of hydrothermal alteration in these rocks also indicate possible deep hydrothermal activity at high temperature in the lower oceanic crust. The existence of a deep high temperature hydrothermal system was first reported from Gregory and Taylor [1981], on basis of oxygen isotopes, and from Lanphere [1981] and McCulloch *et al.* [1980], on the basis of strontium isotopic data of the lower crustal section. These authors proposed that seawater contamination proceeded within the lower crust at high to very high temperatures of the lower crustal section. Later, Nehlig and Juteau [1988] described a complex vein system in the Semail ophiolite composed of amphibole, epidote, and prehnite veins indicating high to low temperature hydrothermal alteration penetrating through the deep sections of the Semail ophiolite. The observation of amphibole- and orthopyroxene-bearing dikes and veins within the gabbroic sections point towards even higher temperature of hydrothermal alteration at “near magmatic” conditions [Bosch *et al.*, 2004; Nicolas *et al.*, 2003]. If the observed hydrothermal systems can be directly applied to modern fast-spreading ridges, studying the hydrothermal record of such deep gabbros from the Semail ophiolite may provide new insights into the geodynamics of hydrothermal circulation at mid-ocean ridges.

---

## A.4 The record of high temperature hydrothermal alteration of the deep oceanic crust

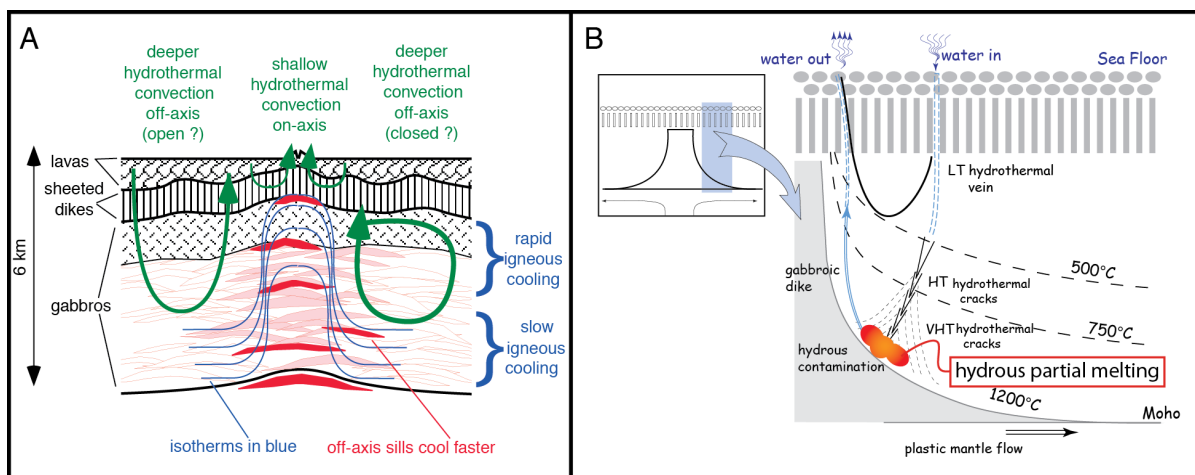


**Figure 5.** Two conceptual models of fast-spreading crust and related high temperature hydrothermal convection derived from the Semail ophiolite. (a) Model of *Garrido et al.* [2001] explaining bimodal cooling rates observed for the lower oceanic crust by different hydrothermal convection systems (green curve). (b) Model of high temperature seawater hydrothermal circulation at fast-spreading ridges [from *Bosch et al.*, 2004]. Double dashed lines indicate the penetration of seawater into the oceanic crust. Seawater is penetrating down to regions of high temperatures causing hydrous partial melting in this region.

The existence of a simultaneous near-ridge deep high temperature hydrothermal system was first postulated by studies in the Semail ophiolite. Most effective is the migration of seawater (recharge) along cracks, which requires relatively low temperatures where the rock behaves brittle. In the last decade the maximum temperatures related to these hydrothermal processes in the lower oceanic crust have been shifted to higher values. It was early postulated that the crack network crosscut both fresh and undeformed rocks and metamorphosed rocks at temperatures below 500°C [*Lister*, 1974]. This leads to an increase of permeability in the crust, which allows seawater to circulate. *Mével and Cannat* [1991] presented a model on natural oceanic gabbros from slow spreading ridges that hydration of the lower crust starts at temperatures about 750°C. Higher temperatures, above 800°C down to the petrological Moho, have been described in gabbros from *Manning et al.* [2000] based on thermometry of amphibole-plagioclase composition in a network of micro fractures. *Koepke et al.* [2005a; 2005b; 2014 in press] showed on characteristic microstructures, found in many samples from natural oceanic gabbro and the Semail ophiolite, that water/rock interaction may occur at temperatures around 900-1000°C. The highest temperatures for deep hydrothermal circulation in gabbros so far recorded have been reported from two studies in the Semail ophiolite, showing that hydrothermal circulation is operating via microcracks at temperatures up to 1000°C [*Bosch et al.*, 2004; *Nicolas et al.*, 2003]. As shown in the previous section, many evidences support a model that high temperature hydrothermal convections operate in the lower oceanic crust and some studies aimed to characterize this system, mostly based on observation from the Semail ophiolite. *Garrido et al.* [2001] estimated cooling rates of the lower crust based on crystal distribution data of plagioclase. Their interpretation implies a bimodal cooling of the lower oceanic crust (Figure 5a).

The possible existence of high-temperature has been published, since the first isotopic studies on lower crustal gabbroic rocks from the Semail ophiolite (see section A.3). The hypothesis was established that lower crustal gabbros underwent high-temperature alteration by seawater-derived fluids that shifted the oxygen isotopic record to lower values, and  $^{87}\text{Sr}/^{86}\text{Sr}$  to higher values. Water/rock ( $W/R$ ) ratios were estimated to be low [Gregory and Taylor, 1981; McCulloch *et al.*, 1980]. Based on these observations, Nicolas *et al.* [2003] and Bosch *et al.* [2004] presented a possible model of the existence of a high-temperature hydrothermal circulation system operating at temperatures up to 1000°C via microcracks (Figure 5b). According to these authors, the microcracks are generated in hot, ductile, just frozen gabbros, initiated by the contradiction of orientated plagioclase due to the high anisotropy of thermal contraction in plagioclase. The isotopic geochemical record of the phases produced (e.g., amphibole) indicates that seawater-derived fluids were involved during the formation of these minerals [Bosch *et al.*, 2004]. Another model obtained from observations in the Oman ophiolite is that of Abily *et al.* [2011] who proposed that fluids might enter the deep, still very hot crust via high-temperature shear zones. Moreover, based on the petrological and isotopic results in decametre-wide zones of highly metamorphosed and strongly faulted rocks within gabbros of the Semail ophiolite, Coogan *et al.* [2006] concluded that these zones are formed by high fluid fluxes derived from seawater associated with faulting through the gabbro at high to medium temperature (300-800°C) with a characteristic shift in isotopic composition ( $\delta^{18}\text{O}$  and  $^{87}\text{Sr}/^{86}\text{Sr}$ ). These zones (so called “*focused fluid flow zones*”) may have the potential to cool newly formed oceanic crust.

## **Determining high temperature hydrothermal circulation in the lower oceanic crust**

The determination of the petrological record of hydrothermal circulation in the lower oceanic crust is challenging and not always straightforward. Due to no direct observation of hydrothermal circulation systems within lower oceanic crust of fast-spreading ridges, most of our knowledge concerning the record of hydrothermal circulation, the composition of involved hydrothermal fluids, and estimations on the temperature conditions must be based on interpretation of the alteration signal observed in natural samples of gabbroic rocks from ophiolite complexes or the recent oceanic crust. Thus, natural rocks give the primary source to study the record of hydrothermal alteration in the lower oceanic crust.

In contrast to the well-known low temperature hydrothermal alteration operating in the pillow basalts and sheeted of the oceanic crust with mainly typical mineral assemblages of the prehnite-pumpellyite to greenschist facies (100-400°C) [e.g., Alt *et al.*, 2010; Humphris and Thompson, 1978], a complete transition from very high to low temperature hydrothermal alteration is proposed to occur in the lower oceanic crust. It is likely that the record of high temperature hydrothermal alteration have been extinguished by low temperature hydrothermal alteration as the crust drifts away from the spreading centre [Stakes and Vanko, 1986]. Furthermore, the expected hydrothermal network in rocks of the oceanic crust becomes less dense with increasing depth [e.g., Bosch *et al.*, 2004; Nehlig

---

and Juteau, 1988]. Consequently, it is difficult to trace seawater circulation within the lower crust section. If interaction of lower crustal rocks with seawater (or a seawater-derived fluids) occurs at such very high temperatures, the general applied tools include chemical and petrological characterization of altered rocks and vein mineral precipitates, fluid inclusions, and analysis of stable isotopes. The primary and most obvious source for the hydrothermal record in the lower oceanic crust is the occurrence of hydrous minerals formed as vein precipitates or in reaction zones.

In terms of high temperatures hydrothermal alteration minerals commonly amphibole is regarded to be the highest temperature hydroxyl-bearing phase crystallizing in magmatic systems, indicating the presence of a water-rich fluid phase. It is obvious from many natural samples that the appearance of amphibole is not related to only one formation event. Amphiboles in mafic plutonic rocks show continuity in chemistry and crystallization temperatures between magmatic, high-grade metamorphic, and hydrothermal conditions, which indeed makes the interpretation of amphibole bearing gabbroic rocks very complex. Based on geochemical and textural features of amphibole many studies pointed out that amphibole occurs in oceanic gabbros as metamorphic [Cortesogno *et al.*, 2000], hydrothermal [Vanko, 1986], late stage magmatic phase [Dick *et al.*, 2002; Tribuzio *et al.*, 2000], or as multiple phases formed under complex formation conditions [Coogan *et al.*, 2001a; Gillis, 1996; Gillis and Meyer, 2001; Maeda *et al.*, 2002].

Beside the occurrence of hydrous phase within the oceanic gabbros, thermodynamic models show that during high temperature water/rock interaction common anhydrous minerals (olivine, plagioclase and clinopyroxene) can form, which may show only small compositional changes compared to their typical magmatic analogues derived from fractional crystallization [McCollom and Shock, 1998]. Other studies show that for certain minerals (e.g., plagioclase, clinopyroxene) water/rock interactions affect mineral composition [Marks *et al.*, 2011; Python *et al.*, 2007; Vanko and Laverne, 1998]. One key observation is that precipitation of commonly anhydrous minerals during interactions tends to produce minerals depleted in trace elements showing very primitive nearly pure endmember composition (e.g., An > 90 for plagioclase) [Vanko and Laverne, 1998].

---

### A.4.1 The discovery of the fluid-triggered hydrous partial melting reaction in the deep oceanic crust

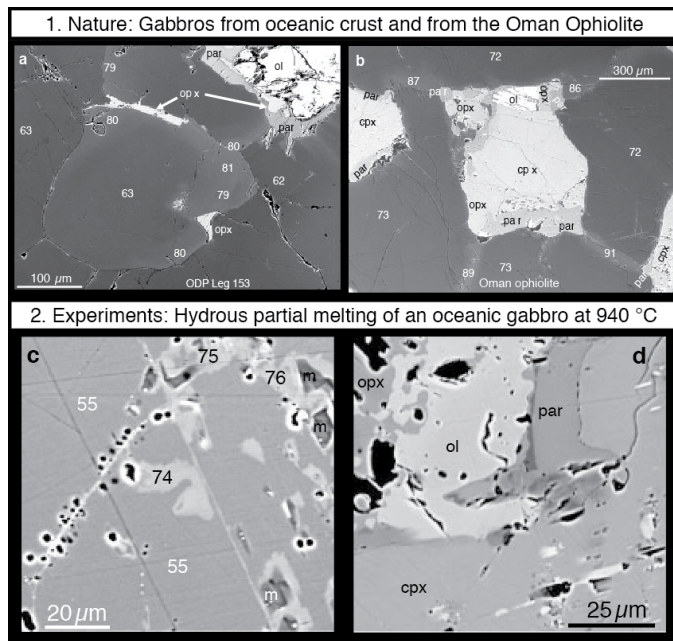


**Figure 6.** Representative backscattered electron (BSE) images of microstructures indicating hydrous partial melting within natural oceanic gabbros and the Oman ophiolite (*top*) and in corresponding experiments (*bottom*) [modified after *Koepke et al., 2005a*]. (a, b) Hydrous partial melting propagation on grain boundaries in gabbros from MAR (a) and Oman ophiolite (b): protolithic plagioclase reacts to new An-rich plagioclase on grain boundaries, which appears in lighter grey under the electron microscope. Where these zones join protolithic olivine (ol) or clinopyroxene (cpx), a reaction to orthopyroxene/pargasite parageneses (opx, par) is visible. (c, d) BSE images showing details of the complex phase relationships in an experimentally hydrous partially molten gabbro (b) Plagioclase of the protolith reacts to An-rich plagioclase and albite-rich melt (m, darker grey level). The numbers indicate the An content obtained by electron microprobe in mol.%. (c) Clinopyroxene and olivine of the protolith react to orthopyroxene and pargasite.

Most recently, one important observation concerning water/rock interactions operating at very high temperature in the lower oceanic crust is the discovery of characteristic microstructures found in many oceanic gabbros and also in gabbros from the Semail ophiolite. The occurrence of a zoning in plagioclase with plagioclase rims strongly enriched in An associated with the formation of interstitial orthopyroxene and amphibole enriched in the pargasite component suggests a partial melting reaction in the gabbro triggered by seawater-derived fluids (Figure 6) [*Koepke et al., 2005a; 2005b; 2004; 2014 in press*]. The generalised melt reaction was primarily evaluated by *Koepke et al. [2004]* and later defined by *Wolff et al. [2013]*: at temperatures between 900 and 980°C, the main constituent minerals (olivine, plagioclase, and clinopyroxene) of the gabbroic protolith react with water to form orthopyroxene, pargasitic amphibole, newly formed An-rich plagioclase, and a hydrous, silica rich melt (plagiogranitic). The observed microtextures in the natural gabbros – interstitial pargasite and orthopyroxene in intimate contact to newly formed plagioclase strongly enriched in An and depleted in trace elements – imply the propagation of water-rich fluids along grain boundaries within the deep oceanic crust at very high temperatures (900-980°C), which is in the magmatic regime.

One fundamental finding of this observation is that the newly formed plagioclase is highly enriched in An and depleted in minor and trace elements [*Koepke et al., 2014 in press*]. This does not correlate with late-stage magmatic plagioclase composition, which typically shows lower An content and enrichment in trace elements. Thus, in the observed gabbros a seawater-derived fluid triggers the formation of An-rich plagioclase, which records the first water-rock interactions in the lower oceanic crust.

Preliminary in-situ measurements of Sr isotopes performed on the newly formed plagioclase of some gabbros from the Oman using femtosecond LA-MC-ICP-MS (laser

ablation multi collector inductively coupled plasma mass spectroscopy) indicate that these plagioclase are enriched in  $^{87}\text{Sr}/^{86}\text{Sr}$  compared to the protolithic “magmatic” ratio implying a model of seawater-derived fluids percolating along grain boundaries and trigger hydrous partial melting in the gabbroic rock [Stichnothe, 2007].

One aim of the presented thesis is to verify the obtained results and to shed new light on the reaction mechanism of fluid triggered hydrous partial melting of oceanic gabbro by performing an experimental study, which complement and extend the findings of Koepke *et al.* [2004]. On the other hand plagioclase enriched in An can also formed at relatively low temperatures by the hydrothermal circulation within the sheeted dikes of Integrated Ocean Drilling Program (IODP) Hole 504B, the Oman ophiolite, and Reykjanes geothermal system [Marks *et al.*, 2011; Vanko and Laverne, 1998].

#### A.4.2 Using isotopic data as indicator for water/rock interactions

Measuring the isotopic composition in hydrothermally altered rocks and veins has been proven to be a strong tool to demonstrate the influence of water on the isotopic composition after water-rock interactions. Usually, the most common isotopic systems used are strontium and oxygen isotopes.

The alkaline earth element Sr is a divalent cation that simply substitutes for  $\text{Ca}^{2+}$  in feldspars, carbonates, sulphates and many other rock-forming minerals. Very similar to  $\text{Ca}^{2+}$ , it participates in many water/rock reactions. Strontium has four stable isotopes occur in nature:  $^{84}\text{Sr}$ ,  $^{86}\text{Sr}$ ,  $^{87}\text{Sr}$ , and  $^{88}\text{Sr}$  with relative abundances of  $\sim 7\%$ ,  $\sim 0.56\%$ ,  $\sim 9.86\%$ , and  $\sim 82.58\%$  respectively. The  $^{87}\text{Sr}/^{86}\text{Sr}$  ratios of rocks have proven to be a useful tracer of water/rock interactions, because fresh oceanic crust is relatively unradiogenic showing  $^{87}\text{Sr}/^{86}\text{Sr}$  ratios between 0.7025 and 0.7030. In contrast, seawater shows a high amount of radiogenic component with  $^{87}\text{Sr}/^{86}\text{Sr}$  ratio of 0.7092 [Faure, 1977]. During fluid/rock interaction, fluid and rock will tend towards equilibrium. This leads to more radiogenic alteration signal in the investigated rocks. Due to the temperature-independent fractionation of the Sr, the  $^{87}\text{Sr}/^{86}\text{Sr}$  ratio measured in metamorphosed rocks is a good tracer to indicate hydrothermal alteration. By using mass balance the isotopic composition analysed in the metamorphosed rock can be used to calculated water-rock ( $W/R$ ) ratios [Taylor, 1977].

The second isotopic system of interest is oxygen isotopes. Oxygen has three stable isotopes, which have the following abundances:  $^{16}\text{O} = 99.763\%$ ,  $^{17}\text{O} = 0.0375\%$ ,  $^{18}\text{O} = 0.1995\%$ . Mostly, the  $^{18}\text{O}/^{16}\text{O}$  are used and the fractionation is denoted by the  $\delta$  values, which means the relatively change compared to a well-known standard (Standard Mean Ocean Water = SMOW). The isotopic fractionation takes places in three different ways:

- Isotopic exchange reaction between two oxygen-bearing minerals. This fractionation is controlled by bond-strength and follows the general rule that the lighter isotope is preferred in the weaker bond.
- Kinetic processes

- Physico-chemical processes such as evaporation and condensation, melting and crystallization and diffusion

The temperature-dependent fractionation of oxygen between water and minerals is expressed by the fractionation factor  $\alpha$ . Using mass balance calculation for determine  $W/R$  ratios, which was first presented by *Taylor* [1974], at constant  $W/R$  ratios the final isotopic composition of the rock will only depend on the fractionation factor and consequently on temperatures. Thus, measuring oxygen isotopes is a good indicator to estimate alteration temperatures. By combining the two presented isotopic systems ( $^{87}\text{Sr}/^{86}\text{Sr}$  versus  $\delta^{18}\text{O}$  plot), a strong tool is established, which can be used to describe water-rock interactions and alteration temperatures in hydrothermal systems.

## A.5 Outline and aims of this study

There are quite many unresolved problems concerning the petrological record of hydrothermal alteration within the lower oceanic crust, however, the presented study focus on a few key-points:

**Chapter B** is a detailed petrological and geochemical study of hydrothermal dikes, veins, and related lithologies from a lower crustal section of the Wadi Wariyah (Semail ophiolite). Petrological, geochemical, and isotopic investigation of whole rocks and constituent minerals are used to demonstrate the record of possible very high to low temperature hydrothermal alteration in the lower crustal section of the Semail ophiolite. One of the most interesting findings is that the lower crustal section affected by very high to low temperature hydrothermal alteration using the same pathways.

**Chapter C** is a complementary experimental study providing new insights into the reaction mechanism of fluid-induced partial melting of oceanic gabbro at water-saturated ( $a_{\text{H}_2\text{O}} = 1$ ), ambient pressure (200 MPa), high temperature (860-1020°C) and oxidizing ( $f_{\text{O}_2} \sim \text{NNO}$ ) conditions. The study uses a typical olivine gabbro from the Southwest Indian Ridge (SWIR), highlighting the incongruent behaviour of the hydrous partial melting reaction during fluid-rock interaction at very high temperatures.

**Chapter D** presents a concluding statement of how the achieved results presented in Chapter B and C can be used for a better understanding of hydrothermal circulation in the lower crust at modern fast-spreading ridges. A model is presented, which summarize the main reaction stages during hydrothermal alteration.

The aim of this study is to shed light on the petrological record of hydrothermal alteration in the lower oceanic with a special focus on the reactions related to high temperature hydrothermal alteration.

---



# Chapter B

## The record of hydrothermal imprint from magmatic to low temperature in a layered gabbro series from the Wadi Wariyah (Oman ophiolite)

### B.1 Geological setting and previous work

In order to investigate the petrological record of hydrothermal alteration in the gabbroic crust, this chapter presents a detailed petrological, geochemical, and isotopic study of a system composed of magmatic dikes and hydrothermal veins formed during the fluid-rock interaction in a lower crustal gabbro section of the Wadi Wariyah. The Wadi Wariyah (N 22°58'51.49", E 58°15'53.98") is situated in the Western part of the Wadi Tayin massif, the most Southern massif of the Semail ophiolite in the Oman (Figure 7). The rocks at this locality are very suitable to study the record of hydrothermal activity in the lower oceanic crust for the following reasons: (1) According to *Nicolas et al.* [2003] and *Bosch et al.* [2004] the Wadi Wariyah outcrop is characterized by the presence of a well-exposed microcrack alteration system indicating the presence of hydrothermal activity in the lower oceanic crust operating at different temperatures. (2) The Wadi Tayin massif of the Semail ophiolite is regarded to represent a relatively primordial (“*normal*”) ridge part of the ophiolite, where the characteristic “*late stage magmatism*”, which is regarded as untypical for “*normal*” mid-ocean ridges, is nearly absent [*Nicolas et al.*, 2000].

In the Wadi Wariyah outcrop, the hydrothermal microcrack system is enclosed within a deep lower crustal section, which is classified about 0.1 km above the Moho transition

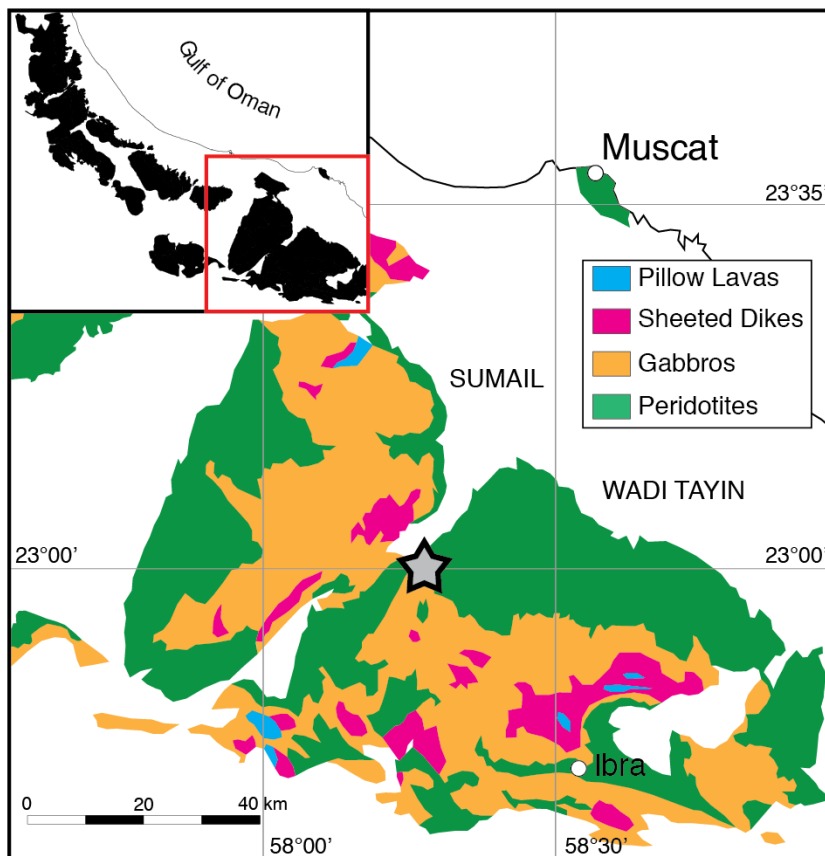


**Figure 7.** Simplified lithological map of the Sumail and Wadi Tayin massif in the Southern Semail ophiolite in the Oman [after *Nicolas et al.*, 2000]. The main lithologies are shown in different colours. The grey star indicates the location of the Wadi Wariyah outcrop.

zone [*Bosch et al.*, 2004]. *Nicolas et al.* [2003] were the first authors, who presented a textural and petrographic study of the microcrack system from the Wadi Wariyah, concluding that hydrothermal alteration in the Semail ophiolite is an example for oceanic ridges hydrothermal alteration of the lower crust. According to their findings it includes very high temperature hydrothermal dikes, high temperature “green” veins, as well as low temperature (LT) hydrothermal epidote veins (“white veins”) (temperature definition according to *Nicolas et al.* [2003]). *Bosch et al.* [2004] conducted a systematic petrographic, geochemical, and isotopic study on the dikes and veins. Their results imply that hydrothermal alteration in the gabbros started above 975°C and ended below 500°C. The reactions proceeded at very high temperatures are recorded by orthopyroxene and pargasite coronas followed by lower high-temperature conditions with replacement of the primary mineral by mainly hornblende. Finally, typical mineral assemblages of the greenschist facies indicate low-temperature alteration. Strontium and oxygen isotopic composition of the dikes and veins and their associated minerals clearly differ from typical mid-ocean ridges basalt ( $^{87}\text{Sr}/^{86}\text{Sr} > 0.7032$  and  $\delta^{18}\text{O} < 6\text{‰}$ ) indicating seawater as the most likely contaminant. The occurrence and isotopic composition of epidote within several veins indicate that hydrothermal alteration ended somewhere around 500°C. The obtained results make the Wadi Wariyah to a perfect site to study hydrothermal alteration of the lower crustal section in the Semail ophiolite and may be a good example for the hydrothermal alteration of the lower oceanic crust at fast-spreading ridges. However, the precise reactions related to the hydrothermal processes are still poorly constraint.

Additionally, the lower crust of the Wadi Tayin massif is well exposed in the Wadi Tayin massif. Cross sections through the plutonic section of the Wadi Tayin massif show thickness of ~3-5 km [Pallister and Hopson, 1981], which is more comparable to the thickness of the lower oceanic crust at modern mid-ocean ridges. In other massif of the Semail ophiolite the plutonic section shows smaller thicknesses (e.g., Wadi Abyad) [MacLeod and Yaouancq, 2000], indicating strong influence of tectonic stress during obduction.

## B.2 Field description of dikes and veins from the Wadi Wariyah

The Wadi Wariyah (Figure 8a) outcrop is mainly composed of a 50 m wide and 20 m high, layered gabbro series with nearly horizontal alternating light and dark layers in cm to dm scale (Figure 8b). The magmatic layering of the gabbro corresponds to the general orientation in the Wadi Tayin massif (measured value: striking: NE-SW, dipping ~20° SE; Figure 10), which is perpendicular to the general trend of the sheeted dikes showing more or less NW-SE orientation in the massif [Nicolas *et al.*, 2003]. Most striking feature of the outcrop is the very frequent occurrence of several types of dikes and veins (Figure 8a; area I-V) forming a complex veining system.

The dike/vein system is distributed over the whole outcrop. Based on field observation and mineralogy they can be divided into four groups (Figure 8, 9):

- (1) Dark brownish amphibole-bearing gabbroic dikes with thickness of 1.5-5 cm. They meander through the layered gabbro irregular, although the general trend is perpendicular to the magmatic layering (area I, II, and V). Frequently, gabbroic dikes show a branched connectivity (Figure 8c, d). The texture is medium-grained with amphiboles showing a vitreous lustre and occasionally being elongated as comb structures at the rim of the dike. The contact to the surrounding layered gabbro is sharp with no visible chilled margins. These entire features indicate intrusion of the dikes at very high temperatures (“*near magmatic*”), as the layered gabbro was still very hot. The absence of any chilled margins indicate formation temperatures above 600°C.
- (2) Single dark, black to dark greenish veins with thickness of 0.01 to 0.38 cm (Figure 8e, f) occur in the same area together with the gabbroic dikes. These veins occasionally occur as small fillings of 1-2 mm thick microcracks within the layered gabbro, which are only visible on a chipped rock surface. Similar to the gabbroic dikes they also show black amphibole with vitreous lustre. The dark veins run straight through the layered gabbro perpendicular to the magmatic layering. The contact to the surrounding layered gabbro is mostly sharp, while some dark veins are surrounded by a greenish altered gabbro indicating a reaction zone.
- (3) Whitish veins with a thickness from 0.1-2 cm mainly composed of epidote (in the following named as “*epidote veins*”; Figure 9a-d). In contrast to the gabbroic

dikes and dark veins, epidote-rich veins are diagonal shifted but follow the general trend perpendicular to the magmatic layering. One 2 cm thick epidote vein shows complex vein-parallel zoning (Figure 9d), dividing the vein into an epidote rich zone (*Wa\_43A*) and a zone consists of greenish, blackish fibrous amphibole and leucoxene (*Wa\_43B*). In area I the epidote veins form a well-visible branch structure (Figure 9a).

(4) In two areas of the outcrop (area III & IV) up to 5 cm thick massive whitish veins running straight to irregular perpendicular to the general orientation of the magmatic layering of the gabbro. These veins are mostly composed of monomineralic prehnite (in the following named "*prehnite veins*") and are surrounded by an up to several meters thick zone of highly metamorphosed gabbro.

In contrast sharp contact to the layered gabbro by the gabbroic dikes and dark veins, the epidote and prehnite veins are surrounded by slightly to highly altered gabbro showing a diffuse contact to the layered gabbro. Four types of altered gabbros can be observed: (1) close to the epidote veins (in the following named "*halo*"); (2) away from the epidote veins (in the following named "*altered gabbro*"); (3) surrounding the prehnite veins (in the following named as "*highly altered gabbro*"); and (4) massive blocks enclosed in the highly altered gabbro with a characteristic mineralogy (see sections below; in following named as "*An-bearing metagabbro*").

The epidote veins are primary surrounded by up to 4 cm wide whitish halos. The halo is moderately altered and the primary magmatic layering has been completely extinguished. Zones of up to 10 cm of the altered gabbro follow the halo. The altered gabbro is mostly of greenish colour and shows slight to medium alteration. Occasionally, the primary magmatic layering of the layered gabbro is still visible in the altered gabbro. The halo/altered gabbro represent a complex reaction zone surrounding the epidote veins possible formed due to an interplay between vein formation and reactions, which caused exchanges between vein and wall-rock. Sometimes the epidote veins are so close spaced that the gabbro between them is completely composed of halo/altered gabbro.

Generally, dm- to m-sized thick zones of the highly altered gabbro surround the prehnite veins. As expressed by the name, the highly altered gabbro has a high degree of alteration and is typically characterized by plenty of cm-sized sub parallel epidote veins running irregularly through it. In area III, one prehnite vein crosscuts the layered gabbro straight and perpendicular to the magmatic layering. The contact to the layered gabbro is characterized by highly altered gabbro forming a vein-parallel zoning defined by the degree in of alteration. The prehnite vein marks the centre followed by an up to 10 cm thick highly altered gabbro (Figure 9e). The highly altered gabbro is surrounded by a 20 cm thick less altered gabbro, where the grade of alteration decreases with distance from the vein. In contrast, zone IV is characterized by a 3 to 5 cm thick prehnite vein running irregularly through an approximately up to 5 m thick zone of highly altered gabbro. The precise dimension of this zone cannot be determined, because the zone runs out in the left part of the outcrop covered by Quaternary sediments. Within area IV irregular orientated, separated blocks of An-bearing metagabbros can be observed. In contrast to the altered gabbro described and

---

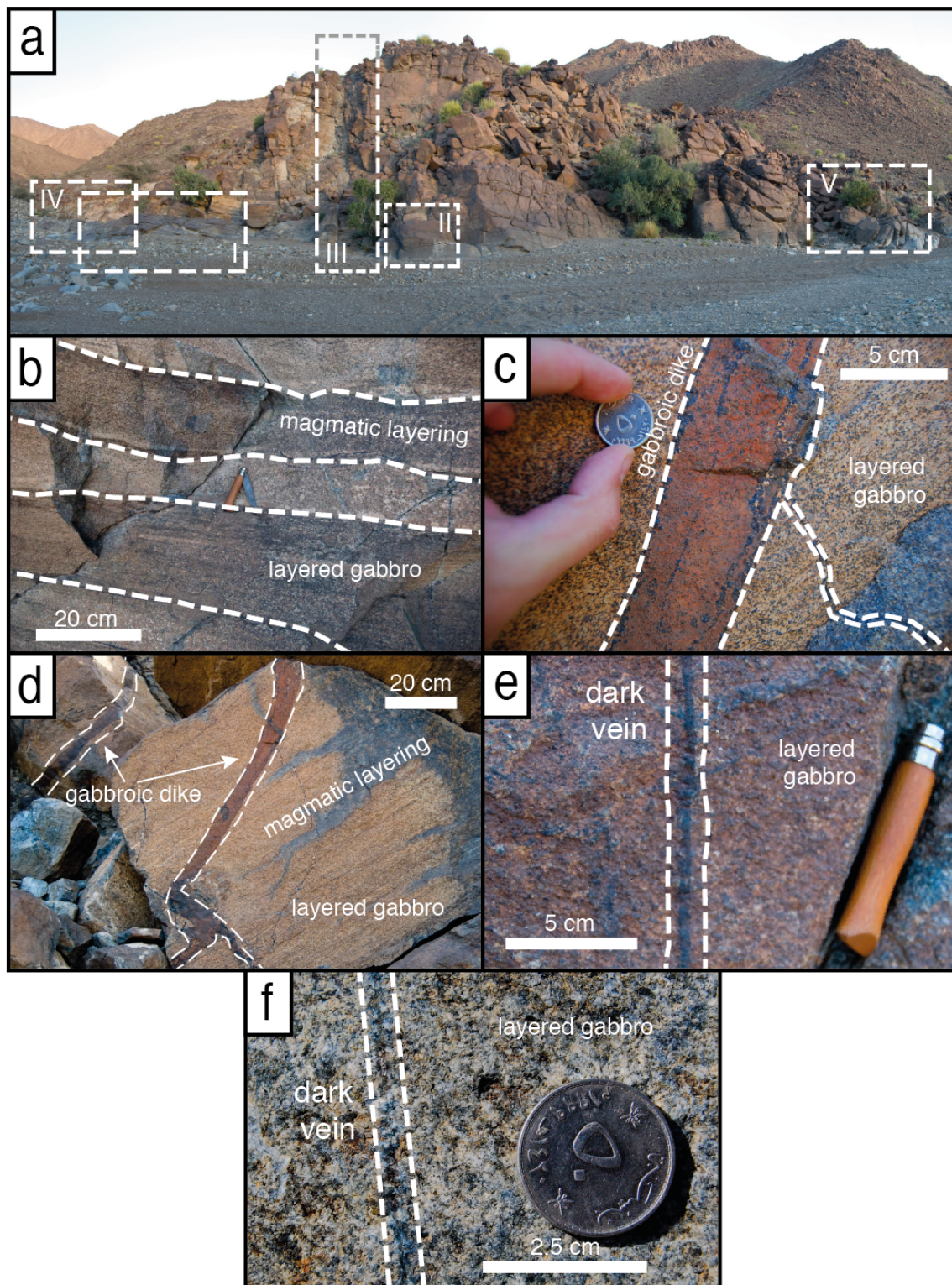


**Figure 8.** (a) The layered gabbro outcrop of the Wadi Wariyah. The number I-IV represents area of several different dikes and veins identified as products of hydrothermal alteration. (b) Modal layering of the layered gabbro indicated by light to dark alternating layering. (c-d) Gabbroic dike within the layered gabbro. (e-f) Two thin dark veins crosscutting straight the layered gabbro.

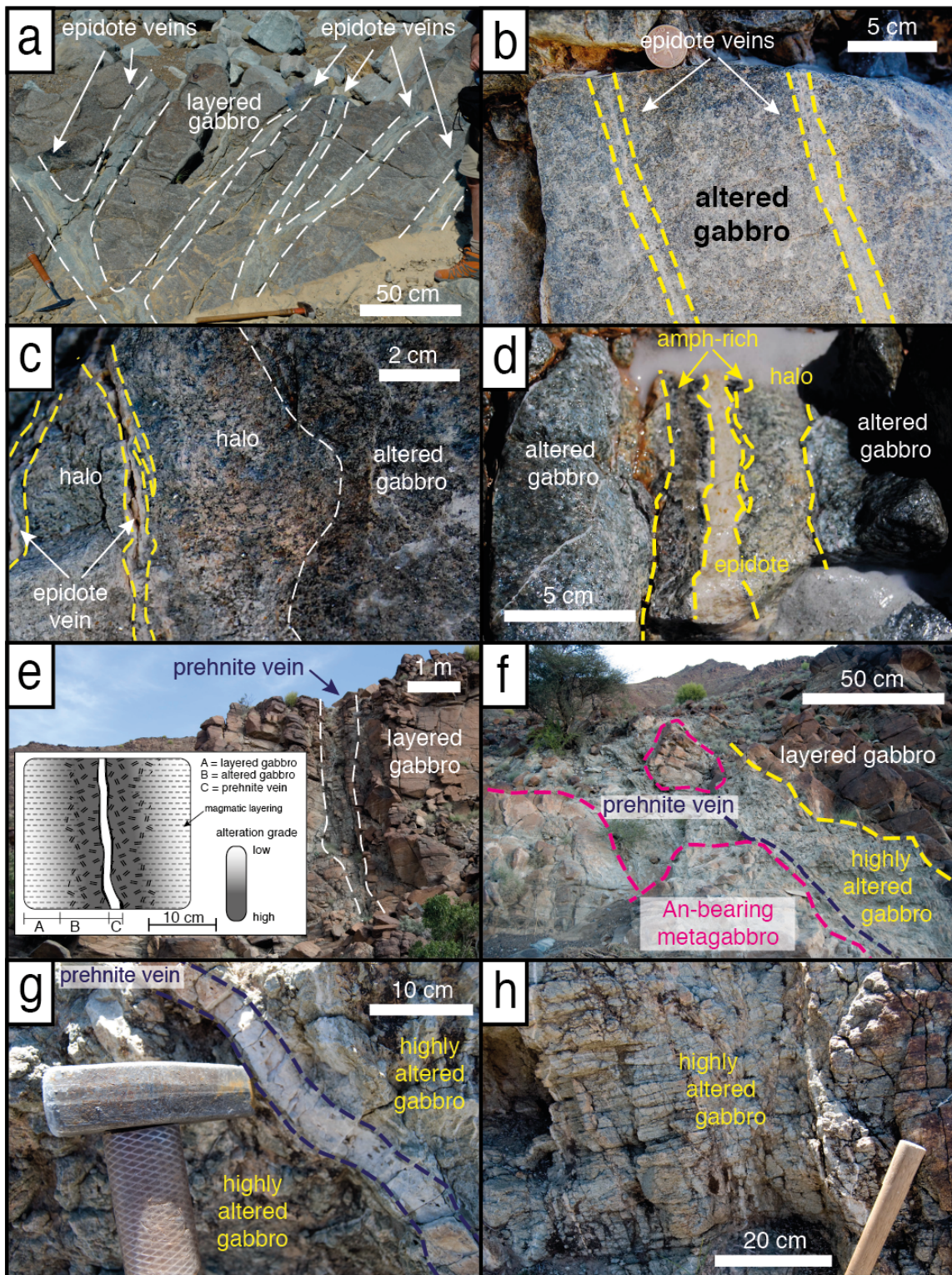


**Figure 9.** (a) Complex vein network composed of epidote veins in area I. (b) Two epidote veins surrounded by greenish altered gabbro. (c) Epidote vein surrounded by altered gabbro identified as reaction halo followed by greenish altered gabbro. (d) Vein-parallel zoning in the epidote vein (*samples Wa\_43A, B, and C*). The zones consist of one epidote-rich zone (*Wa\_43A*) and one zone enriched in greenish, blackish amphibole (*Wa\_43B*). This vein is on one side surrounded by a reaction halo followed by altered gabbro (*Wa\_43C*). (e) Zone III of the Wadi Wariyah. The small sketch indicates the field relation. The zone is characterized by thick prehnite vein surrounded by an altered gabbro, which alteration degree decrease with distance from the prehnite vein. (f) Area IV of the Wad Wariyah. This zone extends to the left side of the outcrop and consists of mainly highly altered gabbro with one thick prehnite veins. Several blocks of a massive An-bearing metagabbro occur irregular within the zone. (g) Prehnite vein in area IV surrounded by highly altered gabbro. (h) Close up view of the highly altered gabbro. The igneous layering of the layered gabbro can be still observed.

lithology (Figure 9f). The An-bearing metagabbro still preserves the magmatic layering above, these blocks show characteristic features, which requires describing them as a separated lithology. Compared to the other altered gabbros it is moderately altered. Combined with the mineralogical and geochemical results presented below (high An plagioclase, magmatic clinopyroxene, high  $^{87}\text{Sr}/^{86}\text{Sr}$  ratios), this lithology is very unique and has been not described from the Semail ophiolite or any other ophiolite so far.

### **B.2.1 Field orientation, amount and spacing of dikes, veins, and halos within the layered gabbro of Wadi Wariyah**

In order to quantify the overall hydrothermal imprint within the investigated section of the layered gabbro, the amount, thickness, and spacing of the different dikes, vein, and halos/altered gabbro has been determined. This is possible due to the excellent outcrop conditions, enabling two- and even three-dimensional views on the dike/vein network on polished rock surface. However, without additional detailed mapping in other areas of the Wadi Wariyah (and the Semail ophiolite), the result obtained in this study might be only valid for the investigated outcrop.

In general, products of hydrothermal alteration make up approximately 10% of the whole outcrop (90% layered gabbro). From this, the prehnite veins and the surrounding highly altered gabbro cover the largest fraction. They make up 87% of the hydrothermal products. Epidote veins make up approximately 10% of the hydrothermal system (this does not include the epidote veins in the highly altered gabbro of the prehnite veins). The gabbroic dikes and dark veins represent the smallest fraction of hydrothermal products with together only 3%.

The spacing and distribution of the hydrothermal products vary over the whole outcrop. In most cases, the gabbroic dikes and dark veins occur in “*swarms*” of several dikes/veins in area I + II + V. While the space between single dikes and veins is only a few cm, the distance between the “*swarms*” can easily reach several metres. The epidote veins only occur within area I as a branched vein network (Figure 10) with a vein-to-vein distance of several dm. Sometimes, the epidote veins are so close spaced that the wall rock is completely composed of halo/altered gabbro. Although only two prehnite veins can be observed, they form the largest fraction of hydrothermal alteration products in the lower crustal section. The prehnite veins including the zone of highly altered gabbro occur within a distance of several meters between them. There seems to be no correlation between type of vein and spacing between them.

As indicated by the cutting relation of the dikes and veins in the layered gabbro, the general trend is perpendicular to the igneous layering. One dark vein is crosscut and offset by an epidote vein, which indicates that the dark veins formed in an earlier stage of alteration. Figure 10 shows a detailed sketch of the field orientation of the gabbroic dikes and veins from area I of the Wadi Wariyah outcrop. This block represents a very unique and exceptional well-exposed zone to demonstrate the orientation of the hydrothermal system. In this zone, the layered gabbro is cut three-dimensionally so that the complex dike/vein network is well exposed. The corresponding orientation of the dikes and veins is

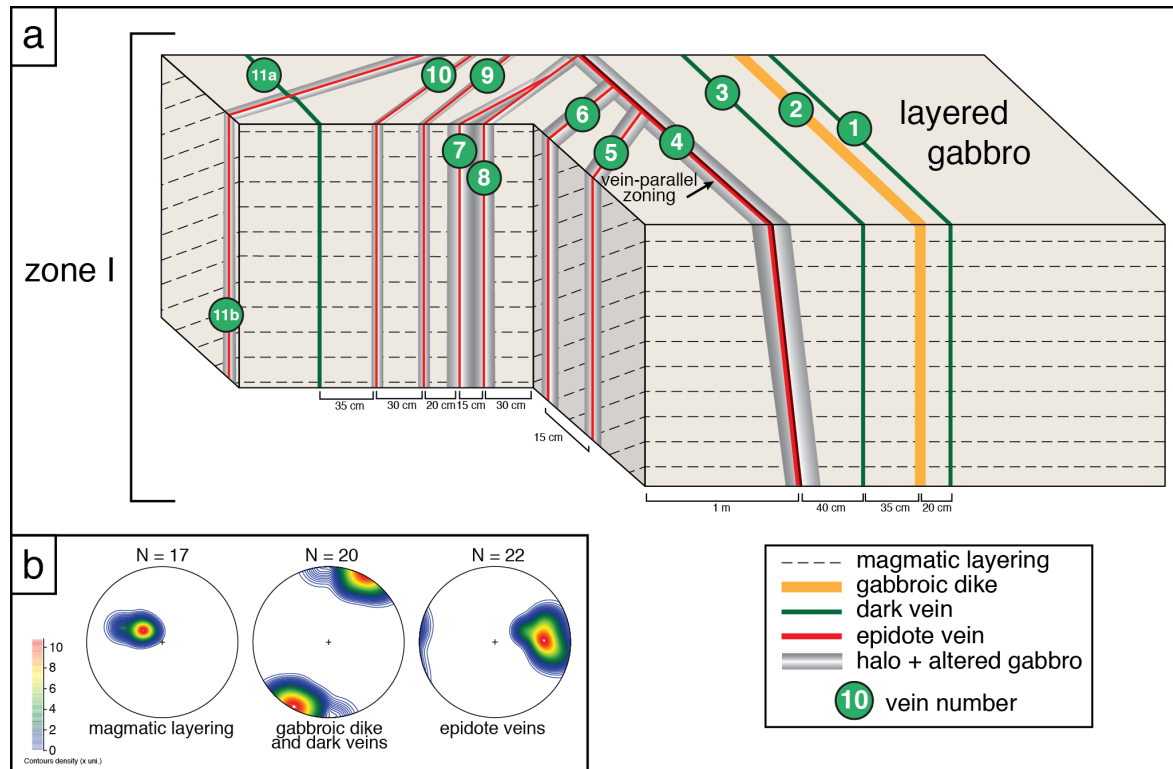


**Figure 10.** (a) Schematic sketch of the area I of the Wadi Wariyah outcrop, where the different types of veins and dikes are exceptionally well exposed. Here, the layered gabbro is cut in three dimensions nearly perpendicular to each other (two perpendicular and one parallel to the layering of the gabbro). This allows a nearly perfect, three-dimensional view of the orientation of the dikes and veins. The sketch includes the orientation of the reaction zone (halo/alterated gabbro) if present. The numbers correspond to the vein numbers given in Table 8. (b) Corresponding contour stereonet obtained from the structural measurements of the magmatic layering, the gabbroic dikes/dark veins, and the epidote veins.

presented by the stereonet based on field measurements presented in Figure 10b. This is also valid for the prehnite veins and zones of highly altered gabbro, although the precise orientation of the prehnite vein in area IV can not be accurately determined due to this zones runs out in the left part of the outcrop.

### B.3 Analytical Techniques

This section describes the sampling and analytical techniques carried out to characterize the petrological, geochemical, and isotopic record of the dikes, veins, and layered gabbro and their main constituent mineral phases. Analytical techniques used in this study include X-ray Fluorescence (XRF), Inductively Coupled Plasma Mass Spectrometry (ICP-MS), Electron microprobe analysis (EMPA), Laser Ablation-ICP-MS (LA-ICP-MS), Multi Collector ICP-MS (MC-ICP-MS), and laser fluorination (LF). The compiled dataset produced from these techniques are: Major elements, trace and rare earth element (REE) concentration of whole rock and main constituent minerals as well as bulk  $^{86}\text{Sr}/^{87}\text{Sr}$  and  $\delta^{18}\text{O}$  isotopic composition. Analytical errors, precision, accuracy and uncertainty of each technique are presented in the following sections.



### B.3.1 Sample selection and preparation

A total of thirty-six samples were collected from the Wariyah outcrop including several kinds of dikes/veins and basement rock. Sampling method was either rock drilling ( $\varnothing$  5 cm) or handpicked sampling (Table 1). For samples of the hydrothermal dikes/veins it was ensured, if possible, that these samples also contain a certain amount of surrounding rock in order to describe the transition between dike/vein and host rock. For a better systematic and description, the samples are divided into several domains (suffix A, B, or C of each sample). One domain consists of the dike/vein and the other domain consists of the surrounding rock (layered gabbro or altered gabbro). In samples where the transition between the host rock and the vein is characterized by a halo or vein-parallel zoning, these have been added as individual domains. Additionally, several samples of the layered gabbro has been collected with a certain distance from the dikes/veins well distributed over the whole outcrop in order to have a reference material of fresh unmodified igneous host rock.

In order to perform mineralogical and petrological description and analysis, thin sections of all the samples were prepared. Thin sections from the rock drills were prepared using a double sized glass (4.7 cm x 5 cm) as object plate. Handpicked samples were glued on a standard sized object plate (4.7 cm x 2.8 cm). Thin sections have been polished to a thickness of approximately 40-60  $\mu\text{m}$ , which is slightly thicker compared to normal thin section for EMPA (30  $\mu\text{m}$ ). However, the thicker section allows better LA-ICP-MS analysis due to more material, which is available during ablation.

For major and trace bulk-rock composition dikes/veins, halos and surrounding rock were separated using a conventional steel circular saw. Since veins and halos often show thicknesses of only a few millimetres, this work was performed very carefully to avoid contamination by the surrounding rock. Saw blade and surrounding rock leftovers on the cuttings were removed using a diamond file. Afterwards, the cuttings were cleaned in a 50% ethanol dilution for at least 15 minutes using an ultrasonic cleaning system at a temperature of 60°C. Subsequently, the cuttings were pre-crushed using conventional steel mortar and then grinded for at least 2 hours to a very fine-grained powder (<10  $\mu\text{m}$ ) using an achate swing-mill. Rock powders were dried at 110°C over 24 hours and then filled into glass containers.

### B.3.2 X-ray fluorescence (XRF)

An aliquot of the rock powder of each sample was pressed and fused to glassy pellets, which contain 600 mg rock powder and 3600 mg of lithiumtetraborat ( $\text{Li}_2\text{B}_4\text{O}_7$ ) as matrix. Major element composition was determined by wavelength-dispersive X-ray fluorescence (XRF) spectroscopy [*Van Grieken and Markowicz, 2002*] using a PANalytical MagiX PRO (PW-2440) equipped with an Rh 4 kV anode and an automated sample changer (PW 2540) by the Mineralogisch-Petrographisches Institut (University of Hamburg, Germany). Loss on ignition (L.O.I.) was determined gravimetrically as sum of  $\text{H}_2\text{O}^+$  and  $\text{H}_2\text{O}^-$  and includes  $\text{SO}_3$  and  $\text{CO}_2$ . Three international standard materials (JGB-1, JB-3, JB-2) were analysed to control analytical precision. Typical analytical accuracy of the major elements

as estimated by applying the preferred values from the GeoRem database (Version 04/2012) [Jochum *et al.*, 2005] is better than 2%, except for Na<sub>2</sub>O (averaging 7.4 %), MnO (averaging 6 %), P<sub>2</sub>O<sub>5</sub> (averaging 3.4 %), and L.O.I. (-17.5 %). The accuracy of the XRF technique is shown in Table 2. Additionally, 20 trace elements concentrations were measured simultaneously. Due to low analytical precision of the trace elements, determined by XRF mostly the ICP-MS results were used for trace element concentration evaluation of the whole rock (see Section B.3.4 for a detailed comparison).

### **B.3.3 Inductively Coupled Plasma Mass Spectrometry (ICP-MS)**

Bulk rock trace element concentration were determined by conventional solution-based ICP-MS after two step HF aquaria digestion of approximately 100 mg powder using the method described in detail by Garbe-Schönberg [1993] using an Agilent 7500cs mass spectrometer at the Institut für Geowissenschaften (University of Kiel, Germany). Three international standard materials (BIR-1G, BVHO-2, and JGB-1) were analysed for external calibration and to control analytical precision. Typically analytical precision as estimated from replicate analyses of the standard material range between 1-8% RSD (1 $\sigma$ ). Elements showing low analytical precision from 9-110% RSD (1 $\sigma$ ) have been eliminated from the data evaluation. Two samples were prepared and analysed in double manner to control reproducibility. In general, reproducibility is better than 2% RSD (1 $\sigma$ ). Results of the standard material are listed in Table 3.

### **B.3.4 Comparison between XRF and ICP-MS analysis**

A total of 20 elements have been measured by XRF as well as by ICP-MS analysis. Thus, the results allow to check the analytical quality of both techniques by comparing these results. The comparison includes the minimum detection limit, accuracy, and analytical precision. Applying the preferred values of the JGB-1 standard material from the GeoRem reference material database, version 04/2012 [Jochum *et al.*, 2005] and comparing the element concentration of the samples measured by both techniques, evaluates the analytical precision. Table 4 shows the comparison between the two techniques. As indicated by the minimum detection limit the XRF technique provides detection limits of > 5 ppm, while the ICP-MS analysis show detection limit between 0.1-5 ppm. Thus, eight element concentrations (Ce, La, Nb, Nd, Pb, Rb, Th, and U) of the JGB-1 standard material are below the detection limit of XRF analysis and thus cannot be included in the comparison.

Analytical accuracy has been calculated for both techniques. Results show that except for one element (Zr), the accuracy of the ICP-MS analysis is better than the XRF analysis. ICP-MS analysis accuracy for most of the elements is ranging from 1-12%, while the XRF accuracy ranging from 1-73%. The low precision in Zr (34%) of the ICP-MS technique may be caused by the digestion technique, which may not dissolve zircons and other Zr-bearing mineral and thus lead to a low precision of Zr via the ICP-MS analysis. Therefore Zr data of the XRF analysis has been used in the evaluation.

---

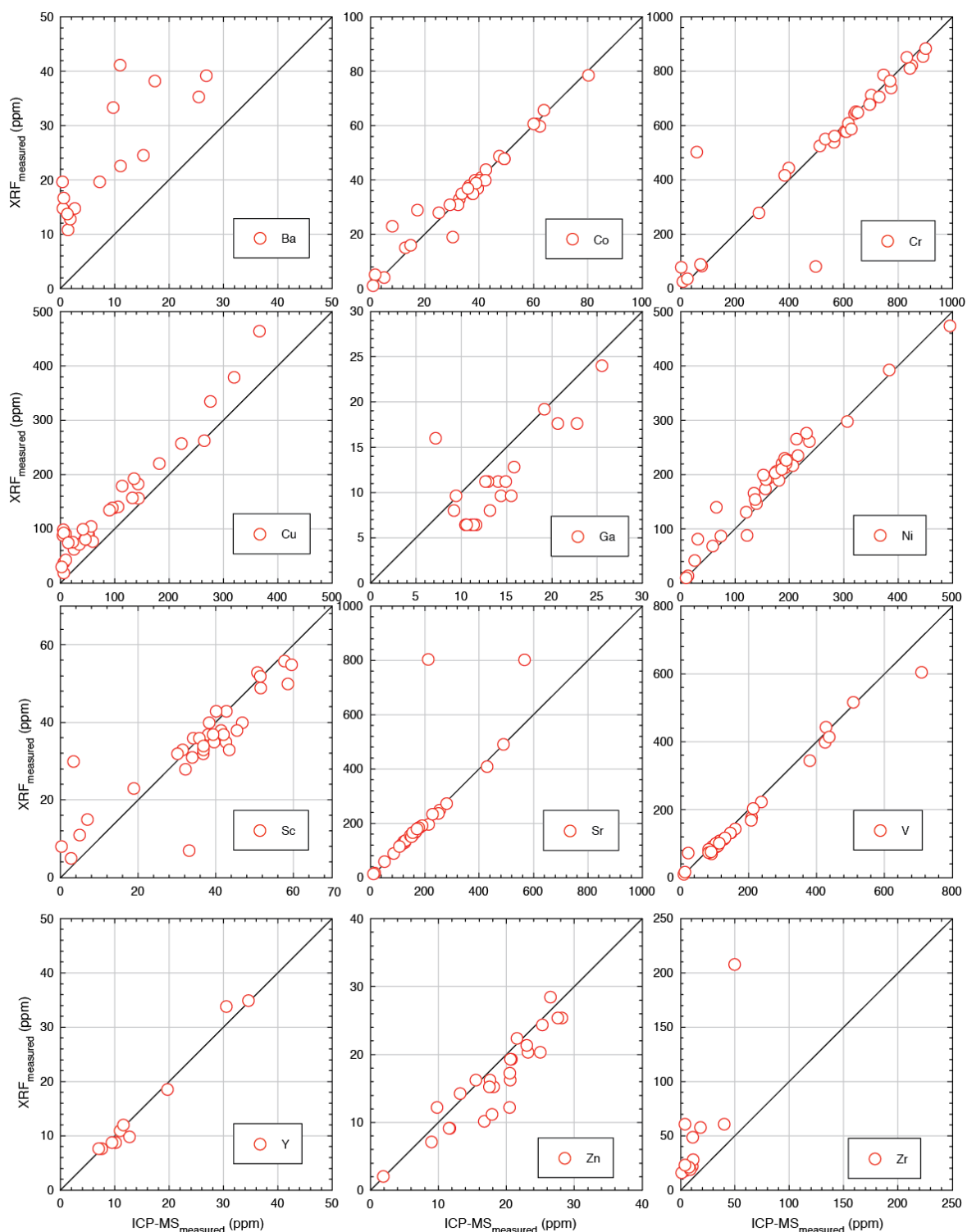


**Figure 11.** Comparison between ICP-MS and XRF element concentration for the samples. Each point represent one sample analysed with ICP-MS and XRF. The straight line represents the 1:1 line.

By comparing the accuracy of each element of the two techniques, the reproducibility of the JGB-1 values can be calculated. Reproducibility of Sr, V, Co, Cu, Sc and Zn are better than 10%. For other elements (Ba, Cr, Ni, and Y) reproducibility is ranging from 11-21%. Zr and Ga show very low reproducibility of 32% and 74%, respectively. Figure 11 shows a comparison of the detection limit corrected element concentrations measured by ICP-MS

and XRF analysis, respectively. The data indicate that some element concentrations are well reproduced (Co, Cr, Ni, Sr, V, Y). For other elements the XRF analysis shows higher (Cu, Ba, Zr) or lower (Ga, Sc, Zn) concentration. In summary, for evaluating the trace element concentration of the bulk-rock dikes, veins, altered gabbro, and layered gabbro, mostly the analysis of the ICP-MS technique were used for the following reason:

- Detection limits are much lower
- Accuracy of the standard material is better
- Good reproducibility of the XRF analysis is only given by a few elements
- ICP-MS allows to analyse 39 trace elements simultaneously (compared to only 20 with XRF)
- Zirconium concentration of the XRF analysis is used, because it shows better accuracy

### **B.3.5 Electron microprobe analysis (EMPA)**

Major element concentrations of minerals were determined using a Cameca SX100 equipped with five spectrometers and the operating software “*Peak Sight*” at the Institut für Mineralogie (University of Hannover, Germany). All data were obtained using 15kV acceleration potential,  $K\alpha$  or  $K\beta$  emission for all elements and the matrix correction “*PAP*” according to *Pouchou and Pichoir* [1991]. Calibration material includes natural wollastonite (Si and Ca), albite (Na), orthoclase (K), halite (Cl), strontium fluoride (F), apatite (P) and synthetic  $Al_2O_3$ ,  $Fe_2O_3$ , MgO,  $TiO_2$ ,  $Mn_3O_4$ ,  $V_2O_3$ ,  $Cr_2O_3$ , NiO. TAP was used as the diffracting crystal for Na, Mg, Si, and Al; PET for Ca, P, and Cr; LIF for Fe and Mn, Ni; LPET for K, Ti, V, and Cl; and PC1 for F. Most of the data were obtained using a 15nA beam current and static (focused) beam. Counting times were 10 s for major elements, 40s for Ca in olivine, 30s for Cr in pyroxenes and 60s for F and Cl in hydrous minerals. Detection limits for all microprobe analyses are listed in Table 5.

The international standard materials USNM 111356 (Hornblende Kakanui) and USNM 2566 (Olivine Spring water Meteorite) [*Jarosewich et al.*, 1980] were measured continuously throughout every electron microprobe session to monitor analytical precision. Typical analytical precision was better than 4% (RSD) ( $1\sigma$ ) for the major elements, except for MnO, which shows analytical precision of 16–22 % (RSD) ( $1\sigma$ ) depending on concentration in the standard material. Measured values of the standard material are listed in Table 6. The halogen concentration of the Kakanui Hornblende (USNM 111356) has been measured and the results were  $205 \pm 22$  ( $1\sigma$ ) ppm for Cl and  $3666 \pm 222$  ( $1\sigma$ ) ppm for F, which are higher compared to the only so far published values of the halogen content in the Kakanui Hornblende [*Zhang et al.*, 2012].

Due to the X-ray sensitivities and due to the importance of crystallographic orientation of apatite grains, the quantitative analysis by electron microprobe of Cl and particularly F can be problematic [*Stormer Jr. et al.*, 1993]. Therefore a beam current of 10nA were applied

---

for Cl and F, and 15nA for all other elements using a defocused beam of 5-10  $\mu\text{m}$ . Counting times were 40 s for F and 60 for Cl. Other elements counting times were 10s.

### B.3.6 Laser Ablation ICP-MS

Trace-element analyses were performed using a LA-ICP-MS mass spectrometer (Element 2, ThermoFisher) equipped with a UP193HE (New Wave Research) 193 nm ArF excimer laser at the Institut für Mineralogie (University of Münster, Germany). Laser repetition rates were 5 Hz using an energy density of 4 J/cm<sup>2</sup>. Gas flow rates were 0.847 l/min for He (carrier gas of ablated material), 0.91 l/min and 0.987 l/min for the Ar-auxiliary and sample gas, respectively. Cooling gas flow rates were 16 l/min. Beam-spot diameter varied from 30 to 60  $\mu\text{m}$ , depending on the grain size of the mineral. Total measuring time was 75 s with 35 s for the background and 40 s for the signal. Before sample analyses, the system was tuned using the NIST SRM 612 international reference glass to guarantee maximal intensity. In that case, <sup>139</sup>La, <sup>232</sup>Th and <sup>232</sup>Th<sup>16</sup>O were monitored in order to obtain stable peak signals, high sensitivity, and low oxides rates (<sup>232</sup>Th<sup>16</sup>O/<sup>232</sup>Th, 0.1 %) during ablation. Calibration was against the NIST SRM 612 [Jochum *et al.*, 2011] standard glass using the pre-analysed CaO of the electron microprobe analyses for internal standardization and the GLITTER software for data processing. In a second step the international reference material BIR-1G was measured for external calibration, applying the preferred values of the GeoReM reference material database, version 04/2012 [Jochum *et al.*, 2005]. A group of five spots on the sample material was bracket by three internal and three external calibration standards on both sides in order to follow instrumental drift and analytical precision. Typically analytical precision as estimated from replicate analyses of the external standard is better than 6% RSD (1 $\sigma$ ) for a concentration in the glass down to 0.5 ppm, whereas lower concentrations (e.g., Rb 0.22 ppm; Ta 0.03 ppm) in the glass yield analytical precision from seven to a few tenths of percentage. A full list of the measured standard material is presented in Table 7.

A second batch of samples were analysed using a LA-ICP-MS mass spectrometer (Element XR, ThermoFisher) equipped with a UP193HE (New Wave Research) 196 fs Ti-sapphire excimer laser at the Institut für Mineralogie (University of Hannover, Germany). Laser repetition rates were 10 Hz using an energy density of 1.25 J/cm<sup>2</sup>. Beam-spot diameter was 20  $\mu\text{m}$ . Gas flow rates were 0.77 l/min for He (carrier gas), 0.60 l/min and 1.085 l/min for Ar-auxiliary and sample gas, respectively. Gas flow rates of the cooling gas was 15.05 l/min. Total measure-time was 120 s with 60 s for the background and 60 s for the signal. Before sample analyses, the system was tuned using the NIST SRM 610 international reference glass to guarantee maximal intensity. In that case, <sup>232</sup>Th<sup>16</sup>O were monitored in order to obtain low oxides rates (<sup>232</sup>Th<sup>16</sup>O/<sup>232</sup>Th, 0.1 %) during ablation. Calibration was against the NIST SRM 610 [Jochum *et al.*, 2011] standard glass using the pre-analysed CaO content for internal standardization and the Lamtrace software for data processing. Typical analytical precision as estimated from applying the preferred values of the GeoReM reference material database, version 04/2012 [Jochum *et al.*, 2005] was better than 5% RSD (1 $\sigma$ ) for all elements. A group of a maximum of fifteen spots on the sample material was bracket by two calibration standards on both sides in order to monitor instrumental drift and analytical precision.

### B.3.7 Multi Collector-ICP-MS

Strontium was separated from approximately 25 ml of the ICP-MS solution using an extraction chromatographic method with an additional H<sub>2</sub>O<sub>4</sub> cleaning step after *Pin et al.* [1994]. Strontium isotope analyses were carried out using a MC-ICP-MS mass spectrometer (Neptune, ThermoFinnigan) at the Institut für Mineralogie (University of Hannover, Germany). Argon was used as sample and auxiliary gas. Gas flow rates were 1.1 l/min and 0.8 l/min for the sample and the auxiliary gas, respectively. Sensitivity on <sup>86</sup>Sr was approximately 15 V/ppm after pre-concentrated the solution. Krypton interferences of <sup>84</sup>Kr on <sup>84</sup>Sr and <sup>86</sup>Kr on <sup>86</sup>Sr were subtracted by primary on-peak-zero measurements of a blank solution.

The international standard material NIST SRM 987 was measured during the session to monitor analytical precision. Results yielded an average <sup>87</sup>Sr/<sup>86</sup>Sr ratio of 0.710288 ± 0.0010 (2σ) during the measurements. Data were corrected using a compiled <sup>87</sup>Sr/<sup>86</sup>Sr value of 0.71034 from the GeoRem database. Initial <sup>87</sup>Sr/<sup>86</sup>Sr<sub>initial</sub> were calculated by correcting the measured isotopic ratio following the method of *Bosch et al.* [2004]. Three samples were measured doubly in order to control reproducibility. In general, reproducibility was better than ±0.0001 % (RSD) (1σ).

### B.3.8 Laser Fluorination

The NERC Isotope Community Support Facility in Killbride (Scotland) carried out the oxygen isotopic compositions. All separates were analysed using a laser fluorination procedure, involving total sample reaction with excess ClF<sub>3</sub> using a CO<sub>2</sub> laser as a heat source (in excess of 1500°C) following *Sharp* [1990]. All combustions resulted in 100% release of O<sub>2</sub> from the silica lattice. This O<sub>2</sub> was then converted to CO<sub>2</sub> by reaction with hot graphite, then analysed on-line by a VG Optima spectrometer. Repeat analyses of international and lab standards during the running of these samples gave values for UWG-2, SES, and GP147 standards of 5.8 (versus a accepted value of 5.8 by *Valley et al.* [1995]), 10.1 (10.1), and 7.3 (7.2) with reproducibility better than ±0.2‰ (1σ). Results are reported in standard notation (δ<sup>18</sup>O) as per mil (‰) deviations from the Vienna Standard Mean Ocean Water (V-SMOW) standard.

## B.4 Petrographic record of dikes/veins, altered gabbro, and layered gabbro

In order to describe the petrographic record of hydrothermal alteration in the layered gabbro of the Wadi Wariyah, thin sections of the hydrothermal dikes, veins, surrounding lithologies, and the layered gabbro have been carefully examined by light microscopy. The mineralogical assemblage and textural features provides new insights in the mineralogy and reactions related to hydrothermal alteration. Table 8 lists a full overview of the mineralogy of the hydrothermal dikes and veins, their classification and a description of the surrounding lithologies.

---

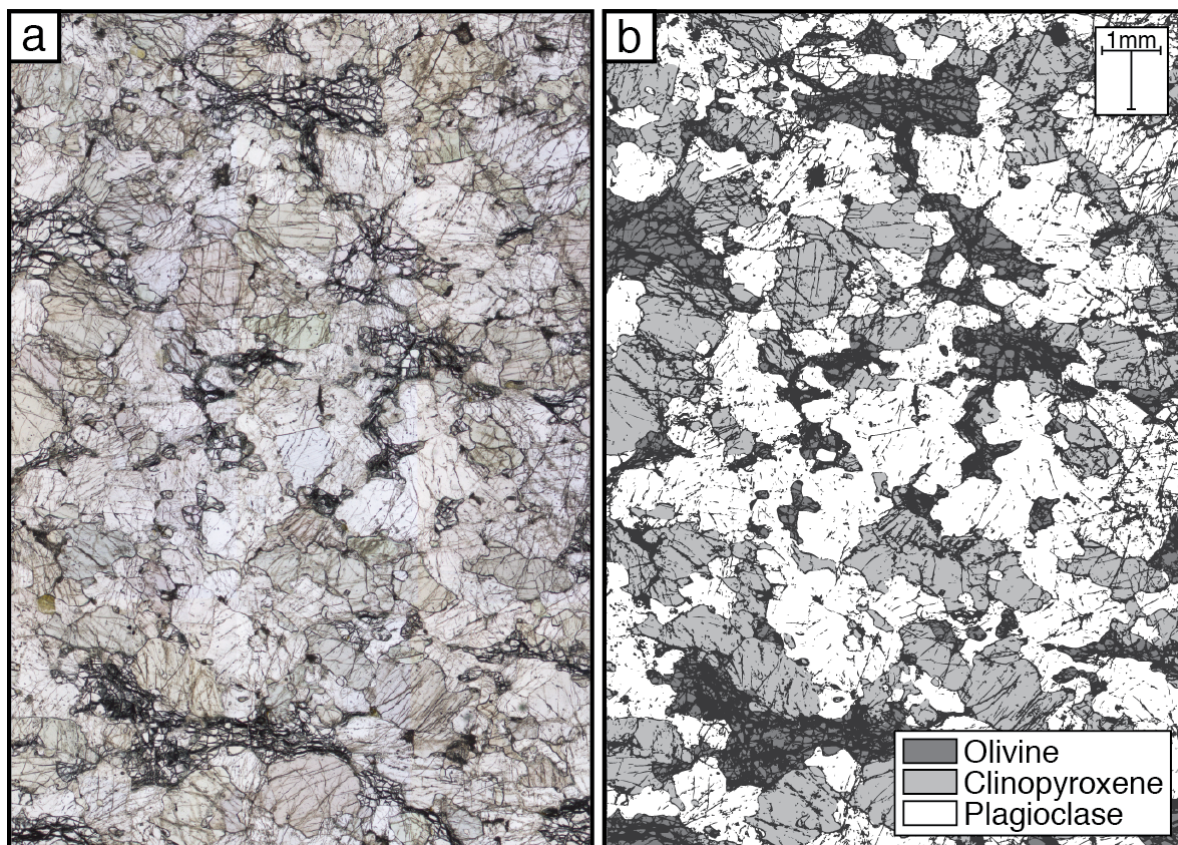


**Figure 12.** (a) Microphotography of the layered gabbro (plane-polarized light). (b) Sketch of the same area showing the main mineral constituents and the textural relation of the layered gabbro. Both figures have the same scale. Sample: *Wa\_42B*.

### B.4.1 Layered gabbro

The layered gabbro typically represents a mineral assemblage consisting of the primary magmatic constituents olivine, plagioclase, and clinopyroxene forming an anhedral equigranular framework, with a medium-grained (average grain size: 1.5 mm) cumulate texture (Figure 12). The layering of the olivine gabbro is characterized by differences in mineral proportions (olivine-rich or olivine-poor layers), the average modal proportion determined from mass balance calculation [Albarède and Provost, 1977] based on 6 samples is: 13 wt% olivine, 53 wt% plagioclase, and 34 wt% clinopyroxene, which is comparable to the average composition of lower oceanic crust gabbros [Coogan, 2007]. In microscopic scale, the igneous layering is visible by orientated olivine and plagioclase crystals. Primary minerals are mostly fresh, except for olivine showing typically mesh structure indicating the beginning of low-grade alteration (serpentinisation). In some samples, orthopyroxene occurs as interstitial phase between olivine and clinopyroxene. All primary minerals show no visible zonation under the microscope.

The petrographic texture and mineral assemblage of the layered gabbro sequence is very typical for the lower gabbro in the Wadi Tayin massif [Pallister and Hopson, 1981]. The order of crystallization derived from the cumulate texture is generally olivine followed by plagioclase and/or clinopyroxene, which is typical for anhydrous mid-ocean ridge basalts

crystallization in mid-ocean ridge magma chambers at shallow depth [e.g., *Feig et al.*, 2006; *Gaetani et al.*, 1993; *Grove and Bryan*, 1983].

#### **B.4.2 Gabbroic Dikes**

The gabbroic dikes show typical mineral assemblages of the magmatic constituents plagioclase + clinopyroxene + amphibole + FeTi-oxides ± olivine ± orthopyroxene forming a complex magmatic texture. Two sub-types of textures can be observed (Figure 13): (1) the dominant texture in the gabbroic dikes is a fine-grained granular texture composed of anhedral plagioclase + clinopyroxene ± orthopyroxene ± olivine with interstitial brown pargasitic amphibole often associated with FeTi-oxides. (2) Anhedral, mm sized brown pargasitic amphibole forms poikilitic clusters, enclosing lath-shaped plagioclase and granular olivine, often associated with FeTi-oxides. Plagioclase laths sometimes show swallowtail-shapes indicating a rapid cooling during formation.

Remarkably, the olivine shows plenty of tiny inclusions ( $\mu\text{m}$  to tens of  $\mu\text{m}$ ) of clinopyroxene, plagioclase and even FeTi-oxides. Such a feature is not typical for simple magmatic crystallization in a tholeiitic system under low pressure, but indicates a more complex formation history at the transition between magmatic to metamorphic conditions. In places, the gabbroic dikes are of composite character, with poikilitic pargasite at the rim of the dike and the granular matrix in the centre.

A complex replacing texture of most of the primary phases within the gabbroic dikes can be observed. Pargasitic amphibole often shows vein-controlled or zonally (at the rims) overprints by secondary light brownish to greenish hornblende (Figure 13 and 14). Within these secondary veins, a greenish bluish amphibole occurs (Figure 14a, b) which is characterised by extreme high chlorine content (up to 4.8 wt%.) Clinopyroxenes within the gabbroic dikes (especially those at the rim of the dike) show intergrowth with secondary greenish amphibole and bear typical blebs of light brown pargasitic amphibole [*Coogan et al.*, 2001a]. This typical interfingering texture of clinopyroxene and amphibole may indicate water/rock interactions at high temperatures [*Maeda et al.*, 2002], probably at the interface between magmatic and metamorphic processes. These entire peculiar petrographic features imply that the dikes are not simple products formed by a crystallization of a melt, but indicate complex formation conditions in a regime between magmatic to metamorphic (hydrothermal) processes. Immediately after the magmatic formation, secondary metamorphic/hydrothermal overprint at still very high temperatures played a significant role, leaving behinds a complex textural and mineralogical replacement assemblage in a high grade of disequilibrium. This phase was followed by a low temperature hydrothermal overprint, expressed by alteration of the mafic phases to chlorite and/or low temperature amphibole (actinolite or tremolite). Both minerals are typical for the greenschist facies in metabasites [*Liou et al.*, 1985].

Textural relation between the gabbroic dikes and layered gabbro host indicates that the dike formation is restricted to a cracking network, with only little signs for alteration in the gabbro adjacent to the dikes. Further away from the dikes, the layered gabbro remains completely fresh. An important discovery is the presence of those typical microstructures

---



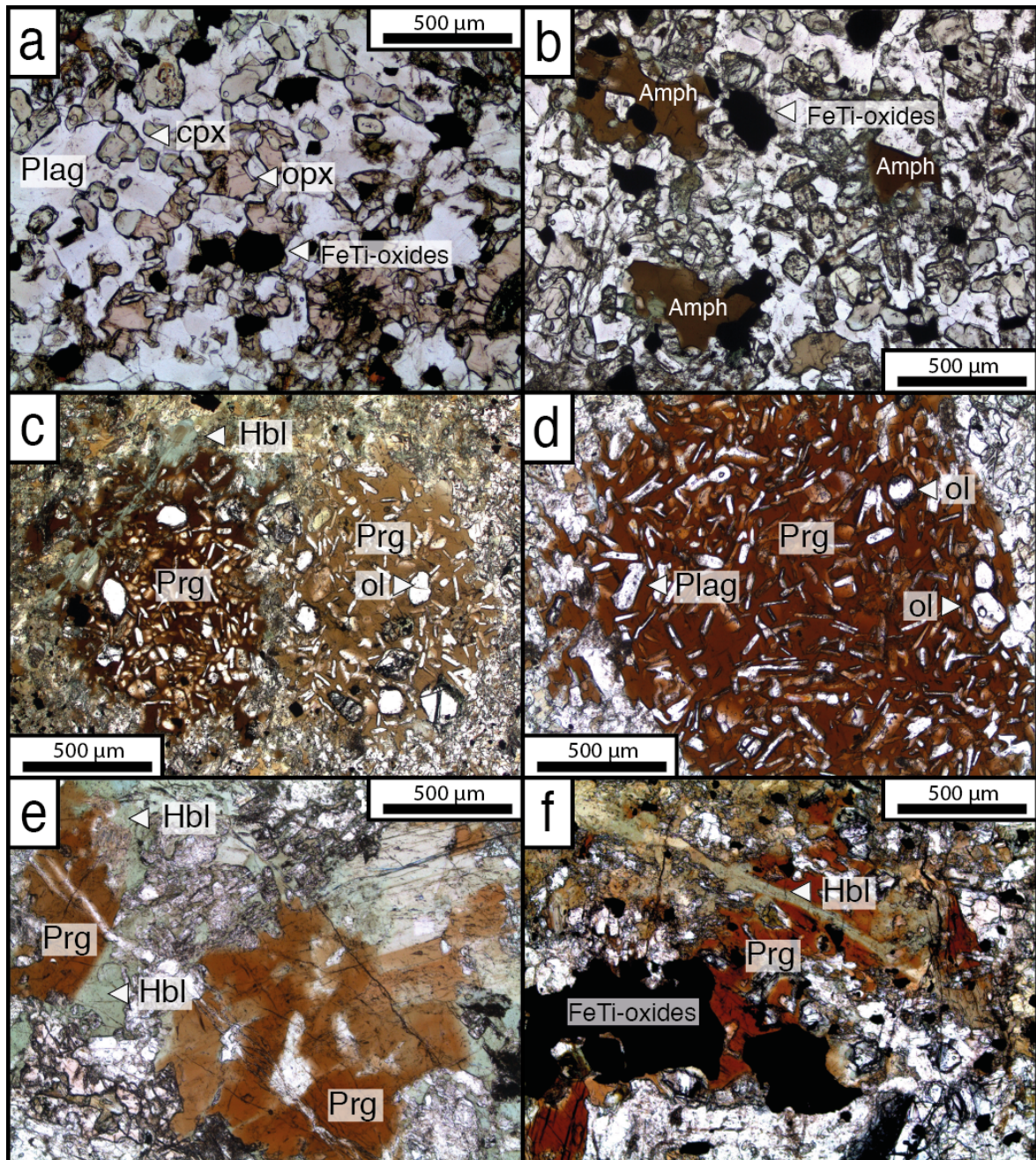


**Figure 13.** Microphotographs of the principle textural and mineralogical features of the gabbroic dikes from the Wadi Wariyah. All photos are taken under plane-polarized light. (a) Centre of the dike showing a fine-grained granular texture composed of plagioclase (Plag), clinopyroxene (cpx), orthopyroxene (opx), and FeTi-oxides (*sample: Wa\_42A*). (b) Interstitial brown pargasite (Amph) associated with FeTi-oxides within the granoblastic texture (*Wa\_46A*). (c-d) Poikilitic brown pargasite enclosing granular olivine (ol) and lath shaped plagioclase (Plag). Some of the plagioclase laths show swallowtail texture indicating fast quenching processes. Brown pargasite shows vein-parallel greenish vein, composed of hornblende (Hbl) indicating complex replacement texture in the gabbroic dike (c: *Wa\_04*; d: *Wa\_32A*). (e) Brown pargasite surrounded by secondary greenish hornblende (Hbl; *Wa\_32A*). (f) Greenish vein composed of hornblende (Hbl) running through a primary brown pargasite. The pargasite is associated with FeTi-oxides (*Wa\_42A*).

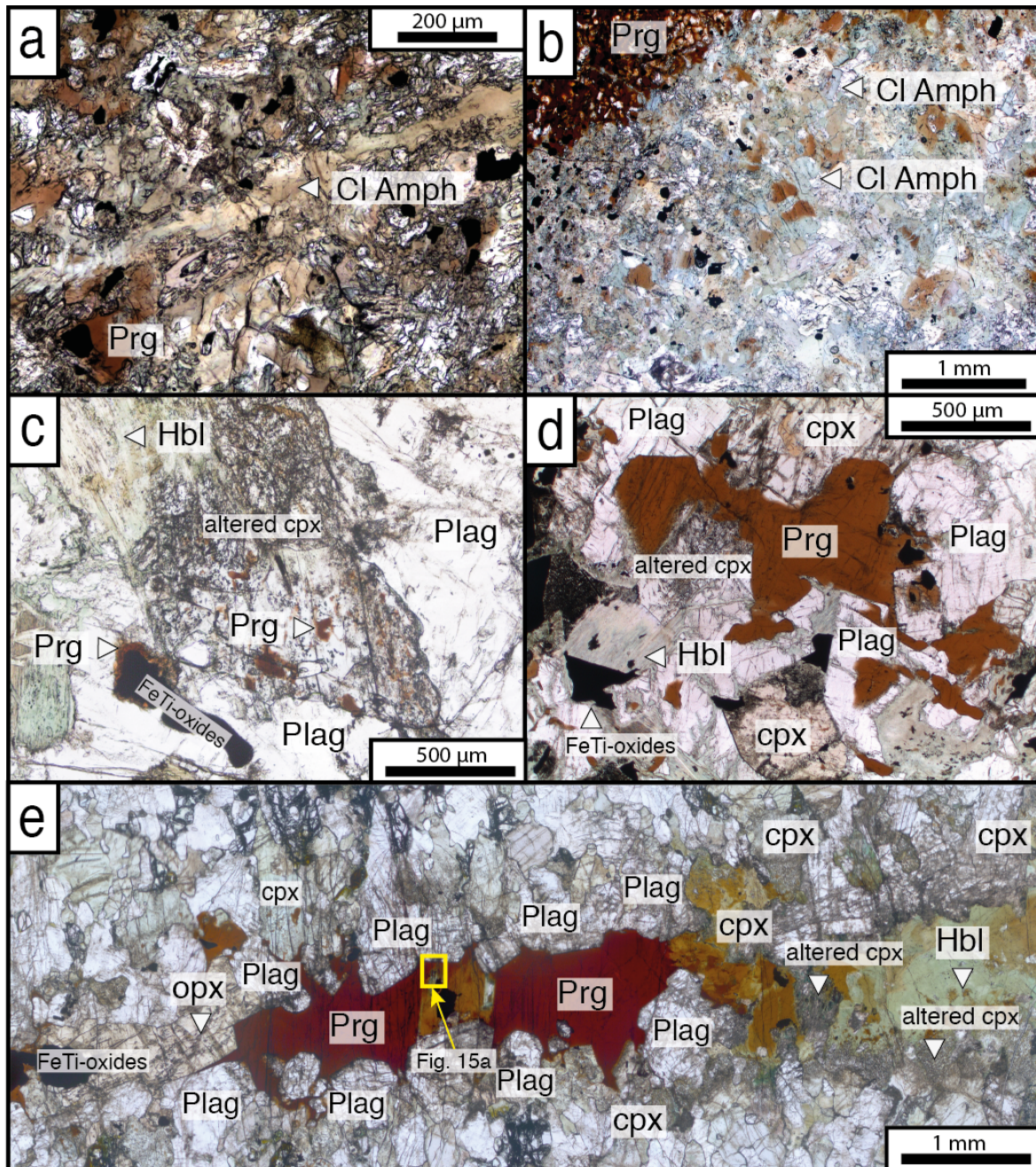


**Figure 14.** Microphotographs of the principle features of the chlorine-rich amphibole (Cl Amph) and altered clinopyroxene in gabbroic dikes and principle texture and mineralogy of the dark veins. (a) Central part of a gabbroic dike showing cluster of dark reddish brown pargasite (Prg) with a vein-controlled overprint to a more pale, greenish to brownish amphibole. The vein is orientated parallel to the contact of the gabbroic dike (running from middle left to lower right corner; *sample: Wa\_42A*). (b) Poikilitic dark brownish pargasite surrounded by cluster of pargasite associated with FeTi-oxides (black spots). Within these zones a pale greenish, bluish amphibole occurs. The peculiar amphiboles presented in (a) and (b) are characterized by extreme high contents of Cl (up to 4.8 wt%) (see section B.6 for more details; *Wa\_04*). (c) Altered clinopyroxene (altered cpx) in the gabbroic dike surrounded by hornblende (Hbl), plagioclase (Plag) and FeTi-oxides. The altered gabbro bears several “blebs” of brown pargasite (*Wa\_46A*). (d) Typical mineralogy of the dark veins. The vein is filled with dark brown pargasite surrounded by anhydral plagioclase, clinopyroxene (sometimes the clinopyroxene is altered), and FeTi-oxides. At the rim of the vein green hornblende exists, which is regarded to form at lower temperature (*Wa\_47A*). (e) Overview of typical textural and mineralogical features of one dark vein (*sample: Wa\_02A; vein 23* in Table 8). The dark vein is dominated by pargasite surrounded by anhydral plagioclase, clinopyroxene, orthopyroxene, and FeTi-oxides. Greenish hornblende on the right side is formed by a secondary hydrothermal overprint at lower temperatures. The yellow box indicates the location of a detailed view presented in Figure 15a.

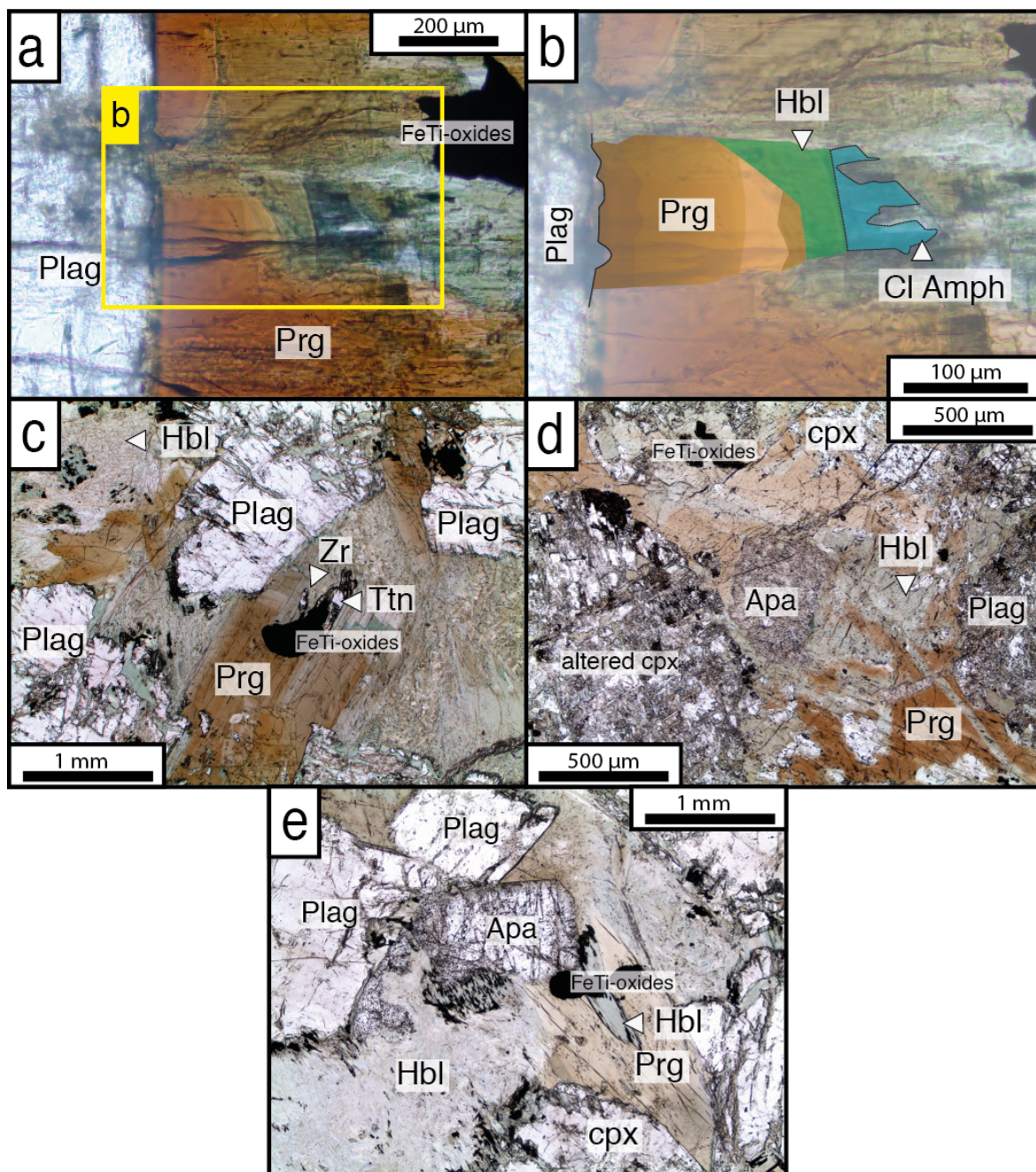


**Figure 15.** Microphotographs of the principle petrographic and textural features of the dark veins from the Wadi Wariyah. (a) Close up view of the area presented in Figure 14e. A multiple zoned amphibole occurs within brownish pargasite. At the rim of the vein plagioclase (Plag) occurs. FeTi-oxides forms in association with the amphibole. (b) Details sketch of the multiple-zoned amphibole. Beginning from the plagioclase (rim of the vein), the amphibole consists of several zones of brown pargasite (Prg) followed by greenish hornblende (Hbl). Further to the right, the greenish hornblende grades into a pale bluish greenish hornblende that is characterized by high Cl content. A measured concentration profile across all of the zones is presented in Figure 23. (c) Brown pargasite formed in an early stage replaced by green hornblende formed under lower temperatures encloses FeTi-oxides and tiny zircon (Zr) + titanite (Ttn). Plagioclase initially coexisting with primary amphibole shows replacement at the rim by low temperature alteration products (*sample: Wa\_47A*). (d) Anhedra apatite (Apa) within brown pargasite, which is progressively replaced by greenish hornblende. At the rim altered clinopyroxene (altered cpx) and plagioclase occur (*Wa\_58A*). (e) Cluster of pargasite with signs of secondary replacement by hornblende enclosing euhedral apatite and FeTi-oxides (*Wa\_58A*).

in the gabbro close to the dike contact, implying the proceeding of hydrous partial melting within the layered gabbro [Stichnothe, 2007] expressed by plagioclase rims strongly enriched in the anorthite component in association with the formation of orthopyroxene and pargasitic amphibole on grain boundaries [e.g., Wolff *et al.*, 2013]. This implies a working hypothesis that water-rich fluids released from the dike percolating on grain boundaries into the still very hot gabbro, triggering partial melting, at temperatures slightly above the wet gabbro solidus (870-900°C) [Beard and Lofgren, 1991; Koepke *et al.*, 2004; Wolff *et al.*, 2013]. For details see section B.6.1.

### **B.4.3 Dark veins**

Based on their mineralogy the dark veins can be classified into two groups (Figure 14 and 15): (1) Dark veins, dominated by a mineral assemblage composed of igneous plagioclase + clinopyroxene + orthopyroxene + amphibole and FeTi-oxides, forming a complex textural relation. This type of texture forms the majority of the dark veins. Accessory minerals, such as apatite, zircon, and titanite occur as euhedral minerals. (2) Amphibole dominated veins have a mineral assemblage of hornblende + plagioclase ± clinopyroxene. This type of dark veins is characterized by the absence of FeTi-oxides (or contain ilmenite only). Commonly, apatite occurs as accessory mineral within these veins.

In all dark veins a complex replacing textures of the primary formed minerals can be observed. Plagioclase forms euhedral to subhedral crystals mostly arranged at the rim of the veins. It is moderately altered and transected by numerous  $\mu\text{m}$ -sized fractures, mostly filled with epidote. In some dark veins, the plagioclase is regular zoned towards the centre of the veins. Anhedral clinopyroxene is mostly altered showing interfingering texture with intergrowth of amphibole and amphibole blebs, which is similar to the gabbroic dike. Anhedral orthopyroxene is both fresh and altered to low temperature amphibole. Pyroxenes are replaced by secondary greenish hornblende or acicular actinolite. Amphibole forms patches of vein-filling dark brown pargasite, mostly associated with FeTi-oxides, which dominates the centre of the dark veins. Very similar to the gabbroic dike the amphibole is characterized by a complex replacive texture. Pargasite is replaced by hornblende or actinolite indicating a metamorphic overprint within the dark veins. In some places the amphibole shows complex multiple zoning (Figure 15a, b), ranging from dark brown pargasite to greenish hornblende. In places, rims consist of a bluish greenish pargasite. As in the gabbroic dikes, the bluish, greenish pargasite is characterized by high Cl-concentrations (up to 5 wt%). Comparable to the gabbroic dike, the dark veins show significant textural evidences for a complex formation history from magmatic to metamorphic (hydrothermal). Furthermore, the mafic minerals in the dark veins are secondarily overprinted by greenschist facies minerals dominated by actinolitic/tremolitic amphibole and chlorite.

Similar to the gabbroic dikes the textural relations between dark veins and the layered gabbro indicates that the formation of the dark veins is restricted to a cracking network within the layered gabbro. The contact to the layered gabbro is sharp with general no signs of alteration close to the dark veins. Only a few dark veins show a few cm-thin halos,

---

composed of altered gabbro, where olivine is replaced by chlorite. Further away from the veins, the layered remains completely fresh.

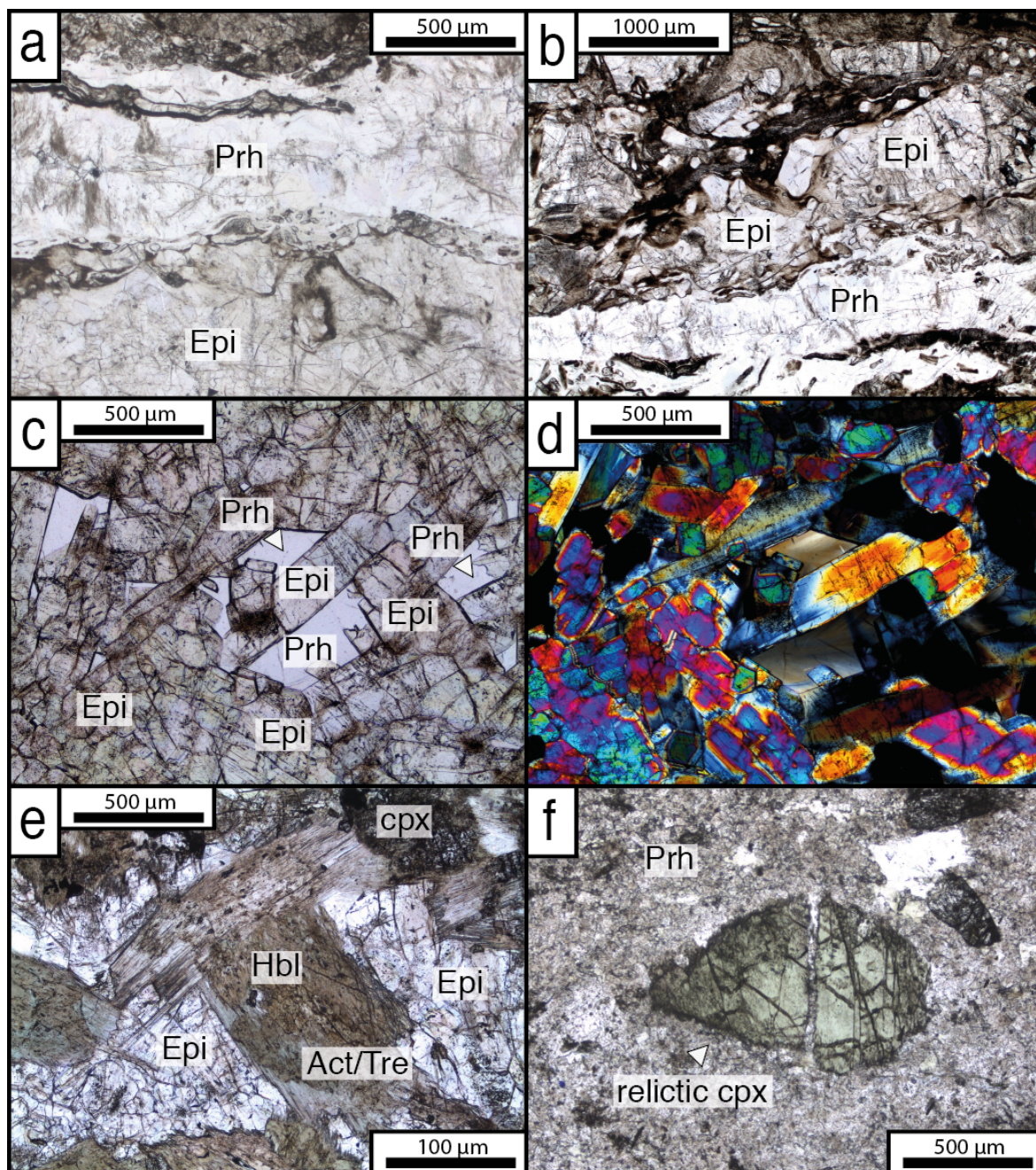


**Figure 16.** Microphotographs showing the principle petrographic and textural features of the epidote veins and prehnite veins. (a-b) The epidote vein is characterized by vein-parallel zoning composed of nearly monomineralic epidote (Epi; clinzoisite) and late stage prehnite (prh) forming a metamorphic fluidal texture (*sample: Wa\_40A*). (c-d) Dense network of zoned epidote (*Wa\_43A*) under (c) plane-polarized light and (d) cross-polarized light with interstitial prehnite (Prh). (e) Clusters of hornblende (Hbl) with rims of late-stage (low temperature) actinolite/tremolite (Act/Tre) surrounded by epidote and altered clinopyroxene (cpx; *Wa\_43B*). (f) Prehnite vein composed mainly of monomineralic prehnite. The veins are characterized by a cataclastic imprint showing augen-like deformed clasts of relicts of clinopyroxene (relictic cpx) swimming in the matrix (*Wa\_61*).

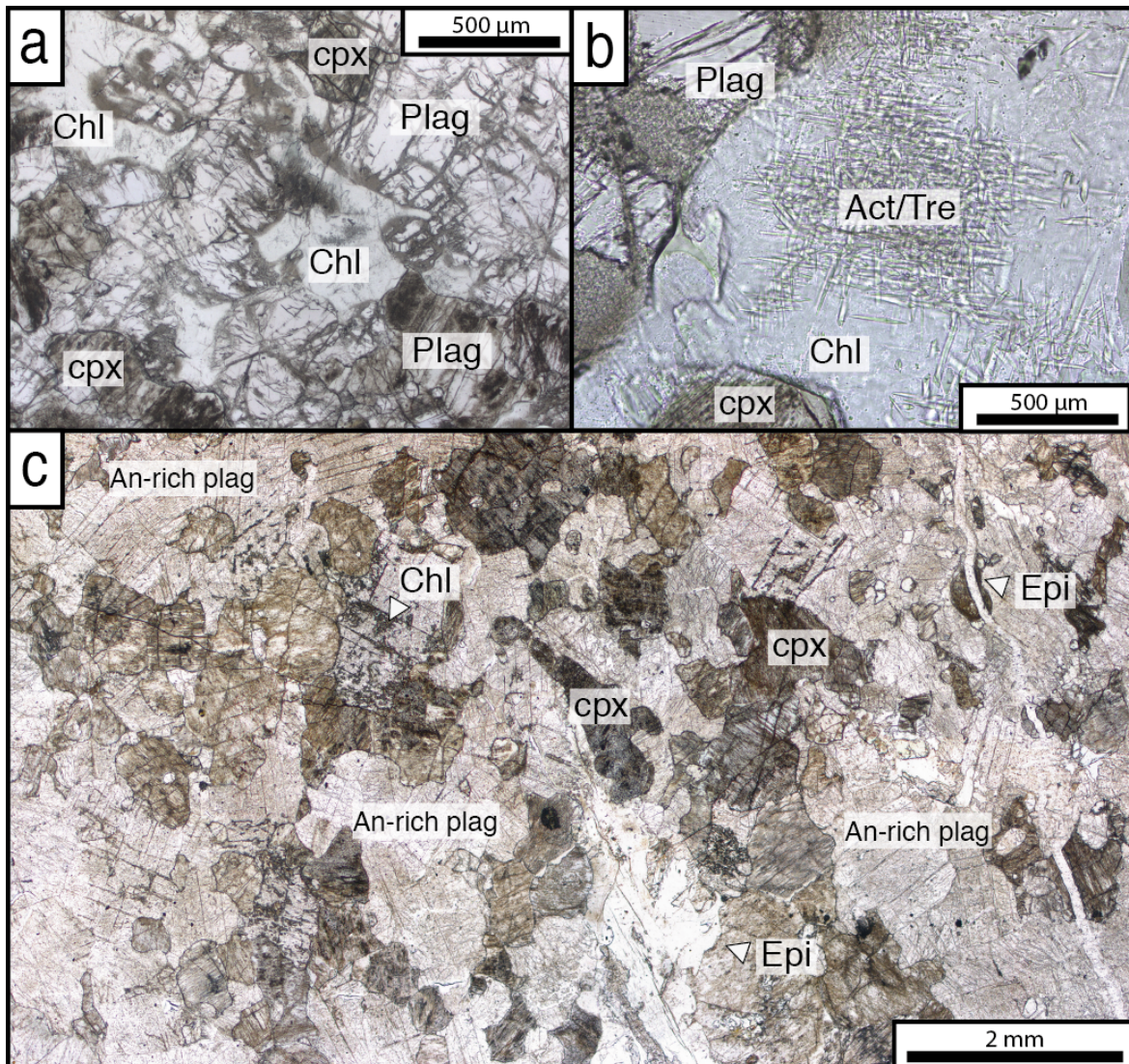


**Figure 17.** Microphotographs showing the principle petrographic and textural features of the altered gabbros and An-bearing metagabbro. (a-b) Typical mineralogy of the altered gabbro (*sample: Wa\_40C*). The altered gabbro is characterized by typical replacement of the primary minerals of the layered gabbro. A mixture of chlorite (Chl) and fine needles of actinolite/tremolite (Act/Tre) replaces primary olivine and parts of clinopyroxene (cpx) and plagioclase (Plag). Clinopyroxene and plagioclase are highly fractured. These veins are mostly composed of epidote (not shown in this Figure). The replacement of the primary minerals by typical minerals of the greenschist facies indicates hydrothermal alteration at medium temperature (for temperature definition see section B.8.1.1). (c) Typical mineralogy of the An-bearing metagabbro. Primary magmatic plagioclase has been completely replaced by a plagioclase strongly enriched in An-content (An-rich plag) and low in minor and trace elements (see section for more details). Clinopyroxene (cpx) is highly altered but still show in places the typical composition of clinopyroxene in the original layered gabbro. Several veins composed of epidote (Epi) fracture the An-bearing metagabbro (*Wa\_69*).

#### B.4.4 Epidote veins

Veins consisting mainly of epidote minerals (epidote s. str. (*sensu stricto*)) are often arranged in vein-parallel zones consisting of minerals of different metamorphic facies, often involved in complex replacement relationships. Commonly, the epidote veins are dominated by monomineralic zones of a dense network of epidote sometimes associated with interstice filled with late prehnite (Figure 16). The epidote is typically unzoned, except for the epidote vein of the sample *Wa\_43*, where the epidote shows continuous

zoning. Other domains of the epidote vein (e.g., *Wa\_43B*) are composed of patches of hornblende/actinolite with actinolite/tremolite at the rim (Figure 16c) often associated with lumpy, brownish alteration product of a former Ti-phase (leucoxene) and chlorite. Chlorite mostly forms aggregates of chlorite and tiny needles of actinolite/tremolite. The vein minerals - mostly clinozoisite, hornblende to actinolitic hornblende, chlorite - are characteristic of the greenschist facies. In places, typical low-grade metamorphic minerals like prehnite and minor pumpellyite replace them. The prehnite mostly occur as interstitial phase showing radiating birefringent blades.

#### **B.4.5 Prehnite veins**

A dense network of monomineralic fine-grained prehnite dominates the prehnite veins. In places, prehnite is associated with augen-like shaped, deformed clasts of clinopyroxene swimming in a matrix of undeformed prehnite indicating a phase of cataclasis before the filling of the vein (Figure 16f). Often, these clasts show a distinct undulatory extinction.

#### **B.4.6 Halos, altered gabbros, and highly altered gabbros**

The halos, altered gabbros, and highly altered gabbros have a similar petrographic record consist of a complex replacement of the primary magmatic minerals of the layered gabbro. They are characterized by different degrees of alteration as a function of distance from the veins. The degree of alteration is defined by the amount of replacement of the primary constituent minerals of the layered gabbro. The replacive nature of the primary mineral constituents, forming the altered gabbros, indicates progressively alteration of the layered gabbro, which penetrates more or less into the fresh gabbro. Typical minerals of the greenschist facies have replaced the primary minerals of the layered gabbro. In all samples a mixture of chlorite and tiny needles composed of actinolite/tremolite replaces olivine leaving behind typical ghost textures (Figure 17a). In the altered gabbro, other primary constituents (plagioclase and clinopyroxene) remain mostly fresh. However, with increasing alteration degree, plagioclase joins the reaction of olivine replacement and show strong alteration of the rims and numerous veins transecting, filled with  $\mu\text{m}$ -sized epidote. The reaction is leaving behind plagioclase cores (Figure 17b). In the halo, plagioclase is progressively replaced by epidote. Close to the epidote veins, plagioclase is completely altered to epidote. Altered clinopyroxenes show a dark, lumpy appearance under the microscope, but still have the typical composition from the fresh layered gabbro. Even in the highly altered gabbro surrounding the prehnite veins, clinopyroxene still preserves the magmatic texture as in the layered gabbro.

#### **B.4.7 An-bearing metagabbro**

The An-bearing metagabbro is an altered gabbro with characteristic feature that the former plagioclase was transformed to nearly pure anorthite. Similar to the altered gabbro olivine show complete replacement by a mixture of chlorite and fine needles of actinolite/tremolite and clinopyroxene is altered to dark, lumpy aggregates. Clinopyroxene and plagioclase

form a dense network (Figure 17c). The appearance of a newly formed plagioclase composed of nearly pure anorthite (An), which is also significantly depleted in minor elements and trace elements, is remarkably (see section B.6). It indicates a complex replacement of primary plagioclase, which is not a peculiar feature observed in the halos/altered gabbro surrounding the epidote veins (see previous section). Clinopyroxene appears black under the microscope indicating possible alteration. The clinopyroxenes still preserved their primary composition (see section B.6) and structure of the layered gabbro.

## B.5 Bulk rock chemistry

The bulk-rock chemistry of the layered gabbro, gabbroic dikes, dark veins, epidote veins, prehnite veins, halos, altered gabbros, and An-bearing metagabbro is shown in Table 9.

### B.5.1 Major elements

*Layered gabbro.* Major element composition obtained for the average (based on modal proportions) layered gabbro reveals typical cumulate bulk-rock composition with low SiO<sub>2</sub>. The Mg#’s of the layered gabbro are ranging from 78.53 - 81.26 indicating very primitive composition. Al<sub>2</sub>O<sub>3</sub> and CaO content are 18.58 wt% and 16.44 wt%, respectively. Minor elements show generally low contents. K<sub>2</sub>O content is averaging 0.01 wt% and TiO<sub>2</sub> is averaging 0.17 wt%. Noteworthy, is the remarkably high content of loss on ignition (L.O.I.) averaging 1.04 wt%, probably due to the local abundance of secondary alteration products. In summary, the layered gabbro show typical composition compared to mafic cumulate from modern fast-spreading ocean ridges [Gillis *et al.*, 2013; Lehnert *et al.*, 2000] and the Semail ophiolite [Browning, 1982; MacLeod and Yaouancq, 2000; Pallister and Hopson, 1981]. The high Mg# and low SiO<sub>2</sub> is characteristic for gabbroic cumulates of the deep crustal section near the Moho transition zone. The composition of the layered gabbro can be regarded as host igneous rock before hydrothermal alteration started.

*Gabbroic dikes.* The gabbroic dikes show similar SiO<sub>2</sub> content averaging 44.58 wt% compared to the layered gabbro, but Mg# number is lower with an average of 66.05. This low Mg# is the result of significant enrichment in Fe<sub>2</sub>O<sub>3</sub> content (11.07 wt%) compared to the layered gabbro reflecting the accumulation of FeTi-oxides in the gabbroic dikes. Al<sub>2</sub>O<sub>3</sub> and CaO are depleted compared to the layered gabbro showing an average of 13.69 wt% and 10.97 wt%, respectively. The gabbroic dikes are characterized by enrichment in minor elements (K<sub>2</sub>O and TiO<sub>2</sub>). K<sub>2</sub>O content averaging 0.08 wt% and TiO<sub>2</sub> shows an average of 1.38 wt%. The gabbroic dikes show increased L.O.I. content of 2.00 wt%.

*Dark veins.* The composition of the dark veins can be classified into two groups, which strongly reflects the differences in mineralogy (see section B.4.3). The dark veins without FeTi-oxides show SiO<sub>2</sub> content of 48.36 wt% and Mg# of 77.73. FeTi-oxide-bearing dark vein show lower SiO<sub>2</sub> content of 45.66 wt% and lower Mg# 64.45. The higher Mg# number of the dark veins without FeTi-oxides reflects the absence of FeTi-oxides. The SiO<sub>2</sub> content of both types of dark veins is similar relatively to the layered gabbro. Al<sub>2</sub>O<sub>3</sub>

---



and CaO are constant in all dark veins showing an average of 16.78 wt% and 14.44 wt%, which is slightly lower compared to the layered gabbro. Similar to the obtained results of the gabbroic dike, the dark veins are enriched in minor elements. Thereby, K<sub>2</sub>O is constant showing an average of 0.06 wt% and TiO<sub>2</sub> is higher in the dark veins containing FeTi-oxides (1.59 wt%) and slightly enriched in the dark veins without FeTi-oxides (0.27 wt%). The L.O.I. content for all dark veins is averaging 1.83 wt%, which is slightly enriched, compared to the layered gabbro.

*Epidote veins.* The bulk-rock composition of the epidote veins is relatively heterogeneous and strongly reflects the vein mineralogy. This heterogeneity is related to the different types of epidote veins. The thin epidote veins show SiO<sub>2</sub> content of 41.07 wt% with a constant Mg# of 58.8. The low Mg# reflect a strong decrease in MgO content (4.97 wt%), while Fe<sub>2</sub>O<sub>3</sub> (6.19 wt%) is enriched compared to the layered gabbro. The high amount of epidote with subordinated prehnite is expressed by an increase in Al<sub>2</sub>O<sub>3</sub> (22.65 wt%) and CaO (20.98 wt%) content relatively to the layered gabbro. Minor elements are generally low. K<sub>2</sub>O is under the limit of quantification and TiO<sub>2</sub> (0.02 wt%) show lower concentration compared to the layered gabbro. L.O.I. (3.13 wt%) is significantly enriched compared to the layered gabbro. In contrast, the epidote vein of sample *Wa\_43A* is characterized by nearly similar SiO<sub>2</sub> content of 41.07 wt% and very low Mg# of 49.18, which strongly reflects the decrease of MgO (1.78 wt%). Al<sub>2</sub>O<sub>3</sub> (26.05 wt%) and CaO (23.63 wt%) concentrations are slightly enriched compared to the layered gabbro and to the thin epidote veins. K<sub>2</sub>O is also below the limit of quantification, but in contrast to the thin epidote veins the TiO<sub>2</sub> (0.35 wt%) content is significantly enriched. L.O.I. content is 2.60 wt%. The amphibole-rich zone (*Wa\_43B*) with patches of actinolite/tremolite shows SiO<sub>2</sub> content of 41.51 wt%. Although this part of the vein is characterized by amphibole the Mg# (34.61), which is the lowest recorded in the lithologies of the Wadi Wariyah. Al<sub>2</sub>O<sub>3</sub> (20.84 wt%) and CaO (21.82) show enriched concentrations compared to the layered gabbro. Minor elements follow the trend of the thin epidote veins. K<sub>2</sub>O is below the detection limit and TiO<sub>2</sub> (1.43 wt%) is strongly enriched, which is due to the high amount of leucoxene and amphibole in these veins. L.O.I. content is 2.22 wt% which also reflects the increase of hydration of in the veins.

*Prehnite veins.* Similar to the epidote veins, the composition of the prehnite veins reflects high amount of prehnite. SiO<sub>2</sub> content is 43.10 wt%. In contrast to the epidote veins the bulk Mg# (78.71) tends towards the composition of the layered gabbro, although Fe<sub>2</sub>O<sub>3</sub> and MgO are strongly depleted (< 1 wt%) in the prehnite veins. Al<sub>2</sub>O<sub>3</sub> (24.26 wt%) and CaO (26.83 wt%) are enriched compared to the layered gabbro. Minor elements are low showing the same values as the thin epidote veins (K<sub>2</sub>O below detection limit and TiO<sub>2</sub> 0.02 wt%). L.O.I. (4.76 wt%) is strongly enriched.

*Halos, altered gabbro, and highly altered gabbro.* The altered gabbro and the highly altered gabbro show homogeneous composition very similar to the layered gabbro with no signs for any element concentration being enriched or depleted, except for a strong increase in L.O.I. (3.14 wt%). The halos show heterogeneous composition. The halos surrounding the thin epidote veins are characterized by only slight compositional variation compared to the layered gabbro. Al<sub>2</sub>O<sub>3</sub> and MgO contents are increased averaging 14.44 wt% and 12.25 wt%. The Mg# is similar like in the layered gabbro (81.70). Only L.O.I.

shows significant higher concentration of 4.05 wt%. In contrast, the halo (*Wa\_43C*) surrounding the epidote vein *Wa\_43A* is characterized by a significant enrichment in CaO (20.57 wt%), while Al<sub>2</sub>O<sub>3</sub> is depleted (10.14 wt%). Interestingly, is the enrichment of TiO<sub>2</sub> of 0.68 wt% that cannot be observed in the other halos. Although the Mg# is similar to the layered gabbro and other altered gabbro, the halos are characterized by an increase in MgO (13.79 wt%) and Fe<sub>2</sub>O<sub>3</sub> (5.35 wt%). L.O.I. is lower compared to the other halo/altered gabbro, but a value of 2.41 wt% indicates an increase in hydration compared to the layered gabbro.

*An-bearing metagabbro.* The An-bearing metagabbro shows similar composition compared to the layered gabbro. SiO<sub>2</sub> (44.42 wt%) is slightly decreased and Mg# is 81.61. It is enriched in Al<sub>2</sub>O<sub>3</sub> (20.54 wt%) and depleted in CaO (15.47 wt%). Minor elements show no difference between layered gabbro and the An-bearing metagabbro show L.O.I. of 3.86 wt%.

## **B.5.2 Trace elements**

Trace and transitional metals element patterns of the layered gabbro, gabbroic dikes, dark veins, epidote veins, prehnite veins, and altered gabbro are shown in Figure 18. Normalisation is against primitive mantle values of *Sun and McDonough* [1989] for the trace elements and *Sun* [1982] for the transitional metals.

*Layered gabbro.* The layered gabbro shows transitional metal concentration in the range of MORB compositions (Figure 18a) [*Gale et al.*, 2013]. Cu content is averaging 88 ppm, which is in typical magmatic range [*Coogan et al.*, 2006]. Trace element concentrations are typically depleted, which strongly reflects the primitive cumulative origin of the gabbro. Especially, the high field strength elements (HFSE) are commonly below the limit quantification. The layered gabbro is enriched in Sr (average of 166 ppm) compared to other elements reflecting the high amount of plagioclase in the layered gabbro.

*Gabbroic Dikes.* The gabbroic dikes are enriched in most elements relatively to the layered gabbro (Figure 18b). Transitional metals are mostly slightly enriched relatively to the layered gabbro, reflecting the occurrence of FeTi-oxides. Especially, Cu (114 ppm) and V (362 ppm) are strongly enriched, while Cr show nearly constant (710 ppm) compared to the layered gabbro. Except for Sr (average 160 ppm) and in some samples P, all trace elements are enriched relatively to the layered gabbro. Especially, the HFSE (e.g., Zr) show higher concentration.

*Dark veins.* Similar to the gabbroic dikes trace elements are enriched in the dark veins (Figure 18c). Dark vein without FeTi-oxides show lower transitional metals concentration (e.g., V and Cu), which strongly reflects the absence of FeTi-oxides. This is also indicated by low Ti concentration of the dark veins without FeTi-oxides. Trace elements are generally enriched, except for Sr (167-190 ppm). Similar to the gabbroic dikes, the HFSE are enriched relatively to the layered gabbro.

---

Epidote veins. The epidote veins show heterogeneous trace element concentrations (Figure 18d). While the thin epidote veins are mostly depleted in trace elements (except for Sr and Eu), the epidote vein of sample *Wa\_43A* shows constant to enriched element concentrations relatively to the layered gabbro. Transitional metals are mostly depleted in all the epidote veins. Remarkably, Sr is highly enriched in all epidote veins. Ba is generally highly depleted (below limit of quantification) relatively to the layered gabbro. The heterogeneous trace element concentration of the epidote veins indicating possible complex formation history. The amphibole-rich zone of the vein-parallel epidote (*Wa\_43B*) vein is depleted in Cr and Cu, while V is enriched compared to the layered gabbro. Trace element concentrations are generally enriched except for P. Sr concentration is in the range of the epidote veins showing 430 ppm.

Prehnite veins. The prehnite veins are generally depleted in transitional metals and trace elements relatively to the layered gabbro showing generally very low values (Figure 18e). Notably is the very low Sr concentration of 14 ppm compared to the epidote veins.

Halos, altered gabbro, and highly altered gabbro. The halos/altered gabbros surrounding show variable trace element concentrations (Figure 18f). Halos surrounding the thin epidote are characterized by depletion in trace elements (e.g., Ba, La, K are below detection limit). In contrast, in the halo (*Wa\_43C*) surrounding the thick epidote vein (*Wa\_43A and B*), the trace elements are characterized by an enrichment compared to the layered gabbro. The altered gabbro is characterized by similar element concentration compared to the layered gabbro, except for Ba and K being slightly enriched. The highly altered gabbro shows low Sr concentration of 53 ppm, whereas other trace elements are in the range of the layered gabbro. Transitional metals of halos/altered gabbros show same range compared to the layered gabbro with no significant enrichments or depletions.

An-bearing metagabbro. The An-bearing metagabbro is characterized by enrichment in Sr (251 ppm), which indicate the formation of high An plagioclase (Figure 18g). Some elements (Ba, K) are enriched compared to the layered gabbro, while most of the elements are in the same range of the layered gabbro or slightly depleted (Zr = 6 ppm). Transitional elements are in the range of the layered gabbro, except for Cu (6 ppm), which is slightly depleted.

---

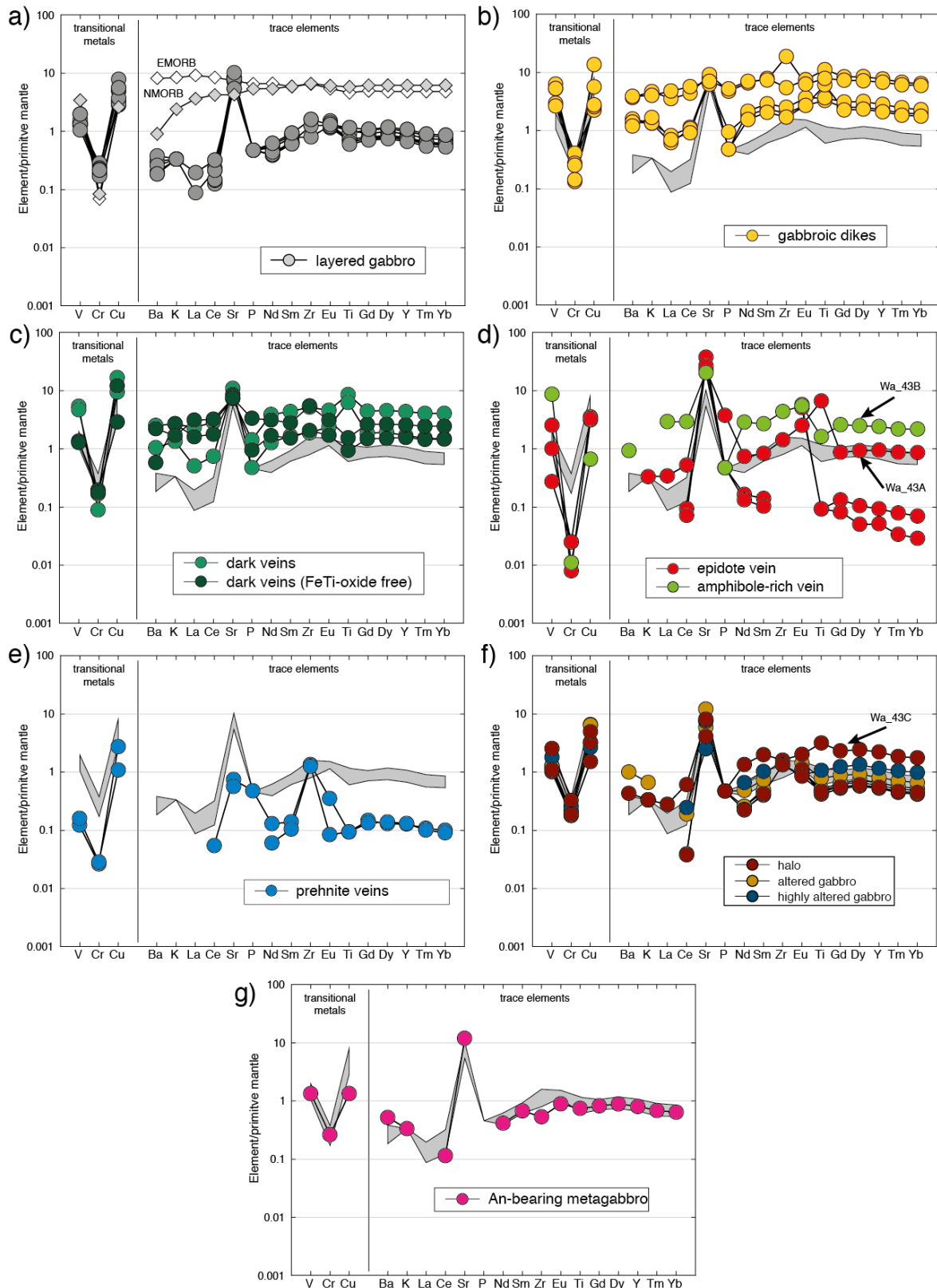


**Figure 18.** Primitive mantle-normalised element pattern for the transitional and trace elements of the (a) layered gabbro; (b) gabbroic dikes; (c) dark veins; (d) epidote veins; (e) prehnite veins; (f) halos/altered gabbro; and (g) An-bearing metagabbro. The trace elements and transitional metals values have normalised against chondritic value of *Sun and McDonough* [1989] and *Sun* [1982]. For comparison the pattern for normal MORB (NMORB) and enriched MORB (EMORB) are shown in (a) [*Gale et al.*, 2013; *Sun and McDonough*, 1989]. The grey area in Figure b-g indicates the pattern of the layered gabbro from the Wadi Wariyah from (a).

### B.5.3 Rare earth elements (REE)

Rare earth element patterns are normalised against chondritic values after *Sun and McDonough* [1989] of the layered gabbro, gabbroic dike, dark vein, epidote vein, and prehnite vein, halos, and altered gabbro are shown in Figure 19.

*Layered gabbro.* REE pattern of the layered gabbro are depleted compared to MORB values with a positive slope in light REE (LREE) reflecting a strong fractionation of the LREE compared to the HREE (Figure 19a). The accumulation of plagioclase in the layered gabbro leads to a small positive Eu anomaly ( $\text{Eu}/\text{Eu}_N^* = 1.64$  in average) and it shows a slight negative slope in the heavy REE (HREE). The REE patterns of the layered gabbro from the Wadi Wariyah are in good agreement with typical lower crustal gabbros of the Semail ophiolite [*Pallister and Knight*, 1981]. Compared to the gabbroic analogues from the upper sections of the Semail ophiolite, the layered gabbro show even more depleted REE pattern [*Coleman*, 1977].

*Gabbroic dikes.* The gabbroic dikes show elevated REE pattern indicated by chondritic value ranging from 1.7 to 25.2 relatively to the layered gabbro (Figure 19b). REE pattern show a slight depletion in LREE and are both a negative and positive Eu anomaly characterize the gabbroic dikes ( $\text{Eu}/\text{Eu}_N^* = 0.85-1.25$ ). Gabbroic dikes with low REE pattern are characterized by a positive Eu anomaly and depletion in LREE very similar like REE of the layered gabbro. In contrast, gabbroic dikes with high REE pattern show a negative Eu anomaly and more flat REE pattern compared to the layered gabbro and the gabbroic dikes with low REE pattern.

*Dark veins.* REE patterns show distinctive differences between the dark veins and dark vein without FeTi-oxides (Figure 19c). Similar to the gabbroic dikes they show generally elevated REE patterns with chondritic values between 1.4 and 13.5. Dark veins without FeTi-oxides are characterized by a nearly flat REE patterns. In contrast, the dark veins with low REE pattern are similar the patterns to the layered gabbro at higher chondritic values with a small positive Eu anomaly.

*Epidote veins.* Generally, the epidote veins are characterized by a strong pronounced positive Eu anomaly (Figure 19d), but variable REE patterns. Based on the chondrite-normalised REE patterns, the epidote veins can be classified into two groups: (1) Epidote veins without internal zonation show depleted REE pattern with chondritic values range between 0.09 and 17.1, whereupon the high chondritic value refers to a strong pronounced Eu anomaly ( $\text{Eu}/\text{Eu}_N^* = 37-62$ ). (2) Thick zoned epidote vein (*Wa\_43A and B*) shows elevated REE concentrations compared to the layered gabbro. In the epidote rich (*Wa\_43B*) zone chondritic values range between 0.9 and 7.5 with a less pronounced Eu anomaly ( $\text{Eu}/\text{Eu}_N^* = 2.9$ ). The amphibole-rich zone (*Wa\_43B*) is enriched in REE compared to the layered gabbro showing chondritic values between 6.5 and 16.4, while the high REE concentration refer to a pronounced Eu anomaly ( $\text{Eu}/\text{Eu}_N^* = 2$ ).

*Prehnite veins.* Chondrite-normalised patterns of the prehnite veins show depleted REE pattern compared to the layered gabbro with chondritic values range between 0.12 and 1.03 (Figure 19e). Both a slight negative and a positive Eu anomaly is visible in the prehnite

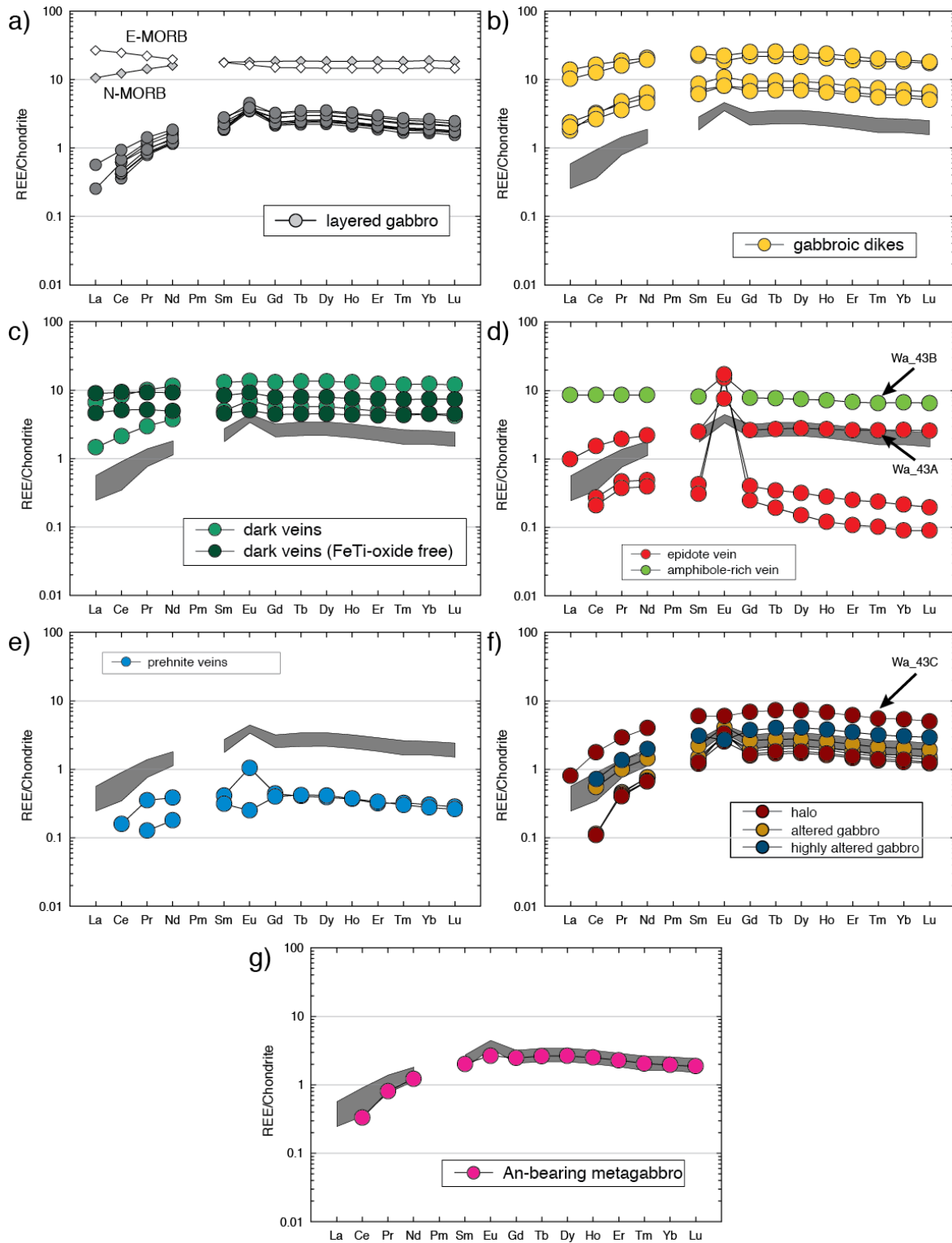


**Figure 19.** Rare earth element (REE) pattern of (a) layered gabbro; (b) gabbroic dikes; (c) dark veins; (d) epidote veins and amphibole-rich vein of the vein-parallel zone associated with epidote veins; (e) prehnite veins; (f) altered gabbro, halo, and highly altered gabbro; and (g) An-bearing metagabbro. The REE values have normalized against chondritic value of *Sun and McDonough* [1989]. For comparison the pattern for normal MORB (NMORB) and enriched MORB (EMORB) are shown [*Sun and McDonough*, 1989]. The grey area in Figure b-g indicates the pattern of the layered gabbro from the Wadi Wariyah, which shows depleted element pattern with an increase in heavy REE (HREE) and a positive Eu anomaly ( $Eu/Eu^* > 1$ ).

veins ( $\text{Eu}/\text{Eu}_N^* = 0.7\text{-}2.45$ ). However, Eu is significantly depleted compared to the other dikes and veins.

*Halos, altered gabbro, and highly altered gabbro.* The halos/altered gabbros surrounding epidote veins show variable chondritic value compared to the layered gabbro with depletion in LREE (Figure 19f). A positive Eu anomaly exists for the halo ( $\text{Eu}/\text{Eu}_N^* = 1.73\text{-}2.41$ ). Halo of sample *Wa\_43C* is significantly enriched in REE compared to the other halos showing chondritic values ranging between 0.8 and 7.25. This peculiar halo shows a slight negative Eu anomaly ( $\text{Eu}/\text{Eu}_N^* = 0.93$ ). The altered gabbro show similar REE pattern compared to the layered gabbro with no significant changes, except for one pattern, which shows lower REE pattern compared to the layered gabbro. In the highly altered gabbro the REE pattern show similar chondritic values compared to the layered gabbro show chondritic with values ranging between 0.7 and 4.01. A small negative Eu anomaly exists in the highly altered gabbro ( $\text{Eu}/\text{Eu}_N^* = 0.79$ ).

*An-bearing metagabbro.* The An-bearing metagabbro is characterized by slightly depleted REE pattern compared to the layered gabbro with chondritic values range between 0.31 and 2.65 (Figure 19g). In contrast to the layered gabbro it is characterized by only a small positive Eu anomaly ( $\text{Eu}/\text{Eu}_N^* = 1.18$ ), which indicates the lack of igneous plagioclase and maybe reflects the formation of high An-rich plagioclase low in trace elements.

## B.6 Mineral chemistry

### B.6.1 Major elements

*Olivine.* Olivine is a constituent of the layered gabbro showing homogeneous primitive composition typical for lower crustal gabbroic rocks from the Semail ophiolite. Composition of olivine from the Wadi Wariyah is listed in Table 10. Olivine is  $\text{Fo}_{81}$  ( $\text{Mg}^{2+}/[\text{Mg}^{2+}+\text{Fe}^{2+}] \times 100$  on a molar base) with a NiO content of 0.11 wt%. In the dikes and veins olivine only occurs in the gabbroic dikes and shows homogeneous and slightly more evolved composition of  $\text{Fo}_{73}$  compared to the layered gabbro, but similar NiO content of 0.12 wt%.

*Plagioclase.* In the layered gabbro plagioclase makes up the largest modal proportion and it is also one of the most abundant minerals in the gabbroic dikes, dark veins, and altered gabbros showing a wide compositional range. Representative plagioclase compositions are listed in Table 11. Plagioclase cores of the layered gabbro are  $\text{An}_{83}$  ( $\text{An} = (\text{Ca}^{2+}/[\text{Ca}^{2+}+\text{Na}^{2+}+\text{K}^{2+}] \times 100$  on a molar base). Minor elements in the plagioclase cores are generally low with  $\text{K}_2\text{O}$  and  $\text{FeO}^{\text{tot}}$  showing 0.01 wt% and 0.47 wt%, respectively. Notably, plagioclase rims in the layered gabbro near to the contact to a magmatic dike are enriched in An averaging 86 mol% (Figure 20a). *Stichnothe* [2007] measured corresponding concentration profiles across grain boundary between two plagioclases. Since An-rich rims in plagioclases from the layered gabbro in the Semail ophiolite are normally not observed

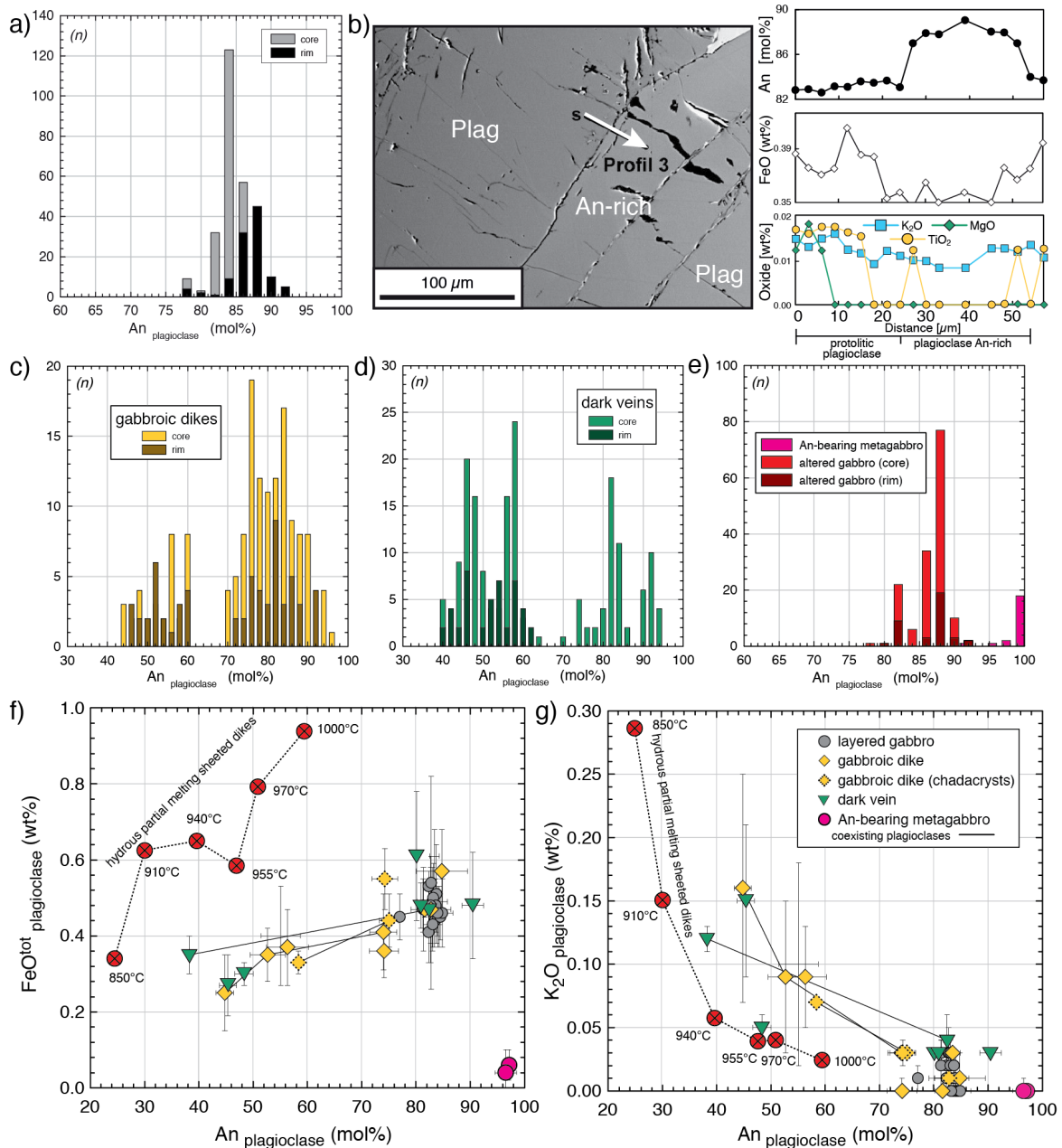


**Figure 20.** Compositional variation of plagioclase from the Wadi Wariyah. (a) An content in plagioclase cores and rims of the layered gabbro from the Wadi Wariyah. Plagioclase rims show a systematic enrichment in An component. (b) Corresponding concentration profile from plagioclase core to rim in the layered gabbro near the contact to a gabbroic dike. The results show a correlation between the enrichment in An-content and depletion in minor elements (K<sub>2</sub>O, FeO, MgO, and TiO<sub>2</sub>) indicating the beginning of a partial melting reaction (modified after *Stichnothe* [2007]; for details see text). (c-e) An content in plagioclase cores and rims of the (c) gabbroic dikes, (d) dark vein, and (e) altered gabbro/An-bearing metagabbro;  $n$  is the number of single point analysis. (f-g) Compositional correlation between An content and (f) FeO<sup>tot</sup> and (g) K<sub>2</sub>O in plagioclases from the Wadi Wariyah. Plagioclase from the gabbroic dikes and dark veins show similar compositional evolution compared to residual plagioclase expected from hydrous partial melting reaction of the sheeted dikes (crossed red dots, number indicate temperature of the experiment) [*France et al.*, 2010]. In contrast, composition of plagioclase in the An-bearing metagabbro is clearly distinguished from compositional evolution of hydrous partial melting, indicated by high An content and low FeO<sup>tot</sup> and K<sub>2</sub>O content. Composition of plagioclase from the altered gabbros is similar to the layered gabbro and is not shown here.

(*Müller, personal communication*), it implies a model that these plagioclase rims represent a residual phase after a hydrous partial melting event in the layered gabbro triggered by water-rich fluid percolating on grain boundaries in the plagioclase near the contact. Such



plagioclase compositions are characterized by enrichment in An (up to An<sub>88</sub>) and depletion in minor elements (TiO<sub>2</sub>, K<sub>2</sub>O, and FeO<sup>total</sup>) [for details see *Koepke et al.*, 2014 in press; *Wolff et al.*, 2013].

Plagioclase in the gabbroic dikes (crystals in the granoblastic texture and chadacrysts) show a variable composition from An<sub>87</sub> to An<sub>45</sub> leading to bimodal distribution in the An content (Figure 20c, d). No core rim correlation can be observed. Especially, one gabbroic dike shows three different populations from An<sub>73</sub> via An<sub>52</sub> down to An<sub>45</sub>. A positive correlation between An content and K<sub>2</sub>O concentration can be observed, which reaches a maximum of 0.19 wt% at An<sub>45</sub>. Plagioclase shows a weak negative correlation between An and FeO<sup>tot</sup> content (Figure 20e). They show lower FeO<sup>tot</sup> content with decreasing An content. Plagioclase in the dark veins follows the compositional trend (An vs. K<sub>2</sub>O, FeO<sup>tot</sup>) of the gabbroic dikes and shows variable composition An<sub>91</sub> to An<sub>38</sub> in the cores. Similar to the gabbroic dikes plagioclase cores in the dark veins show bimodal distribution (Figure 20d). In contrast, plagioclase rims are low in An ranging from An<sub>55</sub> to An<sub>43</sub>. The bimodal distribution of the An content in plagioclase implies a model that the plagioclase record complex formation history of the gabbroic dikes and dark veins. Similar to the high An rims found in the layered gabbro, the high An content (up to An<sub>93</sub> in gabbroic dikes and An<sub>92</sub> in the dark veins) and low in trace elements represents residual phases after a hydrous partial melting event. Since partial melting produces a silica-rich plagiogranitic melt [*Wolff et al.*, 2013], the low An plagioclase might represent products formed by crystallization of the melts after the hydrous partial melting event. These plagioclases show typical element trace element enrichment.

Remarkably, is the plagioclase composition in the An-bearing metagabbro. As shown in Figure 20e-g it is characterized by high (“nearly pure”) An content of 97 mol%. Furthermore, these plagioclases are significantly depleted in minor and trace elements. Plagioclase in the altered gabbro show the same composition compared to the layered gabbro.

*Pyroxene.* Clinopyroxene compositions are listed in Table 12. In the layered gabbro clinopyroxene is augite with the endmember composition of En<sub>46</sub>Fs<sub>9</sub>Wo<sub>45</sub> [endmember calculation according to *Morimoto et al.*, 1988] and typical “primitive” composition with a high Mg# of 89. Al<sub>2</sub>O<sub>3</sub> (3.00 wt%) and TiO<sub>2</sub> (0.41 wt%) show composition very typical values for high Mg# clinopyroxenes in gabbroic cumulates of the oceanic crust [*Coogan et al.*, 2002c; *Dick et al.*, 1991]. Cr<sub>2</sub>O<sub>3</sub> content is averaging 0.29 wt%, but it shows high variability (Figure 21b). Clinopyroxene in the gabbroic dikes (En<sub>43</sub>Fs<sub>12</sub>Wo<sub>45</sub>) and dark veins (En<sub>44</sub>Fs<sub>9</sub>Wo<sub>47</sub>) show Mg#, which are slightly lower compared to the layered gabbro (gabbroic dikes: ~85; dark veins: ~86). They show a strong variability in TiO<sub>2</sub> and Al<sub>2</sub>O<sub>3</sub>, which clearly differs them from the layered gabbro (Figure 21a), with generally higher Al<sub>2</sub>O<sub>3</sub> and TiO<sub>2</sub> contents for the clinopyroxene in the gabbroic dikes and lower Al<sub>2</sub>O<sub>3</sub> and TiO<sub>2</sub> content for the clinopyroxenes in the dark veins. One group is showing high Al<sub>2</sub>O<sub>3</sub> content (~2-3 wt%) and high TiO<sub>2</sub> (~0.7-1.0 wt%).

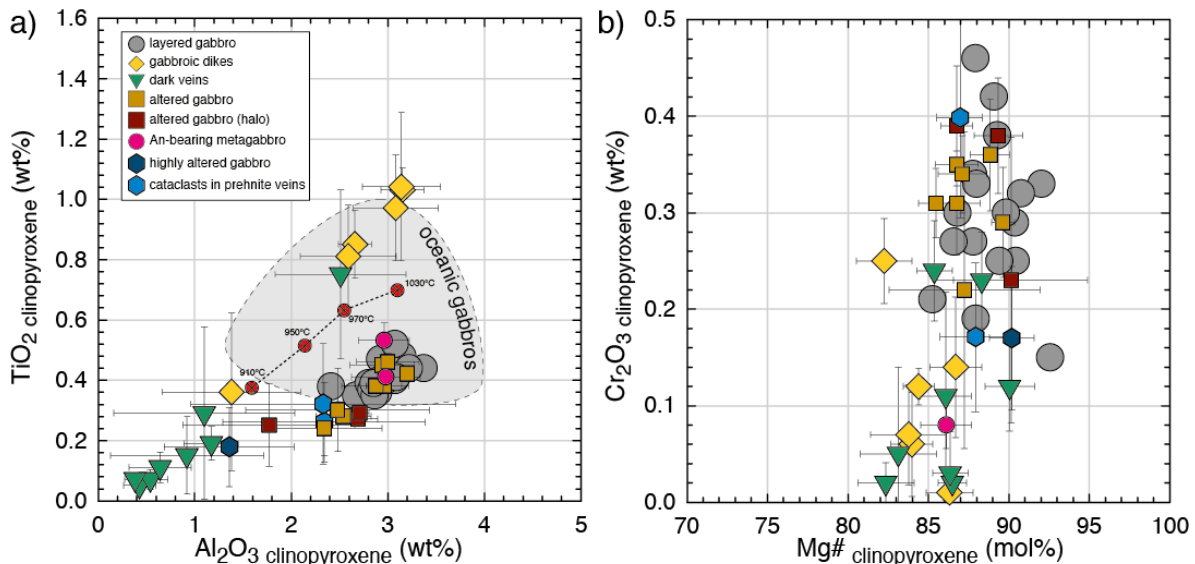
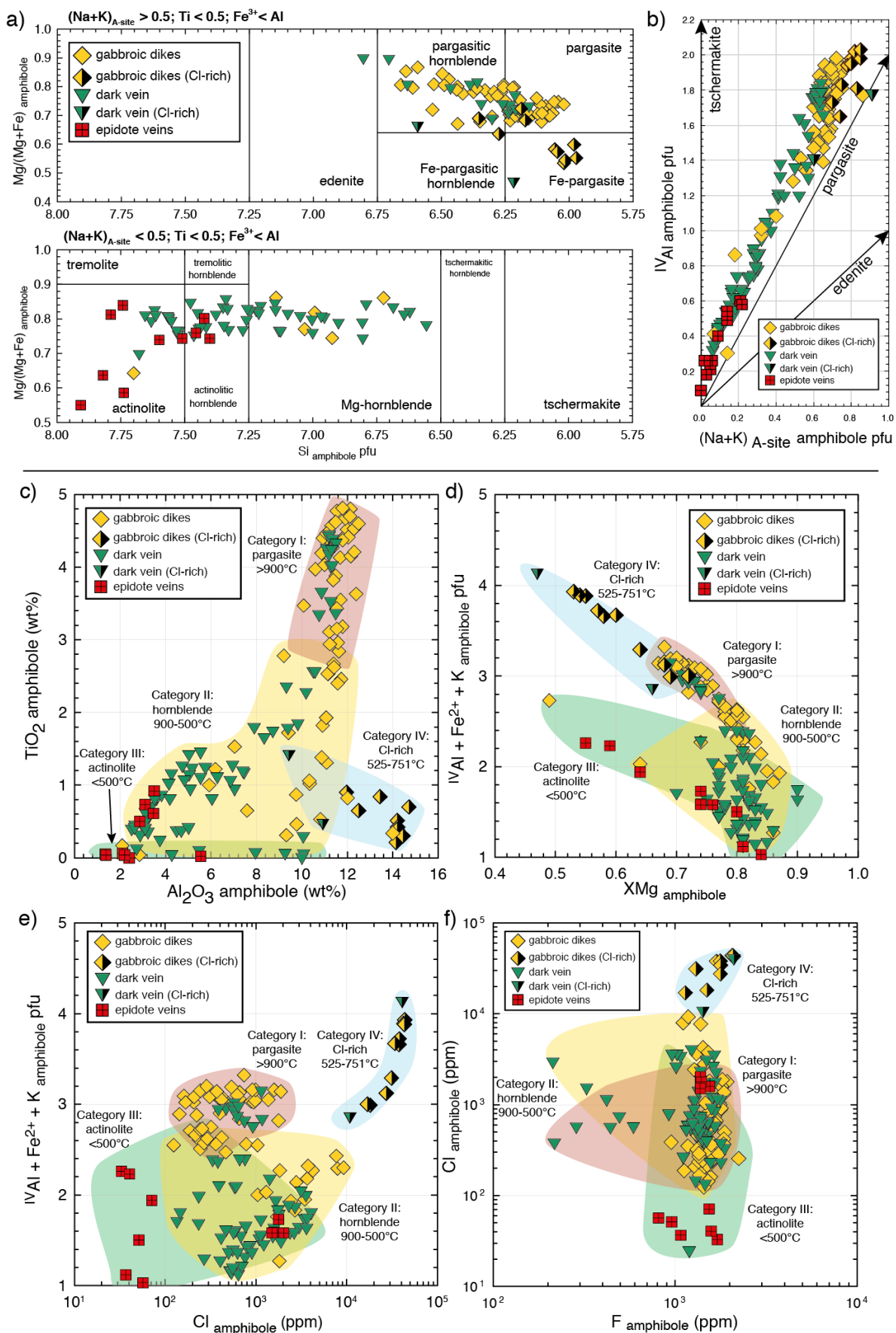


**Figure 21.** Compositional variation in clinopyroxene from the Wadi Wariyah. (a) TiO<sub>2</sub> versus Al<sub>2</sub>O<sub>3</sub>. For comparison the composition of clinopyroxenes from oceanic gabbros (grey field) are shown (after *Koepke et al.*, 2011). Additionally the compositional trend for residual clinopyroxenes of hydrous partial melting of the sheeted dikes (crossed red dots) is shown (number refers to the temperature of the experiment) [*France et al.*, 2010]. (b) Mg# versus Cr<sub>2</sub>O<sub>3</sub> showing the narrow range of Mg# in clinopyroxenes from the Wadi Wariyah and decreasing Cr<sub>2</sub>O<sub>3</sub> content in the gabbroic dikes, dark veins and An-bearing metagabbro.

Clinopyroxene in the all four types of altered gabbro and cataclasts in the prehnite show similar composition compared to the layered gabbro (Figure 21b). Cr<sub>2</sub>O<sub>3</sub> content in the clinopyroxene of the An-bearing metagabbro is depleted relatively to clinopyroxene from the layered gabbro.

Orthopyroxene in the gabbroic dikes and dark veins is low Ca-pyroxene (pigeonite) and show homogeneous composition. Endmember composition is averaging En<sub>74</sub>Fs<sub>24</sub>Wo<sub>2</sub> with Mg# of 77. TiO<sub>2</sub> and Al<sub>2</sub>O<sub>3</sub> are relatively low, with averages of 0.27 wt% and 1.14 wt%, respectively.

**Amphibole.** Amphibole structural formula and water content has been calculated on basis of 23 oxygen atoms assuming F + Cl + OH = 2. Ferric iron has been calculated as the mean value of the 13eCNK (excluding Ca, Na, K) and 15eCNK method after *Robinson* [1982] and terminology/classification is after *Leake et al.* [1997]. Representative results of different amphiboles from the gabbroic dikes, dark veins, and epidote veins are listed in Table 13. Amphibole shows continuity in chemistry from pargasitic via hornblende to actinolitic composition characterized by a strong <sup>[IV]</sup>Al and Sum A-site<sub>(Na+K)</sub> cationic substitution (Figure 22a, b) [*Spear*, 1980]. This continuity in chemistry is very common for Ca-amphiboles in oceanic gabbros [e.g., *Coogan et al.*, 2001a; *Gillis and Meyer*, 2001; *Mével and Cannat*, 1991; *Maeda et al.*, 2002; *Vanko*, 1986] reflecting the different formation conditions of amphibole within the oceanic crust. In the dikes and veins from the Wadi Wariyah the amphiboles can be divided into four categories based on texture, composition, and temperature classification (see section B.8.1.1): (I) Pargasite with very high (“magmatic”) formation temperature (>900°C); (II) hornblende with high formation temperature (500-900°C); (III) actinolite with medium formation temperature (<500°C); and (IV) Fe-pargasite characterized by high Cl-content and formation temperature between



◀ **Figure 22.** (a) Classification of Ca-amphiboles after *Leake et al.* [1997]. (b)  $^{[4]}Al$  versus  $Na+K_{A-site}$  in amphiboles from the Wadi Wariyah showing a clear trend close to the pargasite substitution. (c-f) Compositional variation in amphibole. The coloured areas indicate the different categories, which based on amphibole texture, composition, and temperature estimation (see text for more detail). (d)  $Al_2O_3$  versus  $TiO_2$ . (e)  $^{[IV]}Al + K + Fe$  versus  $XMg$  ( $Mg^{2+}/[Mg^{2+}+Fe^{2+}]$ ). (f) Halogen compositional variation (Cl and F) of amphiboles. One data point in all Figures represents a single grain average based of at least three analyses performed by electron microprobe.

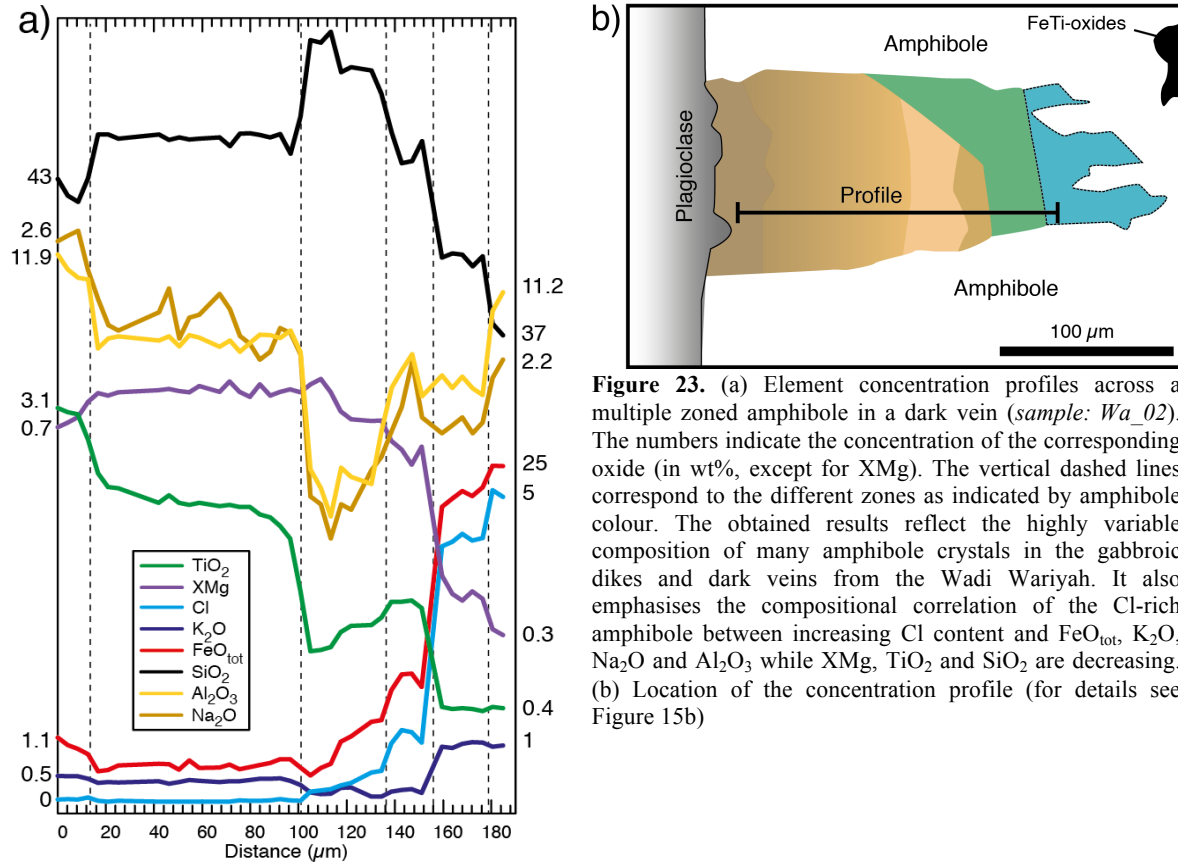


**Figure 23.** (a) Element concentration profiles across a multiple zoned amphibole in a dark vein (*sample: Wa\_02*). The numbers indicate the concentration of the corresponding oxide (in wt%, except for XMg). The vertical dashed lines correspond to the different zones as indicated by amphibole colour. The obtained results reflect the highly variable composition of many amphibole crystals in the gabbroic dikes and dark veins from the Wadi Wariyah. It also emphasises the compositional correlation of the Cl-rich amphibole between increasing Cl content and  $FeO_{tot}$ ,  $K_2O$ ,  $Na_2O$  and  $Al_2O_3$  while XMg,  $TiO_2$  and  $SiO_2$  are decreasing. (b) Location of the concentration profile (for details see Figure 15b)

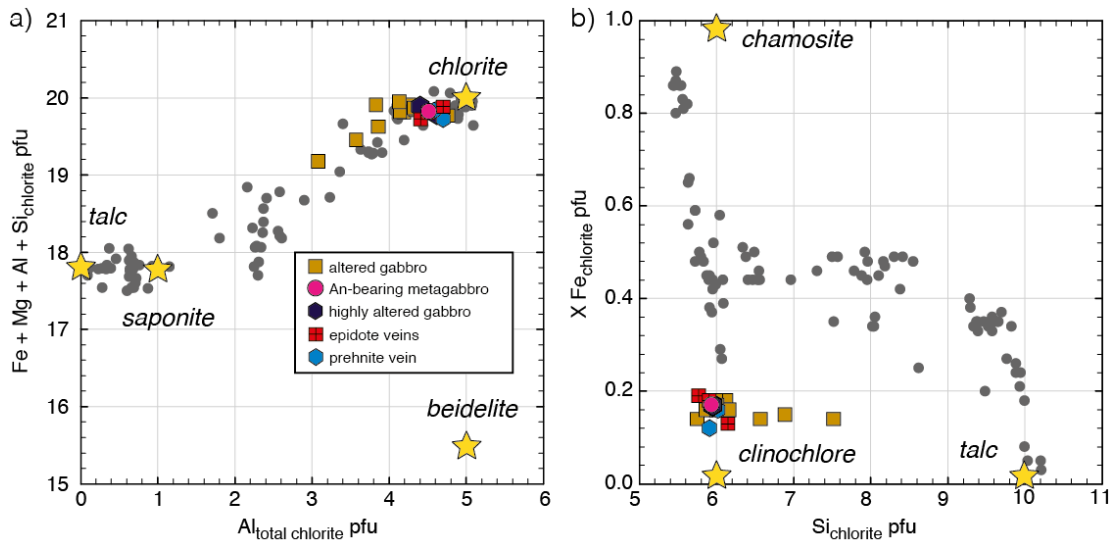


**Figure 24.** Composition of chlorite in the epidote/prehnite veins and altered gabbro from the Wadi Wariyah. (a) Yellow stars indicate endmember composition. Chlorite occupies a weak trend from chlorite towards saponite [after *Schiffman and Fridleifsson*, 1991]. (b) Chlorite classification diagram showing that chlorites are close to clinochlore composition with a slight enrichment in  $XFe_{chlorite}$  and a trend to higher  $Si_{chlorite}$  content (mostly in the altered gabbro). For comparison the composition of phyllosilicates from gabbros of the IODP Hole 1256D are shown in the grey dots after *Alt et al.* [2010] indicating that chlorites occurring in the Wadi Wariyah are strongly depleted in iron compared to the chlorites from IODP Hole 1256D.

500-750°C. Although it is obvious that the obtained amphibole composition does not follow the presented categories exactly, each category is characterized by typical element concentrations. The pargasite with very high formation temperature are characterized by high TiO<sub>2</sub> (3-5 wt%), Al<sub>2</sub>O<sub>3</sub> (9-12 wt%) and Na<sub>2</sub>O (2-3 wt%) content with a medium Mg# ranging from 67-80. Some crystals even show Ti ≥ 0.50 pfu, which is close to the defined composition of kaersutite, an indicator for very high formation temperature (~1000°C) [Deer *et al.*, 1997]. The second category is dominated by a continuous chemistry covering a wide range of composition. These amphiboles show a strong decrease in TiO<sub>2</sub> (0.11-2.5 wt%), Al<sub>2</sub>O<sub>3</sub> (2-12 wt%) and Na<sub>2</sub>O (0.5-2.7 wt%). Mg# is constantly increasing from 64 to 86. Category III is characterized by actinolite showing typical composition of the greenschists facies. They are low in TiO<sub>2</sub>, Na<sub>2</sub>O and variable in Al<sub>2</sub>O<sub>3</sub>. Mg# is decreasing from 90 to 50. Figure 22c shows that some amphiboles of category II and III still preserve the high Al<sub>2</sub>O<sub>3</sub> content, which is usually a characteristic feature of the pargasite. High chlorine content of up to 4.88 wt% characterizes the category IV. They are strongly enriched in K<sub>2</sub>O, Al<sub>2</sub>O<sub>3</sub>, FeO<sup>tot</sup>, and depleted in TiO<sub>2</sub> and SiO<sub>2</sub>, which is clearly emphasised by a corresponding concentration profile through a multiple zoned amphibole from the dark veins (Figure 23a). A positive correlation between the Cl content and <sup>IV</sup>Al + Fe<sup>2+</sup> + K in the Cl-rich amphiboles can be observed (Figure 22e). Mg# is relatively low ranging between 48 and 70. The chemical systematics is typical for Cl-rich amphiboles [Kullerud, 1996; McCormick and McDonald, 1999; Sato *et al.*, 1997; Sautter *et al.*, 2006; Xiao *et al.*, 2005]. Fluorine content in all analysed amphiboles is relatively constant, except for some amphiboles in one dark vein showing depleted F content, probably due to the formation of F-rich apatite (see apatite composition of *Wa\_47A*).

*FeTi-oxides.* FeTi-oxides are magnetite and ilmenite showing granules of ilmenite within the magnetite interpreted as the result by oxidation of magnetite-ulvöspinel solid solution [Buddington and Lindsley, 1964]. Magnetite and ilmenite in the gabbroic dikes and dark veins show homogeneous nearly pure endmember composition (Table 14). Compositional component for ilmenite and magnetite have been calculated using the method of *Stormer Jr.* [1983]. Ilmenite shows X<sub>Ilm</sub> ranging from 92 to 99 with V<sub>2</sub>O<sub>3</sub> averaging 1.13 ± 0.54 wt%. Magnetite shows X<sub>Mag</sub> ranging from 90 to 99 with V<sub>2</sub>O<sub>3</sub> averaging 1.50 ± 0.80 wt%.

*Apatite.* Apatite in the dark veins is generally low in F (0.03-1.03 wt%) and rich in Cl (0.87-3.34 wt%). Assuming F + Cl + OH = 2 for an apatite formula based on 25 oxygen atoms, the OH concentration can be calculated knowing the F and Cl concentration. In the F-Cl-OH ternary space, all the apatites are enriched in the hydroxylapatite component (HAp) with a trend toward chlorapatite (ClAp).

*Chlorite.* Chlorite is a common mineral of the greenschist facies. In the Wadi Wariyah it occurs as alteration product in the halos, altered gabbro, An-bearing metagabbro, and epidote veins formed during metamorphism of the layered gabbro. The chemical formula has been calculated on the basis of 28 oxygen atoms with all iron as Fe<sup>2+</sup>. Representative composition of chlorite is shown in Table 16. The composition is close to clinocllore with homogeneous composition in all lithologies (Figure 24). A slight trend towards low silica content (saponite/talc composition) can be observed. Mg# is ranging from 82 to 83 in the altered gabbros/epidote veins and is slightly enriched in the prehnite veins (Mg# = 86). *Alt et al.* [2010] presented phyllosilicates composition from the upper gabbro section of IODP

Hole 1256D (East Pacific Rise). They showed that most of the phyllosilicates are chlorites to saponite. In comparison to these results, phyllosilicates from the Wadi Wariyah are lower in  $X_{Fe} (Fe^{2+}/[Mg^{2+}+Fe^{2+}])$  on a molar base) close to clinocllore composition.

*Epidote.* Epidote (sensu lato) is the major constituent mineral of the epidote veins and occurs as alteration product of plagioclase in the altered gabbro. All analysed epidotes are close to stoichiometric composition of clinozoisite,  $Ca_2Al_3(SiO_4)_3(OH)$  [Armbruster *et al.*, 2006] with some Si and Ca being in excess (Table 17). The chemical formula has been calculated on the basis of 12.5 oxygen atoms and  $H_2O$  can be estimated by assuming  $OH + Cl + F = 2$ , calculating the OH concentration if the F and Cl concentration is known. Total iron is assumed to be  $Fe^{3+}$ . Epidote in the epidote veins is  $Fe^{3+}$ -poor clinozoisite with an  $X_{Fe^{3+}} (Al^{3+}/[Al^{3+}+Fe^{3+}])$  on a molar base) ranging from 0.11 to 0.16. In the epidote vein, of sample *Wa\_43A*, rims are enriched in  $X_{Fe^{3+}}$  showing a value of 0.18 (compared to 0.11 in the cores). In the halo of sample *Wa\_43C* epidote shows  $Fe^{3+}$ -rich composition with  $X_{Fe^{3+}}$  of 0.16. In the altered gabbro low  $X_{Fe^{3+}}$  ranging from 0.05 to 0.06 characterizes epidote. This can be also observed in the An-bearing metagabbro, where epidote shows  $X_{Fe^{3+}}$  ranging from 0.04 to 0.07.

*Prehnite.* Monomineralic prehnite as well as interstitial prehnite in the epidote veins is close to the stoichiometric composition of  $Ca_2Al_2Si_3O_{10}(OH)_2$  with minor amount of Al and Ca in excess (Table 17). The chemical formula has been calculated on basis of 11 oxygen atoms with all iron as  $Fe^{2+}$ . Prehnite contains little amount of FeO (0.07-0.35 wt%) and sometimes crystals show a minor amount of MgO (< 0.5 wt%), which is consistent with prehnite formed in mafic to ultramafic systems [Deer *et al.*, 1992].

*Pumpellyite.* Pumpellyite occurs in association with prehnite in the epidote veins. Formula structure has been calculated on the basis of 24.5 oxygen atoms with total iron as stoichiometric  $Fe^{2+}$  and  $Fe^{3+}$ . Pumpellyite is Mg-rich with an average Mg# of 85. The composition is homogeneous (Table 17).

## B.6.2 Trace elements including REE

*Plagioclase.* The trace element concentration of plagioclase is listed in Table 18. Plagioclase from the layered gabbro shows typical low trace element and REE concentrations reflecting the primitive composition of the plagioclase. For many HREE the concentration is below the limit of detection, which strongly reflects the high incompatible behaviour of the HREE incorporate into plagioclase. Plagioclases are characterized by a strong pronounced Eu anomaly. Trace element concentration of plagioclases from the gabbroic dikes and dark veins show enriched trace element concentration including the REE. A negative correlation between An content and trace element (Ba and REE) concentration can be observed (Figure 25a, b). Furthermore, with decreasing An content the REE pattern flatten and the positive Eu anomaly decreases. While the layered gabbro show nearly flat LREE pattern, the plagioclases from the gabbroic dikes and dark veins are characterized by a elevated LREE content with a steeply negative slope in the LREE, which becomes more distinctive at low An content of plagioclase (Figure 25c, d). In contrast to the variation of

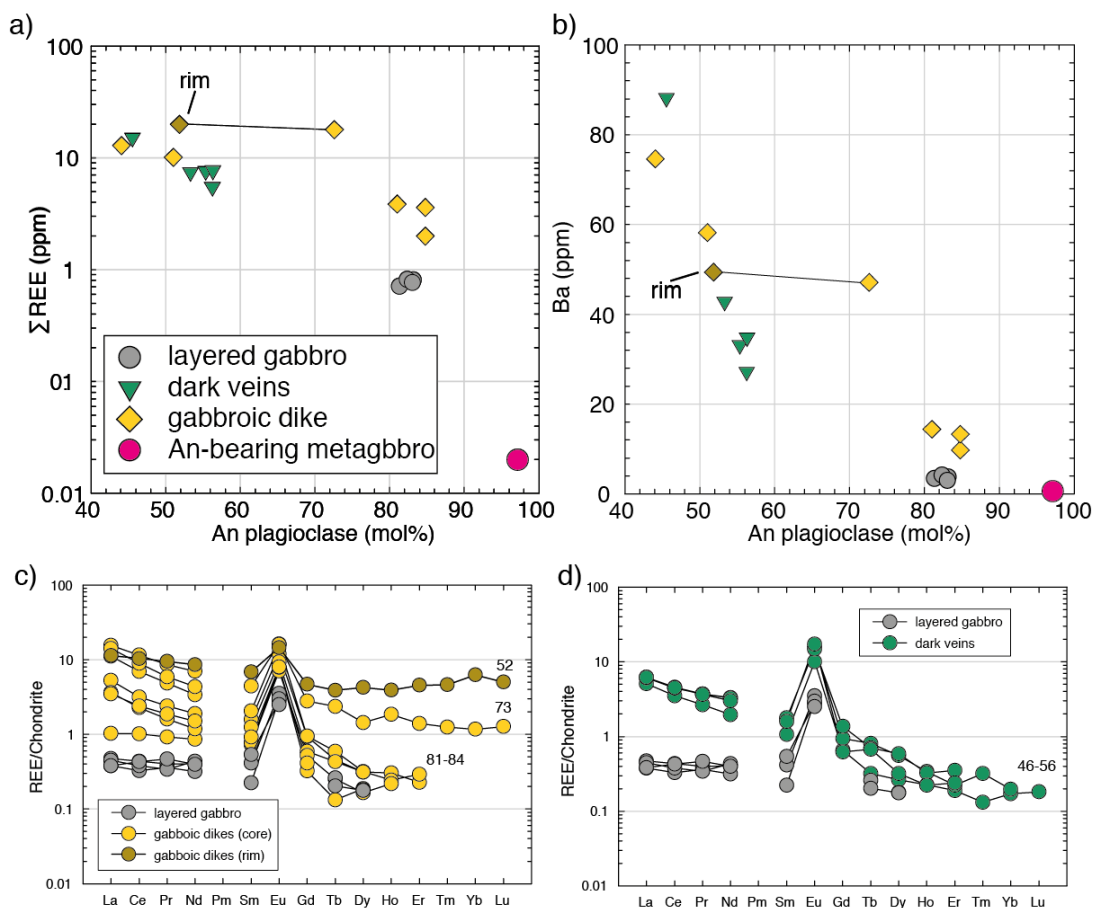


**Figure 25.** Trace and REE composition of plagioclase from the Wadi Wariyah. (a) and (b) shows trace element concentration of plagioclase vs. An content in the plagioclase. A strong enrichment in (a) REE and (b) Ba with decreasing An content can be observed. REE pattern of plagioclase from the (c) gabbroic dikes and (d) dark veins. Again the strong correlation between REE and An content (*numbers*) result in elevated REE pattern with elevated LREE and lower positive Eu anomaly. Normalised against chondritic values of *Sun and McDonough* [1989].

plagioclase in the gabbroic dikes and dark veins, plagioclase from the An-bearing metagabbro is strongly depleted in trace and REE elements often below the limit of quantification.

*Pyroxene.* Figure 26 shows the REE patterns of clinopyroxene from the layered gabbro, gabbroic dikes, and dark veins. All samples show similar patterns with a characteristic depletion in LREE. While clinopyroxenes of the layered gabbro show REE patterns, which plot in the compositional range of gabbroic clinopyroxenes from fast-spreading ridges (Hess Deep) [*Coogan et al.*, 2001b], clinopyroxenes of the gabbroic dikes and dark veins show elevated REE pattern. Furthermore, clinopyroxenes of the layered gabbro are characterized by a small positive Eu anomaly ( $Eu_N/Eu_N^* = 1.04$ ). In the gabbroic dikes and dark veins, however, the Eu anomaly is either absent or is negative (lowest  $Eu_N/Eu_N^* = 0.59$ ). In contrast clinopyroxene of the altered gabbro show similar to slightly depleted REE pattern compared to the layered gabbro, which is more pronounced for the LREE. Clinopyroxene of the An-bearing metagabbro show similar REE pattern and trace element concentration compared to the layered gabbro.

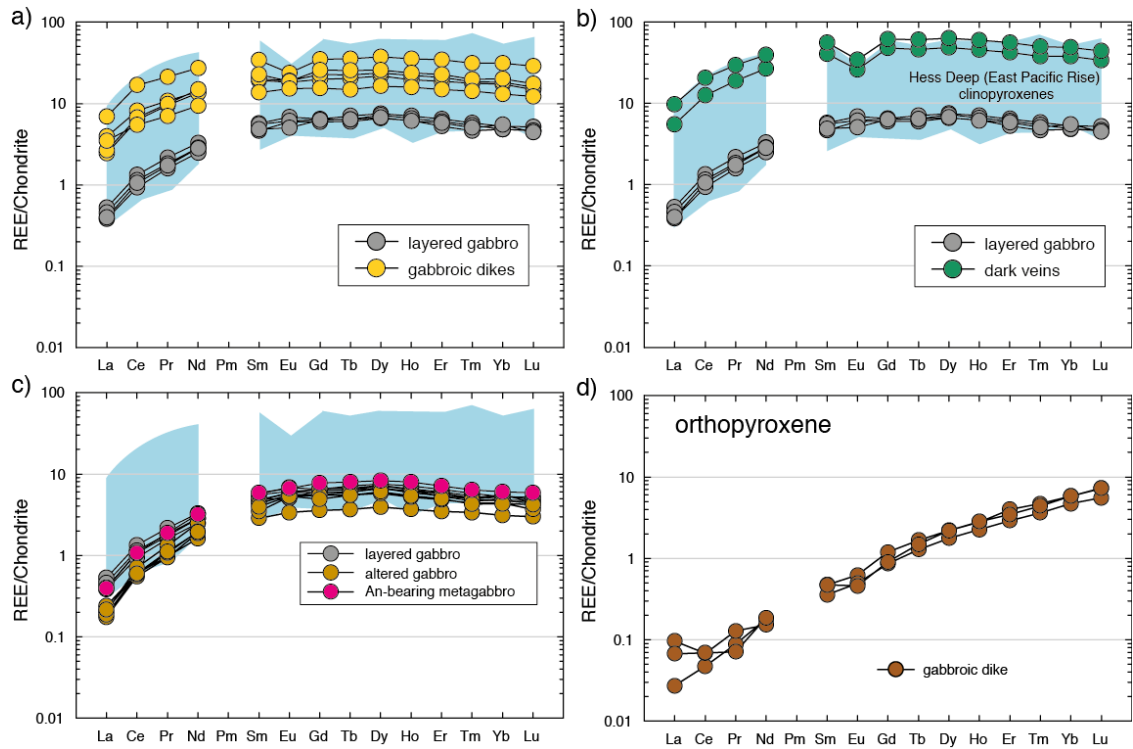


**Figure 26.** REE pattern of clinopyroxene from (a) the layered gabbro and gabbroic dikes, (b) dark veins, (c) An-bearing metagabbro and altered gabbro. The blue shaded field indicate igneous clinopyroxene REE concentration from the Hess Deep (East Pacific Rise, *Coogan et al.* [2002c]). (d) REE pattern of orthopyroxene from the gabbroic dike. Normalised against chondritic values of *Sun and McDonough* [1989].

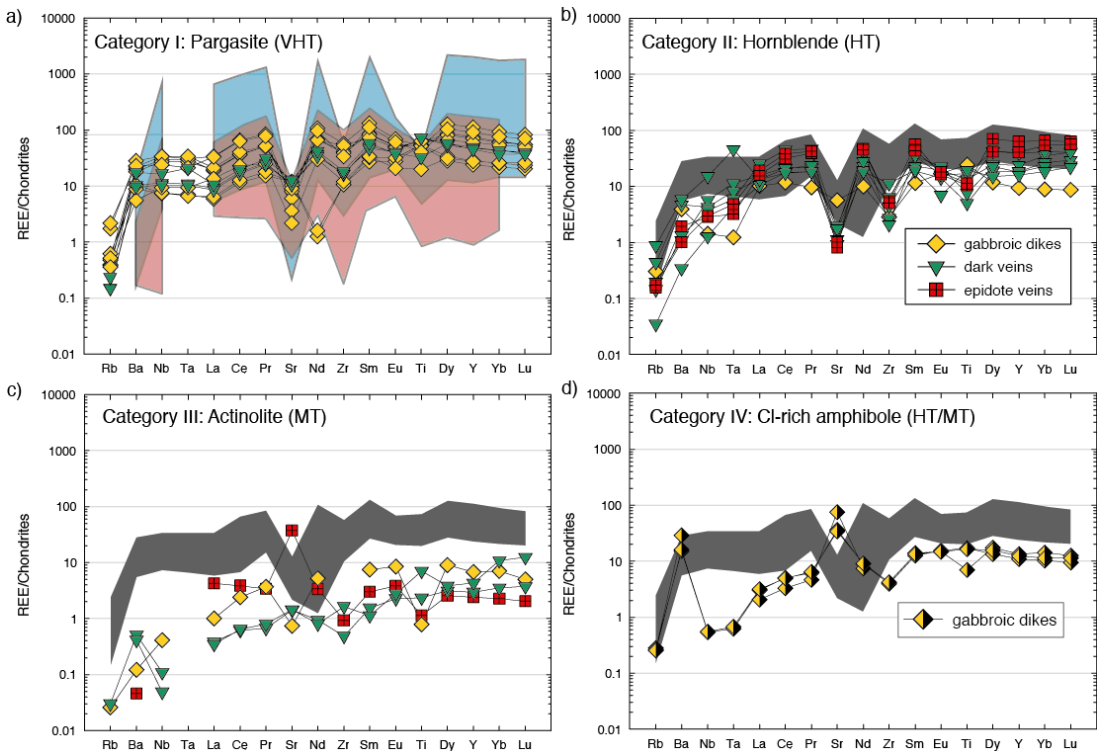


**Figure 27.** Chondrite-normalised [*Sun and McDonough*, 1989] trace element pattern of (a) pargasite, (b) hornblende, (c) actinolite, and (d) Cl-rich amphibole from the gabbroic dikes, dark veins, and epidote veins of the Wadi Wariyah. For comparison amphibole pattern of the roof of the axial magma chamber from the East Pacific Rise (blue shaded field; *Gillis et al.* [2003] and gabbros from the Mid Atlantic Ridge are shown (red shaded field) [*Coogan et al.*, 2001a]. The grey shaded area represents the amphibole composition of the pargasite in (a). Categories are described in section B.6.1 and the VHT = very high temperature, HT = high temperature, MT = medium temperature are based on a temperature scheme presented in section B.8.1.1.



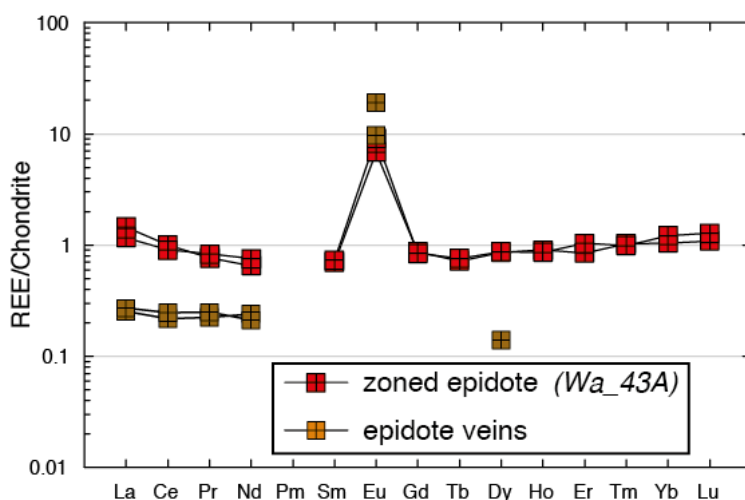


**Figure 28.** REE pattern epidote from the different epidote veins. Note the strong depletion of REE in the thin epidote veins (brown squares; concentration of most elements below the detection limit) compared to the elevated REE pattern of the zoned epidote vein (red squares).

**Amphibole.** Trace element concentrations of amphiboles are listed in Table 20. Amphiboles from the Wadi Wariyah display a wide range of trace element abundances, for example, chondrite-normalised trace element concentrations range from  $<0.1$  to 100 (Figure 27). The pargasitic amphiboles (category I) from the gabbroic dikes and dark veins show the highest trace element concentration with similar trace element systematic compared to magmatic amphiboles from the roof of the axial magma chamber from the East Pacific Rise [Gillis *et al.*, 2003] and gabbros from the MARK area (Mid Atlantic Ridge) [Coogan *et al.*, 2001a]. They show a strong fractionation of Sr, Zr, and a slight negative Eu ( $Eu_N/Eu^*_N = 0.6-0.8$ ) anomaly. A fractionation of the LREE ( $La_N/Sm_N = 0.18-0.41$ ) can be also observed in these amphiboles. Some amphiboles show additionally a strong depletion of Nd.  $Nb_N$  values range between 7 and 34 chondritic values. Hornblende amphiboles (category II) from the dikes and veins are characterized by a slight decrease in trace element concentration relatively to the pargasites. Trace element systematic remains similar compared to the pargasitic amphiboles. However, LREE are less fractionated ( $La_N/Sm_N = 0.29-0.9$ ) and a positive and negative Eu anomaly can be observed ( $Eu_N/Eu^*_N = 0.4-1.2$ ).  $Nb_N$  value ranges between 1 and 15. The actinolitic amphibole (category III) in the dikes and veins show the lowest trace element concentrations. Chondrite-normalized trace element concentrations range from  $<0.1$  to 20. Although the trace element systematics remain mostly similar to the pargasites and hornblende, the actinolite from the amphibole patches of the thick epidote vein (*Wa\_43A*) shows a strong enrichment in Sr, while all other amphiboles from the gabbroic dikes and dark veins show a strong negative anomaly of Sr, implying a different formation history. The chlorine-rich amphiboles (category IV) show medium trace element concentrations. In contrast to the other presented chondrite-normalised trace element pattern, they show significant differences, especially in terms of Sr and Ba concentration, which show strong positive anomaly in the patterns (Figure 27d). LREE are strongly fractionated ( $La_N/Sm_N = 0.15-0.9$ ) and a Eu anomaly is mostly positive averaging  $Eu_N/Eu^*_N$  of 1.14.

**Epidote.** Trace element concentrations of epidote are listed in Table 21. REE patterns are characterized by typical medium to low chondritic values with a strong pronounced positive Eu anomaly (Figure 28). However, there are differences between REE pattern and trace element concentration between the different epidote veins. While epidote in the thin epidote veins usually shows very low trace and rare earth element concentration often

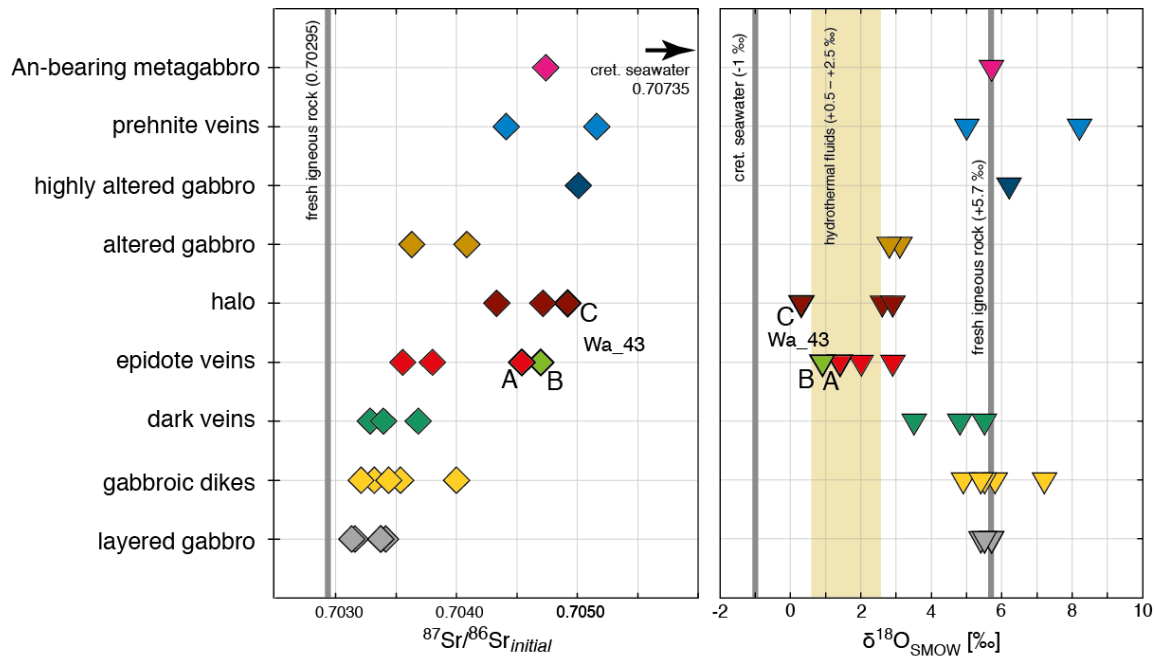


**Figure 29.**  $^{87}\text{Sr}/^{86}\text{Sr}$  (left) and  $\delta^{18}\text{O}$  (right) composition of whole rock analysis of the different lithologies of the Wadi Wariyah. For comparison the isotopic concentration of fresh igneous rock of the lower crustal section of the Semail ophiolite [Lanphere *et al.*, 1981], Cretaceous (cret.) seawater [Veizer *et al.*, 1999], and hydrothermal fluids [Shanks, 2001] are shown.

below detection limit, Sr shows very high concentration of 1157 ppm, which is the highest concentration for Sr recorded in the minerals from the Wadi Wariyah. In contrast, the zoned epidote of sample *Wa\_43A* shows less depletion in trace elements (Figure 28). Ti concentration (1153 ppm) is highly enriched compared to the former epidote, but Sr concentration is lower (561 ppm).

*Prehnite.* Trace element concentration of prehnite is listed in Table 21. Prehnite is strongly depleted in all trace elements resulting in values usually below the limit of quantification. In general it can be observed that the interstitial prehnite within the epidote veins are slightly less depleted than the monomineralic prehnite of the prehnite veins.

## B.7 Isotopic composition

The strontium and rubidium content,  $^{87}\text{Sr}/^{86}\text{Sr}$  isotopic composition, and  $\delta^{18}\text{O}$  isotopic composition obtained in this study are listed in Table 22. Results are shown in Figure 29. Compared to general accepted  $\delta^{18}\text{O}$  value range of  $+5.7 \pm 0.2\text{‰}$  for normal-MORB [Ito *et al.*, 1987] and  $^{87}\text{Sr}/^{86}\text{Sr}$  of  $0.70295 \pm 12$  for fresh igneous lower crustal rocks in the Oman ophiolite [Lanphere *et al.*, 1981], the layered gabbros show similar to depleted  $\delta^{18}\text{O}$  values of  $+4.9\text{‰}$  to  $+5.7\text{‰}$ , whereas they are slightly enriched in  $^{87}\text{Sr}/^{86}\text{Sr}$  showing ratios of 0.70313 to 0.70341. The gabbroic dikes show depleted and enriched  $\delta^{18}\text{O}$  values ranging from  $+4.9\text{‰}$  to  $+7.2\text{‰}$ . The  $^{87}\text{Sr}/^{86}\text{Sr}$  ratios of the gabbroic dikes ranging from 0.70321 to 0.70400 and are enriched compared to the layered gabbro. Dark veins show depleted  $\delta^{18}\text{O}$  values ranging from  $+2.0\text{‰}$  to  $+5.5\text{‰}$  with enriched  $^{87}\text{Sr}/^{86}\text{Sr}$  ratios ranging from 0.70329-0.70368. Epidote veins show a significant depletion in  $\delta^{18}\text{O}$  values of  $+1.4\text{‰}$  to  $+2.9\text{‰}$  with a stronger more radiogenic  $^{87}\text{Sr}/^{86}\text{Sr}$  record of 0.70380-0.70470. The amphibole-rich

zone (*Wa\_43B*) within the epidote vein shows  $\delta^{18}\text{O}$  values of +0.9‰ and  $^{87}\text{Sr}/^{86}\text{Sr}$  ratio of 0.70454. Prehnite veins show  $\delta^{18}\text{O}$  values of +5.0‰ and +8.2‰ with the highest  $^{87}\text{Sr}/^{86}\text{Sr}$  values ranging from 0.70441 to 0.70516. The altered gabbros surrounding the epidote and prehnite veins show complex isotopic composition. The halos of the epidote veins show low  $\delta^{18}\text{O}$  values ranging from +0.3‰ to +2.9‰ with strongly enriched  $^{87}\text{Sr}/^{86}\text{Sr}$  ratio ranging from 0.70433 to 0.70492. Altered gabbro away from the epidote veins shows  $\delta^{18}\text{O}$  values of +1.6‰ and +4.0‰ with enriched  $^{87}\text{Sr}/^{86}\text{Sr}$  ratio of 0.70363 and 0.70409. The highly altered gabbro has  $\delta^{18}\text{O}$  values of +6.2‰ and  $^{87}\text{Sr}/^{86}\text{Sr}$  ratio of 0.70501. The An-bearing metagabbro shows  $\delta^{18}\text{O}$  values of +4.6‰ with  $^{87}\text{Sr}/^{86}\text{Sr}$  ratio of 0.70474.

## B.8 Discussion

### B.8.1 Formation conditions of the hydrothermal system

#### B.8.1.1 Estimations of formation temperature

In order to evaluate the formation conditions of the hydrothermal dike and vein system in the lower crustal section of the Semail ophiolite, in a first step equilibrium temperatures have been calculated and estimated. Determining the formation temperatures of the dikes, veins, and alteration products is challenging and the estimated temperatures contain significant uncertainties. However, in order to understand the mechanism of hydrothermal alteration of the deep gabbro section in the Wadi Wariyah, the estimation of equilibrium temperatures is an essential and necessarily step. Equilibrium temperatures have been calculated based on pyroxene composition using the Al-in-clinopyroxene thermometer of *France et al.* [2010] and the two-pyroxene thermometer using the *Quilf* software [*Andersen et al.*, 1993]. For amphibole parageneses the semi quantitative Ti-in-amphibole thermometer of *Ernst and Liu* [1998] is used, which is generally applicable since most amphiboles are associated with a Ti-phase (e.g., ilmenite). For dark veins without any Ti-phase the presented temperatures might be underestimated. The benefit of this thermometer, however, is that it could be also applied to those amphiboles, where the coexisting, corresponding plagioclase is not clearly in equilibrium with amphibole, since both amphibole and plagioclase in dikes and veins shows a wide compositional range. *Manning et al.* [2000] pointed out that during rapid hydrothermal reactions rates at the temperature of amphibole formation the system is expected to ensure a close approach to equilibrium conditions. The reliability of the Ti-in-amphibole for the application in hydrous tholeiitic systems, equilibrated at low pressure, was confirmed in experimental studies [*France et al.*, 2010; *Koepke et al.*, 2003; *Koepke et al.*, 2004] and in studies on natural gabbros [e.g., *McCaig and Harris*, 2012; *Koepke et al.*, 2005a; 2011]. Epidote formation temperatures have been calculated using the empirical equation for minimum temperature of clinozoisite of *Brunsmann et al.* [2002]. Other constrains on the formation temperature must be based on mineral stability and relation to provide a complete description

of the formation temperatures during hydrothermal alteration. A list of calculated temperatures is given in Table 23.

For formation temperature classification of dikes and veins the scheme of *Nicolas et al.* [2003] is used and modified by defining temperature range for the dike/vein formation of: very high temperature (VHT):  $T > 900^{\circ}\text{C}$  (above the “wet” solidus of gabbro) [*Beard and Lofgren*, 1991; *Koepke et al.*, 2005a; see also Chapter C]; high temperature (HT):  $T = 500\text{--}900^{\circ}\text{C}$ ; medium temperature (MT):  $T = 300\text{--}500^{\circ}\text{C}$ ; and low temperature (LT):  $T = < 250\text{--}300^{\circ}\text{C}$ .

The use of the Al-in-clinopyroxene geothermometer reveals an average equilibrium temperature equilibrium of  $990^{\circ}\text{C}$  for the gabbroic dikes, indicating formation dominantly at VHT conditions. Equilibrium temperatures obtained with the same geothermometer for the dark veins range from  $778^{\circ}\text{C}$  to  $946^{\circ}\text{C}$ , indicating formation at the transition between VHT/HT conditions. Very interesting, the application of the Ti-in-amphibole thermometer to all amphibole bearing dikes and veins (Figure 30), since due to internal consistency of this geothermometer; it allows a coherent overview of the temperature conditions during dike/vein formation. Figure 30 shows a histogram of the calculated temperatures for the amphiboles from the different dikes and veins. It is obvious that the results show a coherent continuous transition in the recorded temperatures from the magmatic stage, VHT, down to the MT stage. The gabbroic dikes from the Wadi Wariyah, which are according to previous work regarded as products of hydrothermal alteration at VHT [*Bosch et al.*, 2004; *Nicolas et al.*, 2003], are dominated by amphibole formation at VHT, but clearly indicate a transition from VHT down to HT/MT conditions. Moreover, dark veins classically regarded as HT (amphibolite facies), also cover the VHT range and amphiboles found in the epidote veins, classically assigned to typical greenschist facies, bear also relics of the HT range, indicating that a continuous transition from VHT to MT exists in the dikes and veins. The Cl-rich amphibole within the gabbroic dikes and dark veins show a temperature range from  $525\text{--}751^{\circ}\text{C}$ . Due to the exceptional high chlorine content within these results may reflect the first unambiguous imprint of a seawater-derived fluid at the transition to the HT/MT range. The lowest temperatures recorded by the Ti-in-amphibole thermometer are  $480^{\circ}\text{C}$ , but this is only the limitation of the used thermometer, which is not calibrated for such low temperatures. The fact that Al-poor actinolite ( $\text{Al}_2\text{O}_3 < 4 \text{ wt}\%$ ) is in assemblage with An-poor plagioclase ( $\text{An}_{0-40}$ ) in some veins indicate formation temperature at the transition between the amphibolite and greenschist facies at temperatures between  $450^{\circ}\text{C}$  and  $550^{\circ}\text{C}$  [*Liou et al.*, 1974]. Furthermore, equilibrium temperatures calculated for ilmenite/magnetite pairs using the *ILMAT* excel sheet [*Lepage*, 2003] obtain temperatures from  $537\text{--}663^{\circ}\text{C}$  [after the calculation scheme of *Stormer Jr.*, 1983] and oxygen fugacity ranging from  $\Delta\text{QFM} -1.7$  to  $+2.53$  (quartz-fayalite-magnetite buffer). It is well known that the two-oxide geothermometer applied to plutonic rocks does not reveal the formation temperatures, but reflect the cooling history, since the FeTi-oxides show a strong tendency to fast re-equilibration during cooling. The equilibrium temperatures recorded here are all around  $600^{\circ}\text{C}$ , and according to *Sauerzapf et al.* [2008], calculated temperatures below  $600^{\circ}\text{C}$  are out of the recommended temperature range. Thus, the calculated presented here by the two-oxide geothermometer are only of limited use for the estimation of the formation conditions [see also *Dziony et al.*, 2013]. *Coogan et al.* [2006] used the occurrence of FeTi-oxides to estimate the oxygen fugacity during

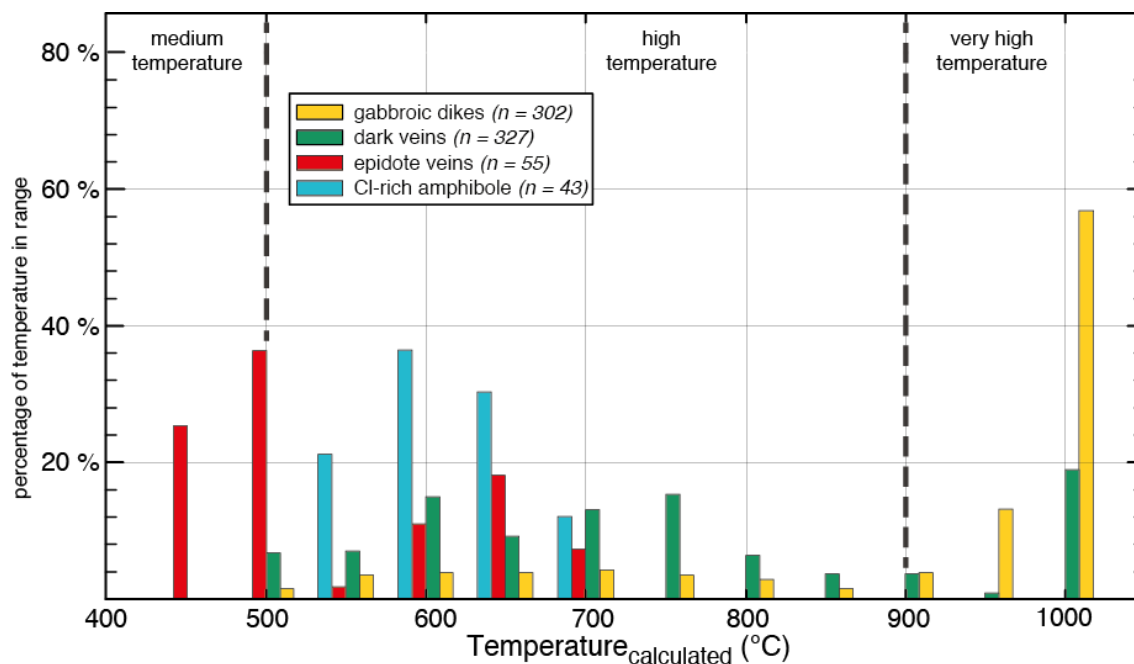


**Figure 30.** Percentage of temperature distribution of amphiboles from the gabbroic dikes, dark veins, epidote veins, and Cl-rich amphibole.  $n$  = number of single point analysis.

cooling of the lower oceanic crust. Their results show that during cooling of the crust the oxygen fugacity more or less follows the QFM buffer. Thus, the range of oxygen fugacity presented in this study is typical for the cooling history of the gabbroic dikes and dark veins.

It must be pointed out that the application of the Ti-in-amphibole on the chlorine-rich amphiboles contains significant uncertainties. According to the temperature estimation the Cl-rich amphiboles can be assigned to the HT temperature regime. The fact that Cl-rich amphiboles crystallize over a wide range of temperatures ( $\sim 350$ - $800^\circ\text{C}$ ) and pressure (0-800 MPa) suggest that neither temperature nor pressure is a strong factor in controlling the crystallization of these amphiboles [McCormick and McDonald, 1999]. As shown by the chemistry they contain a high amount of  $\text{Al}_2\text{O}_3$  (up to 15 wt%) and  $\text{Na}+\text{K}_{\text{A-site}}$  (0.6-0.8) very similar to amphiboles clearly assigned to the VHT regime, but low  $\text{TiO}_2$  ( $< 1.5$  wt%). Since the Cl-rich amphiboles often form patches in the VHT pargasite (see Figure 14), it is not clear whether they are really in equilibrium with FeTi-oxides, which is a requirement for the use of the geothermometer. Thus, temperatures estimated by the Ti-in-amphibole thermometer in these amphiboles might be underestimated. Generally Ernst and Liu [1998] calibrated the thermometer based on  $^{\text{IV}}\text{Al}$  and Ti structural composition of Ca-amphiboles. They showed that both components are sensitive to temperature. Consequently, high  $^{\text{IV}}\text{Al}$  and Ti content in amphiboles should reflect high temperatures. However, they pointed out that during slow cooling natural Ca-amphiboles can exsolve  $\text{TiO}_2$ -rich phases (e.g., rutile, ilmenite) without any redistribution of the  $\text{Al}_2\text{O}_3$  content in the Ca-amphibole resulting that the use of the thermometer might be handled with care when estimating temperatures for inhomogeneous amphiboles. Cl-rich amphibole in oceanic rocks from the Mathematician Ridge [Vanko, 1986] show similar compositional variation as the Cl-rich amphiboles presented here. Vanko [1986] pointed out that the occurrence of actinolite and other

minerals of the greenschist facies in assemblage with the Cl-rich amphibole might indicate formation at lower temperatures than presented here. The gabbroic dikes and dark veins in this study also show the presence of actinolite, but these are thought to form later than the Cl-rich amphiboles at lower temperatures. In summary, precise formation temperature for the Cl-rich amphiboles cannot be fully established by the presented study.

For formation temperature classification of the epidote and prehnite veins, the stability relation of the coexisting phases is used. The mineral paragenesis of epidote – chlorite – actinolite observed in the epidote veins indicates formation temperature in the MT regime with typical mineral assemblage of the greenschist facies. The mineral composition of the clinozoisite, which is low in  $X_{Fe^{3+}}$  implies that the epidote formed close to the transition between greenschist and amphibolite facies at temperatures around 500°C [Grapes and Hoskins, 2004 and references therein]. Based on reaction path modelling [McCollom and Shock, 1998], experimental [see review in Poli *et al.*, 2004], and phase equilibria studies Liou *et al.* [1985], epidote coexisting with chlorite is stable between 350°C and 550°C at low pressures metamorphosed mid-ocean ridges basalts. Temperature estimation using the thermometer of Brunsmann *et al.* [2002] reveals temperatures of 421-587°C clearly supporting the formation of epidote veins in the MT regime. However, the presence of prehnite and especially Mg-rich pumpellyite indicates a progressive alteration to lower temperatures within the epidote veins since Mg-rich pumpellyite is stable from temperature 350-400°C at low pressure [Liou *et al.*, 1985; Schiffman and Liou, 1980] and prehnite is a low temperature product of epidote breakdown (see below). Thus, the presence of prehnite and pumpellyite indicate the transition from the greenschists facies down to the prehnite pumpellyite facies.

Formation of prehnite veins indicates LT hydrothermal alteration in the Wadi Wariyah, since prehnite is a breakdown product of epidote, pumpellyite, and clinocllore at low temperatures. Prehnite coexisting with actinolite (fine fibrous actinolite aggregates) indicates higher temperatures within the prehnite stability field, probably near the reaction curve where prehnite/pumpellyite breaks down to actinolite (+ chlorite) [Bucher, 2002]. Liou *et al.* [1983] and Frey *et al.* [1991] showed that prehnite is stable in the range between 200°C and 350°C (at  $fO_2 \sim QFM$ ) and then breaks down to clinozoisite and tremolite at higher temperatures. Frost *et al.* [2008] presented a thermodynamic model on phase stability during micro-rodignization of gabbro. Their model imply that the thermal limit for prehnite is 425°C during alteration of plagioclase and hydration of olivine, which represents an upper limit for prehnite stability. Alt *et al.* [2010] estimated formation temperature for prehnite in association with laumontite for the sheeted dike and plutonic section of the IODP Hole 1256D from the EPR. They suggested that the mineral assemblages have formed during evolved hydrothermal alteration at low temperature of ~100°C, which thought to be the lower temperature limit for prehnite. Thus, the formation of thick prehnite veins can be regarded as LT hydrothermal alteration.

The exact temperature estimation for the altered gabbros around the veins is difficult due to the lack of suitable geothermometers. As indicated by the petrographic record of the altered gabbro they are formed by pervasive alteration of the layered gabbro, leaving behind a certain amount of primary magmatic minerals. Clinopyroxene structure in combination with major/trace element composition clearly indicate that relics of

---

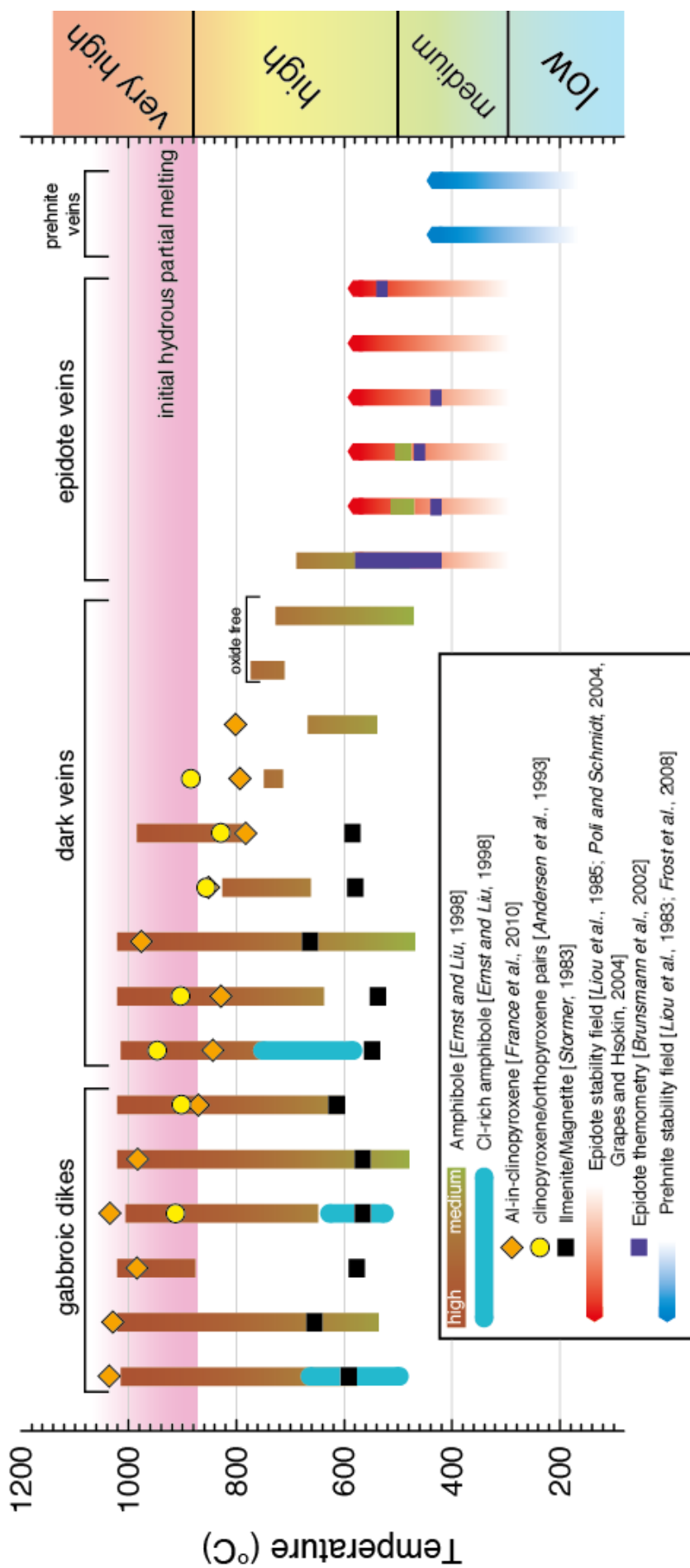


**Figure 31.** Summary of the constraints on the hydrothermal mineral formation in dikes and veins from the Wadi Wariyah. There is no evidence for any significant break in temperature of hydrothermal alteration between 1000°C down to 250°C indicating a continuous hydrothermal alteration from very high to low temperature of the layered gabbro. See text for a description of the approach used and discussion of the results.

clinopyroxene often survived the hydrothermal alteration imprint coming from the veins and show only slight alteration. The phase assemblage of chlorite + actinolite/tremolite clearly indicate typical hydrothermal alteration in the greenschists facies. Due to the wide range of chlorite stability in metamorphosed gabbroic rocks, estimating the precise formation temperature is challenging. It is obvious that chlorite + actinolite/tremolite are reaction products of the primary olivine and plagioclase in the layered gabbro. *Apted et al.* [1983] presented a phase relation study of metamorphosed basaltic rocks indicating that chlorite is stable up to 550°C. However, *McCullom and Shock* [1998] showed thermodynamically that high-Mg# chlorite is stable at temperature up to 650°C. The presence of actinolite very low in TiO<sub>2</sub> in the presence of a Ti-phase (leucoxene) also point to low temperatures of the greenschist facies. Thus, the alteration of the altered gabbro indicate formation temperature of 550-650°C. The formation of epidote in the halos clearly indicates formation temperatures in the MT regime (see above).

The combined results of geothermometry presented above, together with the results of the mineralogy and geochemistry, imply that the observed hydrothermal dike and vein system in the Wadi Wariyah correspond to hydrothermal alteration in the layered gabbro spanning temperature range from the magmatic VHT regime down to the LT range with typical mineral assemblage of the prehnite-pumpellyite facies (Figure 31).

Very important is the observation presented above that many gabbroic dikes and dark veins show formation temperatures well above the solidus of a wet, primitive gabbro (~870-900°C) [*Beard and Lofgren*, 1991; *Koepke et al.*, 2004], with the consequence that the corresponding water/rock interaction at such temperatures can trigger partial melting of the host gabbro. The geothermometry results imply that water/rock interactions starts at temperatures of around 1000°C with the formation of pargasite bearing dikes and veins. Decreasing temperature leads to the formation of epidote veins at MT conditions followed by a LT hydrothermal formation of prehnite, which extinguish the record of VHT to MT hydrothermal alteration signal. Importantly, relics found in many of the veins belonging to a previous/earlier stage of hydrothermal imprint indicate a continuous hydrothermal reaction from very high (“near magmatic”) down to very low temperatures (prehnite-pumpellyite), using the same pathways during the hydrothermal alteration process in the layered gabbro.

The presence of “nearly pure” anorthite in the absence of an epidote phase in equilibrium within the An-bearing metagabbro suggests that the stability of epidote is exceeded, because epidote breaks down to produce anorthite at temperatures depending on redox conditions: 500°C at reducing conditions and up to >700°C at oxidizing conditions [see review in *Poli and Schmidt*, 2004]. Since the epidote is mostly Fe<sup>3+</sup>-poor clinozoisite reducing conditions and temperature in excess of 500°C can be assumed during formation of pure anorthite in the An-bearing metagabbro. Since this anorthite is very low in trace elements (Figure 25), it is indicated this it formed by the influence of a hydrothermal fluid [*Vanko and Laverne*, 1998] in the MT/HT regime, instead of crystallization from a melt. *McCullom and Shock* [1998] proposed that common anhydrous minerals, such as pyroxene, plagioclase, and olivine might crystallise from high temperature water/rock interactions intermediate between silicate melts and supercritical fluids.

---



### B.8.1.2 Determination of water/rock ( $W/R$ ) ratios and alteration temperatures

In order to understand the role of water and to estimate the flux of hydrothermal fluids during the hydrothermal alteration processes related to the different dikes, veins, and altered gabbros of the Wadi Wariyah,  $W/R$  ratios (using strontium isotopes) and alteration temperatures (using oxygen isotopes) have been estimated for the whole rocks analysed in this study. Since the first isotopic studies on gabbroic rocks from the Semail ophiolite,  $^{87}\text{Sr}/^{86}\text{Sr}$  and  $\delta^{18}\text{O}$  isotopic composition of the bulk rock and their constituent minerals are regarded to be useful tracers for fluid/rock interactions in the lower crustal section [Gregory and Taylor, 1981; Lanphere et al., 1981; McCulloch et al., 1981; Pallister and Knight, 1981]. Kawahata et al. [2001] and later Yamaoka et al. [2012] used the relation between  $^{87}\text{Sr}/^{86}\text{Sr}$  and  $\delta^{18}\text{O}$  to demonstrate alteration conditions for a complete crustal section from the Wadi Fizh, one of the northern massifs of the Semail ophiolite. They showed that the lower crustal section is metamorphosed at low  $W/R$  ratios and high temperatures ( $>450^\circ\text{C}$ ). In the context of the Wadi Wariyah outcrop studied here, Bosch et al. [2004] showed that the isotopic record found in dikes and veins and their mineral constituents were caused water/rock interactions at very high temperatures ( $900\text{--}1000^\circ\text{C}$ ) and at low  $W/R$  ratios. The occurrence of epidosite veins indicates LT hydrothermal alteration at higher  $W/R$  ratios. Bosch et al. [2004] pointed out that seawater derived hydrothermal fluids are the contaminant to be considered, causing the observed isotopic compositions.

The model, used to constrain the  $W/R$  ratios in this study here, is mainly based on the calculation of the effective  $W/R$  ratio by considering a closed system [McCulloch et al., 1981]. The wide range in the  $W/R$  ratios presented in Table 22 are mainly due to the use of different Sr concentrations of the initial fluid. Modern seawater has an Sr concentration of 8 ppm, whereas Coogan [2009] showed that Cretaceous seawater might be enriched in Sr showing values of 38 ppm. Yamaoka et al. [2012] pointed out that the use of modern seawater will lead to an overestimation of the  $W/R$  and thus, the reported values using modern seawater composition are maximum values. Furthermore, the use of pristine  $^{87}\text{Sr}/^{86}\text{Sr}$  isotopic ratios for the initial fluid might indicate minimum values, because it maximizes the value in the denominator. Moreover, the precise  $^{87}\text{Sr}/^{86}\text{Sr}$  ratio of the involved fluid might be less radiogenic due to buffering effects from typical seawater during downstream of the fluid through the upper crustal sections [Bickle and Teagle, 1992]. Furthermore, the measured  $^{87}\text{Sr}/^{86}\text{Sr}$  isotopic ratios in the whole rock might reflect variable  $W/R$  ratios apart from equilibrium, due to differences in fluid and rock isotopic compositions on an advancing isotopic alteration front [McCaig et al., 2013]. The alteration temperature can be determined calculating the  $\delta^{18}\text{O}$  values of the final rock at constant  $W/R$  ratios, where then  $\delta^{18}\text{O}$  of the rock will be only determined by the temperature dependent isotopic fractionation factor between the layered gabbro and the involved fluid. In the presented model an isotopic fractionation factor between water and gabbro presented by Zhao and Zheng [2003] is used. Details of the calculation procedure can be found in the appendix.

The initial  $^{87}\text{Sr}/^{86}\text{Sr}$  ratios are plotted against the  $\delta^{18}\text{O}$  of whole rocks in Figure 32. With few exceptions show all samples studied from the Wadi Wariyah  $^{87}\text{Sr}/^{86}\text{Sr}$  initial ratios and

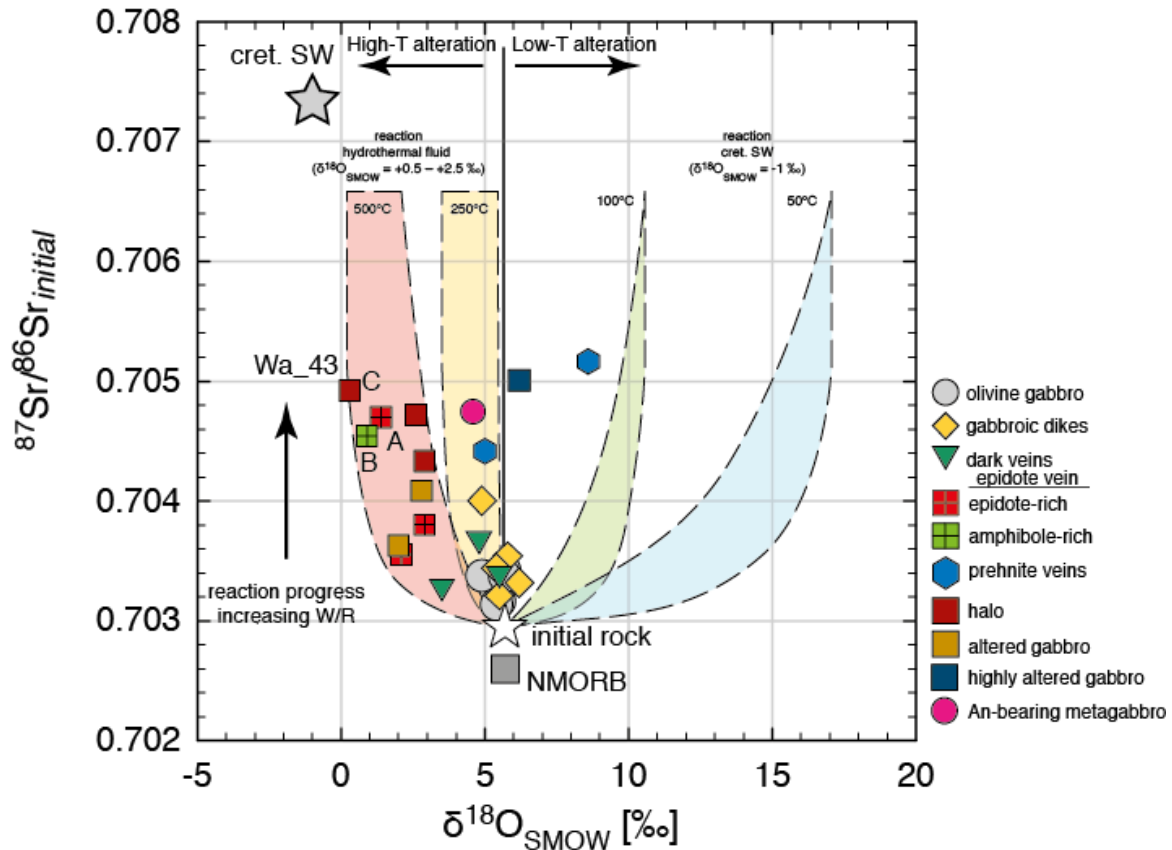


**Figure 32.**  $\delta^{18}\text{O}$  versus  $^{87}\text{Sr}/^{86}\text{Sr}$  diagram for whole rock samples from the Wadi Wariyah. The coloured areas correspond to the isotopic composition of a rock that is in equilibrium with the fluid ( $^{87}\text{Sr}/^{86}\text{Sr} = 0.70735$ , at  $50^\circ\text{C}$  and  $100^\circ\text{C}$  with  $\delta^{18}\text{O} = -1\text{‰}$ ; at  $250^\circ\text{C}$  and  $500^\circ\text{C}$  with  $\delta^{18}\text{O} = +0.5\text{‰}$  and  $+2.5\text{‰}$ ). Sr concentration of 8 ppm (modern seawater) and 38 ppm (Cretaceous seawater) were taken into account in the calculation. White star indicate initial rock isotopic composition of  $^{87}\text{Sr}/^{86}\text{Sr} = 0.70295$  [Lanphere *et al.*, 1981] and  $\delta^{18}\text{O} = +5.7\text{‰}$ . Grey square is the isotopic composition of NMORB taken from the GeoRem Database. Grey star indicates isotopic composition of Cretaceous seawater. Details of the calculation are described in the appendix.

$\delta^{18}\text{O}$  values apart from fresh igneous lower crust value of the Semail ophiolite, which commonly has  $^{87}\text{Sr}/^{86}\text{Sr}$  ratios of  $0.70295 \pm 12$  [Lanphere *et al.*, 1981] and  $\delta^{18}\text{O}$  of  $+5.7\text{‰}$  [Pallister and Knight, 1981]. Even the layered gabbro, showing the lowest  $^{87}\text{Sr}/^{86}\text{Sr}$  ratios of 0.70316 to 0.70348, is slightly enriched in  $^{87}\text{Sr}/^{86}\text{Sr}$ .  $\delta^{18}\text{O}$  values of the layered gabbro slightly tend to lower values. Combined with the observations that the plagioclase rims are enriched in An (see section B.6.1), a model is implied that the layered gabbro is affected by hydrothermal alteration, possibly by fluid percolating along grain boundaries at very low  $W/R$ .

The calculated  $W/R$  ratios for the dikes, veins, and altered gabbros range between 0.3 and 18.8, which are lower compared to the values presented by Bosch *et al.* [2004]. The differences are mainly due to the use of different  $^{87}\text{Sr}/^{86}\text{Sr}$  isotopic composition of the initial rock (fresh Oman gabbro versus normal-MORB). The use of fresh igneous gabbro  $^{87}\text{Sr}/^{86}\text{Sr}$  in this study seems to be more reliable due to the layered gabbro is considered to be the initial rock, fractionated from typical MORB-like melts. On the basis of the  $W/R$  ratios three different groups can be recognised. Dark veins and gabbroic dikes show enriched  $^{87}\text{Sr}/^{86}\text{Sr}$  ratios and tend to lower  $\delta^{18}\text{O}$  values indicating hydrothermal alteration at low  $W/R$  ratios (0.4-6) and high alteration temperatures. The more radiogenic signal of

some dikes and veins are mostly due to the progressively replacement of the primary magmatic minerals by hornblende/actinolite and chlorite, since the VHT formation conditions (“*magmatic*”) were followed continuously by HT and MT hydrothermal alteration with increasing  $W/R$  ratios. Epidote veins and surrounding altered gabbros (halo and altered gabbro) show  $W/R$  ratios between 0.7-15.2 and alteration temperatures of around 500°C. The high-calculated  $W/R$  ratios refer to the thick epidote vein (*Wa\_43A*) showing  $W/R$  ratios of 10.8-12.5, which indicates higher fluid flux during the formation of this specific vein. Interestingly, the high  $W/R$  ratios calculated for the altered gabbros and halos reveal always higher  $W/R$  ratios compared to the epidote veins. The mineralogy of the greenschists facies mineral assemblage (chlorite + actinolite/tremolite) in the altered gabbro indicate slightly higher formation temperatures compared to the epidote veins, and this could be interpreted that there was a stronger fluid flux at slightly higher temperatures in the HT/MT regime before this vein was sealed by the epidote precipitation under MT conditions. The high  $^{87}\text{Sr}/^{86}\text{Sr}$  radiogenic signal and the trend toward heavier  $\delta^{18}\text{O}$  values observed in the prehnite veins and surrounding lithologies (highly altered gabbro and An-bearing metagabbro) indicate high  $W/R$  ratios (2.0-18.8) and low alteration temperatures (<250°C), although the presence of plagioclase highly enriched in An component suggest higher formation temperature at the MT/HT transition. It is possible that due to the complex mineralogy (magmatic clinopyroxene and hydrothermal plagioclase) the measured isotopic ratio represent an average of both minerals. This suggests further research on the isotopic composition of main mineral constituents of the An-bearing metagabbro is necessary to decipher the precise alteration temperature using isotopic composition. Similar to the epidote veins the highly altered gabbros surrounding the prehnite veins indicate higher  $W/R$  ratios.

### **B.8.1.1 Synopsis of dike and vein formation**

Formation temperature,  $W/R$  ratios, and alterations temperatures presented in the discussion above imply dike and vein formation in a wide range of temperatures at highly varying  $W/R$  ratios. The results can be summarized as follow:

- Gabbroic dikes and some of the dark veins are products of VHT (“*near magmatic*”) temperature hydrothermal alteration at low  $W/R$  ratios.
- Dark veins are products of HT temperature hydrothermal alteration at low  $W/R$  ratios.
- Epidote veins formed at MT conditions at increasing  $W/R$  ratios.
- Prehnite veins formed by LT temperature at highest  $W/R$  ratios.

### **B.8.2 The hydrous partial melting reaction as indicator for water/rock interactions at very high temperatures**

Characteristic mineral assemblage, composition and trace element concentration of the bulk rock and constituent minerals indicate that the gabbroic dikes and some dark veins (with FeTi-oxides) have a similar origin. In the following it is shown, that these dike/vein

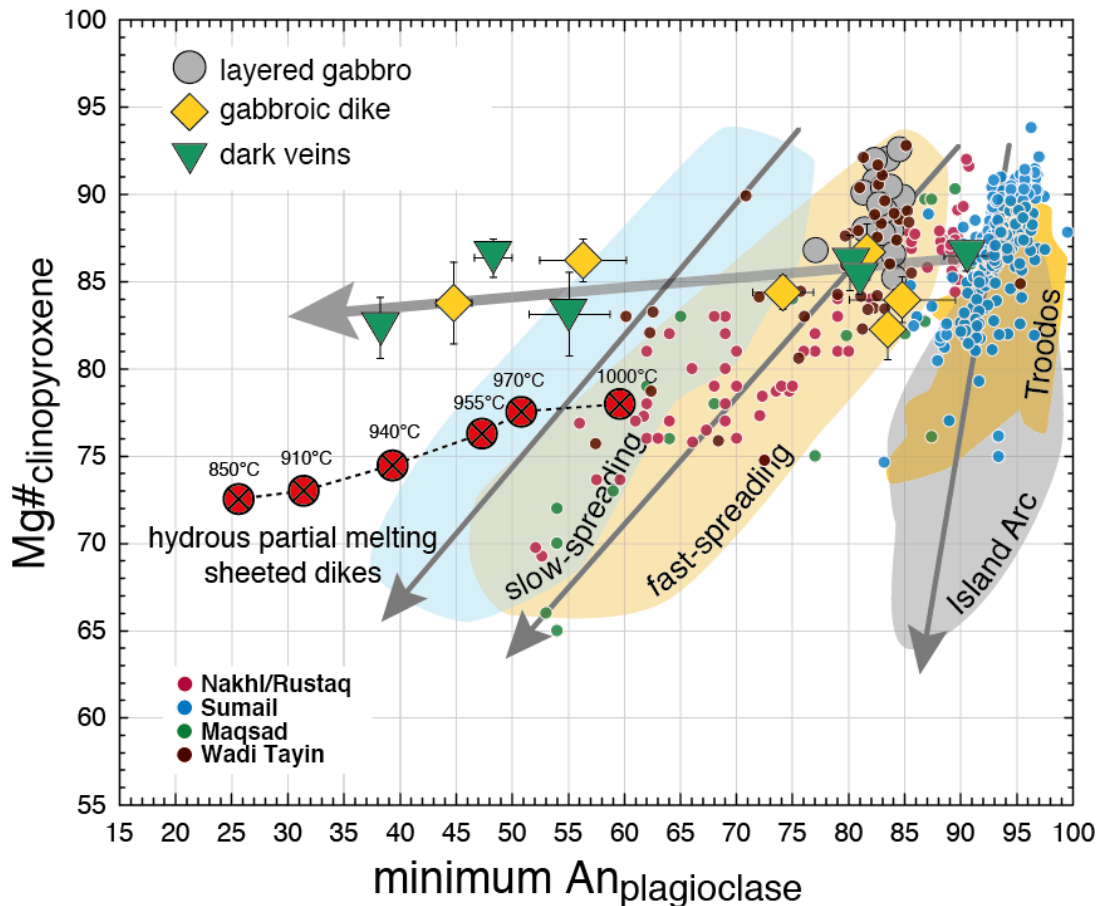


**Figure 33.** Minimum An in plagioclase versus Mg# in clinopyroxene of the layered gabbro, gabbroic dikes, and dark veins. The layered gabbro from the Wadi Wariyah plot into the field of fast-spreading ridges. For comparison the small white outlined dots represents gabbros from different massifs of the Semail ophiolite [Abily *et al.*, 2011; Browning, 1980; 1982; Coogan *et al.*, 2002a; Goodenough, 2010; Koepke, unpubl. data; Korenaga and Kelemen, 1998]. The grey arrows indicate different mineral compositional trends for hydrous partial melting of the layered gabbro (thick arrow), fast- and slow-spreading ridges, and subduction zone related island arc/Troodos ophiolite. Note that the defined trend of the gabbroic dike and dark veins imitate the trend of the residual mineral composition derived from hydrous partial melting of sheeted dikes from the Semail ophiolite [France *et al.*, 2010] and not the island arc trend. This clearly excludes the influence of a subduction zone related process during for the formation of the gabbroic dikes and dark veins from the Wadi Wariyah. Data for gabbros: fast-spreading ridges [Coogan *et al.*, 2002b; Koepke *et al.*, 2008; Lissenberg *et al.*, 2012; Pedersen *et al.*, 1996]; slow spreading ridges [Dick *et al.*, 2000; Koepke *et al.*, 2005a; Ross and Elthon, 1997; Suhr *et al.*, 2008]; Troodos ophiolite [Thy *et al.*, 1989]; and Island Arcs [Burns, 1985].

lithologies can be regarded as products of hydrous partial melting of the layered olivine gabbro at very high temperature. According to the experiment of Koepke *et al.* [2004] and Wolff *et al.* [2013], the mineral assemblage of the gabbroic dikes corresponds exactly to what is expected for a residual assemblage after a hydrous partial melting event of oceanic gabbros at temperatures between 900 and 1000°C. This is also consistent with the mineral composition of the gabbroic dikes: olivine between 71-74 mol% Fo, high An content (up to An<sub>86</sub>), high Mg# in clinopyroxene (up to 86 mol%) and orthopyroxene, and amphiboles with high pargasite component. In the dark veins olivine is generally absent indicating slightly lower formation temperature compared to the gabbroic dikes since olivine only form at temperature above 980°C during the hydrous partial melting reaction of olivine gabbro [Wolff *et al.*, 2013].

The mineral composition of the dark veins shows the same compositional range than those in the gabbroic dike. Plagioclase is even more An enriched (up to An<sub>90</sub>), clinopyroxene and orthopyroxene are high in Mg# (up to 90 mol%), and amphibole with high pargasite component. Such high An content, which are characteristic for residual plagioclases after a hydrous partial melting event of primitive gabbro, are a consequence of high water activities. The high Mg# in clinopyroxene can be interpreted as a result of the high oxygen fugacity, which are typically enhanced due to oxidizing effect of high water activities (according to the relations between water activity, oxygen and hydrogen fugacity) [e.g., *Botcharnikov et al.*, 2005]. Thus, the high An content in plagioclase, the Mg#-rich clinopyroxene, and even the formation of olivine in the gabbroic dikes and dark veins are fully in accord with a model of formation by hydrous partial melting of primitive gabbro at very high temperatures ( $\leq \sim 1000^\circ\text{C}$ ), although the mineral composition are similar and even more “primitive” as the unmodified host gabbro formed at much higher temperatures, but under dry conditions.

Corresponding experimental studies on hydrous partial melting of oceanic gabbros and sheeted dikes from the Semail ophiolite show that at temperature below  $1000^\circ\text{C}$ , the generated melt are silica-rich close to composition of typical oceanic plagiogranite [*France et al.*, 2010; *Koepke et al.*, 2004; *Wolff et al.*, 2013; see also Chapter C; for definition of “oceanic plagiogranite” see *Koepke et al.*, 2007]. Parts of the felsic melt, once formed, were probably constant removed due to pervasive mass transfer in the gabbroic dikes and dark veins, which later act as fluid pathways (see below). A similar conclusion was derived from *Koepke et al.* [2014 in press] for the record of hydrous partial melting in an olivine gabbro from the Semail ophiolite. Other parts of the generated melts were frozen in situ. Arguments for this are the bimodal compositional range of plagioclase cores with rims depleted in An (An<sub>40</sub>), the elevated REE pattern, and the presence of typical euhedral accessories like apatite, zircon, and titanite. In Figure 33 the minimum An content in plagioclase is plotted against the Mg# in clinopyroxene. The compositional evolution of the gabbroic dikes and dark veins imitates the trend of the residual phases after hydrous partial melting of the sheeted dikes [*France et al.*, 2010] with nearly constant Mg# in clinopyroxene while the An content is constantly decreasing. This is also shown in minor element composition of plagioclase and clinopyroxene (see Figure 20 and 21), which follow well the trend of the residual phases after hydrous partial melting of the sheeted dikes. Higher Mg# in clinopyroxene of the gabbroic dikes and dark veins compared to the trend of the hydrous partial melting of the sheeted dikes strongly reflects differences of the starting material since the layered gabbro shows higher Mg# (“more primitive”) compared to clinopyroxene in the sheeted dikes presented in the study of *France et al.* [2010].

Another strong argument for the presence of a melt during the formation of gabbroic dikes and dark veins are the elevated REE patterns observed in all dikes and veins, which might reflect the presence of evolved melt. Thus, trace element modelling of partial melting using the in situ crystallization model [*Langmuir*, 1989] has been performed; assuming plagioclase and clinopyroxene equally enter the liquid (Figure 34). This model uses partition coefficient of *Bédard et al.* [2006a], but congeneric results could be obtained using nearly any published values for clinopyroxene and plagioclase. The composition of the calculated liquids for all different melt fractions lies within the range of gabbroic dike and dark vein composition (Figure 34). The slope of the REE patterns (especially for the

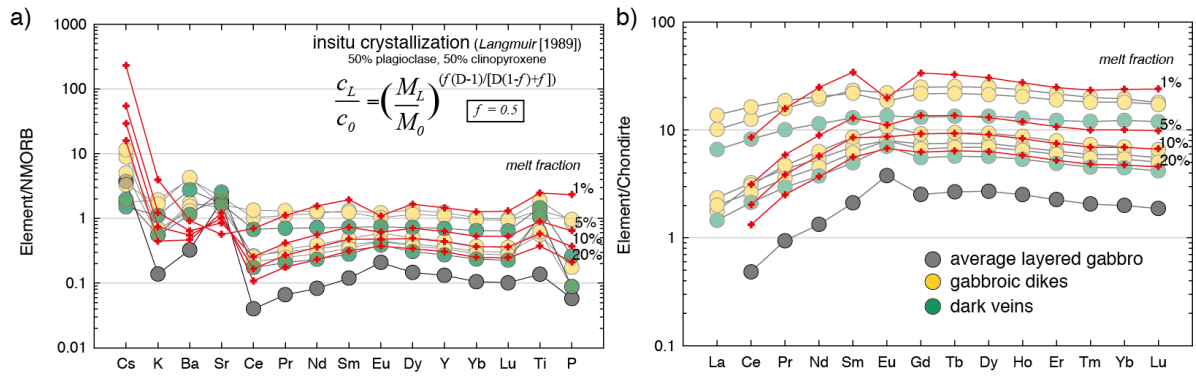


**Figure 34.** Calculated liquids for (a) trace elements (fluid mobility order) and (b) REE elements based on in situ crystallization melt modelling using an average layered gabbro composition. Numbers at the patterns for the calculated liquids (red) indicates different melt fractions. Normalisation against chondritic and normal-MORB values of *Sun and McDonough* [1989]. Details of the calculation can be found in the appendix.

HREE) slope for the calculated liquids are almost identical to the gabbroic dikes and dark veins and tend to negative Eu anomalies, which is also reflected by some of the gabbroic dikes. However, it is obvious that the trace element pattern of the gabbroic dikes and dark veins do not match the ones of the calculated liquids exactly. Combined with the textural results and mineral compositional evolution, this supports the hypothesis that the gabbroic dikes/dark veins are formed by a combined process of accumulation of residual crystals and precipitation from an evolved melt.

As mentioned above, within the layered gabbro directly adjacent to the gabbroic dikes and dark veins, evidences for hydrous partial melting reaction can be observed, expressed by the presence of plagioclase strongly enriched in anorthite. The obtained concentration profile across the grain boundary between two plagioclases (Figure 20b) [*Stichnothe, 2007*] indicates that these zones composed of An-rich plagioclase coexist with newly formed orthopyroxene and pargasitic amphibole. This indicates that the paragenesis can be interpreted as residual phase assemblage after hydrous partial melting triggered by fluids percolating along grain boundaries in the layered gabbro [*Koepke et al., 2004; 2005a; 2005b; 2014 in press; Wolff et al., 2013*]. Since this effect is observed near the contact the dike/veins, a model is implied that very hot, seawater-derived fluids from the VHT veins entered the just frozen gabbro at temperatures above the wet gabbro solidus. Preliminary  $^{87}\text{Sr}/^{86}\text{Sr}$  isotopic composition of the newly formed An-rich plagioclase using in situ LA-ICP MC-MS [*Horn and von Blanckenburg, 2007*] indicates that it is enriched in  $^{87}\text{Sr}/^{86}\text{Sr}$  [*Stichnothe et al., 2008*] compared to the primitive plagioclase in the layered gabbro. Thus, the slight radiogenic  $^{87}\text{Sr}/^{86}\text{Sr}$  isotopic composition obtained for the whole rock analysis in this study might reflect a first imprint of water/rock interactions at VHT. However, more detailed investigations including specific isotopic data are needed to proof this hypothesis. To summarize, two partial melting processes as a consequence of hydrothermal activity operating at VHT were identified, (1) the formation of gabbroic dikes and some of the dark veins within the layered gabbro, and (2) anatexis processes in the layered gabbro directly adjacent to the dikes/veins contact.

### **B.8.3 Formation and evolution of amphibole tracing very high and high temperature reaction at the transition between magmatic to hydrothermal conditions**

Many gabbroic dikes and dark veins record VHT to HT hydrothermal alteration by the complex formation and evolution of amphibole. Amphibole is a common minor phase in mafic rocks and it is regarded to be usually the first hydrous phase crystallizing in magmatic systems tracing volatile-rich (e.g., H<sub>2</sub>O and Cl) magmas, for example in arc volcanic arc magmas [Anderson, 1980; Rutherford and Hill, 1993; Sato *et al.*, 1999; Sisson and Grove, 1993]. In terms of water, amphibole saturation is reached at high water activities [Johnson *et al.*, 1991] with water contents of typically >2 wt% and often as high as 6 wt% in melts at shallow depth, as it is the case for the formation of oceanic crust. However, the direct crystallization of amphibole in rocks derived from MORBs is difficult, due to the general low water content in primitive MORB melts (0.1-0.2 wt% for most MORBs and up to 0.6 wt% for enriched MORB) [Sobolev and Chaussidon, 1996]. Therefore, many researchers pointed out the complex formation history of amphibole in the lower oceanic rock spanning from metamorphic [Cortesogno *et al.*, 2000], hydrothermal [Vanko, 1986], late stage magmatic phase [Dick *et al.*, 2002; Tribuzio *et al.*, 2000], and combination of these phases under varying formation conditions [Coogan *et al.*, 2001a; Gillis, 1996; Gillis and Meyer, 2001; Maeda *et al.*, 2002]. Tracing hydrothermal fluids by the formation of amphibole remains difficult, because amphibole formed in a wide range of temperature (300-800°C) by complex fluid-rock interactions. The aim of this section is to discuss, how the amphibole composition in VHT and HT dikes and veins from the Wadi Wariyah can be used shed light on the hydrothermal alteration processes and tracing the influence of hydrothermal fluids.

#### **B.8.3.1 Origin of magmatic pargasite and metamorphic evolution to hornblende /actinolite**

Temperature of formation, composition, and textural features (poikilitic, enclosing euhedral plagioclase) clearly show that pargasites found in the gabbroic dikes and dark veins are of magmatic origin crystallized from melt rich in H<sub>2</sub>O. As pointed out by Gillis and Meyer [1996] assuming a typical MORB with 0.2 wt% H<sub>2</sub>O, 90-95% of crystallization would be required to increase the water content in the melt (2-4 wt%) and to stabilize amphibole. Consequently, the amount of amphibole would be relatively small (5-10 %). This is contradicting to the high amount (up to 50%, based on mass balance calculation) of pargasite observed in some of the gabbroic dikes and dark veins. Consequently, the formation of pargasitic amphibole cannot be explained by a typical late-stage crystallization from MORB-derived melts. As already shown in the previous section, based on the mineral assemblage, and the composition of the companion minerals, the formation of pargasitic amphibole is linked to the hydrous partial melting reaction of the layered gabbro. It seems possible that pargasite is a residual phase in equilibrium with the melts derived from the hydrous partial melting event. Bulk composition of the VHT dikes/veins and the calculated composition of the partial melting model presented in the previous section indicate that these melts were enriched in incompatible trace elements, incl. REE. Combined with the formation of water-rich melts (see Chapter C), the pargasite should

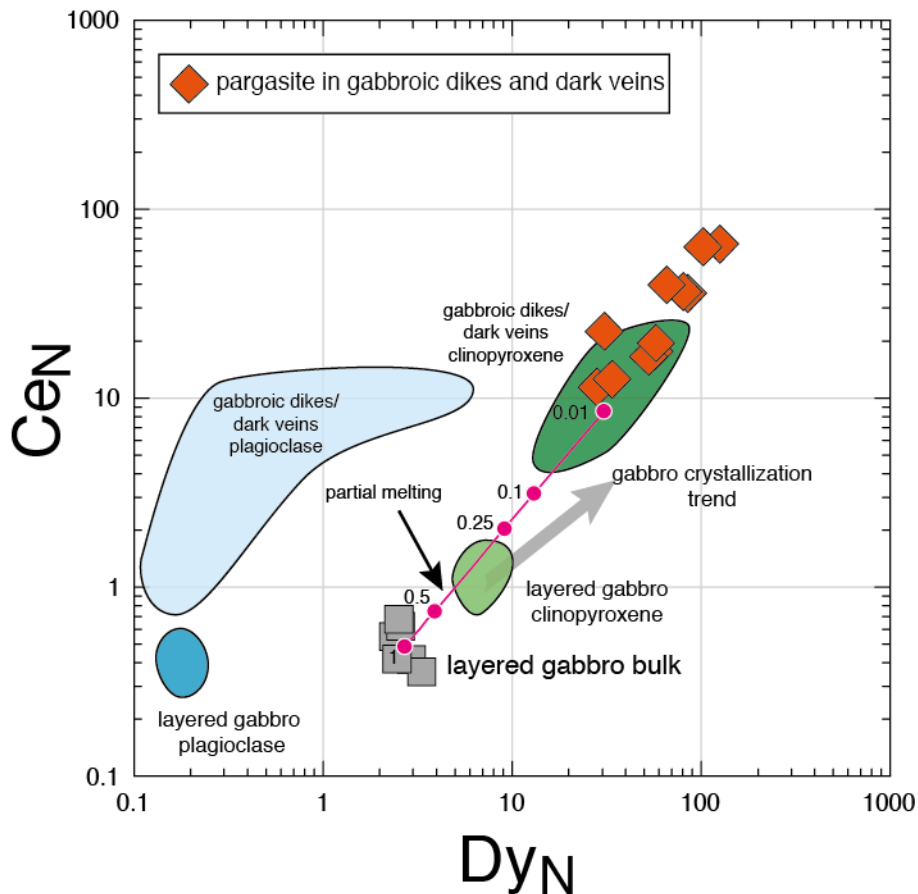


**Figure 35.** Chondrite-normalised [*Sun and McDonough, 1989*]  $Ce_N$  and  $Dy_N$  values for magmatic pargasite from the gabbroic dikes and dark veins of the Wadi Wariyah (dark orange diamonds). The composition of the pargasite indicates enriched  $Ce_N$  and  $Dy_N$  composition incompatible with the typical gabbro crystallization trend (grey arrow) [after *Gillis and Meyer, 1996*]. The pink line with the dots represents the trend modelled partial melt composition at different melt fractions. The blue line with the dots represents the trend for fractional crystallization using a modelled melt composition at very low melt fraction (yellow star). For comparison plagioclase and clinopyroxene composition of the layered gabbro and gabbroic dikes/dark veins are shown.

reflect melt composition and show enriched REE concentration. Thus, the composition of the pargasite might directly trace the element behaviour of the partial melts. To test this hypothesis, the composition of the modelled melts (see previous section) is compared to the pargasite composition for two specific REE elements (Ce and Dy, Figure 35).

The results emphasise that the pargasites show enriched  $Ce_N$ - $Dy_N$  composition compared to the modelled melts and apart from the typical late stage crystallization trend of the layered gabbro. Changing the modal proportions and REE partitions coefficient does not significantly change this relationship. Additionally, the geochemical results indicate that the pargasite is characterized by a negative Eu anomaly. This suggests that the pargasite can be regarded as residual phase in equilibrium with melt derived from hydrous partial melting. This implies that the formation of pargasite does not directly indicate the influence of a fluid at VHT condition, but it forms as a consequence of partial melting triggered by hydrous fluids.



The results presented in section B.6 show that the “*primary*” pargasites in the dikes and veins, are replaced by other amphiboles with a compositional vector to hornblende, in part strongly enriched in Cl (see section below), grading to actinolite/chlorite intergrowth. Temperature estimation reveals that these amphiboles formed under HT conditions of fluid/rock interactions similar to typical high temperature metamorphism of the lower oceanic crust in the amphibolite facies [Gillis and Meyer, 2001; Manning *et al.*, 1996]. Especially, the typical interfingering texture of clinopyroxene and amphibole has been interpreted as complex fluid-rock interactions at high temperature [Maeda *et al.*, 2002]. This suggests that the gabbroic dikes and dark veins after the formation by hydrous partial melting of the layered gabbro underwent more or less continuous metamorphic alteration processes resulting in replacement reaction at HT (and later MT) conditions.

### **B.8.3.2 Formation of hydrothermal amphibole by seawater-derived brines**

The formation of amphiboles extremely enriched in Cl content is a direct indicator for the presence of a seawater-derived hydrothermal fluid. Experimental and structural investigations of Cl incorporation into amphibole [Oberti *et al.*, 1995; Sato *et al.*, 1997; Volfinger *et al.*, 1985] have demonstrated that the fixation of the large Cl anion (0.180 nm) for OH-groups at the O(3)-site is probably related to either an increase in the number of large octahedral cations or in small tetrahedral cation. This site can be accommodated by (1) <sup>[IV]</sup>Al substitution for Si, (2) Fe<sup>2+</sup> at the M1 and M3 sites for Mg (Mg-Cl avoidance), and (3) K is preferred to accommodate the A-site. Anyways, formation of these particular amphiboles is rare and they have been recognized to form by chlorine partitioning between amphiboles and hydrothermal fluids in many metamorphic systems. Their formation had been regarded to be a strong function of fluid composition, temperature and pressure [e.g., Zhu and Sverjensky, 1991]. In contrast, McCormick and McDonald [1999] stated that Cl-rich amphiboles occur over a wide range of temperature (~350-800°C) and pressure (0-800 MPa) revealing that neither temperature nor pressure is a significant factor controlling the growth of these particular amphiboles.

The extremely high chlorine content (up to 5 wt%) combined with the strong enrichment in fluid mobile elements (Sr, Ba) found in the Cl-rich amphiboles suggests the influence of hydrothermal fluid or NaCl-rich brine/vapour separated from hydrothermal fluids under pressure during the formation of these amphiboles. The Cl contents of these particular amphiboles are significant higher compared to amphiboles from the oceanic crust [Coogan *et al.*, 2001a; Gillis *et al.*, 2003]. Fluid inclusions in the roof zones of ophiolites and recent oceanic crust show a wide range of salinities [Alt *et al.*, 2010; Gillis and Roberts, 1999; Nehlig, 1991] from brines with >50 wt% NaCl equivalent to low salinity fluids (<2 wt% NaCl equivalent). Since Cl incorporation in amphibole is generally low during magmatic processes the presented Cl-amphiboles thought to be equilibrated with high saline brine [Vanko, 1986]. The lack of fluid/mineral partitions coefficient of amphibole hinders to quantify the precise composition of the fluid. However, assuming constant pressure of 200 MPa and a range of temperature (500-700°C), at any NaCl content the hydrothermal fluid has the physico-chemical properties that it can gradually change from liquid-like to vapour-like chemical properties without crossing a phase boundary in this region [Driesner

and Heinrich, 2007]. Another possible scenario is that the fluid-saturated magma may exsolve high salinity brines and vapour [Shmulovich *et al.*, 2002], which is more likely to occur at lower pressure. Additionally, the melt composition produced by the addition of seawater to the dry system [Wolff *et al.*, 2013; see also Chapter C] shows that the Cl content is not significantly enriched in the water-rich melts produced after hydrous partial melting compared to the Cl content in typical MORB [Gillis *et al.*, 2003]. Coogan *et al.* [2003] showed that the Cl content in the roof zone of the axial magma chamber is mostly due to the influence of hydrothermal brine. Thus, there are strong evidences for the formation of Cl-rich amphiboles directly linked to the presence of high saline brine phase derived from hydrothermal fluids. Beside the implication from the geochemical results, the presence of such Cl-rich amphiboles is another strong argument indicating the first imprint of seawater-derived hydrothermal circulation at the HT/MT temperature stage in a deep gabbroic crustal horizon near the Moho.

In summary, the complex textural, mineralogical, and geochemical results show that the formation of amphibole within the dikes and veins from the Wadi Wariyah indicate complex fluid/rock interaction spanning VHT to MT conditions. This implies that all gabbroic dikes and dark veins, even if they have clearly magmatic texture, can be regarded as products of water/rock interactions within the lower crustal section of the Semail ophiolite triggered by seawater-derived hydrothermal fluids under varying temperature conditions from VHT down to MT.

#### **B.8.4 Formation of epidote veins as indicator for fluid/rock interactions of the layered gabbro and gabbroic dikes**

The epidote veins observed in the Wadi Wariyah were formed during advancing hydrothermal alteration of the host rock at the transition between the HT and MT conditions. The calculated *W/R* ratios indicate that at this temperature stage the flux of the hydrothermal fluid is increased compared to water/rock interactions at VHT conditions. Formation of epidote is regarded to be a common mineral in metamorphosed mafic to intermediate rocks of higher-grade zeolite to medium-grade amphibolite facies [Liou *et al.*, 1985]. Intensively fluid-rock interactions cause Ca enrichment in the bulk rock, while Mg and Na are depleted. In submarine hydrothermal systems epidote has been mainly reported from the upper sections of recent oceanic crust [e.g., Alt *et al.*, 2010; Humphris and Thompson, 1978; Mével, 1981] and from ophiolites [e.g., Bickle and Teagle, 1992; Liou and Ernst, 1979; Nehlig and Juteau, 1988].

The epidote from the Wadi Wariyah is mostly low in  $X_{Fe^{3+}}$  (0.04-0.16) and forms after An-rich plagioclase indicating that it forms in greenschist to amphibolite facies (500-700°C) [Grapes and Hoskin, 2004]. Berndt *et al.* [1989] showed that plagioclase and epidote buffers cation exchange in hydrothermal fluids, which leads to characteristic REE pattern of the hydrothermal fluids. The epidote shows similar REE patterns compared to the plagioclase, but mostly with lower chondritic values (Figure 25 and 28). This suggests that hydrothermal reaction of plagioclase-epidote yield to the typical REE pattern observed in many hydrothermal fluids [Michard, 1989]. The strong pronounced Eu anomaly (Figure 28) is regarded to indicate that Eu is less fractionating compared to the other REEs [Bau,

---

1991] during hydrothermal interactions. The combined results of low  $X_{Fe^{3+}}$  of clinozoisite and the strong pronounced Eu anomaly indicates that the fluid-rock interactions take place at more reducing conditions than it is reported from epidote formation of the upper sections of the oceanic crust [Nehlig *et al.*, 1994].

Clinozoisite and bulk-rock analysis of epidote veins from the Wadi Wariyah show differences in REE concentration. The thick epidote vein (*Wa\_43A*) shows enriched REE composition compared to the thin epidote veins (*Wa\_39* and *Wa\_40*). This suggests a different pre-alteration host rock for the different epidote veins. In the following two possible host rocks are discussed: (1) layered gabbro and (2) gabbroic dikes. Due to typical low concentration of REE in hydrothermal fluids ( $>10^{-2}$ - $10^{-5}$  chondritic value) [Bau, 1991; Michard *et al.*, 1983; Schmidt *et al.*, 2007; 2010] significant REE depletion of the rock from the oceanic crust is regarded to occur only at very high *W/R* ratios. Due to mostly low fluid/rock partition coefficients of epidote [Brunsmann *et al.*, 2002], enrichment in REE of the host rock during hydrothermal alteration seems to be unlikely. The enriched REE pattern of the thick epidote vein *Wa\_43A* compared to the layered gabbro indicates that it is problematic to relate them to typical alteration process of the layered gabbro. Most likely this epidote forms due to hydrothermal alteration of a gabbroic dike, which is generally enriched in incompatible trace elements including REE due to the hydrous partial melting reaction (Figure 19b). Another strong argument for this hypothesis is the observation of HT amphibole relics in sample *Wa\_43B*, which is in contact to the epidote vein of sample *Wa\_43A*. Formation temperature estimation of these particular amphiboles reveals that they were primary formed in the HT stage (or even higher, see section B.8.3.1). This suggest that the epidote vein of sample *Wa\_43A* formed by progressively hydrothermal alteration of a gabbroic dike. This implies a model that the hydrothermal alteration spanning VHT to MT conditions used the same pathways. High *W/R* ratios of the *Wa\_43A* and *B* compared to the thin epidote veins indicate that the epidote veins formed from the gabbroic dike are influenced by higher fluid fluxes. In contrast, the thin epidote veins and the observed depleted REE pattern compared to the layered gabbro suggest that these veins formed by hydrothermal alteration of the layered gabbro at lower *W/R* ratios (see Figure 28), implying formation at lower temperatures.

In summary, hydrothermal fluids at the transition of HT/MT conditions and variable *W/R* ratios formed the epidote veins. The fluid/rock interaction causes a breakdown of plagioclase and precipitation of clinozoisite from a hydrothermal fluid. Hydrothermal fluids primary use pathways of the VHT/HT alteration stage or formed new vein in the MT stage.

#### **B.8.4.1 $^{87}\text{Sr}/^{86}\text{Sr}$ systematic between epidote veins and altered gabbros - complex element exchange with a transient fluid-vapour during hydrothermal alteration**

Two sampling profiles have been obtained from alteration zones around epidote veins. These are transecting from the fresh layered gabbro via altered gabbro and the halo into the vein (Figure 36a). Chemical variation in the profiles clearly correlates with optically visible, hydrothermally alteration-related mineralogical changes of the host rock (Figure

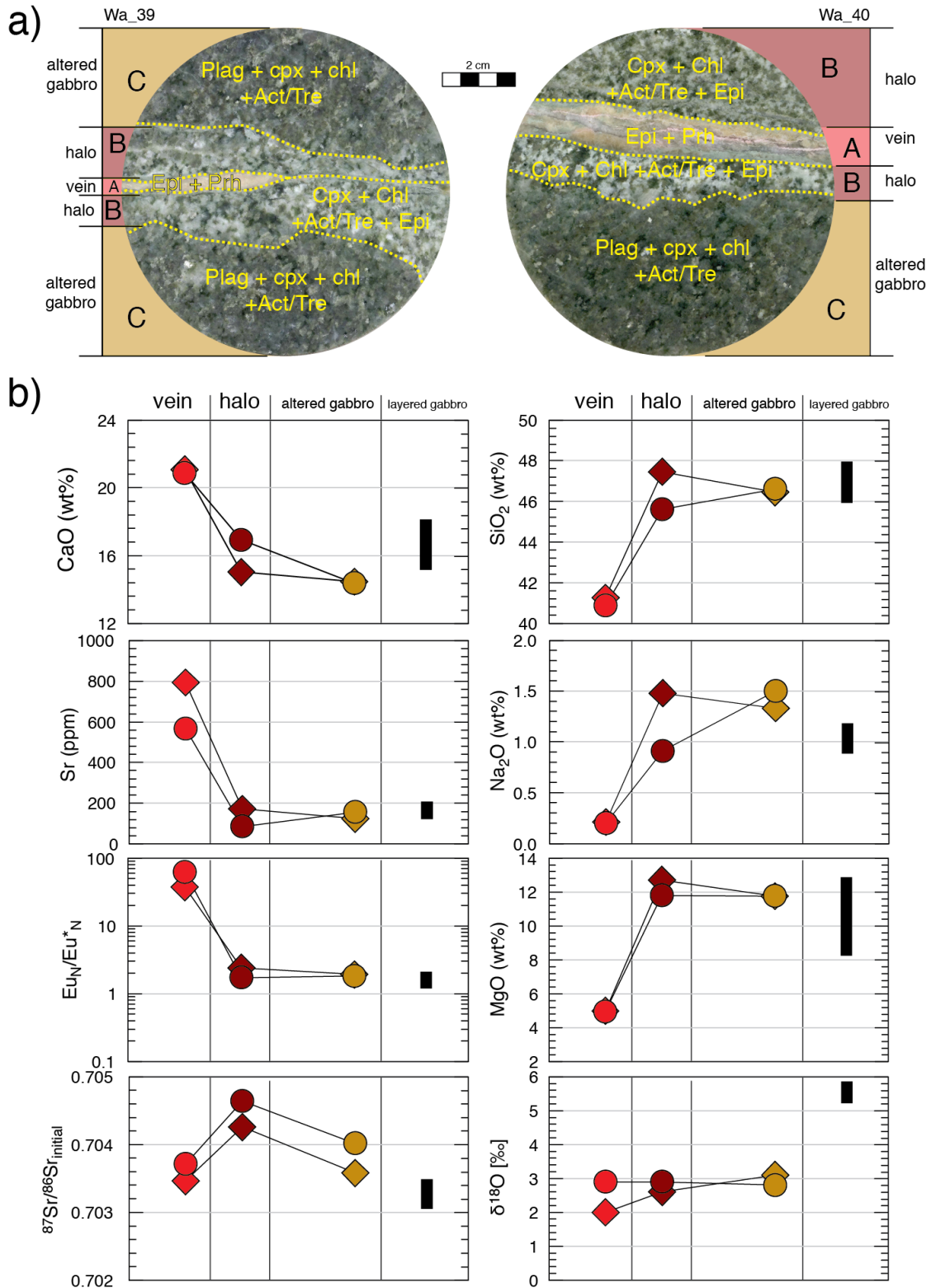


**Figure 36.** Chemical profile across alteration zone of the epidote veins (Samples: *Wa\_39*, *Wa\_40*). (a) Polished drill core samples showing the different zones surrounding the epidote veins. The veins are surrounded by a whitish altered gabbro indicating the formation of epidote replacing protolithic plagioclase. Further away from the vein the layered gabbro appears greenish indicating low-grade alteration by the replacement of olivine and partly plagioclase by chlorite and actinolite/tremolite. (b) Chemical variation of different oxides, ratios, and isotopic composition for sample *Wa\_39* (circles) and *Wa\_40* (diamonds). The black bar indicates the composition of the layered gabbro.

36a). The high values of Ca, Sr, and  $\text{Eu}_N/\text{Eu}_N^*$ , while low values of Na, Mg, and Si, in the vein is mainly due to the precipitation of epidote from a hydrothermal fluid (see section B.8.4). The epidote veins are regarded to present the last stage of hydrothermal alteration under MT conditions where sealing via epidote mineralization finally stopped the fluid flux in these veins. In contrast, the halo and the altered gabbro show no variation in major and trace element composition compared to the layered gabbro, although they show different mineral assemblages. In the halo plagioclase and olivine are replaced by epidote, chlorite, and actinolite/tremolite. In the altered gabbro the plagioclase is only partly replaced and joining olivine replacement reaction to chlorite and actinolite/tremolite, without epidote.

The  $^{87}\text{Sr}/^{86}\text{Sr}$  and  $\delta^{18}\text{O}$  isotopic composition along the two profiles are very similar emphasizing the spatial evolution of isotopic composition during hydrothermal activity. Figure 36b shows that fluid/rock interactions caused a change in the pre-alteration isotopic composition of the layered gabbro. Starting from the layered gabbro, the  $^{87}\text{Sr}/^{86}\text{Sr}$  ratio increases reaching a maximum in the halo close to the vein, and then rapidly decreases towards the interior of the vein. In contrast, the  $\delta^{18}\text{O}$  values are generally significantly depleted in the halo and the altered gabbro with similar values for the different zones. The presented characteristics in isotopic composition are difficult to explain and might reflect complex fluid/rock interactions during hydrothermal alteration of the layered gabbro. Most reasonably, several different origins of the variation in  $^{87}\text{Sr}/^{86}\text{Sr}$  and  $\delta^{18}\text{O}$  must be considered, the most possible are:

- Phase separation occurs during the formation of the alteration zone. It seems to be possible that the fluid underwent liquid-vapour phase separation, which will lead to an isotopic lighter vapour and a heavier liquid. The isotopic lighter vapour forms the vein, which consequently has a lower isotopic record ( $\delta^{18}\text{O}_{\text{vein}}/^{87}\text{Sr}/^{86}\text{Sr}_{\text{vein}} < \delta^{18}\text{O}_{\text{halo}}/^{87}\text{Sr}/^{86}\text{Sr}_{\text{halo}}$ ). The coexisting fluid infiltrated the layered gabbro and led to heavier isotopic composition.
- The continuous Sr profile from the halo through the altered gabbro into the fresh gabbro reflects a coherent evolution of an influx of a hydrothermal fluid from a vein into the host gabbro. The lower  $^{87}\text{Sr}/^{86}\text{Sr}$  ratios in the vein reflect only the last stage of epidote mineralization (snapshot-like), while the enriched ratios in the halo reflect an accumulated signal gained by the fluid infiltration over a much longer period.

Although, the precise process of the observed spatial isotopic composition in these alteration zones cannot be resolved in the frame of this study, the data presented here show the complexity of fluid/rock interactions during hydrothermal alteration. Furthermore, it shows that in the MT regime hydrothermal alteration is not limited to a veining system anymore, but infiltration of the wall rock leads to chemical exchange between the vein and the wall rock forming a complex reaction zone around the vein. Due to the lack of exact fluid properties and composition involved in the processes, it is not possible to quantify the observed record in the alteration zone, yet. More studies on this specific topic are suggested. It can be hypothesised that most likely the isotopic record observed in the halo and altered gabbro reflect fluid infiltration, which started in an earlier stage of

hydrothermal alteration. Thus, the isotopic record in the halo and altered gabbro record reflect that they were more in equilibrium with a hydrothermal. However, since phase separation is regarded to be a common process in hydrothermal systems [German and Von Damm, 2006], this process cannot be fully excluded.

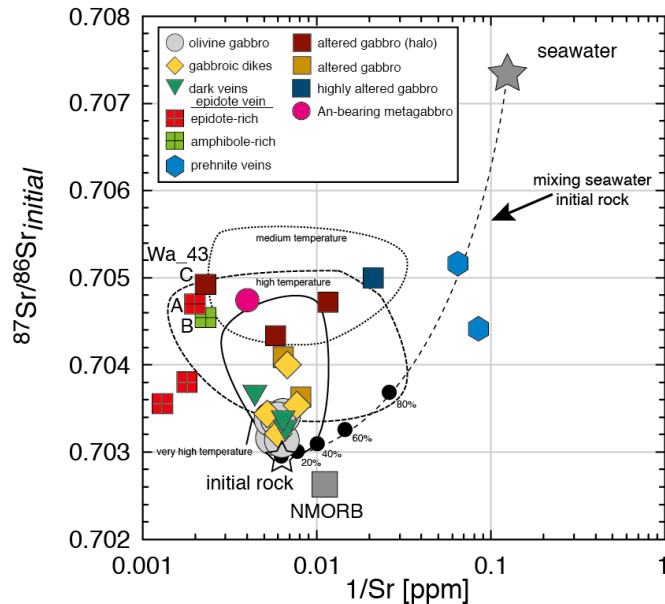


**Figure 37.**  $1/\text{Sr}$  versus  $^{87}\text{Sr}/^{86}\text{Sr}$  of whole rocks analysed from the Wadi Wariyah. For comparison the fields for very high, high temperature, and medium temperatures are re shown [after Kawahata *et al.*, 2001]. The prehnite veins show  $^{87}\text{Sr}/^{86}\text{Sr}$  and  $1/\text{Sr}$  concentration apart from very high to medium temperatures. They plot more or less on the mixing line (dashed line) between seawater and the initial rock (white star). This indicates that the prehnite veins formed by seawater possibly at lower temperatures.

### B.8.5 Low-temperature seawater-rock interactions in the Wadi Wariyah

Prehnite is commonly formed by hydrothermal breakdown of epidote [Frey *et al.*, 1991; Liou *et al.*, 1983] at lower temperatures. Prehnite in the oceanic crust has been mostly reported from the upper sections [Nehlig and Juteau, 1988]. This suggests that the thick prehnite veins observed in the Wadi Wariyah can be regarded as typical low temperature product of seawater/rock interactions at high  $W/R$  ratios. Figure 37 shows the  $^{87}\text{Sr}/^{86}\text{Sr}$  versus  $1/\text{Sr}$  concentration of the whole rock analysed in this study. While in the VHT, HT and MT hydrothermal products an increase in Sr concentration compared to the initial rock can be observed, the prehnite veins are characterised by Sr depletion with increasing  $^{87}\text{Sr}/^{86}\text{Sr}$  isotopic composition. They plot close to the mixing line between the initial rock and seawater indicating that they were formed by seawater penetrating through the entire crust to form prehnite veins, with thicknesses up to 7 cm. The finding of clasts of clinopyroxene with typical composition of the layered gabbro indicates that the LT hydrothermal stage was accompanied by tectonic events leading to cataclastic deformation of the lower crust. Similar effects were observed in deep gabbros from Hess Deep drilled recently by IODP [Gillis *et al.*, 2014 in press].

Nehlig and Juteau [1988] presented a model that the occurrence of prehnite vein within the Semail ophiolite can be regarded as off-axis hydrothermal alteration penetrating through the entire crust. The prehnite veins crosscut all other hydrothermal related dikes/veins indicating that they present the last stage of hydrothermal alteration in the Wadi Wariyah. As indicated by very high  $W/R$  ratios of the prehnite veins and surrounding highly altered

---

gabbro, they are formed by high fluid fluxes hydrothermalised thick zones within the layered gabbro.

#### **B.8.5.1 Anorthitization of gabbroic rocks as indicator for high temperature pervasive hydrothermal alteration**

The An-bearing metagabbro consisting of nearly pure anorthite and clinopyroxene of “magmatic” composition observed as diffuse patches within the thick zones of highly altered gabbro associated with the formation of prehnite veins, represents a very unique lithology, which has not been described earlier from the Semail ophiolite. The complex mineralogy and texture suggests that they formed under complex formation conditions. On the one hand, clinopyroxene shows nearly the same composition and a textural feature as in the layered gabbro, indicating that it is a relic of the layered gabbro, crystallized from a basaltic melt. On the other hand, the occurrence of nearly pure An plagioclase, extremely low in trace elements, suggests non magmatic formation. The strong enrichment of the anorthite component in plagioclase combined with a strong depletion in trace elements is regarded to strongly reflect the formation in the presences of a fluid/water during partial melting of gabbro [Koepke *et al.*, 2005b; Koepke *et al.*, 2004; Wolff *et al.*, 2013], or at hydrothermal conditions [Marks *et al.*, 2011; Vanko and Laverne, 1998]. McCollom and Shock [1998] showed that fluid-rock interactions affect the composition of typically anhydrous minerals (e.g., plagioclase and clinopyroxene) towards relatively pure composition. Python *et al.* [2007] presented dikes within the mantle section of the Semail ophiolite, composed of nearly pure diopside and anorthite and proposed a model that the formation of this lithology was related to hydrothermal alteration. This suggests that the An-bearing metagabbro record formation under hydrothermal conditions. Vanko and Laverne [1998] presented a model that the formation of An-rich plagioclase at hydrothermal conditions is related to either temperature or high  $a_{Ca}/a_{Na}^2$ . Since plagioclase is forming under higher temperatures hydrothermal conditions to those forming epidote [Frey *et al.*, 1991] it suggests that the An-rich plagioclase forms in excess of epidote stability (>500°C). The texture, geochemical, and structural features of the An-bearing metagabbro suggest that during increasing hydrothermal alteration of the layered gabbro, a complex replacement of the magmatic plagioclase take place by pervasive hydrothermal alteration at high temperatures. Surprisingly, this process has not affected the structure/composition of the clinopyroxene, except that the clinopyroxene of the An-bearing metagabbro shows significantly lower Cr content (Figure 21) and appear black under the microscope. Thus, it seems that the formation of the An-bearing metagabbro is somehow linked to pervasive Ca-metasomatism within the layered gabbro. However, the precise mechanism can be not solved in the frame this study.

One possible formation scenario could be that an already heavily altered gabbro with high amounts of clinozoisite replacing the primary plagioclase, was re-heated causing a metamorphic reaction which converted clinozoisite to nearly pure anorthite while the clinopyroxene which is generally less altered than the plagioclase remained largely unaffected (except re-adjusting of some trace elements like Cr). The re-heating event could be the consequence of re-organization of the hydrothermal system in the MT/HT regime, e.g., by heat addition due to replenishments of the axial magma chamber which may cause

---

vertical moving of the axial magma chamber [see review on this processes in *France et al.*, 2010].

Another possible formation scenario could be that fluids with high  $a_{Ca}/a_{Na}^2$  have pervasively metamorphosed the layered gabbro at high temperature above the stability of the clinozoisite stability field. The primary plagioclase of the layered gabbro was constantly replaced by An-rich plagioclase.

### **B.8.6 The use of the same pathways during multi-stage hydrothermal alteration of the lower gabbro section**

Hydrothermal alteration operating through a vein system at different temperatures has been earlier proposed by a petrographic study of gabbroic rock from the Mathematician Ridge [*Stakes and Vanko*, 1986] and from the Semail ophiolite [*Nehlig and Juteau*, 1988]. The presented study provides new insights into hydrothermal alteration of the lower crustal section of the Semail ophiolite spanning a temperature range from the “near-magmatic” VHT regime down to the LT regime, not known so far. The combined discussion presented above based on the geochemical results and petrographic observations implies a model that the same pathways were used for hydrothermal fluids progressing in a temperature interval from 1000°C down to <250°C. In the first stage, hydrothermal alteration starts with a partial melting reaction triggered by hydrous fluid percolating along grain boundaries of the layered gabbro producing characteristic residual mineral assemblage. The record of this event, probably occurred at temperatures as high as 1000°C, is manifested in the gabbroic dikes and dark veins cutting the layered gabbro. At lower temperatures, at the transition between VHT and HT, typical hydrothermal alteration veining starts, first within the residual dikes and veins, later as individual dark veins formed under HT conditions. Relics of VHT (pargasite) within many dark veins are evident for a former VHT stage, at least in some of the dark veins. The replacement of many newly formed phases within the dikes and vein indicate the advancing hydrothermal alteration in the HT regime. Later, a veining stage at MT conditions follows using the same pathways as for the VHT/HT stages. This model is established by the presence of mineral relics of the HT stage found in many epidote veins and by the enriched REE pattern of some of the epidote veins. In a later stage, from these relatively broad, often zoned veins, new epidote veins may diverge, which are characterized by significant lower trace element concentration and lower *W/R* ratios. Furthermore, the occurrence of typical LT minerals observed in many MT veins indicates the advancing hydrothermal alteration at MT/LT transition. The observed massive epidote veins also associated with LT hydrothermal veining supports the hypotheses that most of the LT hydrothermal alteration uses the same vein system than in the previous MT stage. At this LT the hydrothermal veining system penetrates through m-thick zones of highly altered gabbro surrounding the prehnite veins at the highest fluid flow recorded in this study. These zone can identified as fractured fluid flow zones providing pathways for fluids directly from seawater penetrating through the crust down near in the lower sections, crosscutting all earlier stage hydrothermal systems.

A requirement for this hypothesis is the establishment of a well-operating cracking system under VHT conditions, which is not in accord with old fracturing models where the

---



temperatures of the cracking front was estimated as  $\sim 550^{\circ}\text{C}$  [e.g., *Lister*, 1974; *Mével and Cannat*, 1991], supporting the microcrack model of *Nicolas et al.* [2003] and *Nicolas and Mainprice* [2005]. The first developed crack system forms zones of weakness within the still very hot layered gabbro and provide pathways for hydrothermal fluid flow, percolating at VHT and LT. Hydrothermal veins from the MT stage are surrounded by up to dm-thick reaction halos composed of altered gabbro indicating that tremendous amounts of hydrothermal fluids interact with the layered gabbro, changing the system from a more simple veining system to a more complex veining system with strong metasomatic effects, like the formation of reaction halos in the host rock. This complex vein-halo relation is obviously the result of repeated crack-flow-seal episodes [*Ague*, 1997] within the vein. This causes fluid infiltrating into the surrounding rock, and pervasive fluid-rock interaction has the potential to change its mineralogy and composition.

The complex cutting relation observed by structural observation in the field indicates that the presented hydrothermal cracking system is more or less orientated parallel to the lithospheric stress field of the ridges. *Nicolas et al.* [2003] showed that the magmatic layering of the layered gabbros in the Wadi Tayin massif is perpendicular to the general trend of the sheeted dike complex. Consequently the orientation of the dikes and veins is parallel to the to the sheeted dikes, which suggest that the formation of the dikes and veins are controlled by the lithospheric tensional stress field parallel to the ridge axis. However, *Nicolas et al.* [2003] pointed out that, especially in the Wadi Tayin massif, the hydrothermal dikes and veins can be also parallel to the sheeted dikes orientation, which may be indicate that the orientation is controlled by a deeper stress field responsible.

## B.9 Conclusions

The detailed mapping/sampling and the analytical results performed of dikes/veins, halos, altered gabbro and background layered gabbro from the Wadi Wariyah reveals details of insights into the interactions between rock and hydrothermal fluids not known so far, especially with respect to the first hydrothermal imprint at very high temperatures, the estimation of the temperature of the different hydrothermal stages in the lower crust, and the related reactions. As demonstrated in the previous discussion, the hydrothermal alteration of the lower crustal section in the Wadi Wariyah is complex and highly variable and still not fully constraint. The presented study shows that hydrothermal alteration is not limited to a specific temperature interval, but it covers a broad range from nearly all stages from VHT to LT, starting with fluid induced hydrous partial melting, followed by complex mineral replacements in the HT and MT stage, and finalized by a LT stage, where high amounts of seawater were transported via veins through the lower oceanic crust. The main results can be concluded as:

- The mineralogical and geochemical results show that gabbroic dikes and dark veins could be interpreted as the results of partial melting of primary layered gabbro triggered by hydrous fluids at very high temperatures ( $900\text{-}1000^{\circ}\text{C}$ ), which can be regarded as the first imprint of hydrothermal alteration in the layered gabbro of the Wadi Wariyah. At this stage at very high temperatures the *W/R* ratios are small. At

the contact to the host rock (layered gabbro) the occurrence of plagioclase rims enriched in An component indicate partial melting of the host rock triggered by VHT fluids percolating on grain boundaries.

- Hornblende of gabbroic dikes and dark veins equilibrated under amphibolite facies conditions (HT to MT) bear relics of a previous VHT (cores of VHT amphiboles) implying that the same pathways were used for hydrothermal veining from VHT down to MT conditions.
  - Veins within the gabbroic dikes running near-parallel to the dikes as well as amphibole rims within the dark vein are characterized by amphiboles, which are in part extremely enriched in chlorine with formation temperatures between 525-751°C providing evidence for a seawater-derived hydrothermal vein activity at the transition between hydrous magmatic to supercritical hydrothermal conditions.
  - Epidote veins with typical greenschist facies mineralogy (epidote + chlorite + actinolite/tremolite) and formation temperatures between 300-500°C bear relics of the previous HT stage, as indicated by the presence of hornblende formed at higher temperatures. This indicates that the same pathways were used for hydrothermal veining from VHT down to MT conditions, and that during advancing of the alteration front, the primary minerals of the early VHT/HT veins the primary minerals have been replaced by typical greenschists facies minerals.
  - The formation of thick prehnite veins surrounded by highly altered gabbro imply that they formed in the latest stage of seawater-rock interactions at LT temperatures down to 200°C and high *W/R* ratios. Relic clinopyroxene clasts within the prehnite veins indicate an increasing influence of cataclastic deformation in the LT regime
  - The structural analysis imply that dikes and veins identified as products of hydrothermal activity at different temperature/stages are controlled by the same stress field, which is orientated for a cracking system established for hydrothermal veining [e.g., *Mével and Cannat, 1991*].
-

# Chapter C

## The reaction mechanism of fluid-induced partial melting of gabbros in the oceanic crust<sup>1</sup>

### C.1 Abstract

Hydrous partial melting of oceanic gabbro as a consequence of fluid/rock interaction at very high temperatures is regarded as important processes for the formation of felsic lithologies within the oceanic crust. In order to investigate the principle reaction mechanism of hydrous partial melting in detail, we performed water-saturated partial melting experiments using an internally heated pressure vessel (temperature: 860 - 1020°C; pressure: 200 MPa;  $fO_2 \sim NNO$ ). As starting material we used mm-sized blocks of unmodified olivine gabbro (*“microrocks”*). The use of a coarse-grained starting material allows us to study the principle reaction mechanism of hydrous partial melting of oceanic gabbro in detail. Although far from global equilibrium, we observed phase relations and compositional trends as expected from a similar experimental survey designed for achieving global equilibrium using a fine-grained powder of the same starting gabbro. The experimental results allow us to formulate a general fluid-induced reaction for hydrous partial melting of olivine gabbro as a function of temperature:

At  $T \leq 980^\circ\text{C}$ : olivine + clinopyroxene + plagioclase (I) +  $\text{H}_2\text{O} \Rightarrow$  amphibole + orthopyroxene + plagioclase (II) + hydrous plagiogranitic melt

At  $T \geq 980^\circ\text{C}$ : olivine (I) + clinopyroxene (I) + plagioclase (I) +  $\text{H}_2\text{O} \Rightarrow$  olivine (II) + clinopyroxene (II) + plagioclase (II) + hydrous plagiogranitic melt

Textural features and compositional characteristics obtained in our partial melting experiments on microrock are in good agreement with corresponding features of late-stage

<sup>1</sup>A modified version of Chapter C has been published as: **Wolff, P.E.; Koepke, J.; Feig, S.T.** [2013]: The reaction mechanism of fluid-induced partial melting reaction of gabbros in the oceanic crust. *European Journal of Mineralogy*, **25**, 3, 279-298.

assemblages of some natural oceanic gabbros from slow-spreading ridges, implying that some of the natural late-stage parageneses can be better explained as residual phases left back after a hydrous partial melting event rather than by crystallization of a late evolved percolating melt.

In one experiment performed at 940°C, we observe pools of silicate melt containing droplets of a second melt strongly enriched in typical trace elements (P, Zr, Cl as proxies). We interpret this as an effect of liquid immiscibility. The observation of unusual high concentrations of some trace elements within the first melts is in contradiction with trace element concentration derived from trace element modelling using equilibrium partition coefficients. A model is implied that during the very first stage of hydrous partial melting, sub-micron sized phases like apatite, zircon and oxides crystallized on grain boundaries from a late-stage melt in the host gabbro, may be forced into the very first melt and to incorporate their trace element inventory into the melt phase. A possible consequence is that the very first melts of fluid-induced partial melting of oceanic gabbro may be regarded as one possible source for the contamination of natural MORB or of corresponding felsic lithologies generated at mid-ocean ridges.

## C.2 Introduction

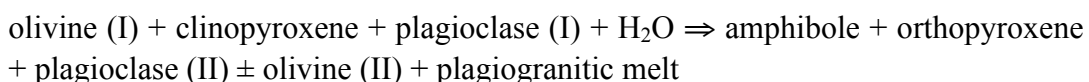
Fluid-triggered partial melting of crustal rocks is one of the major magmatic processes on Earth. For example, it is well known that dehydration melting of amphibolite was responsible for the generation of TTG rocks (tonalites, trondjemites, and granodiorites) in the Archean [Barker, 1979], which is regarded as one important step for the formation of the continental crust. However, in terms of the oceanic crust, it was assumed for a long time that fluid-triggered melting does not play a significant role during the formation of oceanic rocks. This point of view has changed in the last decade, when researchers observed that seawater-rock interaction in the lower oceanic crust proceeded to conditions, where fluid-triggered partial melting of previously hydrothermalised sheeted dikes or gabbro may be initiated [France *et al.*, 2010; Koepke *et al.*, 2004]. Especially, for the formation of felsic lithologies within the oceanic crust, more and more models of formation were presented, where fluid-triggered partial melting was involved. For example, geochemical modelling revealed that partial melting of hydrothermalised amphibole-bearing protolith residing in the mid-crust from fast-spreading ocean ridges played a significant role for explaining the trace element budget of some extrusive andesites and dacites [Haase *et al.*, 2005; Wanless *et al.*, 2010]. Moreover, trondjemitic intrusive veins at the dike/gabbro transitions from the East Pacific Rise (EPR) and from some ophiolites (e.g., Oman ophiolite, Troodos ophiolite) have been explained by hydrous partial melting of contact-metamorphosed, hydrothermalised sheeted dike rocks within the sheeted dike rooting zone, as a consequence of the thermal imprint of an up-moving axial magma chamber [e.g., Alt *et al.*, 2010; France *et al.*, 2009; Gillis and Roberts, 1999; Gillis and Coogan, 2002; Koepke *et al.*, 2009]. Felsic rocks, so called oceanic plagiogranites [for definition of the term see Koepke *et al.*, 2007], also occur in the deep oceanic crust of both slow and fast-spreading ridge systems and many of them are attributed to hydrous partial melting of gabbro. Examples for this are reported both from ophiolite sections [e.g., Amri

---

*et al.*, 1996; *Brophy*, 2008; *Brophy and Pu*, 2012; *Flagler and Spray*, 1991; *Gerlach et al.*, 1981; *Malpas*, 1979; *Rollinson*, 2009; *Spray and Dunn*, 1991] as well as from recent oceanic crust [*Haase et al.*, 2005; *Koepke et al.*, 2004; 2005a; 2005b; *Wanless et al.*, 2010]. *Koepke et al.* [2005a; 2005b] pointed out that many of the late stage parageneses in gabbros sampled near the Kane fracture zone at the slow-spreading Mid-Atlantic Ridge (MAR) consisting of amphibole + orthopyroxene + anorthite (An) enriched plagioclase could be interpreted as the residual parageneses after a hydrous partial melting event instead of typical late crystallization at the end of differentiation. The keys for this hypothesis are zones of plagioclases at grain boundaries, which are strongly enriched in An and depleted in trace elements (Ti, K), implying a model that hydrothermal fluids percolating on grain boundaries could trigger partial melting at near solidus conditions.

A requirement for anatectic processes in the deep crust is the availability of hydrous fluids depressing the solidus of gabbro to relatively low temperatures ( $\sim 870^{\circ}\text{C}$ ) [*Beard and Lofgren*, 1991]. In principal, this fluids could be of magmatic origin (exsolved after extensive fractional crystallization) or seawater-derived, as a result of a deep hydrothermal activity. Since several geochemical studies report seawater-rock interactions in the lower oceanic crust or in the shallow sub-MOHO mantle in the magmatic regime [*Bosch et al.*, 2004; *Hart et al.*, 1999; *Nonnotte et al.*, 2005], models are implied that seawater could be the source for the fluid triggering hydrous partial melting in the deep oceanic crust. Some models have been proposed how seawater-derived fluids may reach the deep oceanic crust. Based on studies on the Oman ophiolite, as an example for fast-spreading ridges, a fluid transport mechanism via a microcrack system operating at up to  $1000^{\circ}\text{C}$  was proposed [*Nicolas and Mainprice*, 2005; *Nicolas et al.*, 2003], which was later confirmed by isotopic studies [*Bosch et al.*, 2004]. Another model obtained from observations in the Oman ophiolite is that of *Abily et al.* [2011] who proposed that fluids might enter the deep, still very hot crust via high temperature shear zones. For slow spreading ridges, a model was presented by *Koepke et al.* [2007], based on observations in gabbros from MAR, these authors presented a model that seawater-derived fluids deliberated by a thermal event may percolate along grain boundaries and initiate partial melting. Another model for fluid flux in the deep crust formed at slow spreading ridges, is provided by *McCaig and Harris* [2012] based on fluid pathways via fault zones for transporting the water-rich fluids to deeper regions of the oceanic crust.

In an experimental study on hydrous partial melting of oceanic gabbro at shallow pressure, *Koepke et al.* [2004] used three different gabbros as starting material, established both phase relations and phase compositions and presented the general reaction for hydrous partial melting of gabbro at temperatures below  $980^{\circ}\text{C}$ :



A key observation of that study was that the residual plagioclase (II) was strongly enriched in An relatively to the plagioclase of the starting gabbro (e.g. at  $980^{\circ}\text{C}$ : 15 to 25 mol%, depending on the starting material).

Furthermore, *Koepke et al.* [2005a] presented BSE (backscattered electron) images of one hydrous partial experiment using a small mm-sized piece of unmodified gabbro as starting material. This gabbro was one of the three starting gabbros used by *Koepke et al.* [2004], which were in that study milled to fine-grained powders, in order to achieve global equilibrium. This single experiment presented in *Koepke et al.* [2005a] showed phase compositions and textures very similar to features from late stage assemblages in natural gabbros from MAR, leading to the general conclusion that many of the typical late stage phases (e.g., amphibole, apatite) in gabbros from MAR can be explained by hydrous partial melting of natural gabbro.

In this paper we repeated the experiments for one starting material of *Koepke et al.* [2004], but using mm-sized pieces of the gabbroic protolith ("*microrocks*"), instead of fine-grained powder. We also included the pilot experiment of *Koepke et al.* [2005a] mentioned above ("*run 12a*"), from which two BSE images were shown in that paper (but no further data have been presented). Although it is obvious, that these experiments are far away from global equilibrium conditions, this technique provides insight into details of the partial melting reactions, not possible with conventional powder experiments. While *Koepke et al.* [2005a] performed only one experiment at one temperature, the experiments of this study span a range of temperature of interest, starting in the subsolidus regime up to a temperature of 1020°C. The results of these experiments shed light on the detailed reaction mechanism of hydrous partial melting of gabbro in the deep oceanic crust, and reveal implications for the formation of SiO<sub>2</sub> rich melts in the oceanic crust.

## C.3 Experimental and analytical techniques

### C.3.1 Experimental techniques

Blocks of the unmodified starting gabbro ("*microrocks*") were sealed in Au capsules together with 10 wt% of fluid, which was either pure water (runs marked with "*a*" in Table 24) or with water plus 3.3% NaCl simulating approximately seawater (runs marked with "*b*"). Since water solubility in basaltic melts at 200 MPa is ~ 5 wt% [*Berndt et al.*, 2002], all experiments were performed under water-saturation. Experiments have been performed in a vertically mounted internally heated pressure vessel (IHPV) at the Institute for Mineralogy (Hannover, Germany) pressurized with a mixture of argon and hydrogen with a total pressure of 200 MPa and in the temperature range between 860 and 1020°C. This pressure is related to the deeper parts of the oceanic crust, where the corresponding hydrothermally induced anatectic processes are assumed to proceed. Pressure was monitored with a strain gauge manometer with an uncertainty of  $\pm 5$  MPa. Temperatures were measured by using Pt-Pt<sub>90</sub>Rh<sub>10</sub> thermocouples, with an uncertainty of less than  $\pm 10^\circ\text{C}$ . Oxygen fugacity was controlled by adjusting a defined partial pressure of hydrogen at the beginning of the experiment. During the experiment, the hydrogen pressure in the vessel was measured with the help of a Pt membrane [*Shaw*, 1963]. The measured hydrogen pressure was used to calculate the prevailing oxygen fugacity in the vessel

---

during each experiment. In all experiments the prevailing  $fO_2$  corresponds to NNO (nickel-nickel oxide) buffer. Run duration of all runs was 168 hours. At the end of the run, the capsules were quenched isobarically with the help of a rapid quench device to prevent the formation of quench crystals during cooling. Details of the IHPV are presented in *Berndt et al.* [2002]. The same equipment and the same experimental conditions (use of Au capsules, pressure of 200 MPa, water saturation,  $fO_2$  corresponding to the NNO buffer) were used in the corresponding hydrous partial melting study of *Koepke et al.* [2004], where equilibrium conditions have been achieved, so that the experimental results of both surveys are directly comparable. Experimental conditions and observed phase assemblages are summarized in Table 24.

### C.3.2 Starting material

Starting material was the gabbro 61a, which is one of the three gabbros, used by *Koepke et al.* [2004] for their fluid-induced partial melting study. It is a typical olivine gabbro from the ultra-deep ODP (Ocean Drilling Program) drilling hole 735B from SWIR (Southwest Indian Ridge; Leg 176) [*Dick et al.*, 2000]. It is a representative medium-grained olivine gabbro of ~1 mm in grain size with plagioclase ( $An_{55}$ ), olivine ( $Fo_{71}$ ,  $Fo$  = forsterite content), and clinopyroxene ( $Mg\# = 80$ ; with  $Mg\# = Mg/(Mg+Fe) * 100$  on a molar basis; Figure 38). The mineral compositions of the starting material are presented in Table 2. Modal proportions have been determined by least square fit mass balance [*Albarède and Provost*, 1977]: 59 wt% plagioclase, 12 wt% olivine, and 29 wt% clinopyroxene. The rock is fresh, with very few signs of alteration, mainly related to the beginning of serpentinization of olivine. Traces of typical late stage mineralization are present (< 1 % of the mode), like pargasitic to ferropargasitic amphibole ( $Mg\# = 69$ ), orthopyroxene ( $Mg\# = 75$ ), and FeTi-oxides. Except a very few grains of sulphides, no other accessories like apatite or zircon was observed under the microscope. All minerals are virtually unzoned. The chemical composition of the starting gabbro 61a is given in *Koepke et al.* [2004].

After crushing the starting rock, we selected 0.5-1 mm sized pieces, representative of the starting material (“*microrocks*”). Although, it is obvious that partial melting experiments with such large grain size will never reach global equilibrium, we applied this procedure in order to detect better details of the mechanism of the melting reaction with special focus on the incongruent characteristic of this reaction, meaning that the reaction products are “*disrupted*”, expressed in the record of new interstitial growth of mafic phases, while new plagioclase is formed in discrete zones within plagioclase clusters (mostly on grain boundaries; see below). Since *Koepke et al.* [2004] used the same gabbro as starting material but as a fine-grained powder (2-10  $\mu m$ ; separated by applying the Atterberg sedimentation method) with the focus to achieve global equilibrium, a comprehensive set of experimental results is available, which allows us to compare the results of this study with the results achieved under equilibrium conditions.

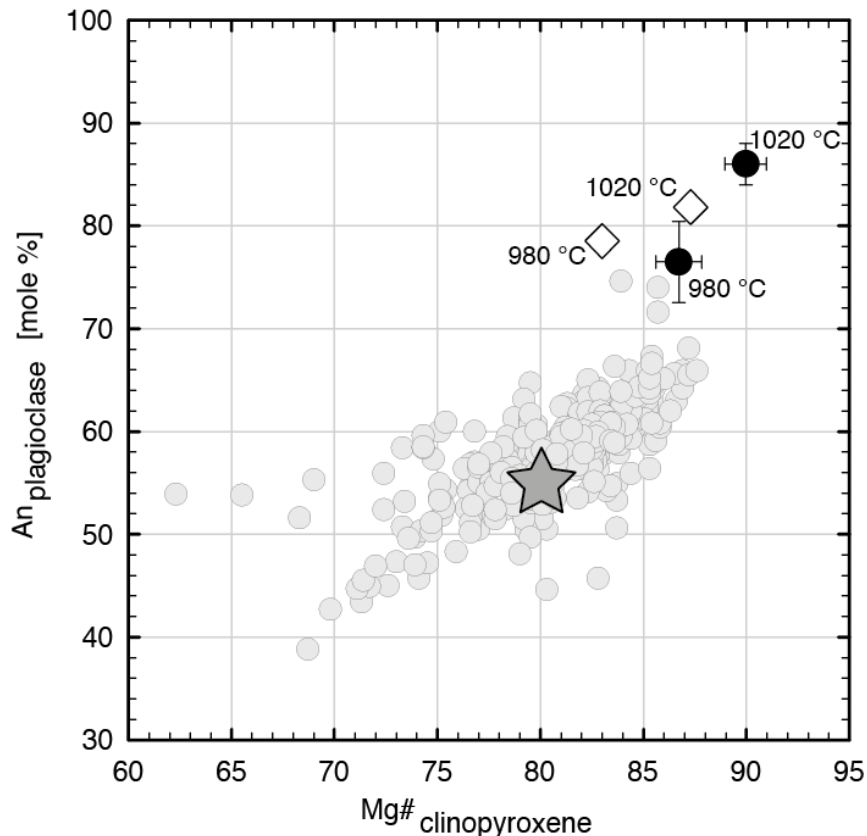


**Figure 38.** Comparison of the mineral compositions (An content in plagioclase versus Mg# in clinopyroxene) of the starting material with those from olivine gabbros from the South West Indian Ridge (SWIR). Symbols: *grey star*: starting material; *grey dots*: single-spot and average mineral composition of gabbros from Leg 176 ODP Hole 735B [Dick *et al.*, 2000]; *black dots*: experimentally formed clinopyroxene and plagioclase from the runs performed at 980 and 1020°C (this study); *white diamonds*: composition of coexisting plagioclase and clinopyroxene from the corresponding experiments of Koepke *et al.* [2004] which were performed under equilibrium conditions.

### C.3.3 Electron microprobe analysis

Major and minor element composition of the experimental phases and of the minerals of the starting material was determined using a Cameca SX100 electron microprobe (Institute for Mineralogy, Hannover, Germany) equipped with five spectrometers and the “*Peak Sight*” software. All analyses were performed using 15 kV acceleration potential and the matrix correction based on Pouchou and Pichoir [1991]. Crystals were analysed using a 15 nA beam current and a focused beam size. Counting time for major elements was usually 10 s except for Ca in olivine (40 s) and F, Cl in amphiboles (30 s). Electron microprobe results for F content in amphiboles are always below the detection limit (0.25 wt%). Element concentration profiles across plagioclase minerals were performed using a two-condition setting. Major elements (Si, Na, Ca, Al) were measured using a 15 nA beam current and focused beam size. Counting time was 10 sec for each element. Minor elements (Mg, K, Ti and Fe) were analysed with a second condition using a 40 nA beam current and focused beam size as well. Counting time was 120 s for Mg and Fe and 60 s for K and Ti.

High beam current and long counting times may lead to migration and volatilization of alkalis elements (e.g., Na) resulting in a loss of X-ray intensities during electron microprobe analysis of hydrous glasses [Morgan and London, 1996]. Therefore we have chosen an analysis setup with a low beam current (4 nA) and short counting rates for Na (4 sec). Analyses of glasses were performed using a two-condition setting. Major elements were measured with a beam current of 4 nA. Counting time was 4 s for Na and 8 s for other major elements. Minor elements (Cl, F, and Zr) were measured in the glasses using a



second analysis condition of 40 nA beam current and counting time of 60 sec for each elements. To overcome the interference between Zr  $L\alpha$  and Si  $K\alpha$  on the used TAP spectrometer crystal, we have setup an interference correction using a high purity quartz standard. In those experiments where melt pools have been large enough, the beam was defocused to a spot size of 5 microns. Small melt pools were analysed using a focused beam. To test the accuracy of the glass analyses performed with focused beam, large melt pools were measured with focused and defocused beam. Both results show the same element concentrations.

To check accuracy electron microprobe analysis we analysed three US National Museum (USNM) reference materials continuously during each microprobe session [Jarosewich, 2002; Jarosewich *et al.*, 1980]. Analysing olivine of the Spring water meteorite and hornblende from Kakanui monitored the accuracy of the microprobe. General precision was in the range of 1 to 5% relative standard deviation (RSD) for all elements, depending on the element abundance in the standard. Glass composition accuracy was monitored by analysing the VG-2 Juan de Fuca glass. General precision for all elements in glasses was in the range from 1 to 6% RSD. Measured chlorine average in the VG-2 standard was 281 ppm, which is in good comparison to reported values [de Hoog *et al.*, 2001; Sun *et al.*, 2007].

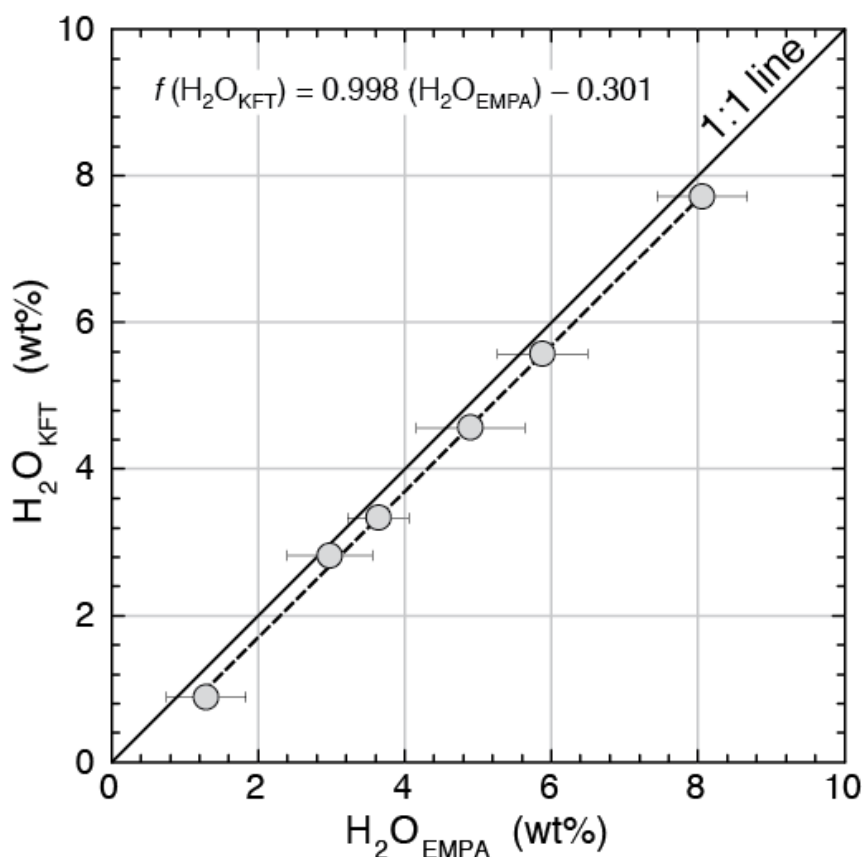


**Figure 39.** Total volatile content estimated by difference from electron microprobe analysis versus KFT-determined H<sub>2</sub>O content. Equation is used to calibrate the “by difference” H<sub>2</sub>O content of the electron microprobe analysis.

To determine the H<sub>2</sub>O concentration in the quenched experimental glasses we applied the “*by difference*” method Figure 39. The water content of the hydrous glasses is 100 wt% minus the analytical total of an electron microprobe measurement. However, this method may lead to an overestimation of the water content in hydrous glasses [Devine *et al.*, 1995]. To improve the quality of the “*by-difference*” technique, hydrous andesitic glasses with well-characterized water contents from 0.89 to 7.72 wt % H<sub>2</sub>O (determined by Karl Fischer Titration, KFT) [Botcharnikov *et al.*, 2006] were analysed with the same electron microprobe setting. The comparison between H<sub>2</sub>O content determined “*by difference*” and H<sub>2</sub>O measured with KFT has been used to calibrate the water content of the hydrous glasses in this study [as described in Devine *et al.*, 1995].

## C.4 Experimental results

### C.4.1 Phase relation and textural features

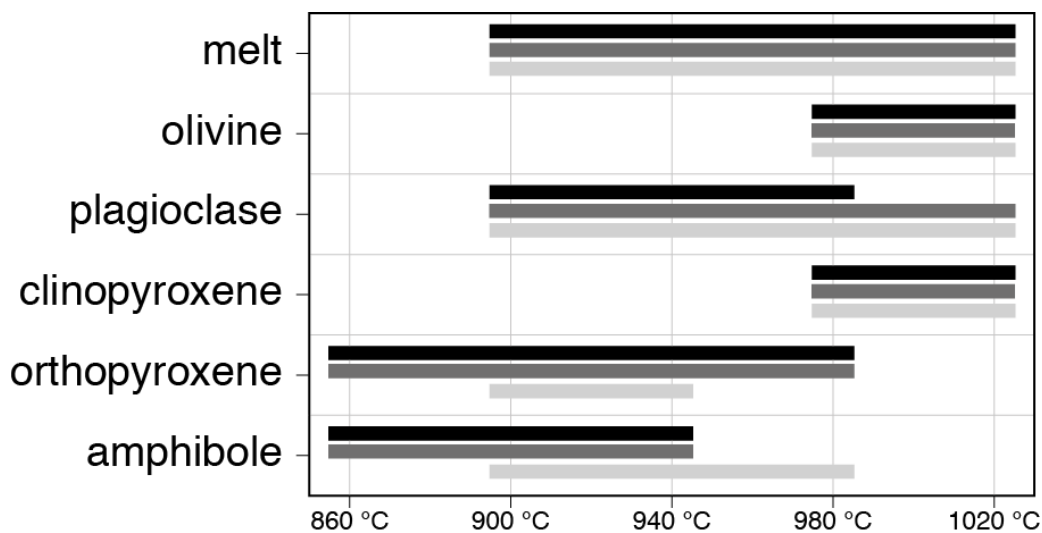


**Figure 40.** Temperature range of stabilities of the newly formed phases observed in the microrock experiments of runs with pure H<sub>2</sub>O (*black bars*) and H<sub>2</sub>O plus NaCl (*dark gray bars*). *Light gray bars* show the stabilities of the experimental phases in the partial melting experiments performed under equilibrium using the same starting material [Koepke *et al.*, 2004].

As expected, the use of microrocks as starting material in our partial melting experiments instead of a fine-grained powder prevented the achievement of global equilibrium, which is visible in each experiment run. It is generally expressed by the presence of cores of protolithic minerals, which remained unreacted, even at the highest temperature (1020°C). Newly formed mineral phases generally coexist with a melt (Figure 40) or formed interstitially between the protolithic phases. In these reaction zones we observed amphibole, orthopyroxene, clinopyroxene and plagioclase, which differ in compositions significantly from the phases of the starting gabbro. Furthermore, we observed the presence of newly formed, typical late stage phases like apatite and FeTi-oxides. Due to the use of the coarse-grained starting material newly formed phases after the experiment

are generally large enough for suitable electron microprobe analysis. Due to the compositional differences, it was easily distinguish between new phases and relict phases of the protolith. Back-scattered electron imaging revealed that the nature of the partial melting reaction is highly irregular, in the sense that the observed reaction zones are disrupted and quite different, depending on the local characteristic of the protolithic mineral assemblage. For example, at temperatures between 940 and 980°C protolithic plagioclase crystals show typical “sieve” structures [Nelson and Montana, 1992] both in the centre as well as in the outer regions of the crystal, with a spongy matrix consisting of newly formed plagioclase enriched in An and enclosed melt pools enriched in albite component (Figure 41d). Very similar textural features were observed in experiments using plagioclase single crystals as reviewed in Johannes *et al.* [1994]. In contrast, olivine and clinopyroxene typically show reaction zones at rims, expressed in dissolution effects and overgrowth of new clinopyroxene, orthopyroxene or amphibole (Figure 41a). Very often, new mafic minerals grew directly at the grain boundaries between clinopyroxene and olivine, in a manner of typical interstitial growth well known from so-called late-stage assemblages in oceanic gabbros.

We observed first melts in the runs performed at temperatures of 900°C, which evolve quite heterogeneous. Beside the evolution of rectangular melt pools in plagioclase and irregular melt pools in olivine, seams of melts associated with the interstitial growth of mafic minerals between the protolithic minerals can be observed. Only in the runs performed at higher temperatures (980-1020°C), larger melt regions can be observed, often with newly formed mineral phases crystallizing within the melt (Figure 41a). These features are very similar to those observed in conventional partial melting experiments using a fine-grained powder as starting material. Despite the use of microrocks as starting material, the obtained phase relations are in good agreement with the results of the equilibrium experiments of Koepke *et al.* [2004]; Figure 40). In the runs performed at 860°C we did not detect any melt pools, but we observed newly formed amphibole and orthopyroxene occurring interstitially between the mafic phases. Both phases show different composition compared to the starting material indicating that the reaction already started, probably in the subsolidus conditions. Primary plagioclase remains unreacted. Thus, we assume that the experiments at 860°C represent subsolidus conditions and that the fluid-triggered partial melting reaction starts above 860°C, which is in agreement with the results of the equilibrium experiments of Koepke *et al.* [2004]. In the experiments performed at 900°C we observed very tiny melt pools within olivine and plagioclase. However, these melt pools are too small for suitable electron microprobe analysis. Very probable, the amount of produced melt in this experiment is very small and most parts of melt escaped into pores, cracks and holes produced by the partial melting reactions.

As mentioned above, two experimental series have been performed with different types of fluid added: pure water, and water with 3.3% NaCl in order to simulate the effect of seawater instead of pure water. No significant differences between both series have been recorded in terms of phase relations, phase compositions, of textural features, except for chlorine content in both melts and amphiboles, which is slightly increased in the runs, where the seawater analogue was added (see below). Furthermore, in the runs at 1020°C newly formed plagioclase was detected in the run with water + NaCl added (17b) but not in the

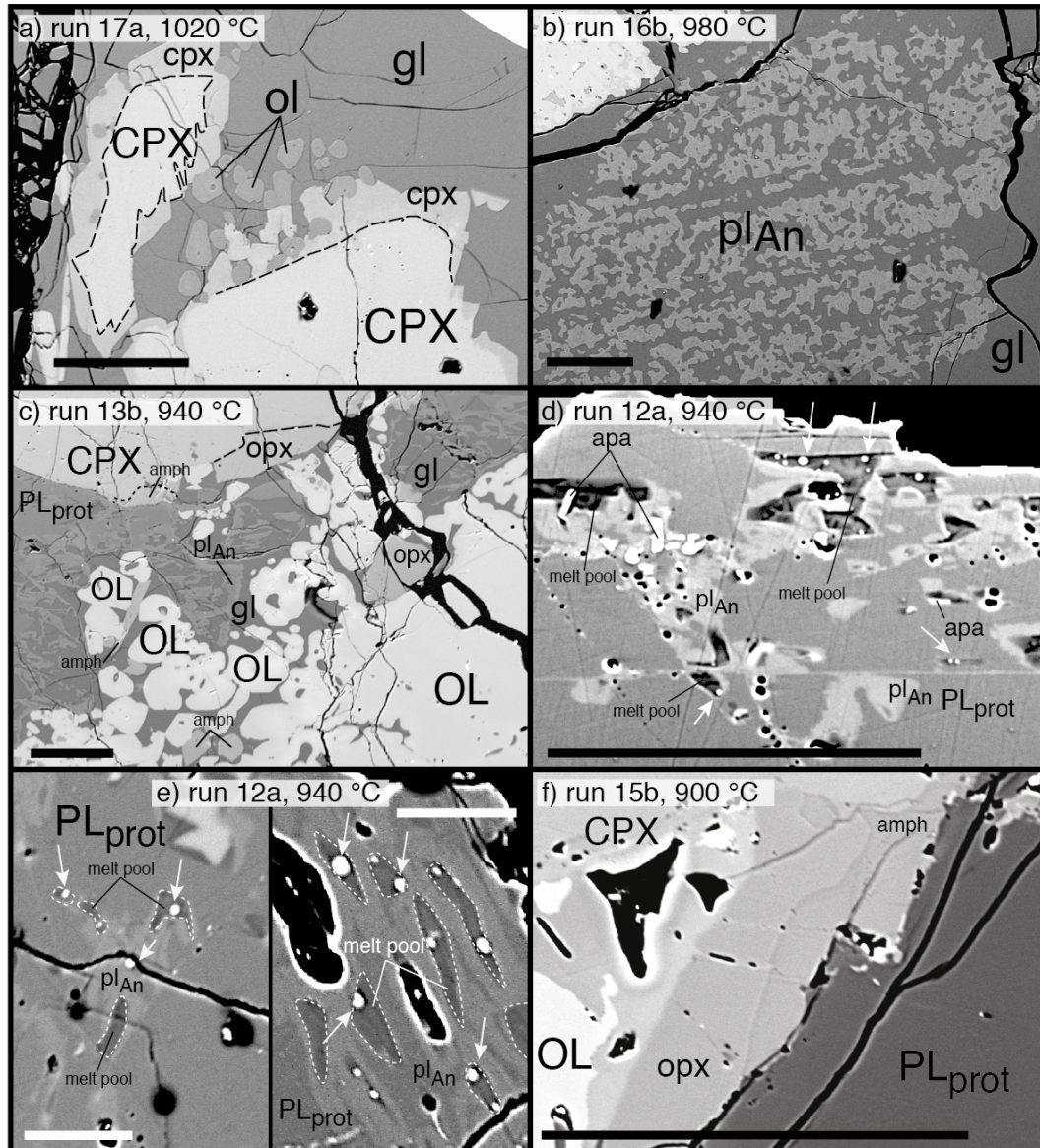


**Figure 41.** Backscattered electron images of the experimental run products. (a) Experimental phase assemblage produced at a temperature of 1020°C. New olivine forms isolated hypidiomorphic crystals (ol) surrounded by melt (gl) while new clinopyroxene (cpx) forms a coherent zone around primary clinopyroxene crystals (CPX). (b) Spongy plagioclase of An-enriched (pl<sub>An</sub>) composition filled with melt (gl) in an experimental product performed at 980°C. The plagioclase shows still the shape of the grain of the plagioclase of the starting gabbro, but with a composition corresponding to the equilibrium composition strongly enriched in An. (c) Formation of melt (gl) and new mineral phases between primary olivine (OL) and clinopyroxene (CPX) at a temperature of 940°C. Newly formed amphibole (amph) crystallized mostly at the rim of primary clinopyroxene. Orthopyroxene grew interstitially between olivine and clinopyroxene or at the rim of pyroxene. Primary plagioclase (PL<sub>prot</sub>) shows sieve structure with newly An-rich plagioclase (pl<sub>An</sub>) surrounding melt pools. Primary olivine shows typical dissolution texture. (d) Details of the record of a partial melting reaction at temperature of 940°C documented within a primary plagioclase crystal (PL<sub>prot</sub>). Rectangular melt pools are surrounded by newly formed An-rich plagioclase (pl<sub>An</sub>, light grey). New An-rich plagioclase also forms fine planes parallel to the albite twin boundaries orientated parallel (010) (horizontal bright line in the lower part of the figure). Visible is also the formation of spherical droplets of immiscible melt enriched in trace elements within the melts pools (arrows), as well as some tiny apatite needles (apa). (e) Melt pools in primary plagioclase (PL<sub>prot</sub>) produced at 940°C. The melt pools are surrounded by plagioclase strongly enriched in An content (pl<sub>An</sub>). Within the melt pools, spherical droplets of an immiscible melt can be observed (grey arrows). The right image shows melt pools, which are rectangular elongated, with a direction, which is crystallographically controlled (e.g., parallel (010)). Black areas are holes due to capsule preparation. (f) Newly formed Amphibole (amph) and orthopyroxene (opx) crystallized interstitially between primary olivine (OL), clinopyroxene (CPX) and plagioclase (PL<sub>prot</sub>) at a temperature of 900°C. Capitalized labels indicate minerals of the natural starting material, while labels with small letters indicate newly formed phases; black bars indicate a scale 100 μm; white bars indicate a scale of 25 μm. See text for details.

run where pure H<sub>2</sub>O was added (17a). Concerning the lack of plagioclase in run 17a, it is more probable that this is a consequence of the coarse grained starting material, making it very difficult to have representative thin sections for each experimental run. So, we did not observe plagioclase in the thin section, but we believe that new An-rich plagioclase is present, which is in this type of experiment typically associated with the plagioclase of the starting gabbro. There is no other reason, which can explain the absence of new plagioclase at a temperature where plagioclase is stable without doubt. There is no indication that the presence of small amounts NaCl in the fluid is responsible for the instability of a major phase like plagioclase.

#### C.4.2 Mineral composition

Average mineral compositions of the experimental phases are listed in Table 25, together with the compositions of the phases of the starting gabbro.

Newly formed olivine was only observed in runs performed at higher temperatures (980 and 1020°C). Relatively to the starting composition (Fo = 71 mol%) the experimental olivine showed increased Fo contents with temperature ranging between 76 and 87 mol% except for some olivine formed within melt pool in clinopyroxene showing lower Fo content (75 mol%) compared to other newly formed olivine at 1020°C. In the equilibrium experiments of *Koepke et al.* [2004] olivine was also observed in the same temperature interval with similar Fo contents ranging between 76 and 83 mol%. Newly formed plagioclase was observed in runs performed at temperatures above 900°C where melt was present. At the beginning of the melting reaction, the host plagioclase shows the development of rectangular melt pools, which are surrounded by newly formed plagioclases enriched in An relatively to the host (Figure 41d) At temperature of 900°C we observed very small newly formed An-rich rims surrounding tiny melt pools (see section C.4.3). However, these An-rich plagioclases have been too small for appropriately electron microprobe analysis. With increasing melt fraction at higher temperatures, melt pools and An-rich zones become larger, while domains with relics of the host plagioclase disappear more and more. At highest temperatures the plagioclase typically consists of spongy newly formed An-rich plagioclase filled with melt pools (Figure 41b). The increase of An content is a function of temperature (Figure 42): at temperatures of 940°C, the increase is 16-18 % compared to An content in the host plagioclase, at highest temperature (1020°C), the increase reaches a maximum value of 36 mol%. The observed shift of An in plagioclase to higher values is due to the well-known influence of water on plagioclase composition [e.g., *Feig et al.*, 2006; *Gaetani et al.*, 1993; *Panjasawatwong and Danyushevsky*, 1995; *Scaillet and Evans*, 1999]. Since all our experiments were performed under water-saturated conditions, very high water activities near 1 were achieved in our experiments resulting in the significant enrichment of An in the plagioclase. In contrast, the An content of the plagioclase in the protolith is relatively low, since the crystallization of typical oceanic gabbro is assumed to proceed under “dry” condition. Minor elements (TiO<sub>2</sub> and K<sub>2</sub>O) in the new plagioclases show significantly lower concentrations compared to the protolithic plagioclase. Element concentration profiles through newly formed An-rich plagioclase show a systematic depletion of K<sub>2</sub>O and TiO<sub>2</sub>. This feature can be used for distinguishing plagioclases formed by hydrous

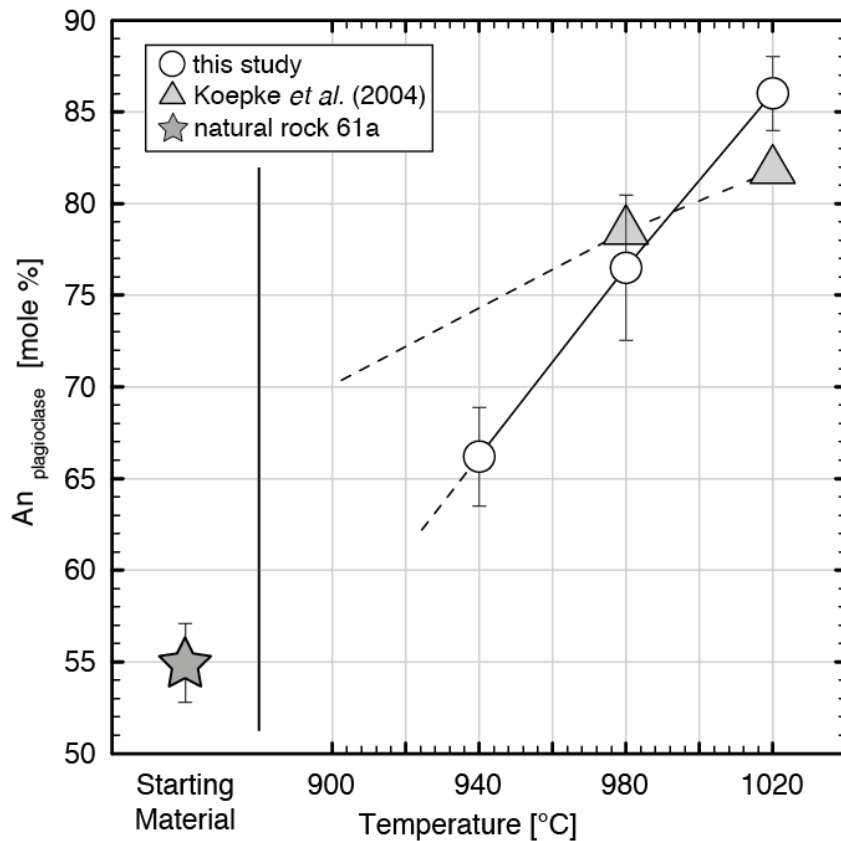


**Figure 42.** Anorthite content of the newly formed plagioclases and of the natural starting material. For comparison, the anorthite content of the experimental products of the corresponding equilibrium experiments of *Koepke et al.* [2004] is shown. The dashed line corresponds to an extrapolation to lower temperatures. Error represents the one sigma standard deviation of the An content.

partial melting of gabbro from those plagioclases crystallized from a late, differentiated melt, which should show higher contents of Ti and K (see section C.5.4.1). The composition of the newly formed plagioclases of this study are in good agreement with the experiments performed by *Koepke et al.* [2004] under equilibrium conditions, at least for those runs performed at 980 and 1020°C (Figure 42). Furthermore, the systematic shift of An in plagioclase to higher values is comparable to natural sample from the MAR [*Koepke et al.*, 2005a; *Koepke et al.*, 2005b]. Due to too small crystal sizes in the equilibrium experiments, *Koepke et al.* [2004] were not able to analyse plagioclases formed at 940°C.

In concordance with the corresponding study under equilibrium conditions of *Koepke et al.* [2004], we observed the formation of new clinopyroxenes at temperatures of 980 to 1020°C. Characteristically, newly formed clinopyroxene only occurs "interstitially" at the rim of primary clinopyroxene (Figure 41a), which acts obviously as sink for crystallization. The Mg# vary with temperature from 86.8 at 980°C to 90.3 at 1020°C, which is significantly higher compared to the natural rock clinopyroxene (Mg# = 80.1). Al<sub>2</sub>O<sub>3</sub> content and TiO<sub>2</sub> scatter considerably but are lower compared to protolithic clinopyroxenes. The compositions are in general in agreement with those of the equilibrium experiments of *Koepke et al.* [2004].

Newly formed orthopyroxene occur in the temperature range between 860 and 980°C. They typically form interstitial growth between olivine and clinopyroxene or often in association with amphibole at the rim of clinopyroxene. In orthopyroxenes coexisting with melt Ca, Ti, and Al vary systematically with temperatures showing increasing values with temperature. Orthopyroxene in the run performed at 860°C interpreted as subsolidus formation shows different compositional trend. In those orthopyroxenes coexisting with a

melt, Mg#, Al, and Ca are significantly enriched compared to the orthopyroxene of starting material. Compared to clinopyroxene and olivine, the increase of Mg# with temperature is not strong systematically: the Mg# for 900°C (Mg# = 79.1) is higher than the Mg# for 940°C (Mg# = 76.4), while the Mg# for is highest for 980°C (Mg# = 85.2). The compositions of the new orthopyroxenes are more or less in agreement with the results of *Koepke et al.* [2004] performed under equilibrium conditions, although these authors measured only 4 grains due to too small grain sizes (only 1 analysis for 900°C), and the question raised whether these results are statistically meaningful.

Newly formed amphiboles generally occur in the temperature range from 860 to 940°C, mostly as interstitial growth between clinopyroxene and olivine (Figure 41f), but also as isolated grains crystallized in the melt (run 13b, Figure 41c). Only the amphiboles of the runs performed at 900 and 940°C are coexisting with a melt, while the one of the run performed at 860°C is interpreted as subsolidus formation. The composition is typical edenitic to pargasitic, with higher <sup>IV</sup>Al and Ti in the amphibole formed at higher temperature (Figure 43), which is consistent with the behaviour of the amphibole structure that the amount of these cations increase with temperature [*Ernst and Liu, 1998*]. Mg-numbers of amphiboles for all temperatures overlap in a relatively small interval varying between 74.9 and 79.6. As shown in Figure 43, the compositions of the two amphiboles coexisting with the melt differ significantly from those generated by *Koepke et al.* [2004] under equilibrium conditions at the same temperature, especially with respect to Ti, which is much lower in the amphiboles of the equilibrium experiments (see section C.5.1 for details). The chlorine content of the newly formed amphiboles are only insignificantly higher in those runs where a seawater analogue instead of pure water was added at a given temperature (Table 25).

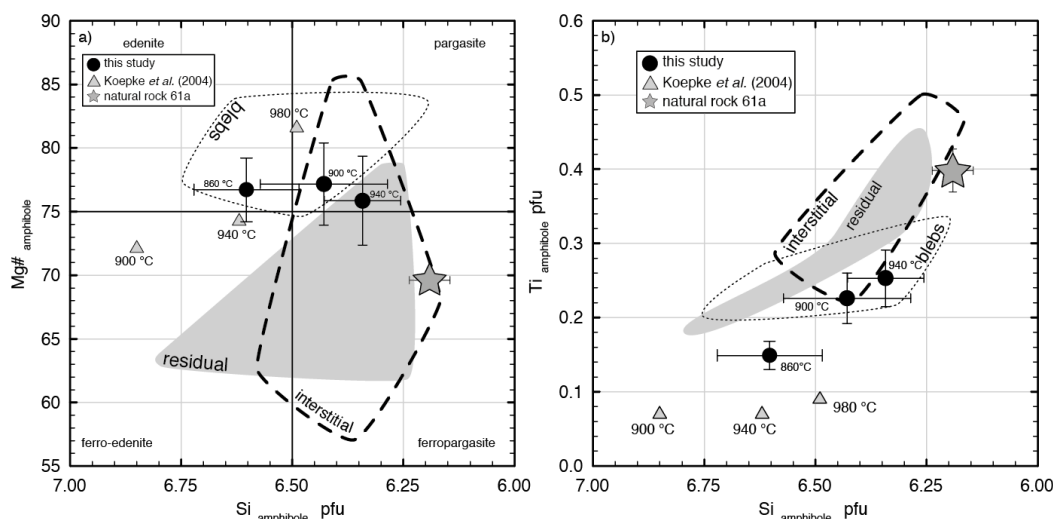


**Figure 43.** (a) Mg# and (b) Ti per formula unit (pfu) versus Si pfu in amphiboles for the experimental runs performed at temperatures of 860°C, 900°C, and 940°C. Each data point is an average of amphibole analyses from experiments performed with pure H<sub>2</sub>O added and H<sub>2</sub>O + NaCl added. Error represents one sigma standard deviation. For comparison compositions of amphiboles forming texturally different groups from natural gabbros from the MAR mostly drilled by ODP (Leg 153) are shown: "blebs" (amphibole blebs grown within clinopyroxene) and "interstitial" amphiboles are from *Coogan et al.* [2001a]; "residual" amphiboles are late-stage amphiboles interpreted from *Koepke et al.* [2005a] as residual phases left back after a hydrous partial melting event. The two compositions of amphiboles produced by the microrock experiments of this study fall into an area where all three field overlap. Included are also compositions of amphiboles produced in the equilibrium partial melting experiments of *Koepke et al.* [2004]. Amphibole classification based on *Leake et al.* [1997].

### C.4.3 Melt composition

Melt pools frozen to homogeneous glass were observed and analysed in the experimental products in the temperature range from 940 to 1020°C. In the run performed at 900°C, melt pools were detected, but were too small for suitable analysis. Water contents of the glasses vary between 5-7 wt% indicating that the melts are water saturated. As expected, with increasing temperature, the melt fraction increases, while the SiO<sub>2</sub> content continuously decreases (Figure 44). As expected, those compositions of the runs with smaller melt fraction correspond to compositions of typical oceanic plagiogranites (see range for SiO<sub>2</sub> contents given in Figure 44a). Chlorine in the melt varies from 110 to 859 ppm. As expected, Cl is systematically higher in those experiments where a seawater analogue as fluid was added, instead of pure water (e.g., for 980°C: 206 ppm in the melt where pure water was added versus 597 ppm in the melt where a seawater analogue was added). While some elements like SiO<sub>2</sub> (Figure 44a), Al<sub>2</sub>O<sub>3</sub> (Figure 44c) and K<sub>2</sub>O (Figure 44g) are in good agreement with the corresponding data of experiments performed under equilibrium of *Koepke et al.* [2004] produced under equilibrium (except for experiment 12a; see below), other elements differ significantly. Mg-number (Figure 44i), CaO (Figure 44e) are significant lower compared to the data of the equilibrium experiment, but follow the same compositional trend with increasing temperature. Other elements like Na<sub>2</sub>O, FeO<sub>T</sub>, or TiO<sub>2</sub> (Figure 44b, d, f, and h) show more or less different trends and variations in concentrations compared to the melts performed under equilibrium conditions. We believe that these effects are related to compositional and mineralogical differences in the very coarse-grained starting material, transposed to the melt compositions. Other than in the experiments of *Koepke et al.* [2004] each charge of the starting material for the experiments has a slight different composition in terms of mode and composition. It is obvious, that experimental compositions of the experimental phases, especially of the melt, show some deviations from coherency.

Of special interest is the experimental run 12a performed at 940°C. Here, we found in some of the ~ 50 µm-sized melt pools within protolithic plagioclases spherical droplets of a second melt (Figure 41e). These droplets are 2-3 µm large and appear as homogeneous glass under the electron microscope. Microprobe analysis reveals that this secondary melt is strongly enriched in iron, phosphorous, and titanium and depleted in silica. Due to small size of the melt pools, the microprobe analyses of both melts were difficult. Results may include surrounding glass yielding to a broad scattering of the data (Table 25). In contrast the melt hosting the droplets of the second melt is significantly enriched in SiO<sub>2</sub> content compared to the melts of the other two runs performed at the same condition (13 a, b) with a content of 79 wt%. Furthermore, this melt show significant lower water content (1.56 wt%). Analyses of the second melt rich in iron and phosphorous revealed an average SiO<sub>2</sub> content of only 35.6 wt% (normalized to 100%). Moreover, these melts show significantly enriched concentrations of P<sub>2</sub>O<sub>5</sub> (11.7 wt%), MgO (8.6 wt%), FeO (22 wt%), and TiO<sub>2</sub> (6.2 wt%). High ZrO<sub>2</sub> contents (0.30 wt%) in these melt droplets implies that these melts show in general a strong enrichment of incompatible elements. Moreover, chlorine concentration is with 2576 ppm also significantly enriched compared to the silica-rich melt (241 ppm). From textural features and from compositional considerations, the observed situation implies an interpretation that the silica poor melt droplets developed by liquid immiscibility of a silicate melt. Obviously, very high concentrations of P<sub>2</sub>O<sub>5</sub>, which is well



known as factor to drive silicate melts to liquid immiscibility [Veskler *et al.*, 2012 and references below], resulted in the formation of the observed spherical low-silica melt droplets. That the precursor melt was oversaturated in  $P_2O_5$ , is also supported by the presence of very tiny apatite crystals in the silica-rich melt pools (Figure 41d), too small for suitable microprobe analysis.

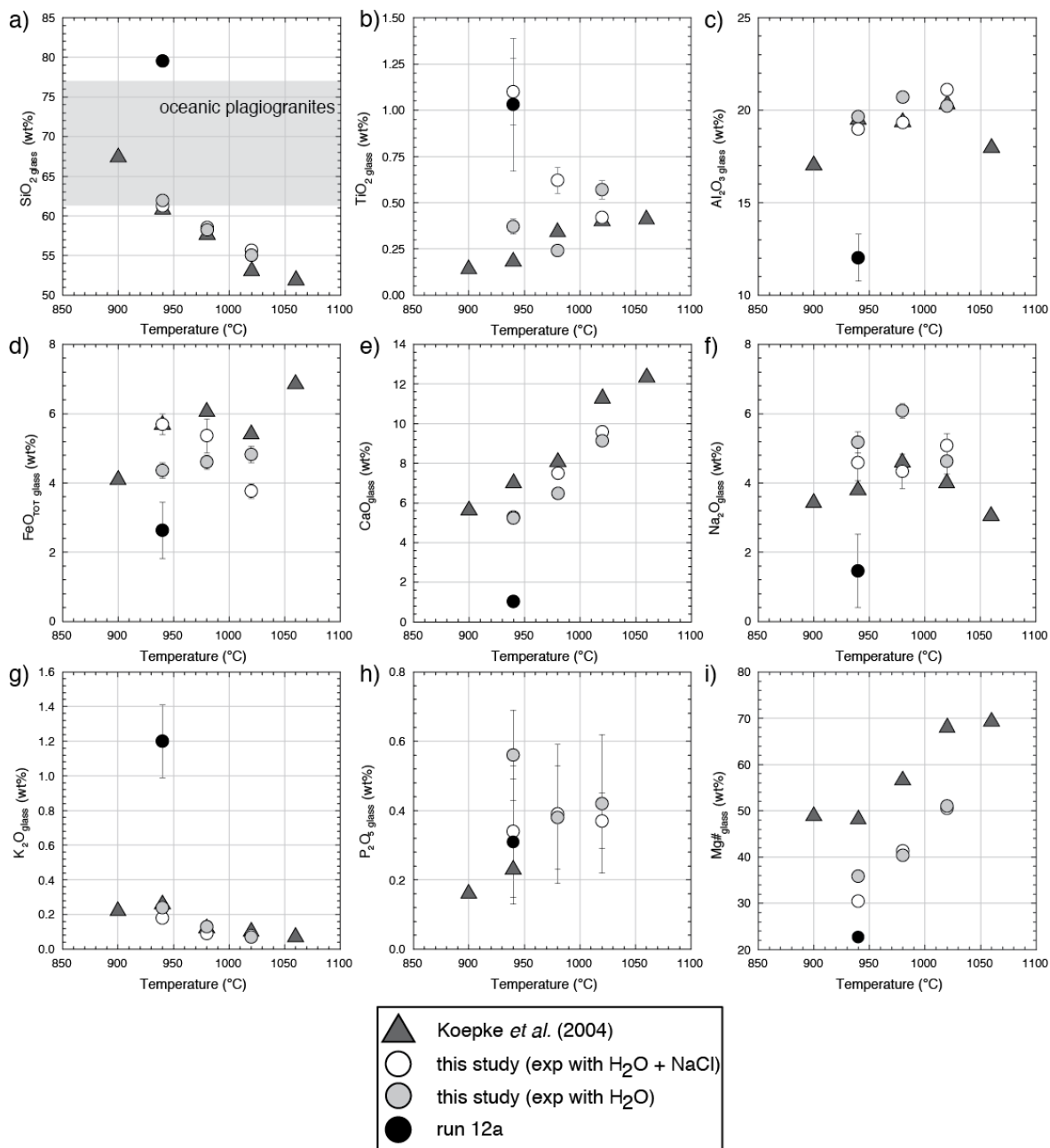


**Figure 44.** Oxide content in the residual melts as a function of experimental temperature (melt is normalized to a total of 100 wt%). Experimental run 12a was excluded from the average melt composition for 940°C due to different melt composition (see text for details). If no error bar is shown, the error is smaller than the symbol. For comparison, the compositions of the residual melts of the corresponding equilibrium partial melting experiments of Koepke *et al.* [2004] are also shown. The range in grey indicates the  $SiO_2$  content of typical oceanic plagiogranites according to the data compilation of Koepke *et al.* [2007].

## C.5 Discussion

### C.5.1 State of equilibrium; comparison to equilibrium experiments

The attainment of global equilibrium in partial melting experiments is problematic when using a charge as starting material, which is too coarse-grained [see *Johannes and Koepke*, 2001, and references therein]. The advantages to use relative coarse-grained starting material instead of a fine-grained powder is the production of relatively large experimental crystals and melt pools, well suited for electron microprobe analysis, especially at near solidus conditions. The disadvantage is that the produced crystals generally show cores of unreacted starting material leading to an attainment of only local equilibrium. Such cores of unreacted starting minerals may be completely encapsulated by the equilibrium composition of the same phase, thus, may persist for periods much longer than the experimental duration, even at high temperatures, especially when the water activity is low, as demonstrated by *Johannes and Koepke* [2001]. As a consequence, the chemical systems of individual runs bearing such zoned crystals are different, since the cores of unreacted starting material do not take part at the general melting reaction, which may lead to unsystematic effects both in phase relations and in phase compositions, especially when comparing experimental runs performed at high and low temperature, since the effect of zoning is strongest at low temperatures.

On the other hand, the use of very fine-grained starting material (e.g.,  $\sim 1 \mu\text{m}$ ) achieves global equilibrium conditions, but leads to the development of only very tiny crystals and melt pools, making the analysis of the experimental phases more difficult, and preventing reliable microprobe analyses of phases from near-solidus runs [e.g., *Koepke et al.*, 2003]. In their study on partial melting of gabbros, *Koepke et al.* [2004] performed a series of experiments at the same temperature using starting material of different grain sizes ( $< 2 \mu\text{m}$ ,  $2\text{-}10 \mu\text{m}$  and  $10\text{-}50 \mu\text{m}$ ) in order to study the effect of grain size of the starting material on the kinetics of the melting reaction. All experimental results show the presence of the same phases, but with different grain sizes and subtly different compositions. In order to trade off between a maximum of grain size of the experimental phases and a minimum of presence of cores of unchanged starting material, *Koepke et al.* [2004] used a powder with a grain size  $2\text{-}10 \mu\text{m}$  for their experiments. However, the presence of unreacted minerals of the starting gabbros as cores within newly formed phases could not be avoided completely, especially at low temperatures. *Koepke et al.* [2004] presented several lines of evidence suggesting that their experiments achieve global equilibrium (e.g., based on textural and compositional criteria, as well as application of known equilibrium element partitioning data).

In this study, very coarse-grained material was used, in the form of pieces of the unmodified starting gabbro with grain sizes of  $0.5\text{-}1 \text{ mm}$ . Since the starting gabbro is medium-grained with grain sizes of  $\sim 1 \text{ mm}$ , it is obvious that individual microrocks show different compositions as a function of the relative abundance of clinopyroxene, plagioclase and olivine. Moreover, the experimental results show a considerable amount of

---

unreacted starting minerals (Figure 41), especially at lower temperatures. On the one hand, it is therefore rather surprising that the results of this study are in quite good agreement with the findings of *Koepke et al.* [2004], especially in terms of phase relations which are practically identical (Figure 40 and 41). In addition, as shown in the previous section, many compositions of newly formed phases (e.g. plagioclase) as well as systematically variations with temperature are in good agreement with the study of *Koepke et al.* [2004], suggesting that local equilibrium obtained in many domains correspond in some aspects to the global equilibrium. On the other hand, the recorded deviations from expected compositional systematics as well as the recorded compositional heterogeneity within one run can be attributed to differences in local equilibrium of different domains due to variation in the proximate primary mineral parageneses, which can vary considerably within a given capsule. This may also result to slight variations in the degree of partial melting in the different domains.

Especially the composition of the melt pools in the experiments performed at 940°C scatter in a large range as a function of the local arrangement of the generated pools with respect to the proximity of the three starting minerals within a given capsule. Strong discrepancies have been also observed for olivine. In the runs performed at 1020°C olivine composition varies in a wide range (e.g., within 11 mol% Fo in the two runs 17a and 17b performed at the same temperatures; see Table 25). This is also supported by a discrepancy for the partition coefficient ( $K_D$ ) for Fe/Mg between crystal and melt (defined as molar  $(\text{Fe/Mg})_{\text{ol}}/(\text{Fe/Mg})_{\text{liq}}$ ), within the run performed at 1020°C. For most olivines at 980°C and 1020°C, the average  $K_D$  values range between 0.27-0.32, which is within the error for olivine in equilibrium ( $K_D = 0.30 \pm 0.02$ ) with a basaltic melt at nominally “dry” conditions [*Roeder and Emslie*, 1970]. On the other hand, those olivines formed in the melt pools within the protolithic clinopyroxene of run 17b reveal a  $K_D$  value of 0.62, which indicates a strong disequilibrium between melt and these olivines.

As shown in Figure 43, strong compositional discrepancies relative to the equilibrium experiments of *Koepke et al.* [2004] are recorded for amphibole, especially with respect to Ti, which is much lower in the amphiboles of the equilibrium experiments. We attribute this discrepancy to the different techniques of starting material preparation. *Koepke et al.* [2004] used the Atterberg sedimentation method to produce a fine powder as starting material with a grain size from 2 to 10  $\mu\text{m}$ , excluding the fraction  $< 2 \mu\text{m}$ , in order to prevent tiniest inclusions in the generated melt pools which prevents reliable microprobe analysis of the melt. We assume that during this procedure, sub- $\mu\text{m}$ -sized grains of late-stage minerals crystallized at the very end of differentiation on grain boundaries of the starting gabbro have been excluded from the experimental system. Since Fe-Ti oxides are such typical late-stage phases (together with amphibole, apatite, zircon), it can be expected that the generated powder used for the equilibrium experiments was impoverished in elements like Ti (plus P, Zr; see below) compared to the complete whole rock, which was used in this study by using “microrocks” of the unchanged starting gabbro.

## C.5.2 Formation of immiscible melts and implication for natural systems

In one experiment we observed the presence of droplets of a second melt strongly enriched in FeO and P<sub>2</sub>O<sub>5</sub> within the silicate melt pools and interpreted this as an effect of liquid immiscibility (Figure 41e). The formation of immiscible melts has been discussed since a long time as possibility to produce felsic melts, often enriched in P<sub>2</sub>O<sub>5</sub> and other incompatible elements in a late stage of magmatic evolution [e.g., *Charlier et al.*, 2011; *Philpotts*, 1982; *Veksler et al.*, 2006]. This model was verified experimentally by *Dixon and Rutherford* [1979] who concluded from experiments in anhydrous MORB that a plagiogranitic melt can be formed due to immiscibility of a felsic and ferrobaltic melt. The most important factor controlling the immiscibility of two liquids appears to be the electric charges and ionic radii of the network-modifying cation [*Hess*, 1995]. In binary systems involving SiO<sub>2</sub> and M<sub>x</sub>O (M = Mg, Ca, K, Na) liquid immiscible occurs due to the miscibility gap of the two oxides [e.g., *Roedder and Weiblen*, 1970] at temperatures near 1700°C, forming two liquids, one ferrobaltic and one felsic. P<sub>2</sub>O<sub>5</sub>, TiO<sub>2</sub> or Fe<sub>2</sub>O<sub>3</sub> tend to enlarge the two-liquid field [e.g., *Visser and van Kross*, 1979].

We observed two liquids only in one experiment at a very low melt fraction in melt pools within primary plagioclase crystals of experimental run 12a performed at a temperature of 940°C, indicating that the formation of two melts is restricted to the very early stage of partial melting, where the melt fraction is very low. Here, immiscibility of two melts seems possible, probably due to a very high content of network-modifying cation like P<sub>2</sub>O<sub>5</sub> and FeO in the first silicate melt, enhancing the miscibility gap between two liquids therefore increasing the probability of formation of two immiscible melts – one silica-rich and one iron-rich. Phosphorus, zirconium, titanium, and chlorine are strongly enriched in the iron-rich melt (Table 25). When regarding these elements as tracers for incompatible elements, it is implied that incompatible elements are forced to enter the immiscible iron-rich melt. This is probably also valid for the rare earth elements (REE), which is also supported by an experimental study of *Veksler et al.* [2012] reporting liquid-liquid partition coefficients in the range from 106 - 128 for the REE between a phosphorus-rich melt and silicic melt at 990°C, indicating the high affinity of the REE to incorporate the phosphor-rich melt.

Our findings imply that at the very early stage of hydrous partial melting of natural oceanic gabbro, before pooling, homogenization and segregation to large melt pools, individual melt volumes may exist, which are strongly enriched in trace elements (here P, Zr, and Cl as proxy) and possible in REE. Such high content of phosphorous and other incompatible trace elements like Zr in melts generated by partial melting in gabbros is in contradiction to predictions for trace element concentration of partial melts derived from trace element modelling applying equilibrium partial melting. The modelling of equilibrium partial melting of our starting gabbro 61a using the bulk P<sub>2</sub>O<sub>5</sub> content (0.01 wt%) and mineral-basaltic melt partition coefficients (olivine: *Anderson and Greenland* [1969]; clinopyroxene: *Brunet and Chazot* [2001]; plagioclase: *Bindeman and Davis* [2000]) reveals a significant lower P<sub>2</sub>O<sub>5</sub> content in the first melts than observed in the melt pools of our partial melting experiment 12a. Calculated P<sub>2</sub>O<sub>5</sub> content for equilibrium partial melting using an equation of [*Hanson*, 1989] for a melt fraction of 0.01 is 0.11 wt%. This value is in strong contrast with the measured values of the two experimentally produced melts in

our microrock experiment 12a which are  $0.3 \pm 0.1$  for the silica-rich and  $11.7 \pm 2.0$  wt% for the iron-rich melt, at an estimated melt fraction of 0.05 (estimated from the BSE images). This rough calculation clearly shows that the enrichment in P (and in other trace elements like Zr, Cl, and REE) in the first anatectic melts cannot be explained by simple equilibrium melting.

A possible explanation for this is that during the very first stage of hydrous partial melting, sub-micron sized phases like apatite, zircon and oxides crystallized on grain boundaries from a late-stage melt in the host gabbro, may be forced into the very first melt and to incorporate their trace element inventory into the melt phase. This results in a significant enrichment of P, Zr, Ti, Fe in the melt, leading to over-saturation (crystallization of apatite or oxides; Figure 41d) or forcing liquid immiscibility due to the presence of enhanced Fe and P concentration. At a higher melt fraction (at higher temperature), the two melts of different compositions pool together forming one coherent melt volume which is still enriched in trace elements during an early stage of pooling, approaching more and more the concentration level of the equilibrium partial melting when the melt fraction increases.

A possible consequence from our findings above is that during fluid-induced partial melting of oceanic gabbro, which are regarded to be low in trace elements like P or Zr, the very first melts may be extremely enriched in such elements, having the potential for significant contamination of primary MORB melts. The amount of such enrichment cannot be predicted, since it depends on the modal amount of interstitial late-stage accessories of the gabbro protolith, which are supposed to enter the melt during the initiation of partial melting. Recent paper on contamination of MORB-derived silica-enriched melts for fast-spreading oceanic ridges refer to equilibrium or fractional partial melting of amphibolitic lithologies in order to explain trace element enriched patterns in the corresponding melts [Haase *et al.*, 2005; Rollinson, 2009; Wanless *et al.*, 2010]. Here, we show that initial disequilibrium hydrous partial melting of oceanic gabbro could also be considered as possible source for MORB contamination.

Interestingly, the effect of a second, P-rich melt was only observed in run 12a, while run 13a (identical conditions) and 13b (identical conditions, except that instead of pure water water + NaCl was added) don't show any sign of liquid immiscibility. So, what is the reason for this spectacular effect? We assume that the presence of P-rich melt in run 12a is due to the presence of accessory late stage minerals in the starting material of run 12a which was not present in that amount in the starting material of run 13a, b. Since each run used different (small) pieces of the same rock, it is very probable, that some pieces may contain more accessories than other. Since beside P, Zr is also enriched in the melt of run 12a, it is very probable that this is due to higher amounts of a late stage mineral assemblage dominated by apatite and zircon in the starting material of run 12a.

### **C.5.3 Details of the hydrous partial melting reaction**

Studies on oceanic gabbros from MAR and SWIR report that hydrous partial melting of oceanic gabbro is a common process during the late stage evolution of oceanic gabbros [Koepke *et al.*, 2005a; 2005b; 2007]. Our microrock experiments allow us to study the

fluid induced partial melting process in detail. Partial melting reaction starts at temperature between 860°C (subsolvus reactions) and 900°C, where  $\mu\text{m}$ -sized melt pools occur within the minerals of the starting material and on grain boundaries have been observed. Below 980°C, new experimental mineral phases are orthopyroxene and amphibole ( $\pm$  Fe-Ti-oxides), which grow exclusively interstitially on grain boundaries associated with mafic minerals (Figure 41f), as well as An-enriched plagioclase which is generally not associated with the new mafic minerals, but crystallize within protolithic plagioclases either as small zones bordering isolated melt pools (Figure 41c, d, and f) or along intracrystalline planes (e.g., twinning plane, cleavages; see Figure 41d). It is remarkable that the incongruent nature of the melting reaction as well as identical textures can be observed in natural oceanic gabbros (see next section).

*Johannes et al.* [1994] studied the kinetics of partial melting reactions using plagioclase single crystals with  $\sim 68$  mol% An as starting material. The partial melting reaction produced Ab-rich melt pools surrounded by new An-rich plagioclase (up to 81 mol% An) showing a characteristic texture. New plagioclase was always formed by crystallographically orientated solution/reprecipitation mechanism. Melting was observed not only at the surface, but also in the interior of the crystals. The melt exhibited plate-like shape with a preferred orientation parallel to the main cleavage. An arrangement of pools of melt along lines was visible. It was assumed that this phenomenon was due to nucleation of melt at dislocations in the crystal and that twin boundaries act as nucleation sites for melts. Often, plates of melt were formed at the albite twin boundaries (parallel to (010)). The new An-rich plagioclase surrounded the melt areas or formed thin plates with a preferred orientation parallel to (010). At the twin boundaries, plates of new plagioclases were found often between melt areas. Identical melting textures within plagioclase grains were produced within this study: rectangular melt pools including seams of An-rich plagioclase are oriented parallel (010) (Figure 41e); planes of new An-rich plagioclase parallel to the albite twin boundaries (Figure 41d).

On the other hand, only at temperatures  $> 980^\circ\text{C}$  larger melt areas have been developed with isolated crystals crystallizing in the melt. New minerals entering the residual phase assemblage are clinopyroxene and olivine crystallizing at the expense of orthopyroxene and amphibole, which were the typical mafic silicates crystallizing interstitially at lower temperature. With the new experimental results obtained in this study we now can redefine the reaction of hydrous partial melting of olivine gabbro formulated by *Koepke et al.* [2004] with respect to temperature:

At  $T \leq 980^\circ\text{C}$ : olivine + clinopyroxene + plagioclase (I) +  $\text{H}_2\text{O} \Rightarrow$  amphibole + orthopyroxene + plagioclase (II) + hydrous plagiogranitic melt

At  $T \geq 980^\circ\text{C}$ : olivine (I) + clinopyroxene (I) + plagioclase (I) +  $\text{H}_2\text{O} \Rightarrow$  olivine (II) + clinopyroxene (II) + plagioclase (II) + hydrous plagiogranitic melt.

It should be mentioned that this reaction is only valid for the system gabbro 61a. Differences in modal proportions and/or compositional shifts to more primitive or more evolved compositions will result in modified reactions. For example, *Koepke et al.* [2004]

showed that the presence or olivine as newly formed phase depends on the starting material.

The two reactions presented above are generalized and based only on silicate phases. In nature, however, accessories may take part in this reaction: on the left side, if accessory late stage minerals are present, like amphibole, apatite, oxides, zircon; and on the right side, if the corresponding melts are saturated with special phases which then have the potential to crystallize in the melt (e.g., apatite, oxide in run 12a).

#### **C.5.4 Application to nature - implication for the late stage evolution of oceanic gabbros**

*Koepke et al.* [2005a] interpreted interstitially grown late-stage mineral assemblages, mainly composed of orthopyroxene and pargasitic amphibole, rimming primary olivines and clinopyroxenes in gabbros from MAR as products of a hydrous partial melting reaction triggered by water-rich fluids (as residual mineral assemblage left back after a partial melting event). This is in contrast to the common model that such phases are the products of crystallization of a late, evolved melt percolating through the nearly frozen gabbroic mush [e.g., *Dick et al.*, 2002]. Key observation for this interpretation was the presence of zones of plagioclase strongly enriched in An on the grain boundaries of the plagioclase, which was identified as residual phase after a partial melting event, triggered by water-rich fluids percolating on grain boundaries. Both observations, combined with the hydrous partial melting experiments of *Koepke et al.* [2004], revealed the integrated model, that both the interstitial growth of mafic minerals and the An-rich zones associated with protolithic plagioclase are parts of a incongruent hydrous partial melting reaction. Our fluid-triggered partial melting experiments performed on microrocks reveal many aspects, which support the model of *Koepke et al.* [2005a; 2005b] as presented in the following.

##### **C.5.4.1 Zone of An-rich plagioclase**

As shown by *Koepke et al.* [2005a; 2005b], the new An-rich plagioclase interpreted as residual phase in the natural gabbros from MAR is strongly depleted in trace elements like Ti and K. This is in disagreement with the crystallization from a late, differentiated melt enriched in Ti and K, which should result in plagioclases with enhanced Ti and K contents. Moreover, it is expected that such evolved melts, in which the Na/Ca ratio is enhanced would not produce plagioclases strongly enriched in An, but rather albite-rich plagioclase. One benefit of the performed microrock experiments is that the observed zones of An-rich plagioclases are large enough to analyse microprobe profiles across zones of new An-rich plagioclase and the protolithic host, well suited for comparison with natural gabbros from MAR investigated by *Koepke et al.* [2005a]. Figure 45 shows such a comparison, revealing a good agreement between the experimental and natural case with extreme low concentrations of Ti and K within the An-enriched zones, implying that the process of formation is similar in both cases. A good agreement between both profiles is also given for iron, which is enriched in the An-rich zones both in our experiment, as well as in the natural example. We interpret the higher iron content in the zones of An-enriched

plagioclase as response of more oxidizing conditions during the reaction [Sugawara, 2000] both in our experiment (performed at prevailing  $fO_2$  corresponding to the NNO buffer) and in nature (oxidizing effect due to water-rich fluids).

We obtained several profiles in the experimental product performed at 940°C which all show a similar pattern as shown in Figure 45. It is implied that these zones are the result of dissolution/precipitation processes, which is indicated by the presence of growth zoning and by the absence of any diffusion-controlled concentration profile. The same is valid for the pairs of An-rich plagioclase and protolithic plagioclase in the natural gabbros Koepke *et al.* [2005a], as well as for the melting experiments of plagioclase single crystals performed by Johannes *et al.* [1994].

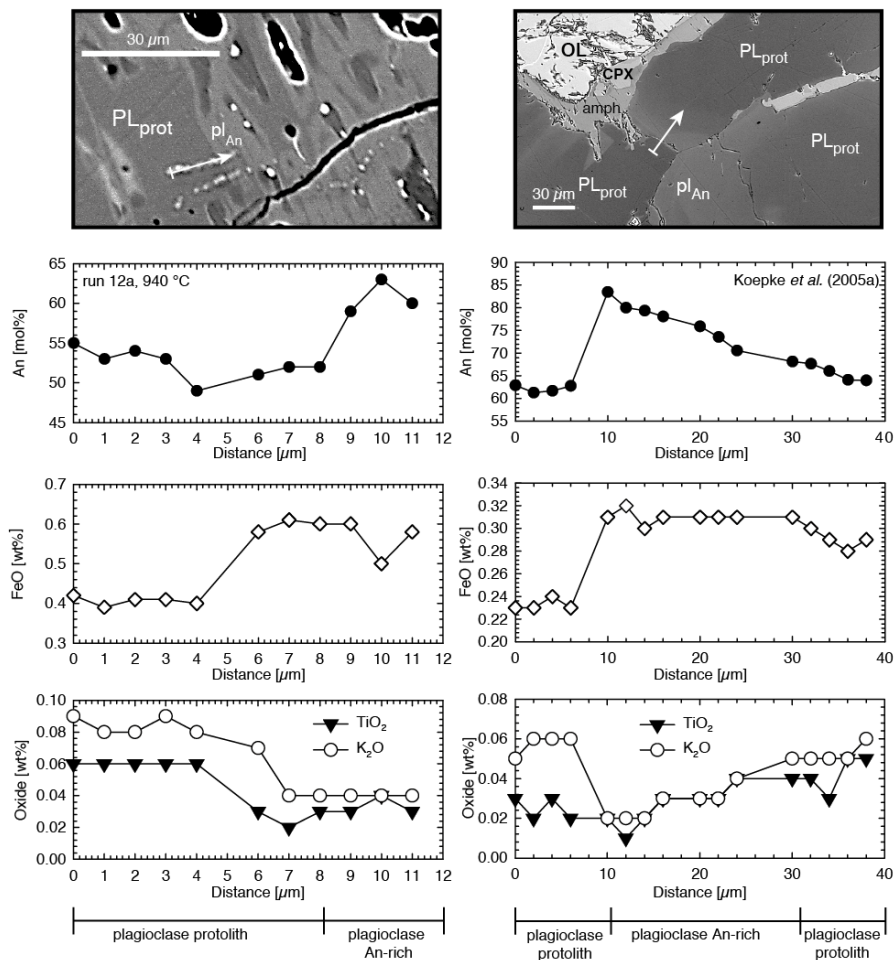


**Figure 45** Element concentration profiles across a newly formed An-rich plagioclase ( $pl_{An}$ ) and the adjacent protolithic plagioclase ( $PL_{prot}$ ) both in an experimental run of a microrock partial melting experiment (left) and in natural gabbro (right). The experimental profile is from the run 12a at 940°C (Figure 41e). Included in the BSE picture is the location of the profile. The element profiles show an increase of An content and FeO and a decrease of  $TiO_2$  and  $K_2O$  in the An-rich plagioclase. For comparison profiles with very similar patterns from a late stage assemblages of a gabbro from MAR drilled by ODP (Leg 153) of Koepke *et al.* [2005a] is shown (sample 153-923A-8R-1, 24–38 cm).



#### C.5.4.2 Consistence in the observed textural details

For a suite of oceanic gabbros from MAR, *Koepke et al.* [2005a] pointed on the incongruent nature of the partial melting reaction, expressed in the record of interstitial growth of mafic phases associated with primary olivine and clinopyroxene, and growth of zones of new An-rich plagioclase within plagioclase clusters (mostly on grain boundaries). Our experiments using microrocks reveal a very similar characteristic as demonstrated in Figure 46b, showing new interstitial amphibole growing around primary clinopyroxene and zones of An-rich plagioclase surrounding rectangular melt pools in the adjacent plagioclase. Very similar textural features are developed in typical late-stage assemblages within an oceanic gabbro from the MAR (Leg 153, Hole 923A drilled by ODP, sample 153-923A-12R-2, 22–45 cm) exhibiting the two “*components*” of the incongruent partial melting reaction: (1) interstitial orthopyroxene and amphibole rimming primary olivine and clinopyroxene (Figure 46a, b) and zones of An-rich plagioclase grown on grain boundaries within plagioclase clusters (only visible with back-scattered electron imaging, Figure 46c). The good concordance between our experimental textures and those from the natural gabbros makes it very likely that the integrated late stage assemblage observed in the oceanic gabbro can be regarded as residual phase assemblage produced by an hydrous partial melting event instead of a product of late-stage crystallization. Another excellent agreement in textural features is presented in Figure 46e and f. The product of a microrock partial melting experiment performed at 940°C (Figure 46e) exhibits a rectangular melt pool within a primary plagioclase crystal, rimmed by a zone of newly formed An-rich plagioclase. Due to the over-saturation of the melt with P<sub>2</sub>O<sub>5</sub>, a small grain of apatite crystallized (see section C.5.2). Exactly the same textural features were observed in a natural oceanic gabbro from the MAR drilled by ODP (Hole 923A drilled by IDOP, sample 153-923A-15R-2, 1–27 cm) as shown in Figure 46f, implying a model that the corresponding melt pool in the natural gabbro was produced in an early phase of hydrous partial melting as part of the incongruent melting reaction proceeded in the plagioclase, and survived as relic (now crystallized to an albite-rich plagioclase) during the cooling of the gabbro.

#### C.5.5 Absence of percolating, highly differentiated melts as source for the precipitation of late-stage silicate minerals in natural gabbros

As mentioned above, rims of ortho- and clinopyroxenes in combination with pargasitic amphibole were commonly interpreted as crystallization products of highly differentiated late-stage melts percolation through the interstices of the cumulate minerals. Based on our experiments and the observations in the ODP Leg 153 gabbros from MAR of *Koepke et al.* [2005a], we present in the following arguments supporting the hypothesis that many of observed interstitial parageneses in the oceanic gabbros of Leg 153 are not formed by a of Mg# in new clinopyroxene and An content of the coexisting new plagioclase rich in An plot in Figure 38 in the top right-hand corner with a trend to very primitive compositions. The same is due for typical late stage assemblages from the Leg 153 MAR gabbros [Table

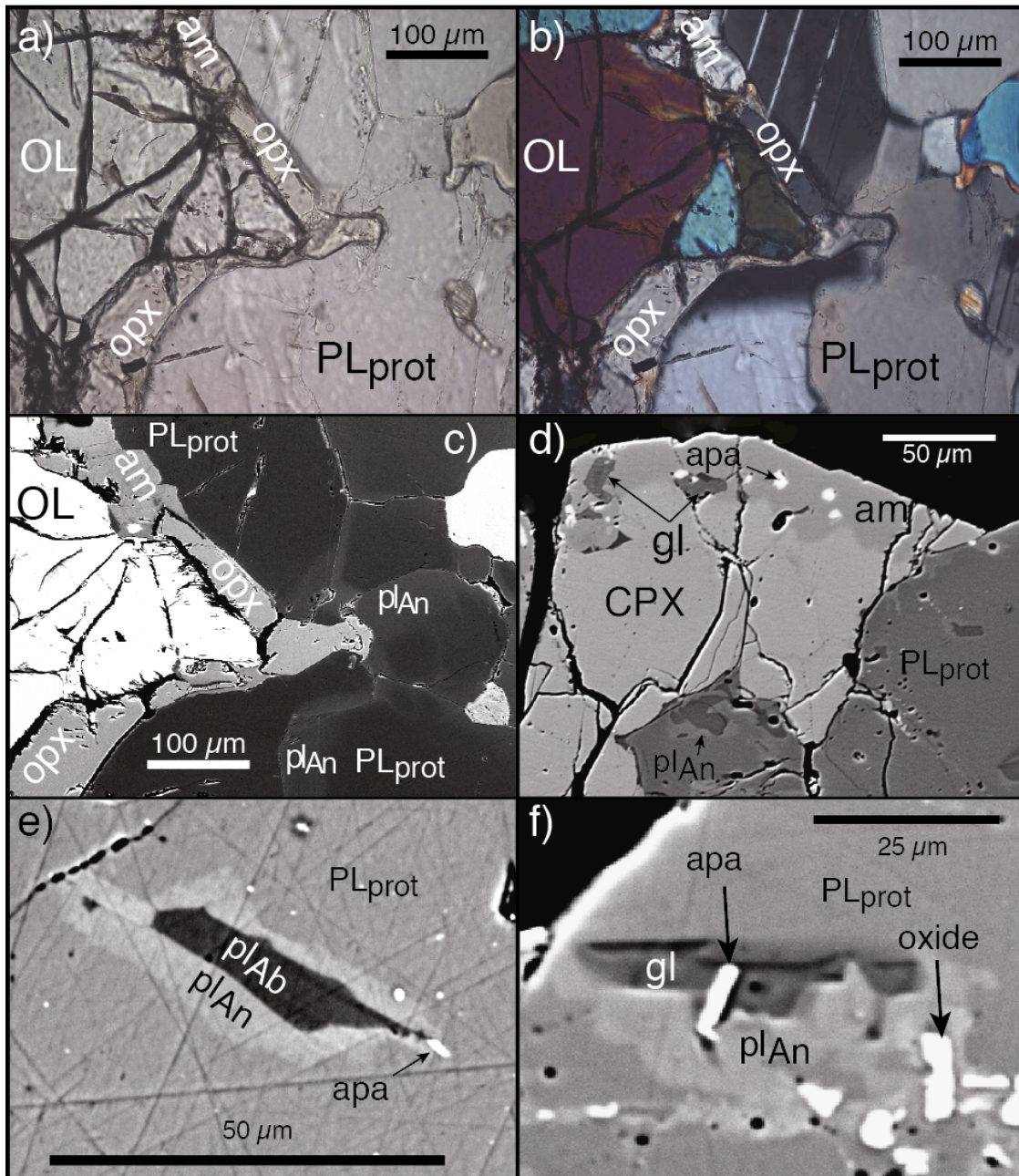


**Figure 46** Comparison between textural details observed in natural oceanic gabbros and in products of our microrock experiments. (a) Microphotograph with plane-polarized light of a natural oceanic gabbro from the MAR drilled by ODP (Leg 153, 153-923A-12R-2, 22–45 cm). Orthopyroxene (opx) and amphibole (am) form an interstitial selvage around olivine (OL) at the contact to plagioclase (PL<sub>prot</sub>). (b) Same sample in cross-polarized light. (c) Same situation recorded as BSE image, displaying zones of An-rich plagioclase (pl<sub>An</sub>) grown on grain boundaries within the primary, protolithic plagioclase PL<sub>prot</sub>. In concordance with our experimental results, the interstitial growth of orthopyroxene and amphibole, together with the formation of An-rich zones within plagioclase, can be interpreted as “disrupted” domains of a incongruent hydrous partial melting reaction of oceanic gabbro. Note that the new, An-rich plagioclase is not visible in the images obtained by optical microscope. (d) BSE picture of experimental run 13b performed at 940°C, showing new interstitial amphibole (am) growing around primary clinopyroxene (CPX) and zones of An-rich plagioclase (pl<sub>An</sub>) surrounding rectangular melt pools in the adjacent plagioclase, demonstrating the incongruent nature of the hydrous partial melting reaction. (e) BSE picture of a gabbro from MAR drilled by ODP (Leg 153, sample 153-923A-15R-2, 1–27 cm). It shows an albite-rich plagioclase (pl<sub>Ab</sub>) interpreted as a former rectangular melt pool surrounded by An-rich plagioclase (pl<sub>An</sub>) within the protolithic plagioclase (PL<sub>prot</sub>). A small needle of apatite (apa) can be observed within albitic plagioclase. This image is a zoom in of the BSE image presented by *Koepke et al.* [2005a] (Figure 41f) (f) BSE image of the experimental run 12a performed at 940°C. Visible is the same situation as shown for the natural rock in (e): Within a protolithic plagioclase (pl<sub>prot</sub>) a rectangular melt pool (gl) bearing a crystal of apatite (apa) is visible, surrounded by An-rich plagioclase (pl<sub>An</sub>).

---

2 in *Koepke et al.*, 2005a] which is not compatible with crystallization from a typical late-stage melt, which should lead to clinopyroxene lower in Mg# and to plagioclase lower in An. Thus, our results fit better with a model that the late-stage interstitial clinopyroxenes rimming primary olivines and clinopyroxenes in natural gabbros can be regarded as residual phases after an proceeded hydrous partial melting process, as the products of the crystallization of a late, differentiated melt.

(2) Evidence against the percolating of highly differentiated melts is provided by experimental work on phase equilibria in hydrous MORB [*Berndt et al.*, 2005; *Feig et al.*, 2006]. The stability of pargasitic/hastingsitic amphibole is restricted to temperatures < 1000°C where the melt shows evolved, SiO<sub>2</sub>-enriched compositions. Thus, the formation of the widespread interstitial pargasite-bearing assemblages in typical oceanic gabbros by precipitation of a suitable late-stage melt would require the presence of significant amounts of evolved residual liquids with plagiogranitic composition (> 60 wt% SiO<sub>2</sub>, *Berndt et al.*, 2005). According to the experimental data of *Berndt et al.* [2005], the fractions of these melts should be significantly higher than ~ 1 %, which is the amount of plagiogranitic veins observed in the gabbroic section of Leg 153 from MAR [*Shipboard Scientific Party*, 1995] or from the gabbros from ODP hole 735B from SWIR [*Dick et al.*, 2000]. On the other hand, *Hart et al.* [1999] for the drill core of hole 735B at SWIR, and *Godard et al.* [2009] for the drill core of hole U1309 at MAR pointed out that the amount of evolved material in these cores derived by macroscopic investigation of the cores was eventually grossly underestimated, suggesting that the amount of leucocratic rocks could be much higher (up to 10 %) [*Hart et al.*, 1999]. But still, the amount of fractionated intermediate and evolved rock necessary for producing must be, according to the experimental study of *Berndt et al.* [2005] much higher than observed in the cores. Another serious complication arises due to those major mineral phases in a potential low-temperature MORB assemblage that coexist with pargasitic amphibole. According to *Berndt et al.* [2005] the residual crystal assemblage at 950°C consists of more than 60 wt% of plagioclase, clinopyroxene, and subordinate olivine. If a percolating late-stage melt is responsible for the precipitation of pargasitic amphibole between the cumulus minerals, then it is to be expected that large amounts of coexisting evolved plagioclase, clinopyroxene, and subordinate olivine would also crystallize interstitially or would overgrow the corresponding primary minerals epitactically producing a marked zoning. Neither of these phenomena are observed in the gabbros of Leg 153.

(3) Further evidence against the percolation model is provided by the absence of any concentration gradients in the outer rims of those olivines surrounded by coronas of pargasite or orthopyroxene in the Leg 153 gabbros. If the rims of protolithic olivine were in contact with a late melt not of equilibrium composition, it is to expect that a crystallization of these melt would produce outer zones of different olivine composition. We carefully searched for systematic zoning effects in those olivines rimmed by orthopyroxene or pargasite in the Leg 153 gabbros, which could be interpreted as results of percolating late-stage melts, but never found that. In contrast, hydrous partial melting involves dissolution/precipitation processes proceeding on grain boundaries triggered by a highly mobile water-rich fluid, very similar to a metamorphic reaction. Due to the reactive progression of this process, it is not to expect that the involved cumulate minerals rimmed by new phases show a significantly zoning, if the duration of the partial melting reaction is

---

short. In the corresponding "*microrock*" experiments performed at 940°C with a run duration of 168 hours, we produced up to several 100 µm thick zones of new pargasite and/or orthopyroxene, without any observable zoning in the involved primary olivines.

In summary, it seems not very probable that the formation of interstitial pargasite, ortho- and clinopyroxene rimming olivine and pyroxene in the ODP Leg 153 gabbros is the product of fractional crystallization of a highly differentiated MORB source. Instead, phase relations, phase compositions and textural features obtained by hydrous partial melting of gabbroic microrocks reveal, that these, together with the formation of An-rich zones within plagioclase, can be regarded as residual mafic phases formed during a fluid-triggered partial melting process.

## C.6 Conclusions

We simulated experimentally the fluid-induced partial melting of natural oceanic gabbro using small pieces (microrocks) of a typical olivine gabbro from the SWIR in order to shed light on compositional and textural details of the partial melting reaction, as it proceeds in the deep oceanic crust under the ridges triggered by fluid/rock interactions at very high temperatures. From the results of our experiments we draw the following conclusions:

- The hydrous partial melting of oceanic gabbro is a highly incongruent reaction resulting at temperatures < 980°C in the formation of interstitial orthopyroxene and amphibole rimming primary olivine and clinopyroxene, and of zones of An-rich plagioclase growing within plagioclase.
  - Despite the large grain size of our starting material, which prevents the achievement of global equilibrium in our experiments, the obtained phase relations and compositions are in good agreement with the results of the corresponding equilibrium experiments in the identical gabbroic system.
  - First melts produced by hydrous partial melting of oceanic gabbro may be extremely enriched in trace elements, having the potential for significant contamination of primary MORB melts. The amount of such enrichment cannot be predicted, since it depends on the modal amount of interstitial late-stage accessories of the gabbro protolith, which are supposed to enter the melt during the initiation of partial melting.
  - With the new experimental results obtained in this study we can redefine the general reaction of partial melting of olivine gabbro with respect to temperature: Below 980°C, amphibole and orthopyroxene are the newly formed mafic minerals (+ An-rich plagioclase and a hydrous plagiogranitic melt). On the other hand, above 980°C the newly formed minerals are clinopyroxene and olivine with different compositions than the phases in the starting gabbro (+ An-rich plagioclase and a hydrous plagiogranitic melt). Thus the residual paragenesis after a hydrous partial melting event above 980°C is again olivine gabbro, but more depleted in mineral compositions.
  - Textural features and compositional characteristics obtained in our partial melting experiments on microrock are in good agreement corresponding features of late-
-

stage assemblages of many natural oceanic gabbros from MAR (drilled by ODP Leg 153), implying that many of the natural late-stage parageneses can be better explained as residual phases left back after a hydrous partial melting than by crystallization of a late evolved percolating melt.

---

# Chapter D

## Implications for the hydrothermal circulation in the lower oceanic crust at fast-spreading ridges

The two chapters presented above provide new insights into the complexity and broad temperature range of a hydrothermal system operating in lower crustal gabbroic rocks of the Semail ophiolite. The most important are:

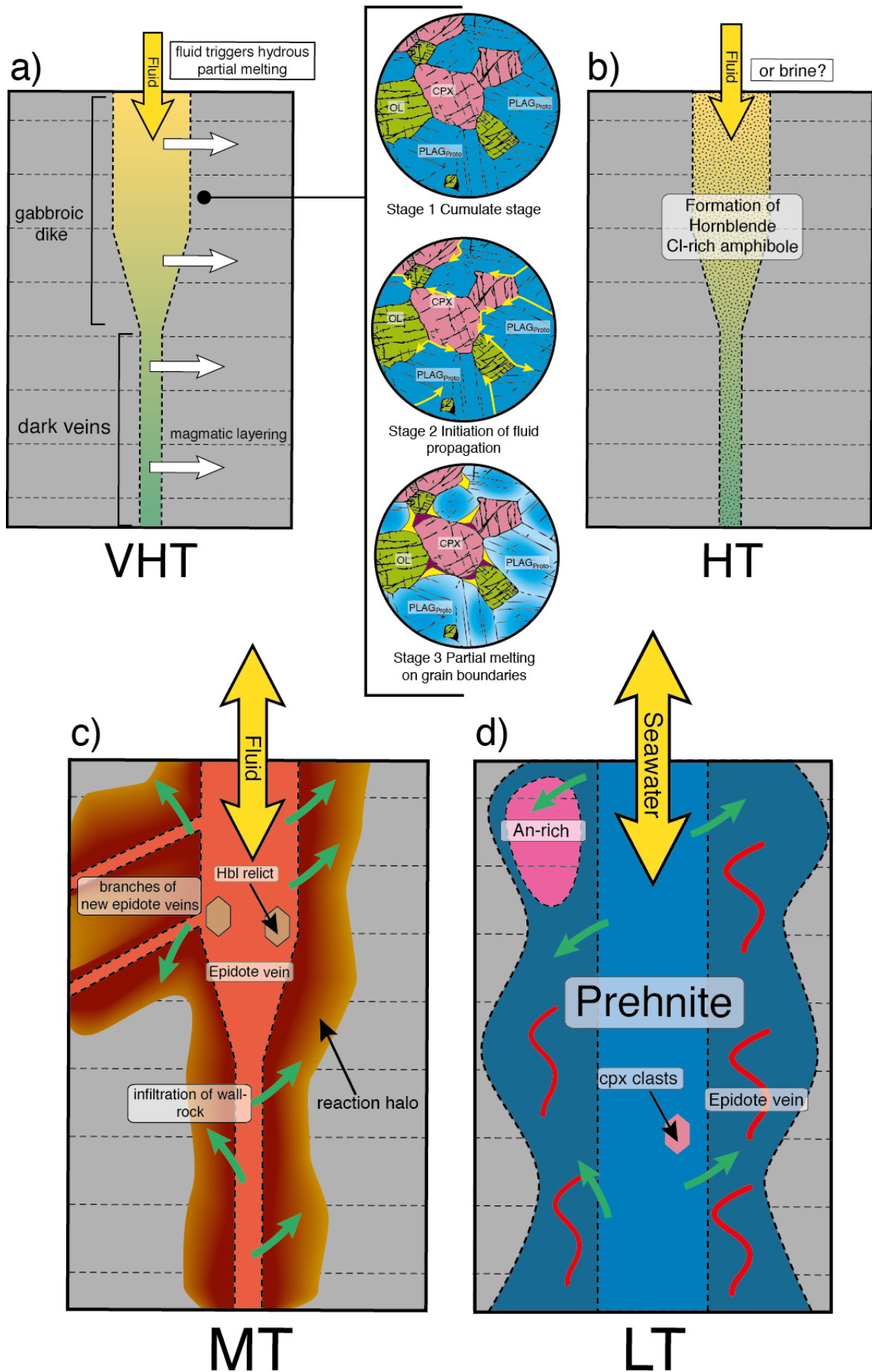
- Hydrothermal activity starts at temperatures  $>900^{\circ}\text{C}$  with a hydrous partial melting forming dikes and veins with characteristic residual mineral assemblages.
- The formation of the dike and vein system at very high temperatures develops pathway for hydrothermal fluid penetrating in the lower crust operating from  $1000^{\circ}\text{C}$  to  $<250^{\circ}\text{C}$ . As temperature decreases,  $W/R$  ratios increase and fluid/rock interactions lead to a complex veining system involving the surrounding host rock. This leads to relatively broad zones within the layered gabbro influenced by hydrothermal alteration at high fluid flux.

Especially, the maximum temperature recorded in this study indicates that fluid/rock interactions starts well above the solidus of a wet gabbro (estimated as  $\sim 870^{\circ}\text{C}$ ) [Beard and Lofgren, 1991; Koepke *et al.*, 2004] with the consequence that water/rock interaction triggers a hydrous partial melting of the host gabbro. Consequently, the melting consumes latent heat, an aspect so far not considered in any thermal modelling for oceanic crust. Up to now, typical hydrothermal veins in gabbros were considered to form under amphibolite facies [e.g., Manning *et al.*, 1996; 2000], at temperatures generally lower as the peak temperatures estimated here. Additionally, the lowest temperatures recorded in this study imply that the lower oceanic crust is also affected by low temperature hydrothermal alterations at high fluid fluxes. There are only a few studies, which show the coherently

broad range of hydrothermal alteration in lower crustal section, mostly obtained from the Semail ophiolite [e.g., *Nehlig and Juteau*, 1988]. The presented study is one of the first so far that shows a continuous profile through all temperature stages possibly operating in the lower gabbroic section. The detailed petrographic and geochemical results allow describing the specific mineral assemblages and reactions related to the different stages of hydrothermal alteration. However, further investigations, such as thermodynamically modelling of mineral stability, analysis of fluid inclusions, or hydrothermal experiments, are necessary to completely understand the highly complex veining system and all related reactions. Another key observation of this study is that the same pathways were used for hydrothermal fluids from very high to low temperatures, another aspect so far not been considered to occur in submarine hydrothermal systems. Thus, this study can be regarded as starting point for further research on the hydrothermal circulation in the lower oceanic crust.

A strong weakness of this study, which makes it difficult applying the results to modern fast-spreading ridges, is that the observations were only done on a narrow spatial area. The Wadi Wariyah outcrop only provides a very small slice of lower crustal gabbros and more studies of comparable approaches from other locations in the Semail ophiolite must be obtained. Studies of the hydrothermal record in lower gabbros of the Semail and other ophiolites is necessary, because ophiolites still remain the primary source to study hydrothermal processes of the lower oceanic crust. If the here presented results can be directly applied to modern fast-spreading ocean ridges they provide new findings for a better understanding of submarine hydrothermal systems operating in the lower oceanic crust and for the cooling history of the crust. Due to the lack of comparable results, it is difficult to apply the findings presented above to modern fast-spreading ocean ridges. The only relevant coherent alteration profile, reaching deeper parts of the crust (sheeted dike transition zone) was obtained from the IODP drilling site 1256D in 15 Ma old EPR crust [*Alt et al.*, 2010]. This study shows that the gabbro directly below the sheeted dikes are affected by hydrothermal alteration temperatures of 200-840°C, which are significant lower compared to the peak temperatures estimated here and in other studies from the Semail ophiolite [*Bosch et al.*, 2004; *Nicolas and Mainprice*, 2005]. The minimum temperature estimated in this study seems to be similar. The combined observations of the imprint of hydrothermal alteration in the lower crustal section from the Wadi Wariyah suggest the following model for hydrothermal alteration operating in the lower oceanic crust, which is also illustrated in Figure 47:

In a first accumulation stage, the primary constituent minerals of primitive olivine gabbro cumulate forms within the axial magma chamber, which in the following cools down to subsolidus conditions. At very high temperatures the hydrothermal imprint starts with the development of a microcrack system [*Nicolas and Mainprice*, 2005], which is orientated perpendicular to the lithospheric stress field at the spreading centre [*Mével and Cannat*, 1991]. This process can be regarded as the first record of hydrothermal imprint within a deep oceanic gabbro starting at temperatures as high as 1000°C and very low *W/R* ratios. Hydrothermal fluids trigger a hydrous partial melting reaction within the gabbro leaving behind a complex mineral assemblage of residual phases of the hydrous partial melting reaction (e.g., plagioclase high in An, clinopyroxene high in Mg#, pargasite) and phases





- ◀ **Figure 47.** Schematic sketch showing the reactions related to the imprint of hydrothermal circulation within the lower crustal section of the Wadi Wariyah operating at different temperatures. (a) First imprint of hydrothermal at very high temperatures. Hydrothermal fluids (yellow arrow, the size of the arrow in the following indicates increasing fluid flux) trigger a hydrous partial melting within the layered gabbro (grey; dashed lines indicate magmatic layering). This is recorded by the formation of gabbroic dikes and dark veins with characteristic residual phases. The white arrows indicate that fluids percolating along grain boundaries initiating an incongruent partial melting reaction in the layered gabbro adjacent to the dikes and veins: *Stage 1*: Formation of the primitive mineral cumulate composed of olivine (Ol), plagioclase (Plag<sub>Proto</sub>), and clinopyroxene (Cpx). *Stage 2*: At temperature of c. 900°C fluids percolating along grain boundaries (yellow arrows) initiating the incongruent hydrous partial melting reaction. *Stage 3*: Advancing of the hydrous partial melting reaction. At plagioclase/plagioclase grain boundaries, zones of An-rich plagioclase are formed (light blue rims). When the hydrous partial melting involves the mafic mineral, interstitial pargasite (yellow) and orthopyroxene (purple) are formed. (b) Hydrothermal alteration at high temperatures. The hydrothermal fluids use the same pathways developed during the very high temperature stage. The primary mafic minerals are replaced by mostly hornblende. The occurrence of amphibole extremely enriched in Cl indicates the presence of high saline brine. (c) Progress of hydrothermal alteration at medium temperatures. During this stage epidote precipitates from hydrothermal fluids. The green arrows indicate that high fluid flux causes infiltration of the wall rock by hydrothermal fluids forming a complex reaction zone. Hornblende relics indicate that same pathways were used for the medium temperature hydrothermal alteration. (d) Hydrothermal alteration at low temperature and high fluid fluxes by seawater. Progress of hydrothermal alteration forms cm-thick vein composed of prehnite. These veins are surrounded by a highly altered gabbro. Occurrence of epidote vein and An-bearing metagabbro (An-rich) indicate previous medium to high temperature hydrothermal stages. Clinopyroxene clasts indicate tectonic forces during formation of the prehnite veins.

crystallizing from the produced melt (e.g., plagioclase low in An). The combined process of microcracking and hydrous partial melting forms the dikes and veins. In a simultaneously stage, the first imprint of hydrothermal activity starts in the rock adjacent to the dikes and veins by water-rich fluids percolating along grain boundaries initiating an incongruent hydrous partial melting reaction at the edges of the primary minerals (according to the reaction mechanisms presented by *Koepke et al.* [2014 in press] and *Wolff et al.* [2013]). This process produces an albite-rich melt and An-rich residual phases highly enriched in the An component and depleted in trace element, which is now visible as An-rich zones decorating the plagioclase/plagioclase grain boundaries. As the hydrous partial melting reaction advances, the mafic phases (olivine and clinopyroxene) are involved. Interstitial orthopyroxene and pargasitic amphiboles are produced, especially at location where the plagioclase/plagioclase boundaries are in contact with primary olivine and clinopyroxene.

In the next step hydrothermal fluids use the same pathways developed at very high temperature to progressively metamorphose the residual phases. This process produces replacement of the mafic minerals by phases typical for amphibolite facies (e.g., hornblende). Some of the primary mafic phases (e.g., clinopyroxene, pargasite) remain as relics recording the previous formation under very high temperatures. During this stage phase separation of the fluid occurs recorded by amphiboles extremely enriched in Cl. The brine may have possible formed by phase separation with or without subsequent separation of a seawater-derived low salinity fluid or a vapour. Isotopic analyses of the Cl-rich amphiboles are suggested to shed more light on the precise formation of those amphiboles and possible information about fluid composition during that stage of hydrothermal alteration.

As temperature decreases to medium condition (300-500°C) the fluid flux increases and CaAl-rich phases, mainly clinozoisite, form most possible due to the hydrothermally breakdown of An-rich plagioclase. Relics of the previous high temperature stage and

characteristic enriched REE patterns of some epidote veins indicate that primarily the pathways of the very high and high temperature stage were used for hydrothermal alteration. Additionally, new veins form as branch connections from the previous high temperature vein system, possible due to water being in excess or changes in the lithospheric stress field. These veins show the same mineralogy, but are significant lower in trace elements. One question still remain unanswered is if these epidote veins have also seen a previous stage of higher temperature hydrothermal alteration than recorded. Hydrothermal alteration causes a shift in isotopic composition towards to low  $\delta^{18}\text{O}$  and enriched  $^{87}\text{Sr}/^{86}\text{Sr}$  ratios similar to epidote composition from modern oceanic crust [e.g., *Alt et al.*, 2010]. One additionally feature of the medium temperature stage is the change of the hydrothermal system from a veining to a more complex system involving the wall rock. Reaction halos composed of typical minerals of the greenschists facies indicate that the high fluid flux within the vein initiate infiltration of the fluid in the wall rock. The water/rock interaction in the wall rock leads to replacement of the primary magmatic minerals by minerals for the greenschists. Higher  $^{87}\text{Sr}/^{86}\text{Sr}$  isotopic recorded in the reaction zone compared to the vein suggest long period of fluid infiltration long before the vein was sealed by epidote precipitation.

In a last stage of hydrothermal alteration, at low temperatures (>250-300°C) massive seawater/rock interactions at occur, possible as the crust drifts away from the spreading centre, forming thick prehnite veins. These veins are formed in a broad zone of highly metamorphosed wall rock high fluid fluxes in broad zones of the deep gabbroic section. Clasts of the primary host rock within the vein system indicate cataclastic deformation of the crust during low temperature hydrothermal alteration. Prehnite has been recently observed in deep gabbros from IODP site U1415 at Hess Deep [*Gillis et al.*, 2014 in press] and in the upper sections of site 1256D at the EPR [*Alt et al.*, 2010] suggesting that the formation of prehnite is a common process during low temperature hydrothermal alteration of gabbroic rocks. The seawater/rock interactions causes shift to high  $\delta^{18}\text{O}$  and very high  $^{87}\text{Sr}/^{86}\text{Sr}$  ratios. Relics of the medium and the high temperature (An-bearing metagabbro) indicate these low temperature hydrothermal alteration uses the same pathways at a very high fluid which mostly extinguish the record of very high temperature hydrothermal alteration.

---

# References

- Abily, B., G. Ceuleneer, and P. Launeau (2011), Synmagmatic normal faulting in the lower oceanic crust: Evidence from the Oman ophiolite, *Geology*, *39*, 391-394.
- Ague, J. J. (1997), Compositional variations in metamorphosed sediments of the Littleton Formation, New Hampshire (Discussion), *Am J Sci*, *297*(4), 440-449.
- Alabaster, T., J. A. Pearce, and J. Malpas (1982), The volcanic stratigraphy and petrogenesis of the Oman ophiolite complex, *Contrib Mineral Petr*, *81*(3), 168-183.
- Albarède, F., and A. Provost (1977), Petrological and geochemical mass-balance equations: an algorithm for least-square fitting and general error analysis, *Comput Geosci*, *3*(2), 309-326.
- Alt, J. C. (1995), Subseafloor Processes in Mid-Ocean Ridge Hydrothermal Systems, *Geophysical Monographs*, *91*, 85-114.
- Alt, J. C., and W. Bach (2008), Alteration of Oceanic Crust, in *Energy and Mass Transfer in Marine Hydrothermal Systems*, edited by P. Halbach, V. Tunnicliffe and J. R. Hein, pp. 7-24, Dahlem Univ. Press, Berlin.
- Alt, J. C., C. Laverne, R. M. Coggon, D. A. H. Teagle, N. R. Banerjee, S. Morgan, C. E. Smith-Duque, M. Harris, and L. Galli (2010), Subsurface structure of a submarine hydrothermal system in ocean crust formed at the East Pacific Rise, ODP/IODP Site 1256, *Geochem Geophys Geosy*, *11*(10), 1-28.
- Amri, I., M. Benoit, and G. Ceuleneer (1996), Tectonic setting for the genesis of oceanic plagiogranites: evidence from a paleo-spreading structure in the Oman ophiolite, *Earth Planet Sc Lett*, *139*(1), 177-194.
- Andersen, D. J., D. H. Lindsley, and P. M. Davidson (1993), QUILF: A pascal program to assess equilibria among Fe-Mg-Mn-Ti oxides, pyroxenes, olivine, and quartz, *Comput Geosci*, *19*(9), 1333-1350.
- Anderson, A. T. (1980), Significance of hornblende in calc-alkaline andesites and basalts, *Am Mineral*, *65*, 837-851.
- Anderson, A. T., and L. P. Greenland (1969), Phosphorus fractionation diagram as a quantitative indicator of crystallization differentiation of basaltic liquids, *Geochi Cosmochim Ac*, *33*(4), 493-505.
- Apted, M. J., and J. G. Liou (1983), Phase relations among greenschist, epidote-amphibolite, and amphibolite in a basaltic system, *Am J Sci*, *283*, 328-354.
- Armbruster, T., et al. (2006), Recommended nomenclature of epidote-group minerals, *Eur J Mineral*, *18*, 551-567.
- Barker, F. (1979), *Trondhjemites, dacites, and related rocks*, 659 pp, Elsevier Scientific Pub. Co. ; New York: distributors for the U.S.A. and Canada, Elsevier/North-Holland, New York; Amsterdam.
- Bau, M. (1991), Rare-earth element mobility during hydrothermal and metamorphic fluid-rock interaction and the significance of the oxidation state of europium, *Chem Geol*, *93*, 219-230.
- Beard, J. S., and G. Lofgren (1991), Dehydration Melting and Water-Saturated Melting of Basaltic and Andesitic Greenstones and Amphibolites at 1, 3, and 6.9 kb, *J Petrol*, *32*(2), 365-401.
- Bédard, J. (2006a), A catalytic delamination-driven model for coupled genesis of Archaean crust and sub-continental lithospheric mantle, *Geochi Cosmochim Ac*, *70*(5), 1188-1214.
- Bédard, J. (2006b), Trace element partitioning in plagioclase feldspar, *Geochi Cosmochim Ac*, *70*(14), 3717-3742.
- Bédard, J. H., R. S. J. Sparks, R. Renner, M. J. Cheadle, and M. A. Hallworth (1988), Peridotite sills and metasomatic gabbros in the Eastern Layered Series of the Rhum complex, *J Geol Soc London*, *145*(2), 207-224.
- Berndt, J., J. Koepke, and F. Holtz (2005), An experimental investigation of the influence of water and oxygen fugacity on differentiation of MORB at 200 MPa, *J Petrol*, *1*, 135-167.
- Berndt, J., C. Lieske, F. Holtz, M. Freise, M. Nowak, D. Ziegenbein, W. Hurkuck, and J. Koepke (2002), A combined rapid-quench and H<sub>2</sub>-membrane setup for internally heated pressure vessels: Description and application for water solubility in basaltic melts, *Am Mineral*, *87*(11-12), 1717-1726.
- Berndt, M. E., W. E. Seyfried, and D. R. Janecky (1989), Plagioclase and epidote buffering of cation ratios in mid-ocean ridge hydrothermal fluids: Experimental results in and near the supercritical region, *Geochi Cosmochim Ac*, *53*, 2283-2300.
- Bickle, M. J., and D. A. H. Teagle (1992), Strontium alteration in the Troodos ophiolite: implications for fluid fluxes and geochemical transport in mid-ocean ridge hydrothermal systems, *Earth Planet Sc Lett*, *113*(1-2), 219-237.
- Bindeman, I., and A. M. Davis (2000), Trace element partitioning between plagioclase and melt: investigation of dopant influence on partition behavior, *Geochi Cosmochim Ac*, *64*(16), 2863-2878.
- Bosch, D., M. Jamais, F. Boudier, and A. Nicolas (2004), Deep and High-temperature Hydrothermal Circulation in the Oman Ophiolite ---- Petrological and Isotopic Evidence, *J Petrol*, *45*(6), 1181-1208.
- Botcharnikov, R. E., H. Behrens, and F. Holtz (2006), Solubility and speciation of C-O-H fluids in andesitic melt at T=1100-1300°C and P=200 and 500MPa, *Chem Geol*, *229*(1-3), 125-143.
- Botcharnikov, R. E., J. Koepke, F. Holtz, C. McCammon, and M. Wilke (2005), The effect of water activity on the oxidation and structural state of Fe in a ferro-basaltic melt, *Geochi Cosmochim Ac*, *69*(21), 5071-5085.
- Boudier, F., and A. Nicolas (1985), Harzburgite and lherzolite subtypes in ophiolitic and oceanic environments, *Earth Planet Sc Lett*, *76*, 84-92.
- Boudier, F., and A. Nicolas (2007), Comment on "dating the geologic history of Oman's Semail ophiolite: insights from

- U–Pb geochronology” by CJ Warren, RR Parrish, DJ Waters and MP Searle, *Contrib Mineral Petr*, 154, 111-113.
- Boudier, F., A. Nicolas, and B. Ildefonse (1996), Magma chambers in the Oman ophiolite: Fed from the top and the bottom, *Earth Planet Sc Lett*, 144, 239-250.
- Brophy, J. G. (2008), A study of rare earth element (REE)–SiO<sub>2</sub> variations in felsic liquids generated by basalt fractionation and amphibolite melting: a potential test for discriminating between the two different processes, *Contrib Mineral Petr*, 156, 337-357.
- Brophy, J. G., and X. Pu (2012), Rare earth element–SiO<sub>2</sub> systematics of mid-ocean ridge plagiogranites and host gabbros from the Fournier oceanic fragment, New Brunswick, Canada: a field evaluation of some model predictions, *Contrib Mineral Petr*, 164(2), 191-204.
- Browning, P. (1980), Cryptic variation within the Cumulate Sequence of the Oman ophiolite: magma chamber depth and petrological implications, *Geological Society London Special Publications*, 13, 71-82.
- Browning, P. (1982), The petrology, geochemistry, and structure of the plutonic rocks of the Oman Ophiolite, PhD Thesis, Open University, 1-431.
- Brunet, F., and G. Chazot (2001), Partitioning of phosphorus between olivine, clinopyroxene and silicate glass in a spinel lherzolite xenolith from Yemen, *Chem Geol*, 176(1-4), 51-72.
- Brunsmann, A., G. Franz, and W. Heinrich (2002), Experimental investigation of zoisite–clinozoisite phase equilibria in the system CaO–Fe<sub>2</sub>O<sub>3</sub>–Al<sub>2</sub>O<sub>3</sub>–SiO<sub>2</sub>–H<sub>2</sub>O - Springer, *Contrib Mineral Petr*, 143, 115-130.
- Bucher, K., and M. Frey (2002), *Petrogenesis of metamorphic rock*, 318 pp, Springer, Heidelberg, New York.
- Buddington, A., and D. Lindsley (1964), Iron-Titanium Oxide Minerals and Synthetic Equivalents, *J Petrol*, 5(2), 310-357.
- Burke, W., R. Denison, and E. Hetherington (1982), Variation of seawater <sup>87</sup>Sr/<sup>86</sup>Sr throughout Phanerozoic time, *Geol Soc Am Bull*, 10(10), 516-519.
- Burns, L. E. (1985), The Border Ranges ultramafic and mafic complex, south-central Alaska: cumulate fractionates of island-arc volcanics, *Canadian Journal of Earth Sciences*, 22(7), 1020-1038.
- Canales, J., R. Detrick, D. R. Toomey, and W. Wilcock (2003), Segment-scale variations in the crustal structure of 150-300 kyr old fast spreading oceanic crust (East Pacific Rise, 8° 15'N - 10°5'N) from wide-angle seismic refraction profiles, *Geophysical Journal International*, 152, 766-794.
- Charlier, B., O. Namur, M. J. Toplis, P. Schiano, N. Cluzel, M. Higgins, and J. Auwera (2011), Large-scale silicate liquid immiscibility during differentiation of tholeiitic basalt to granite and the origin of the Daly gap, *Geology*, 39(10), 907-910.
- Chen, Y. J. (2001), Thermal effects of gabbro accretion from a deeper second melt lens at the fast spreading East Pacific Rise, *J Geophys Res*, 106(B5), 8581-8588.
- Cherkaoui, A. S. M., W. Wilcock, R. A. Dunn, and D. R. Toomey (2003), A numerical model of hydrothermal cooling and crustal accretion at a fast spreading mid-ocean ridge, *Geochem Geophys Geosy*, 4(9).
- Coleman, R. G. (1977), What is an Ophiolite?, in *Ophiolites*, edited by W. von Engelhardt and T. Hahn, pp. 1-7, Springer, Berlin-Heidelberg.
- Coogan, L. A. (2007), The Lower Oceanic Crust, in *Treatise on Geochemistry*, edited by H. D. Holland and K. K. Turekian, pp. 1-37, Elsevier-Pergamon, Oxford.
- Coogan, L. A. (2009), Altered oceanic crust as an inorganic record of paleoseawater Sr concentration, *Geochem Geophys Geosy*, 10(4), 1-11.
- Coogan, L. A., R. N. Wilson, and K. M. Gillis (2001a), Near-solidus evolution of oceanic gabbros: insights from amphibole geochemistry, *Geochi Cosmochim Acta*, 65(23), 4339-4357.
- Coogan, L. A., G. R. T. Jenkin, and R. N. Wilson (2002a), Constraining the cooling rate of the lower oceanic crust: a new approach applied to the Oman ophiolite, *Earth Planet Sc Lett*, 199(1-2), 127-146.
- Coogan, L. A., G. M. Thompson, and C. J. MacLeod (2002b), A textural and geochemical investigation of high level gabbros from the Oman ophiolite: implications for the role of the axial magma chamber at fast-spreading ridges, *Lithos*, 63, 67-82.
- Coogan, L. A., N. C. Mitchell, and M. J. O'Hara (2003), Roof assimilation at fast spreading ridges: An investigation combining geophysical, geochemical, and field evidence, *J Geophys Res*, 108(B1), 2002, doi:10.1029/2001JB001171..
- Coogan, L. A., K. Howard, and K. M. Gillis (2006), Chemical and thermal constraints on focussed fluid flow in the lower oceanic crust, *Am J Sci*, 306, 389-427.
- Coogan, L. A., C. MacLeod, H. J. B. Dick, and S. Edwards (2001b), Whole-rock geochemistry of gabbros from the Southwest Indian Ridge: constraints on geochemical fractionations between the upper and lower oceanic crust and magma chamber processes at (very) slow-spreading ridges, *Chem Geol*, 178, 1-22.
- Coogan, L. A., K. M. Gillis, C. J. MacLeod, G. M. Thompson, and R. Hékinian (2002c), Petrology and geochemistry of the lower oceanic crust formed at the East Pacific Rise and exposed at Hess Deep: A synthesis and new results, *Geochem Geophys Geosy*, 3(11), 1-30.
- Corliss, J. B., J. Dymond, L. I. Gordon, and J. M. Edmond (1979), Submarine thermal springs on the Galapagos Rift, *Science*, 203, 1073-1083.
- Cortesogno, L., L. Gaggero, and A. Zanetti (2000), Rare earth and trace elements in igneous and high-temperature metamorphic minerals of oceanic gabbros (MARK area, Mid-Atlantic Ridge), *Contrib Mineral Petr*, 139, 373-393.
- de Hoog, J., P. Mason, and M. van Bergen (2001), Sulfur and chalcophile elements in subduction zones: constraints from a laser ablation ICP-MS study of melt inclusions from Galunggung Volcano, Indonesia, *Geochi Cosmochim Acta*, 65(18), 3147-3164.
- Deer, W. A., R. A. Howie, and J. Zussman (1992), *An introduction to the rock-forming minerals*, 2nd edition ed., Pearson Education Limited, Essex.
- Deer, W. A., R. A. Howie, and J. Zussman (1997), *Rock-forming minerals. 2B. Double-chain silicates*, Geological Society.
- Devine, J. D., J. E. Gardner, H. P. Brack, G. D. Layne, and M. J. Rutherford (1995), Comparison of microanalytical methods for estimating H<sub>2</sub>O contents of silicic volcanic glasses, *Am Mineral*, 80(3), 319-328.
- Dick, H. J. B., P. S. Meyer, S. H. Bloomer, S. Kirby, D. Stakes, and C. Mawer (1991), 26. Lithostratigraphic evolution of an in-situ section of oceanic Layer 3, edited by R. P. Von Herzen and P.T Robinson, *Proc ODP, Sci Results*, 18, pp. 439-538
- Dick, H. J. B., et al. (2002), 10. Primary Silicate Mineral Chemistry Of A 1.5-KM Section Of Very Slow Spreading Lower Ocean Crust: ODP Hole 735B, Southwest Indian Ridge, in edited by J. H. Natland, H. J. B. Dick, D. J. Miller and R. P. Von Herzen, *Proc ODP, Sci Results*, 176, pp. 1-61, Online.
- Dick, H. J. B., et al. (2000), A long in situ section of the lower ocean crust: results of ODP Leg 176 drilling at the Southwest Indian Ridge, *Earth Planet Sc Lett*, 179(1), 31-51.
- Dilek, Y., and H. Furnes (2011), Ophiolite genesis and global tectonics: Geochemical and tectonic fingerprinting of ancient oceanic lithosphere, *Geol Soc Am Bull*, 123(3-4), 387-411.
- Dixon, S., and M. Rutherford (1979), Plagiogranites as late-stage immiscible liquids in ophiolite and mid-ocean ridge suites: an experimental study, *Earth Planet Sc Lett*, 45(1), 45-60.
- Driesner, T., and C. Heinrich (2007), The system H<sub>2</sub>O–NaCl. Part I: Correlation formulae for phase relations in temperature–pressure–composition space from 0 to 1000°C, 0 to 5000bar, and 0 to 1 XNaCl, *Geochi Cosmochim Acta*, 71(20), 4880-4901.
- Dziony, W., I. Horn, D. Lattard, J. Koepke, and G. Steinhöfel (2013), In-situ Fe isotope ratio determination in Fe-Ti oxides and sulfides from drilled gabbros and basalt from the

- IODP Hole 1256D in the eastern equatorial Pacific, *Chem Geol.*, accepted manuscript.
- Ernewein, M., C. Pflumio, and H. Whitechurch (1988), The death of an accretion zone as evidenced by the magmatic history of the Sumail ophiolite (Oman), *Tectonophysics*, 151(1-4), 247-274.
- Ernst, W. G., and J. Liu (1998), Experimental phase-equilibrium study of Al- and Ti-contents of calcic amphibole in MORB—A semiquantitative thermobarometer, *Am Mineral*, 83, 952-969.
- Faure, G. (1977), *Principles of isotope geology* 2nd Edition ed., John Wiley & Sons, New York.
- Feig, S. T., J. Koepke, and J. E. Snow (2006), Effect of water on tholeiitic basalt phase equilibria: an experimental study under oxidizing conditions, *Contrib Mineral Petr*, 152, 611-638.
- Flagler, P., and J. G. Spray (1991), Generation of plagiogranite by amphibolite anatexis in oceanic shear zones, *Geology*, 19(1), 70-73.
- France, L., B. Ildefonse, and J. Koepke (2009), Interactions between magma and hydrothermal system in Oman ophiolite and in IODP Hole 1256D: Fossilization of a dynamic melt lens at fast spreading ridges, *Geochem Geophys Geosy*, 10, 1-30.
- France, L., J. Koepke, B. Ildefonse, and S. Cichy (2010), Hydrous partial melting in the sheeted dike complex at fast spreading ridges: experimental and natural observations, *Contrib Mineral Petr*, 106(5), 683-704.
- Frey, M., C. D. Capitani, and J. G. Liou (1991), A new petrogenetic grid for low-grade metabasites, *J Metamorph Geol*, 9(4), 497-509.
- Frost, B. R., J. S. Beard, A. M. McCaig, and E. Condliffe (2008), The Formation of Micro-Rodingites from IODP Hole U1309D: Key To Understanding the Process of Serpentinization, *J Petrol*, 49(9), 1579-1588.
- Gaetani, G. A., T. Grove, and W. Bryan (1993), The influence of water on the petrogenesis of subduction-related igneous rocks, *Nature*, 365(6444), 332-334.
- Gale, A., C. A. Dalton, C. H. Langmuir, Y. Su, and J. G. Schilling (2013), The mean composition of ocean ridge basalts, *Geochem Geophys Geosy*, 14.
- Garbe-Schoenberg, D. (1993), Simultaneous determination of thirty-seven trace elements in twenty-eight international rock standards by ICP-MS, *Geostandard Newslett*, 17, 81-97.
- Garrido, C., P. B. Kelemen, and G. Hirth (2001), Variation of cooling rate with depth in lower crust formed at an oceanic spreading ridge: Plagioclase crystal size distributions in gabbros from the Oman ophiolite, *Geochem Geophys Geosy*, 2, 1-21.
- Gerlach, D., W. Leeman, and H. G. Avé Lallemand (1981), Petrology and geochemistry of plagiogranite in the Canyon Mountain Ophiolite, Oregon, *Contrib Mineral Petr*, 77(1), 82-92.
- German, C., and K. Von Damm (2006), Hydrothermal processes, in *The oceans & marine geochemistry (Treatise on geochemistry series, Vol. 6)*, Elsevier, edited by K. K. Turekian and H. D. Holland, pp. 181-222, Elsevier, Oxford.
- Gillis, K. M. (1996), 3. Rare earth element constraints on the origin of amphibole in gabbroic rocks from site 894, Hess Deep, in *Proc ODP, Sci Results*, edited by C. Mével, K. Gillis, J. F. Allan and P. S. Meyer, pp. 59-75, Ocean Drilling Program, College Station, TX.
- Gillis, K. M., and M. D. Roberts (1999), Cracking at the magma-hydrothermal transition: evidence from the Troodos Ophiolite, Cyprus, *Earth Planet Sc Lett*, 169(3), 227-244.
- Gillis, K. M., and P. S. Meyer (2001), Metasomatism of oceanic gabbros by late stage melts and hydrothermal fluids: evidence from the rare earth element composition of amphiboles, *Geochem Geophys Geosy*, 2(3), 1012.
- Gillis, K. M., and L. A. Coogan (2002), Anatectic Migmatites from the Roof of an Ocean Ridge Magma Chamber, *J Petrol*, 43(11), 2075-2095.
- Gillis, K. M., L. A. Coogan, and M. Chaussidon (2003), Volatile element (B, Cl, F) behaviour in the roof of an axial magma chamber from the East, *Earth Planet Sc Lett*, 213, 447-462.
- Gillis, K. M., et al. (2013), Primitive layered gabbros from fast-spreading lower oceanic crust, *Nature*, 1-8.
- Gillis, K. M., et al. (2014 in press), Expedition 345 Summary, in *Proc. IODP*, edited by K. M. Gillis, J. E. Snow and A. Klaus, pp. 1-49, Integrated Ocean Drilling Program, College Station, TX.
- Godard, M., et al. (2009), Geochemistry of a long in-situ section of intrusive slow-spread oceanic lithosphere: Results from IODP Site U1309 (Atlantis Massif, 30°N Mid-Atlantic-Ridge), *Earth Planet Sc Lett*, 279(1-2), 110-122.
- Goodenough, K. M., M. T. Styles, D. Schofield, R. J. Thomas, Q. C. Crowley, R. M. Lilly, J. McKerverey, D. Stephenson, and J. N. Carney (2010), Architecture of the Oman-UAE ophiolite: evidence for a multi-phase magmatic history, *Arab J Geo*, 3(4), 439-458.
- Grapes, R. H., and P. W. Hoskin (2004), Epidote group minerals in low-medium pressure metamorphic terranes, *Rev Mineral Geochem*, 56(1), 301-345.
- Gregory, R., and H. Taylor (1981), An oxygen isotope profile in a section of Cretaceous oceanic crust, Samail Ophiolite, Oman: Evidence for  $\delta^{18}\text{O}$ -buffering of the oceans by deep (>5 km) seawater-hydrothermal circulation at mid-ocean ridges, *J Geophys Res*, 86(B4), 2737-2755.
- Grove, T. (1992), Fractionation of mid-ocean ridge basalt (MORB), *Geoph Monog Series*, 281-311.
- Grove, T., and W. Bryan (1983), Fractionation of pyroxene-phyric MORB at low pressure: An experimental study, *Contrib Mineral Petr*, 84(4), 293-309.
- Haase, K. M., N. A. Stronck, R. Hékinian, and P. Stoffers (2005), Nb-depleted andesites from the Pacific-Antarctic Rise as analogs for early continental crust, *Geology*, 33(12), 921.
- Hannington, M., J. Jamieson, T. Monecke, S. Petersen, and S. Beaulieu (2011), The abundance of seafloor massive sulfide deposits, *Geology*, 39(12), 1155-1158.
- Hanson, G. (1989), An approach to trace element modeling using a simple igneous system as an example, *Rev Mineral Geochem*, 21(1), 79-97.
- Hart, S. R., J. Blusztajn, H. J. B. Dick, P. S. Meyer, and K. Muehlenbachs (1999), The fingerprint of seawater circulation in a 500-meter section of ocean crust gabbros, *Geochi Cosmochim Ac*, 63(23-24), 4059-4080.
- Henstock, T. J. (2002), Compaction control of melt distribution at fast-spreading mid-ocean ridges, *Geophys Res Lett*, 29(7), 1137.
- Henstock, T. J., A. Woods, and R. W. White (1993), The accretion of oceanic crust by episodic sill intrusion, *J Geophys Res*, 29, 4143-4161.
- Hess, P. (1995), Thermodynamic mixing properties and the structure of silicate melts, *Rev Mineral Geochem*, 32(1), 147-189.
- Hopson, C., R. Coleman, R. Gregory, J. Pallister, and E. Bailey (1981), Geologic section through the Samail ophiolite and associated rocks along a Muscat-Ibra transect, southeastern Oman Mountains, *J Geophys Res*, 86(B4), 2527-2544.
- Horn, I., and F. von Blanckenburg (2007), Investigation on elemental and isotopic fractionation during 196 nm femtosecond laser ablation multiple collector inductively coupled plasma mass spectrometry, *Spectrochimica Acta Part B: Atomic Spectroscopy*, 62(4), 410-422.
- Humphris, S. E., and G. Thompson (1978), Hydrothermal alteration of oceanic basalts by seawater, *Geochi Cosmochim Ac*, 42, 107-125.
- Ito, E., W. M. White, and C. Göpel (1987), The O, Sr, Nd and Pb isotope geochemistry of MORB, *Chem Geol*, 62, 157-176.
- Jarosewich, E. (2002), Smithsonian microbeam standards, *J Res Natl Inst Stan*, 107(6), 681-685.
- Jarosewich, E., J. Nelen, and J. Norberg (1980), Reference samples for electron microprobe analysis, *Geostandard Newslett*, 4, 43-47.
- Jochum, K. P., U. Nohl, K. Herwig, E. Lammel, B. Stoll, and A. W. Hofmann (2005), GeoReM: A New Geochemical

- Database for Reference Materials and Isotopic Standards, *Geostandards and Geoanalytical Research*, 29(3), 333-338.
- Jochum, K. P., et al. (2011), Determination of Reference Values for NIST SRM 610–617 Glasses Following ISO Guidelines, *Geostandards and Geoanalytical Research*, 35(4), 397-429.
- Johannes, W., and J. Koepke (2001), Incomplete reaction of plagioclase in experimental dehydration melting of amphibolite, *Aust J Earth Sci*, 48(4), 581-590.
- Johannes, W., J. Koepke, and H. Behrens (1994), Partial melting reactions of plagioclases and plagioclase-bearing systems, in *Feldspar and Their Reactions. Nato ASI Series*, edited by I. Parson, pp. 161-194, Kluwer, Dordrecht.
- Johnson, M. C., M. J. Rutherford, and P. C. Hess (1991), Chassigny petrogenesis: Melt compositions, intensive parameters and water contents of Martian (?) magmas, *Geochi Cosmochim Acta*, 55(1), 349-366.
- Kawahata, H., M. Nohara, H. Ishizuka, S. Hasebe, and H. Chiba (2001), Sr isotope geochemistry and hydrothermal alteration of the Oman ophiolite, *J Geophys Res*, 106(B6), 11083-11099.
- Kelemen, P. B., K. Koga, and N. Shimizuf (1997), Geochemistry of gabbro sills in the crust-mantle transition zone of the Oman: implications for the origin of the lower oceanic crust, *Earth Planet Sc Lett*, 146, 475-488.
- Koepke, J., J. Berndt, and F. Bussy (2003), An experimental study on the shallow-level migmatization of ferrogabbros from the Fuerteventura Basal Complex, Canary Islands, *Lithos*, 69, 105-125.
- Koepke, J., S. T. Feig, and J. E. Snow (2005a), Late stage magmatic evolution of oceanic gabbros as a result of hydrous partial melting: Evidence from the Ocean Drilling Program (ODP) Leg 153 drilling at the Mid-Atlantic Ridge, *Geochem Geophys Geosy*, 6, 1-27.
- Koepke, J., S. Feig, and J. Snow (2005b), Hydrous partial melting within the lower oceanic crust, *Terra Nova*, 17(3), 286-291.
- Koepke, J., S. T. Feig, J. E. Snow, and M. Freise (2004), Petrogenesis of oceanic plagiogranites by partial melting of gabbros: an experimental study, *Contrib Mineral Petr*, 146, 414-432.
- Koepke, J., J. Berndt, S. T. Feig, and F. Holtz (2007), The formation of SiO<sub>2</sub>-rich melts within the deep oceanic crust by hydrous partial melting of gabbros, *Contrib Mineral Petr*, 153(1), 67-84.
- Koepke, J., J. Berndt, I. Horn, J. Fehle, and P. E. Wolff (2014 in press), Partial melting of oceanic gabbro triggered by migrating water-rich fluids: a prime example from the Oman Ophiolite, in *Tectonic Evolution of the Oman Mountains*, edited by H. Rollinson, M. Searle, I. A. Abbasi, A. Al-Lazki and M. H. Al-Kindi, pp. 187-204, Geological Society, Special Publications, London.
- Koepke, J., S. Schoenborn, M. Oelze, H. Wittmann, S. T. Feig, E. Hellebrand, and F. Boudier (2009), Petrogenesis of crustal wehrlites in the Oman ophiolite: Experiments and natural rocks, *Geochem Geophys Geosy*, 10(10), 1-26.
- Koepke, J., L. France, T. Müller, F. Faure, N. Goetze, W. Dziony, and B. Ildefonse (2011), Gabbros from IODP Site 1256, equatorial Pacific: Insight into axial magma chamber processes at fast spreading ocean ridges, *Geochem Geophys Geosy*, 12(9).
- Koepke, J., D. M. Christie, W. Dziony, F. Holtz, D. Lattard, J. MacLennan, S. Park, B. Scheibner, T. Yamasaki, and S. Yamazaki (2008), Petrography of the dike-gabbro transition at IODP Site 1256 (equatorial Pacific): The evolution of the granoblastic dikes, *Geochem Geophys Geosy*, 9(7), 1-29.
- Korenaga, J., and P. B. Kelemen (1998), Melt migration through the oceanic lower crust: a constraint from melt percolation modeling with finite solid diffusion, *Earth Planet Sc Lett*, 156(1-2), 1-11.
- Kullerud, K. (1996), Chlorine-rich amphiboles; interplay between amphibole composition and an evolving fluid, *Eur J Mineral*, 8(2), 355.
- Langmuir, C. H. (1989), Geochemical consequences of in situ crystallization, *Nature*.
- Lanphere, M., R. Coleman, and C. Hopson (1981), Sr isotopic tracer study of the Samail ophiolite, Oman, *J Geophys Res*, 86(B4), 2709-2720.
- Leake, B., et al. (1997), Nomenclature of amphiboles: Report of the subcommittee on amphiboles of the International Mineralogical Association, commission on new minerals and mineral names, *Can Min*, 35, 219-246.
- Lehnert, K., Y. Su, and C. Langmuir (2000), A global geochemical database structure for rocks, *Geochem Geophys Geosy*, 1.
- Lepage, L. D. (2003), ILMAT: an excel worksheet for ilmenite--magnetite geothermometry and geobarometry, *Computers & Geosciences*, 29(5), 673-678.
- Liou, J. G., and W. G. Ernst (1979), Oceanic ridge metamorphism of the East Taiwan Ophiolite, *Contrib Mineral Petr*, 68, 335-348.
- Liou, J. G., S. Kuniyoshi, and K. Ito (1974), Experimental studies of the phase relations between greenschist and amphibolite in a basaltic system, *Am J Sci*, 274(6), 613-632.
- Liou, J. G., H. Kim, and S. Maruyama (1983), Prehnite-epidote equilibria and their petrologic applications, *J Petrol*, 24(4), 321-342.
- Liou, J. G., S. Maruyama, and M. Cho (1985), Phase equilibria and mineral parageneses of metabasites in low-grade metamorphism, *Mineral Mag*, 49(3), 352.
- Lippard, S. J., A. Shelton, and I. Gass (1986), *The ophiolite of northern Oman*, Blackwell Scientific Publications.
- Lissenberg, C. J., J. H. Bédard, and C. R. van Staal (2004), The structure and geochemistry of the gabbro zone of the Annieopsquotch ophiolite, Newfoundland: implications for lower crustal accretion at spreading ridges, *Earth Planet Sc Lett*, 229(1), 105-123.
- Lissenberg, C. J., C. J. MacLeod, K. A. Howard, and M. Godard (2012), Pervasive reactive melt migration through fast-spreading lower oceanic crust (Hess Deep, equatorial Pacific Ocean), *Earth Planet Sc Lett*, 1-12.
- Lister, C. (1974), On the penetration of water into hot rock, *Geophysical Journal Of The Royal Astronomical Society*, 39, 465-509.
- MacLennan, J., T. Hulme, and S. Singh (2004), Thermal models of oceanic crustal accretion: Linking geophysical, geological and petrological observations, *Geochem Geophys Geosy*, 2(5).
- MacLennan, J., T. Hulme, and S. Singh (2005), Cooling of the lower oceanic crust, *Geology*, 33, 357-366.
- MacLeod, C. J., and G. Yaouancq (2000), A fossil melt lens in the Oman ophiolite: Implications for magma chamber processes at fast spreading ridges, *Earth Planet Sc Lett*, 176(3-4), 357-373.
- MacLeod, C. J., C. J. Lissenberg, and L. E. Bibby (2013), "Moist MORB" axial magmatism in the Oman ophiolite: The evidence against a mid-ocean ridge origin, *Geology*, 41(4), 459-462.
- Maeda, J., H. Naslund, Y. Jang, E. Kikawa, T. Tajima, and W. Blackburn (2002), 4. High-Temperature Fluid Migration Within Oceanic Layer 3 Gabbros, Hole 735B, Southwest Indian Ridge: Implications for the Magmatic-Hydrothermal Transition at Slow-Spreading Mid-Ocean Ridges, in *Proc ODP, Sci Results*, edited by J. H. Natland, H. J. B. Dick, D. J. Miller and R. P. Von Herzen, pp. 1-56, Online.
- Malpas, J. (1979), Two contrasting trondhjemite associations from transported ophiolites in western Newfoundland initial report, in *Trondhjemites, Dacites and Related Rocks*, edited by F. Baker, pp. 465-488, Elsevier, New York.
- Manning, C., and C. MacLeod (1996), 10. Fracture-controlled metamorphism of Hess Deep gabbros, Site 894: constraints on the roots of mid-ocean-ridge hydrothermal systems at fast-spreading centers, in *Proc ODP, Sci Results*, edited by C. Mével, K. M. Gillis, J. F. Allan and P. S. Meyer, pp. 189-212, Ocean Drilling Program, College Station, TX.
- Manning, C., P. Weston, and K. Mahon (1996), Rapid high-temperature metamorphism of East Pacific Rise gabbros from Hess Deep, *Earth Planet Sc Lett*, 144, 123-132.
- Manning, C. E., C. J. MacLeod, and P. E. Weston (2000), Lower-crustal cracking front at fast-spreading ridges: Evidence from the East Pacific Rise and the Oman ophiolite,

- in *Ophiolites and Oceanic Crust: New Insights from Field Studies and the Ocean Drilling Program*, edited by Y. Dilek, E. Moores, D. Elthon and A. Nicolas, pp. 261-272, Geological Society of America Special Paper 349, Boulders, Colorado.
- Marks, N., P. Schiffman, and R. A. Zierenberg (2011), High-grade contact metamorphism in the Reykjanes geothermal system: Implications for fluid-rock interactions at mid-oceanic ridge spreading centers, *Geochem Geophys Geosy*, 12(8).
- McCaig, A. M., and M. Harris (2012), Hydrothermal circulation and the dike-gabbro transition in the detachment mode of slow seafloor spreading, *Geology*, 40(4), 367-370.
- McCaig, A. M., A. Delacour, A. E. Fallick, T. Castelain, and G. L. Früh-Green (2013), Detachment Fault Control on Hydrothermal Circulation Systems: Interpreting the Subsurface Beneath The Tag Hydrothermal Field Using The Isotopic and Geological Evolution of Oceanic Core Complexes in The Atlantic, in *Diversity Of Hydrothermal Systems On Slow Spreading Ocean Ridges*, edited, pp. 207-239, American Geophysical Union.
- McCullom, T. M., and E. L. Shock (1998), Fluid-rock interactions in the lower oceanic crust: Thermodynamic models of hydrothermal alteration, *J Geophys Res*, 103(B1), 547-575.
- McCormick, K. A., and A. M. McDonald (1999), Chlorine-bearing amphiboles from the Fraser Mine, Sudbury, Ontario, Canada; description and crystal chemistry, *Can Mineral*, 37(6), 1385-1403.
- McCulloch, M., R. Gregory, and G. Wasserburg (1980), A neodymium, strontium, and oxygen isotopic study of the Cretaceous Samail Ophiolite and implications for the petrogenesis and seawater-hydrothermal alteration of oceanic crust, *Earth Planet Sc Lett*, 46, 201-211.
- McCulloch, M., R. Gregory, G. Wasserburg, and H. Taylor (1981), Sm-Nd, Rb-Sr, and  $^{18}\text{O}/^{16}\text{O}$  isotopic systematics in an oceanic crustal section- Evidence from the Samail ophiolite, *J Geophys Res*, 86, 2721-2735.
- Mével, C. (1981), Occurrence of Pumpellyite in Hydrothermally Altered Basalts from the Vema Fracture Zone (Mid-Atlantic Ridge), *Contrib Mineral Petr*, 76, 386-393.
- Mével, C., and M. Cannat (1991), Lithospheric Stretching and Hydrothermal Processes in Oceanic Gabbros from Slow-Spreading Ridges, in *Ophiolite Genesis and Evolution of the Oceanic Lithosphere*, edited by T. Peters, A. Nicolas and R. G. Coleman, pp. 293-312, Springer Netherlands.
- Mével, C., M. Cannat, P. Gente, E. Marion, J. Auzende, and J. Karson (1991), Emplacement of deep crustal and mantle rocks on the west median valley wall of the MARK area (MAR, 23° N), *Tectonophysics*, 190(1), 31-53.
- Michard, A. (1989), Rare earth element systematics in hydrothermal fluids, *Geochi Cosmochim Acta*, 53, 745-750.
- Michard, A., F. Albarède, G. Michard, and J. Minster (1983), Rare-earth elements and uranium in high-temperature solutions from East Pacific Rise hydrothermal vent field (13° N), *Nature*, 303, 795-797.
- Morgan, G., and D. London (1996), Optimizing the electron microprobe analysis of hydrous alkali aluminosilicate glasses, *Am Mineral*, 81(9-10), 1176-1185.
- Morimoto, N., J. Fabries, A. Ferguson, I. Ginzburg, M. Ross, F. Seifert, J. Zussman, K. I. Aoki, and G. Gottardi (1988), Nomenclature of pyroxenes, *Am Mineral*, 73(9-10), 1123-1133.
- Nehlig, P. (1991), Salinity of oceanic hydrothermal fluids: a fluid inclusion study, *Earth Planet Sc Lett*, 102, 310-325.
- Nehlig, P., and T. Juteau (1988), Deep crustal seawater penetration and circulation at ocean ridges: evidence from the Oman ophiolite, *Mar Geol*, 84, 209-229.
- Nehlig, P., T. Juteau, V. Bendel, and J. Cotten (1994), The root zones of oceanic hydrothermal systems: Constraints from the Samail ophiolite (Oman), *J Geophys Res*, 99(B3), 4703-4713.
- Nelson, S. T., and A. Montana (1992), Sieve-textured plagioclase in volcanic rocks produced by rapid decompression, *Am Mineral*, 77, 1242-1249.
- Nicolas, A. (1989), *Structures of ophiolites and dynamics of oceanic lithosphere*, Kluwer Academic Publishers Dordrecht.
- Nicolas, A., and D. Mainprice (2005), Burst of high-temperature seawater injection throughout accreting oceanic crust: a case study in Oman ophiolite, *Terra Nova*, 17, 326-330.
- Nicolas, A., D. Mainprice, and F. Boudier (2003), High-temperature seawater circulation throughout crust of oceanic ridges: A model derived from the Oman ophiolites, *J Geophys Res*, 108(B8), 1-20.
- Nicolas, A., F. Boudier, B. Ildefonse, and E. Bali (2000), Accretion of Oman and United Arab Emirates ophiolite – Discussion of a new structural map, *Mar Geophys Res*, 21, 147-179.
- Nonnotte, P., G. Ceuleneer, and M. Benoit (2005), Genesis of andesitic-boninitic magmas at mid-ocean ridges by melting of hydrated peridotites: Geochemical evidence from DSDP Site 334 gabbro-norites, *Earth Planet Sc Lett*, 236(3-4), 632-653.
- Oberti, R., N. Sardone, and F. Hawthorne (1995), Synthesis and crystal structure refinement of synthetic fluor-pargasite, *Can Mineral*, 33, 25-31.
- Pallister, J., and C. Hopson (1981), Samail ophiolite plutonic suite: field relations, phase variation, cryptic variation and layering, and a model of a spreading ridge magma chamber, *J Geophys Res*, 86(B4), 2593-2644.
- Pallister, J., and R. Knight (1981), Rare-earth element geochemistry of the Samail ophiolite near Ibra, Oman, *J Geophys Res*, 86(B4), 2673-2697.
- Panjasawatwong, Y., and L. V. Danyushevsky (1995), An experimental study of the effects of melt composition on plagioclase - melt equilibria at 5 and 10 kbar: implications for the origin of magmatic high-An plagioclase, *Contrib Mineral Petr*, 118, 420-432.
- Pearce, J., T. Alabaster, A. Shelton, and M. Searle (1981), The Oman ophiolite as a Cretaceous-arc-basin complex: evidence and implications, *Philosophical Transactions of the Royal Society of London*, 300(1454), 299-317.
- Pedersen, R., J. Malpas, and T. Falloon (1996), Petrology and geochemistry of gabbroic and related rocks from Site 894, Hess Deep, in *Proc ODP, Sci Results*, edited by C. Mével, K. M. Gillis, J. F. Allan and P. S. Meyer, pp. 2-20, College Station, TX.
- Philpotts, A. (1982), Compositions of immiscible liquids in volcanic rocks, *Contrib Mineral Petr*, 80(3), 201-218.
- Phipps Morgan, J., and Y. Chen (1993), Magma Injection, Hydrothermal Circulation, and Crustal Flow, *J Geophys Res*, 98(B4), 6283-6297.
- Pin, C., D. Briot, C. Bassin, and F. Poitrasson (1994), Concomitant separation of strontium and samarium-neodymium for isotopic analysis in silicate samples, based on specific extraction chromatography, *Analytica Chimica Acta*, 298(2), 209-217.
- Poli, S., and M. W. Schmidt (2004), Experimental subsolidus studies on epidote minerals, *Rev Mineral Geochem*, 56(1), 171-195.
- Pouchou, J. L., and F. Pichoir (1991), Quantitative analysis of homogeneous or stratified microvolumes applying the model "PAP", in *Electron probe quantification*, edited by K. Heinrich and D. Newbury, pp. 31-75, Plenum Press, New York.
- Python, M., G. Ceuleneer, Y. Ishida, and J. Barrat (2007), Oman diopsidites: a new lithology diagnostic of very high temperature hydrothermal circulation in mantle peridotite below oceanic spreading centres, *Earth Planet Sc Lett*, 255, 289-305.
- Quick, J. E., and R. P. Denlinger (1993), Ductile Deformation and the Origin of Layered Gabbro in Ophiolites, *J Geophys Res*, 98(B8), 14015-14027.
- Rioux, M., S. Bowring, P. Kelemen, S. Gordon, R. Miller, and F. Dudás (2013), Tectonic development of the Samail ophiolite: High precision U-Pb zircon geochronology and Sm-Nd isotopic constraints on crustal growth and emplacement, *J Petrol*, 118(5), 2085-2101.

- Robinson, P. (1982), Phase relations of metamorphic amphiboles; natural occurrence and theory; Introduction, *Rev Mineral Geochem*, 9(1), 1-3.
- Roedder, E., and P. W. Weiblen (1970), Silicate liquid immiscibility in lunar magmas, evidenced by melt inclusions in lunar rocks, *Science*, 167(3918), 641.
- Roeder, P., and R. Emslie (1970), Olivine-Liquid Equilibrium, *Contrib Mineral Petr*, 29(4), 275-289.
- Rollinson, H. R. (1993), *Using Geochemical Data: Evaluation, Presentation, Interpretation*, Pearson - Prentice Hall, Harlow.
- Rollinson, H. R. (2009), New models for the genesis of plagiogranites in the Oman ophiolite, *Lithos*, 112, 603-614.
- Ross, K., and D. Elthon (1997), 17. Cumulus and postcumulus crystallization in the oceanic crust: major-and trace-element geochemistry of Leg 153 gabbroic rocks, in *Proc ODP, Sci Results*, edited by J. A. Karson, M. Cannat, D. J. Miller, D. Elthon, pp. 333-350, College Station, TX.
- Rutherford, M. J., and P. M. Hill (1993), Magma ascent rates from amphibole breakdown: An experimental study applied to the 1980-1986 Mount St. Helens eruptions - Rutherford - 2012, *J Geophys Res*, 98(B11), 19667-19685.
- Sato, H., Y. Yamaguchi, and K. Makino (1997), Cl incorporation into successively zoned amphiboles from the Ramnes cauldron, Norway, *Am Mineral*, 82, 316-324.
- Sato, H., S. Nakada, T. Fujii, M. Nakamura, and K. Suzuki-Kamata (1999), Groundmass pargasite in the 1991-1995 dacite of Unzen volcano: phase stability experiments and volcanological implications, *J Volcanol Geoth Res*, 89(1), 197-212.
- Sauerzapf, U., D. Lattard, and M. Burchard (2008), The titanomagnetite-ilmenite equilibrium: New experimental data and thermo-oxybarometric application to the crystallization of basic to intermediate rocks, *J Petrol*, 49(6), 1161-1185.
- Sautter, V., A. Jambon, and O. Boudouma (2006), Cl-amphibole in the nakhlite MIL 03346: Evidence for sediment contamination in a Martian meteorite, *Earth Planet Sc Lett*, 252(1-2), 45-55.
- Scaillet, B., and B. Evans (1999), The 15 June 1991 Eruption of Mount Pinatubo. I. Phase Equilibria and Pre-eruption P-T-fO<sub>2</sub>-fH<sub>2</sub>O Conditions of the Dacite Magma, *J Petrol*, 40(3), 381-411.
- Schiffman, P., and J. G. Liou (1980), Synthesis and Stability Relations of Mg-Al Pumpellyite, Ca<sub>4</sub>Al<sub>5</sub>MgSi<sub>6</sub>O<sub>21</sub>(OH)<sub>7</sub>, *J Petrol*, 21(3), 441-474.
- Schiffman, P., and G. Fridleifsson (1991), The smectite-chlorite transition in drillhole NJ-15, Nesjavellir geothermal field, Iceland: XRD, BSE and electron microprobe investigations, *J Metamorph Geol*, 9(6), 679-696.
- Schmidt, K., A. Koschinsky, D. Garbe-Schoenberg, L. M. de Carvalho, and R. Seifert (2007), Geochemistry of hydrothermal fluids from the ultramafic-hosted Logatchev hydrothermal field, 15 degrees N on the Mid-Atlantic Ridge: Temporal and spatial investigation, *Chem Geol*, 242(1-2), 1-21.
- Searle, M., and J. Cox (1999), Tectonic setting, origin, and obduction of the Oman ophiolite, *Geol Soc Am Bull*, 111, 104-122.
- Shanks, W. C. I. (2001), Stable Isotopes in Seafloor Hydrothermal Systems: Vent fluids, hydrothermal deposits, hydrothermal alteration, and microbial processes, *Rev Mineral Geochem*, 43(1), 469.
- Sharp, Z. D. (1990), A laser-based microanalytical method for the *in situ* determination of oxygen isotope ratios of silicates and oxides, *Geochi Cosmochim Acta*, 54(5), 1353-1357.
- Shaw, H. (1963), Hydrogen-Water Vapor Mixtures: Control of Hydrothermal Atmosphere by Hydrogen Osmosis, *Science*, 139, 1220-1222.
- Shipboard Scientific Party (1995), Introduction, in *Proceedings of the Ocean Drilling Program. Initial reports*, edited by M. Cannat, J. Karson and D. J. Miller, p. 798, Ocean Drilling Program, College Station, TX.
- Shmulovich, K., W. Heinrich, P. Möller, and P. Dulski (2002), Experimental determination of REE fractionation between liquid and vapour in the systems NaCl-H<sub>2</sub> and CaCl<sub>2</sub>-H<sub>2</sub>O up to 450°C, *Contrib Mineral Petr*, 144(3), 257-273.
- Sinton, J., and R. Detrick (1992), Mid-Ocean Ridge Magma Chambers, *J Geophys Res*, 97(B1), 197-216.
- Sisson, T. W. (1994), Hornblende-melt trace-element partitioning measured by ion microprobe, *Chem Geol*, 117(1-4), 331-344.
- Sisson, T. W., and T. Grove (1993), Experimental investigations of the role of H<sub>2</sub>O in calc-alkaline differentiation and subduction zone magmatism, *Contrib Mineral Petr*, 113, 143-166.
- Sobolev, A., and M. Chaussidon (1996), H<sub>2</sub>O concentrations in primary melts from supra-subduction zones and mid-ocean ridges: Implications for H<sub>2</sub>O storage and recycling in the mantle, *Earth Planet Sc Lett*, 137(1-4), 45-55.
- Spear, F. (1980), NaSi ⇌ CaAl exchange equilibrium between plagioclase and amphibole, *Contrib Mineral Petr*, 72, 33-41.
- Spray, J. G., and G. R. Dunning (1991), A U/Pb age for the Shetland Islands oceanic fragment, Scottish Caledonides: evidence from anatectic plagiogranites in 'layer 3' shear zones, *Geol Mag*, 128(06), 667-671.
- Stakes, D., and D. Vanko (1986), Multistage hydrothermal alteration of gabbroic rocks from the failed Mathematician Ridge, *Earth Planet Sc Lett*, 79, 75-92.
- Stein, C. A., and S. Stein (1994), Constraints on hydrothermal heat flux through the oceanic lithosphere from global heat flow, *J Geophys Res*, 99(B2), 3081-3095.
- Stern, R. J., M. Reagan, O. Ishizuka, Y. Ohara, and S. Whattam (2012), To understand subduction initiation, study forearc crust: To understand forearc crust, study ophiolites, *LITHOSPHERE*, 4(6), 469-483.
- Stichnothe, J. (2007), *Geochemische in-situ Analysen in ozeanische Gabbros - Meerwasserinduzierte HT-Partialschmelzreaktio in der unteren ozeanischen Kruste*, Diploma thesis, Leibniz Universität Hannover, Hannover.
- Stichnothe, J., J. Koepke, I. Horn, J. Berndt, and F. Boudier (2008), In-situ Sr isotope ratio determined in fluid-derived late-stage parageneses in gabbros from the lower oceanic crust, *Geophysical Research Abstracts*, 10(A-02128).
- Stormer Jr., J. C. (1983), The effects of recalculation on estimates of temperature and oxygen fugacity from analyses of multicomponent iron-titanium oxides, *Am Mineral*, 68, 586-594.
- Stormer Jr., J. C., M. Pierson, and R. Tacker (1993), Variation of F and Cl X-ray intensity due to anisotropic diffusion in apatite, *Am Mineral*, 78, 641-648.
- Sugawara, T. (2000), Thermodynamic analysis of Fe and Mg partitioning between plagioclase and silicate liquid, *Contrib Mineral Petr*, 138(2), 101-113.
- Suhr, G., E. Hellebrand, K. Johnson, and D. Brunelli (2008), Stacked gabbro units and intervening mantle: A detailed look at a section of IODP Leg 305, Hole U1309D, *Geochem Geophys Geosy*, 9(10), 1-31.
- Sun, S. S. (1982), Chemical composition and origin of the Earth's primitive mantle, *Geochi Cosmochim Acta*, 46(2), 179-192.
- Sun, S. S., and W. F. McDonough (1989), Chemical and isotopic systematics of oceanic basalts: implications for mantle composition and processes, *Geological Society London Special Publications*, 42, 313-345.
- Sun, W. D., R. A. Binns, A. C. Fan, V. S. Kamenetsky, R. Wysoczanski, G. J. Wei, Y. H. Hu, and R. J. Arculus (2007), Chlorine in submarine volcanic glasses from the eastern Manus basin, *Geochi Cosmochim Acta*, 71, 1542-1552.
- Tamura, A., S. Arai, S. Ishimaru, and E. S. Andal (2008), Petrology and geochemistry of peridotites from IODP Site U1309 at Atlantis Massif, MAR 30°N: micro- and macro-scale melt penetrations into peridotites, *Contrib Mineral Petr*, 155(4), 491-509.
- Taylor, H. P. (1974), The application of oxygen and hydrogen isotope studies to problems of hydrothermal alteration and ore deposition, *Econ Geol*, 69(6), 843-883.
- Taylor, H. P. (1977), Water/rock interactions and the origin of H<sub>2</sub>O in granitic batholiths, *J Geol Soc London*, 133(6), 509-558.



- Thy, P., P. Schiffman, and E. Moores (1989), Igneous mineral stratigraphy and chemistry of the Cyprus Crustal Study Project drill core in the plutonic sequences of the Troodos ophiolite, *Geol Surv Canada Pap*, 88, 147-186.
- Tribuzio, R., M. Tiepolo, and M. Thirlwall (2000), Origin of titanian pargasite in gabbroic rocks from the Northern Apennine ophiolites (Italy): insights into the late-magmatic evolution of a MOR-type intrusive sequence, *Earth Planet Sc Lett*, 176, 281-293.
- Tribuzio, R., M. Tiepolo, R. Vannucci, and L. A. Coogan (1999), Trace element distribution within olivine-bearing gabbros from the Northern Apennine ophiolites (Italy): evidence for post-cumulus crystallization in MOR-type gabbroic rocks, *Contrib Mineral Petr*, 134, 123-133.
- Tsuchiya, N., T. Shibata, M. Yoshikawa, Y. Adachi, S. Miyashita, T. Adachi, N. Nakano, and Y. Osanai (2012), Petrology of Lasail plutonic complex, northern Oman ophiolite, Oman: An example of arc-like magmatism associated with ophiolite detachment, *Lithos*, 156-159, 120-138.
- Valley, J. W., N. Kitchen, M. J. Kohn, C. R. Niendorf, and M. J. Spicuzza (1995), UWG-2, a garnet standard for oxygen isotope ratios: Strategies for high precision and accuracy with laser heating, *Geochi Cosmochim Ac*, 59(24), 5223-5231.
- Van Grieken, R., and A. Markowicz (2002), *Handbook of X-ray Spectrometry*, 224 pp., Marcel-Dekker Inc., New York.
- Vanko, D. (1986), High-chlorine amphiboles from oceanic rocks: product of highly saline hydrothermal fluids, *Am Mineral*, 71, 51-59.
- Vanko, D., and C. Laverne (1998), Hydrothermal anorthitization of plagioclase within the magmatic/hydrothermal transition at mid-ocean ridges: examples from deep sheeted dikes (Hole 504B, Costa Rica Rift) and a sheeted dike root zone (Oman ophiolite), *Earth Planet Sc Lett*, 162, 27-43.
- Veizer, J., D. Ala, K. Azmy, P. Bruckschen, D. Buhl, F. Bruhn, G. A. F. Carden, A. Diener, S. Ebner, and Y. Godderis (1999),  $^{87}\text{Sr}/^{86}\text{Sr}$ ,  $\delta^{13}\text{C}$  and  $\delta^{18}\text{O}$  evolution of Phanerozoic seawater, *Chem Geol*, 161(1), 59-88.
- Veksler, I. V., A. M. Dorfman, L. V. Danyushevsky, J. K. Jakobsen, and D. B. Dingwell (2006), Immiscible silicate liquid partition coefficients: implications for crystal-melt element partitioning and basalt petrogenesis, *Contrib Mineral Petr*, 152(6), 685-702.
- Veksler, I. V., A. M. Dorfman, P. Dulski, V. S. Kamenetsky, L. V. Danyushevsky, T. Jeffries, and D. B. Dingwell (2012), Partitioning of elements between silicate melt and immiscible fluoride, chloride, carbonate, phosphate and sulfate melts, with implications to the origin of natrocarbonatite, *Geochi Cosmochim Ac*, 79, 20-40.
- Visser, W., and A. Koster van Groos (1979), Effects of  $\text{P}_2\text{O}_5$  and  $\text{TiO}_2$  on liquid-liquid equilibria in the system  $\text{K}_2\text{O}-\text{FeO}-\text{Al}_2\text{O}_3-\text{SiO}_2$ , *Am J Sci*, 279(8), 970-980.
- Volfinger, M., J. Robert, D. Vielzeuf, and A. Neiva (1985), Structural control of the chlorine content of OH-bearing silicates (micas and amphiboles), *Geochi Cosmochim Ac*, 49(1), 37-48.
- Wanless, V. D., M. Perfit, W. I. Ridley, and E. Klein (2010), Dacite Petrogenesis on Mid-Ocean Ridges: Evidence for Oceanic Crustal Melting and Assimilation, *J Petrol*, 51(12), 2377-2410.
- Warren, C., R. Parrish, D. Waters, and M. Searle (2005), Dating the geologic history of Oman's Semail ophiolite: insights from U-Pb geochronology, *Contrib Mineral Petr*, 150(4), 403-422.
- Wolff, P. E., J. Koepke, and S. T. Feig (2013), The reaction mechanism of fluid-induced partial melting of gabbro in the oceanic crust, *Eur J Mineral*, 25, 279-298.
- Xiao, Y., J. Hoefs, and A. Kronz (2005), Compositionally zoned Cl-rich amphiboles from North Dabie Shan, China: monitor of high-pressure metamorphic fluid/rock interaction processes, *Lithos*, 81(1-4), 279-295.
- Yamaoka, K., T. Ishikawa, O. Matsubaya, D. Ishiyama, K. Nagaishi, Y. Hiroyasu, H. Chiba, and H. Kawahata (2012), Boron and oxygen isotope systematics for a complete section of oceanic crustal rocks in the Oman ophiolite, *Geochi Cosmochim Ac*, 84, 543-559.
- Yamasaki, T., J. Maeda, and T. Mizuta (2006), Geochemical evidence in clinopyroxenes from gabbroic sequence for two distinct magmatisms in the Oman ophiolite, *Earth Planet Sc Lett*, 251(1-2), 52-65.
- Yaouancq, G., and C. MacLeod (2000), Petrofabric investigation of gabbros from the Oman ophiolite: comparison between AMS and rock fabric, *Mar Geophys Res*, 21, 289-305.
- Zhang, C., F. Holtz, C. Ma, P. E. Wolff, and X. Li (2012), Tracing the evolution and distribution of F and Cl in plutonic systems from volatile-bearing minerals: a case study from the Liujiawa pluton (Dabie orogen, China), *Contrib Mineral Petr*, 164(5), 859-879.
- Zhao, Z.-F., and Y.-F. Zheng (2003), Calculation of oxygen isotope fractionation in magmatic rocks, *Chem Geol*, 193(1), 59-80.
- Zhu, C., and D. A. Sverjensky (1991), Partitioning of F-Cl-OH between minerals and hydrothermal fluids, *Geochi Cosmochim Ac*, 55(7), 1837-1858.

# Tables

**Table 1.** Sample list from the Wadi Wariyah and analytical techniques applied.

Sample	Domain	Lithology	Method	Analytical technique					
				EPMA	ICP-MS	XRFA	LA-ICP-MS	<sup>87</sup> Sr/ <sup>86</sup> Sr	δ <sup>18</sup> O
Wa_02	A	dark vein	+	✓					
	B	layered gabbro	+	✓			✓		
Wa_04		gabbroic dike	+	✓			✓		
Wa_05	A	dark vein	+	✓					
	B	layered gabbro	+	✓					
Wa_1.5		altered gabbro	+	✓					
Wa_32	A	gabbroic dike	+	✓	✓	✓		✓	✓
	B	layered gabbro	+	✓	✓	✓		✓	✓
Wa_33	A	gabbroic dike	+	✓					
	B	layered gabbro	+	✓	✓	✓		✓	✓
Wa_35		layered gabbro	+	✓					
Wa_37		layered gabbro	+	✓					
Wa_38	A	dark vein	o	✓	✓	✓		✓	✓
	B	layered gabbro	o	✓	✓	✓		✓	✓
Wa_39	A	epidote vein	o	✓	✓	✓	✓	✓	✓
	B	altered gabbro (halo)	o	✓	✓	✓	✓	✓	✓
	C	altered gabbro	o	✓	✓	✓	✓	✓	✓
Wa_40	A	epidote vein	o	✓	✓	✓		✓	✓
	B	altered gabbro (halo)	o	✓	✓	✓		✓	✓
	C	altered gabbro	o	✓	✓	✓		✓	✓
Wa_42	A	gabbroic dike	o	✓	✓	✓	✓	✓	✓
	B	layered gabbro	o	✓	✓	✓	✓	✓	✓
Wa_43	A	epidote vein (I)	o	✓	✓	✓	✓	✓	✓
	B	epidote vein (II)	o	✓	✓	✓	✓	✓	✓
	C	altered gabbro (halo)	o	✓	✓	✓	✓	✓	✓
Wa_45	A	dark vein	+	✓					
	B	altered gabbro	+	✓					
Wa_46	A	gabbroic dike	o	✓	✓	✓	✓	✓	✓
	B	layered gabbro	o	✓	✓	✓	✓	✓	✓
Wa_46A	A	dark vein	o	✓	✓	✓	✓		
	B	layered gabbro	o	✓					
Wa_47	A	dark vein	o	✓	✓	✓	✓	✓	✓
	B	layered gabbro	o	✓	✓	✓	✓	✓	✓
Wa_53		layered gabbro	+	✓	✓	✓			
Wa_55		layered gabbro	+	✓	✓	✓			
Wa_57	A	dark vein	+	✓	✓	✓		✓	✓
	B	layered gabbro	+	✓	✓	✓		✓	✓
Wa_58	A	dark vein	+	✓					
	B	layered gabbro	+	✓	✓	✓	✓		
Wa_60		altered gabbro	+	✓					
Wa_61		prehnite vein	+	✓	✓	✓	✓	✓	✓
Wa_62		altered gabbro	+	✓	✓	✓			
Wa_63		layered gabbro	+	✓			✓		
Wa_64	A	dark vein	o	✓					
	B	layered gabbro	o	✓			✓		
Wa_66	A	dark vein	o	✓	✓	✓	✓	✓	✓
	B	layered gabbro	o	✓	✓	✓	✓	✓	✓
Wa_67	A	epidote vein	o	✓					
	B	altered gabbro	o	✓					
Wa_68	A	gabbroic dike	+	✓	✓	✓		✓	✓
	B	layered gabbro	+	✓					
Wa_69		An-bearing metagabbro	+	✓			✓		
Wa_71		An-bearing metagabbro	+	✓	✓	✓		✓	✓
Wa_72	A	epidote vein	+	✓					
	B	altered gabbro	+	✓					
Wa_73	A	prehnite vein	+	✓	✓	✓		✓	✓
	B	altered gabbro	+	✓	✓	✓		✓	✓
Wa_75	A	epidote vein	+	✓					
	B	altered gabbro	+	✓					
Wa_76	A	epidote vein	+	✓					
	B	altered gabbro	+	✓					
Wa_77	A	dark vein	+	✓					
	B	layered gabbro	+	✓					

+ = hand picked, o = rock drill

**Table 2.** Results of the standard materials JGB-1, JB-3, and JB-2 obtained by XRF analysis.

JGB-1 (Gabbro)								
Oxide	M.D.L.	Measured	GeoRem compiled values (Version 04/2012)	MEAN	SD (1 $\sigma$ )	GeoRem published values (Version 04/2012)	Accuracy	
SiO <sub>2</sub>	<0.01	43.78	43.44 - 43.66	43.55	0.16	-		0.5 %
TiO <sub>2</sub>	<0.01	1.61	1.60 - 1.62	1.61	0.01	1.45 - 1.79		0.0 %
Al <sub>2</sub> O <sub>3</sub>	<0.01	17.72	17.49 - 17.66	17.58	0.12	17.54 - 18.35		0.8 %
Fe <sub>2</sub> O <sub>3</sub> <sup>T</sup>	<0.01	15.31	15.06 - 15.16	15.11	0.07	-		1.3 %
MnO	<0.01	0.19	0.17 - 0.19	0.18	0.01	0.16 - 0.20		5.8 %
MgO	0.01	7.89	7.83 - 7.85	7.84	0.01	8.19 - 8.28		0.6 %
CaO	<0.01	11.89	11.90 - 11.98	11.94	0.06	11.71 - 11.90		-0.4 %
Na <sub>2</sub> O	0.01	1.27	1.20 - 1.23	1.22	0.02	1.01 - 1.30		4.5 %
K <sub>2</sub> O	<0.01	0.23	0.24	0.24		0.20 - 0.21		4.2 %
P <sub>2</sub> O <sub>5</sub>	<0.01	0.06	0.05 - 0.06	0.05	0.00	0.04 - 0.08		13.2 %
L.O.I.	<0.01	0.85	0.21 - 1.85	1.03	1.16			-17.5 %
Total		100.80						
JB-3 (Basalt)								
Oxide (wt%)	M.D.L.	Measured	GeoRem compiled values (Version 04/2012)	MEAN	SD (1 $\sigma$ )	GeoRem published values (Version 04/2012)	Accuracy	
SiO <sub>2</sub>	<0.01	50.53	50.96 - 51.04	51.00	0.06	-		-0.9 %
TiO <sub>2</sub>	<0.01	1.42	1.44 - 1.45	1.45	0.01	-		-1.7 %
Al <sub>2</sub> O <sub>3</sub>	<0.01	17.19	16.89 - 17.20	17.05	0.22	-		0.9 %
Fe <sub>2</sub> O <sub>3</sub> <sup>T</sup>	<0.01	11.86	11.82 - 11.88	11.85	0.04	-		0.1 %
MnO	<0.01	0.18	0.16 - 0.18	0.17	0.01	-		6.8 %
MgO	0.01	5.15	5.19 - 5.20	5.20	0.01	-		-0.9 %
CaO	<0.01	9.74	9.79 - 9.86	9.83	0.05	-		-0.9 %
Na <sub>2</sub> O	0.01	3.19	2.73 - 2.82	2.78	0.06	-		15.0 %
K <sub>2</sub> O	<0.01	0.76	0.78	0.78		-		-2.6 %
P <sub>2</sub> O <sub>5</sub>	<0.01	0.29	0.29	0.29		-		-0.7 %
L.O.I.	<0.01	-	0.50	0.50		-		-
Total		100.31						
JB-2 (Basalt)								
Oxide (wt%)	M.D.L.	Measured	GeoRem compiled values (Version 04/2012)	MEAN	SD (1 $\sigma$ )	GeoRem published values (Version 04/2012)	Accuracy	
SiO <sub>2</sub>	<0.01	53.67	53.20 - 53.25	53.23	0.04	52.57 - 53.69		0.8 %
TiO <sub>2</sub>	<0.01	1.18	1.19	1.19		1.13 - 1.28		-0.8 %
Al <sub>2</sub> O <sub>3</sub>	<0.01	14.86	14.64 - 14.67	14.66	0.02	14.14 - 14.91		1.4 %
Fe <sub>2</sub> O <sub>3</sub> <sup>T</sup>	<0.01	14.37	14.25 - 14.34	14.30	0.06	13.70 - 14.48		0.5 %
MnO	<0.01	0.22	0.20 - 0.22	0.21	0.01	0.17 - 0.26		5.3 %
MgO	0.01	4.64	4.62 - 4.66	4.64	0.03	4.45 - 4.89		0.0 %
CaO	<0.01	9.89	9.82 - 9.89	9.86	0.05	9.06 - 10.17		0.4 %
Na <sub>2</sub> O	0.01	2.09	2.03 - 2.04	2.04	0.01	1.92 - 2.53		2.7 %
K <sub>2</sub> O	<0.01	0.42	0.42	0.42		0.37 - 0.55		0.0 %
P <sub>2</sub> O <sub>5</sub>	<0.01	0.10	0.10	0.10		0.07 - 0.11		-0.5 %
L.O.I.	<0.01	-	0.62	0.62		-		-
Total		101.44						

all values in wt%

reference values (version 14) for standard rocks are listed under <http://georem.mpch-mainz.gwdg.de/> [Jochum et al., 2011]

M.D.L. is the minimum detection limit

MEAN is the average of the compiled values

SD is the standard deviation



**Table 4.** Comparison between JGB-1 standard material measured by XRF and ICP-MS.

Ref. JGB-1 (Gabbro)		Ba	Co	Cr	Cu	Ga	Ni	Sc	Sr	V	Y	Zn	Zr
	<i>XRF</i>												
M.D.L.	ppm	10	15	<5	<5	<5	<5	<5	<5	<5	<5	<5	<5
Mean	n = 1	69	64	50	79	5	29	37	309	629	8	108	34
1 $\sigma$		-	-	-	-	-	-	-	-	-	-	-	-
Accuracy		8 %	5 %	-15 %	-8 %	-73 %	17 %	2 %	-5 %	-1 %	-24 %	-2 %	3 %
	<i>ICP-MS</i>												
M.D.L.	ppm	1	0.1	5	2	1	2	0.1	0.5	5	0.1	2	1
Mean	n = 2	62.48	59.34	56.06	86.06	19.15	23.97	34.26	325	650	9.44	107	25.81
1 $\sigma$		0.134	0.313	0.414	0.780	0.100	0.400	0.070	0.546	8.626	0.009	1.008	0.282
Accuracy		-1 %	-4 %	-5 %	-1 %	1 %	-6 %	-6 %	1 %	2 %	-12 %	-4 %	-23 %
XRF vs ICP-MS		10 %	8 %	-11 %	-8 %	-74 %	21 %	8 %	-5 %	-3 %	-15 %	1%	32 %

M.D.L. = minimum detection limit  
1 $\sigma$  = one sigma standard deviation  
below detection limit XRF: La, Ce (20 ppm), Rb, Nb, Nd, Pb, Th, U (<5 ppm)

**Table 5.** Detection limit of the electron microprobe analysis for each mineral phase.

Mineral	SiO <sub>2</sub>	TiO <sub>2</sub>	Al <sub>2</sub> O <sub>3</sub>	Cr <sub>2</sub> O <sub>3</sub>	V <sub>2</sub> O <sub>3</sub>	MnO	FeO	MgO	NiO	CaO	Na <sub>2</sub> O	K <sub>2</sub> O	Cl	F	P <sub>2</sub> O <sub>5</sub>
Olivine	0.06	0.04	0.06	--	--	0.13	0.14	0.08	0.10	0.03	0.06	0.03	--	--	--
Plagioclase	0.06	0.04	0.07	--	--	0.12	0.13	0.05	--	0.07	0.06	0.02	--	--	--
Pyroxene	0.07	0.04	0.06	0.09	--	0.13	0.13	0.07	--	0.08	0.06	0.02	--	--	--
Amphibole	0.06	0.04	0.06	0.05	--	0.07	0.14	0.06	--	0.08	0.06	0.02	67	390	--
Ilmenite/Magnetite	0.06	0.06	0.07	0.10	0.03	0.15	0.17	0.07	--	0.08	--	--	--	--	--
Chlorite	0.07	0.04	0.08	0.05	--	0.08	0.13	0.08	0.11	0.06	0.06	0.02	24	277	--
Epidote/Prehnite	0.07	0.04	0.08	0.06	--	0.07	0.13	0.06	--	0.08	0.06	0.02	39	426	--
Apatite	0.05	--	--	0.04	--	0.08	0.14	0.07	--	0.09	0.07	0.02	64	522	0.05

oxides in wt%  
Cl and F in ppm  
-- not analysed

**Table 6.** Results of the reference material used for Electron microprobe analysis.

	n	SiO <sub>2</sub>	TiO <sub>2</sub>	Al <sub>2</sub> O <sub>3</sub>	MnO	FeO	MgO	CaO	Na <sub>2</sub> O	K <sub>2</sub> O	Cl <sup>+</sup>	F <sup>+</sup>	NiO	Total
<i>Reference 1</i>	Mean	94	39.61		0.33	17.09	43.72						0.03	100.79
	1 $\sigma$		(0.45)		(0.05)	(0.33)	(0.51)						(0.02)	(0.77)
<i>published</i> <sup>#</sup>			38.95		0.30	16.62	43.58						0.02	99.47
<i>Reference 2</i>	Mean	75	39.86	4.89	14.28	0.10	10.78	12.64	10.26	2.55	2.03	205	3666	97.79
	1 $\sigma$		(0.73)	(0.05)	(0.18)	(0.01)	(0.43)	(0.24)	(0.16)	(0.09)	(0.02)	(42)	(222)	(0.98)
<i>published</i> <sup>#</sup>			40.37	4.72	14.90	0.09	10.92	12.80	10.30	2.60	2.05	180	3460	99.08*

n = number of analysis; 1 $\sigma$  = one sigma standard deviation

*Reference 1* = Olivine (Fo<sub>83</sub>) springwater meteorite - USNM 2566

*Reference 2* = Hornblende Kakanui, New Zealand - USNM 111356

<sup>#</sup>Jaresowich *et al.* (1980)

<sup>+</sup>Cl and F (ppm) values of Zhang *et al.* [2012]

\*includes H<sub>2</sub>O = 0.94 wt%

**Table 7.** Results of the reference material BIR-1G obtained by LA-ICP-MS analysis.

Element	BIR-1G					BIR-1G GeoReM preferred values (Version 04/2012)		BIR-1G GeoReM published range of element concentration
	Mean M.D.L	Mean [n= 37]	SD (1 $\sigma$ )	RSD (%)	Accuracy	Mean	SD (1 $\sigma$ )	
Li	0.744	3.54	0.350	10	-3.18 %	3	0.7	2.3 - 3.6
Si	121	227255	8447.349	4	0.27 %	222030	1402	221095 - 222498
Ca	84.6	95036	117.496	0	0.39 %	95053	1429	94339 - 95053
Sc	0.152	44.8	0.972	2	-2.84 %	43	3	40.2 - 46.1
Ti	1.52	6941	321.484	5	-8.81 %	6233	419	4880 - 6501
Co	0.087	57.9	1.537	3	0.99 %	52	5	47.7 - 63
Ni	14.77	196	12.588	6	2.68 %	178	18	135 - 211
Ni	8.65	208	7.830	4	4.91 %	178	18	136 - 211
Rb	0.064	0.224	0.034	15	8.89 %	0.197	0.007	0 - 0.26
Sr	0.055	106	2.202	2	3.40 %	109	2	97 - 118
Y	0.021	13.2	0.375	3	0.21 %	14.3	1.4	11 - 15.9
Zr	0.420	12.6	0.489	4	5.19 %	14	1.2	11.96 - 17.8
Nb	0.008	0.542	0.025	5	2.42 %	0.52	0.04	0.46 - 0.65
Cs	0.033	0.023	0.024	103	3.20 %	0.007	0.002	0.00483 - 0.03
Ba	0.085	6.374	0.248	4	4.76 %	6.5	0.07	5.66 - 7.01
La	0.003	0.581	0.017	3	1.34 %	0.609	0.02	0.539 - 0.91
Ce	0.005	1.945	0.059	3	0.79 %	1.89	0.04	1.66 - 2.22
Pr	0.005	0.353	0.016	5	2.39 %	0.37	0.02	0.32 - 0.45
Nd	0.029	2.254	0.118	5	0.77 %	2.37	0.03	2.06 - 2.6
Sm	0.035	1.029	0.100	10	3.03 %	1.09	0.02	0.95-1.26
Eu	0.009	0.494	0.030	6	3.43 %	0.517	0.005	0.459 - 0.57
Gd	0.045	1.643	0.084	5	1.64 %	1.85	0.02	1.2 - 1.97
Tb	0.005	0.309	0.015	5	5.00 %	0.35	0.04	0.29 - 0.414
Dy	0.021	2.343	0.086	4	-0.93 %	2.55	0.02	2 - 2.73
Ho	0.004	0.517	0.026	5	1.60 %	0.56	0.03	0.4695 - 0.599
Er	0.018	1.534	0.095	6	1.88 %	1.7	0.02	1.3 - 1.79
Tm	0.005	0.224	0.016	7	-1.96 %	0.24	0.03	0.19 - 0.26
Yb	0.018	1.595	0.099	6	-1.81 %	1.64	0.03	1.3 - 1.79
Lu	0.004	0.222	0.013	6	-1.63 %	0.248	0.009	0.2 - 0.27
Hf	0.016	0.498	0.044	9	5.44 %	0.57	0.03	0.4485 - 0.64
Ta	0.006	0.034	0.007	19	-5.35 %	0.036	0.006	0.026 - 0.087
Pb	0.024	3.829	0.156	4	-0.29 %	3.7	0.3	2.98 - 4.25
Th	0.003	0.028	0.004	15	1.68 %	0.03	0.002	0.026 - 0.041
U	0.002	0.025	0.011	45	0.94 %	0.023	0.006	0.0133 - 0.0749

all values given in ppm

reference values (version 14) for standard rocks are listed under <http://georem.mpch-mainz.gwdg.de/> [Jochum *et al.*, 2011]

**Table 8.** Mineralogy, classification, and description of the dikes/veins and surrounding lithologies from the Wadi Wariyah.

Sample	Domain	Lithology	Mineral assemblage													Vein classification							Surrounding lithology				
			Ol	Plag	Cpx	Opx	Amph	Ilm	Mag	Chl	Epi	Prh	Pmp	#	size	contact	shape	connectivity	feature	structure	Sample	Alteration	type	halo	size	minerals	retics in halo
Wa_02	A	dark vein	✓	✓	✓	✓	✓	✓	✓										Cl-rich Amph	Wa_02B	<2	layered gabbro	-	-	-	Ol + Plag + Cpx	-
Wa_04	A	gabbroic dike	✓	✓	✓	✓	✓	✓	✓	✓									Cl-rich Amph	Wa_05B	<2	layered gabbro	-	-	-	Ol + Plag + Cpx	-
Wa_32	A	gabbroic dike	✓	✓	✓	✓	✓	✓	✓	✓									uniform	Wa_32B	<2	layered gabbro	-	-	-	Ol + Plag + Cpx	-
Wa_33	A	gabbroic dike	✓	✓	✓	✓	✓	✓	✓	✓									uniform	Wa_33B	<2	layered gabbro	-	-	-	Ol + Plag + Cpx	-
Wa_39	A	epidote vein	✓	✓	✓	✓	✓	✓	✓	✓	✓								haloed	Wa_39B	20-40	altered gabbro	✓	5	Acr/Tr + Chl + Epi	Cpx + Plag	
Wa_40	A	epidote vein	✓	✓	✓	✓	✓	✓	✓	✓	✓								haloed	Wa_40B	20-40	altered gabbro	✓	2	Acr/Tr + Chl + Epi	Cpx	
Wa_42	A	gabbroic dike	✓	✓	✓	✓	✓	✓	✓	✓	✓								uniform	Wa_42B	<2	layered gabbro	-	-	-	Ol + Plag + Cpx	-
Wa_43	B	epidote vein (I)																	haloed	Wa_43C	40-80	altered gabbro	✓	5	Epi + Chl	Cpx	
Wa_45	A	dark vein	✓	✓	✓	✓	✓	✓	✓										uniform	Wa_45B	2-20	altered gabbro	✓	4	Acr/Tr + Chl	Cpx + Plag	
Wa_46	A	gabbroic dike	✓	✓	✓	✓	✓	✓	✓	✓									comb	Wa_46B	<2	layered gabbro	-	-	-	Ol + Plag + Cpx	-
Wa_46A	A	dark vein	✓	✓	✓	✓	✓	✓	✓	✓									haloed	Wa_46AB	<2	layered gabbro	-	-	-	Ol + Plag + Cpx	-
Wa_47	A	dark vein	✓	✓	✓	✓	✓	✓	✓	✓									uniform	Wa_47B	<2	layered gabbro	-	-	-	Ol + Plag + Cpx	-
Wa_57	A	dark vein	✓	✓	✓	✓	✓	✓	✓	✓									microcrack	Wa_57B	<2	layered gabbro	-	-	-	Ol + Plag + Cpx	-
Wa_58	A	dark vein	✓	✓	✓	✓	✓	✓	✓	✓									microcrack	Wa_58B	<2	layered gabbro	-	-	-	Ol + Plag + Cpx	-
Wa_61	A	prehnite vein	✓	✓	✓	✓	✓	✓	✓	✓	✓								haloed	Wa_62	40-80	altered gabbro	✓	10	Acr/Tr + Chl + Epi	Cpx	
Wa_66	A	dark vein	✓	✓	✓	✓	✓	✓	✓	✓									uniform	Wa_66B	<2	layered gabbro	-	-	-	Ol + Plag + Cpx	-
Wa_67	A	epidote vein	✓	✓	✓	✓	✓	✓	✓	✓	✓								irregular	Wa_67B	20-40	altered gabbro	✓	7	Ol + Plag + Cpx	Cpx + Plag	
Wa_68	A	gabbroic dike	✓	✓	✓	✓	✓	✓	✓	✓									uniform	Wa_68B	<2	layered gabbro	-	-	-	Ol + Plag + Cpx	-
Wa_69	A	Au-bearing metagabbro*	✓	✓	✓	✓	✓	✓	✓	✓	✓								high-An Plagioclase	-	-	-	-	-	-	-	-
Wa_71	A	Au-bearing metagabbro*	✓	✓	✓	✓	✓	✓	✓	✓	✓								high-An Plagioclase	-	-	-	-	-	-	-	-
Wa_72	A	epidote vein	✓	✓	✓	✓	✓	✓	✓	✓	✓								haloed	Wa_72B	40-80	altered gabbro	✓	5	Acr/Tr + Chl + Epi	Cpx	
Wa_73	A	prehnite vein	✓	✓	✓	✓	✓	✓	✓	✓	✓								haloed	Wa_73B	40-80	altered gabbro	✓	50	Acr/Tr + Chl + Epi	Cpx	
Wa_75	A	epidote vein	✓	✓	✓	✓	✓	✓	✓	✓	✓								uniform	Wa_75B	20-40	altered gabbro	✓	10	Acr/Tr + Chl	Cpx + Plag	
Wa_76	A	epidote vein	✓	✓	✓	✓	✓	✓	✓	✓	✓								haloed	Wa_76B	20-40	altered gabbro	✓	5	Acr/Tr + Chl	Cpx + Plag	
Wa_77	A	dark vein	✓	✓	✓	✓	✓	✓	✓	✓	✓								haloed	Wa_77B	<2	layered gabbro	-	-	-	Ol + Plag + Cpx	-

size in [cm]  
 vein classification based on field observation  
 Mineral abbreviations: Ol - olivine; Plag - plagioclase; Cpx - clinopyroxene; Amph - amphibole; Act/Tre - Actinolite/Tremolite; Ilm - ilmenite; Mag - Magnetite; Epi - epidote; Prh - prehnite; Pmp - pumpellyite; Chl - chlorite  
 halo type: ag - altered gabbro  
 # - vein number  
 \* pervasively altered gabbro occurs as separated blocks within the zone of prehnite veins and altered gabbro  
 Alteration degree in %



**Table 9.** Whole-rock major and trace element concentration of the layered gabbro, gabbroic dikes, dark veins, epidote veins, prehnite veins, and altered gabbro determined by XRF and ICP-MS analysis.

Sample	layered gabbro									gabbroic dikes	
	Wa_32B	Wa_42B	Wa_47B	Wa_57B	Wa_58B	Wa_66B	Wa_46B	Wa_53B	Wa_55B	Wa_32A	Wa_33A
<b>Major elements (wt%)</b>											
SiO <sub>2</sub>	47.00	46.21	47.68	47.39	46.41	46.93	47.41	44.60	46.57	42.98	44.09
TiO <sub>2</sub>	0.15	0.22	0.16	0.20	0.16	0.14	0.13	0.18	0.25	0.70	0.78
Al <sub>2</sub> O <sub>3</sub>	19.38	17.26	18.49	19.31	18.20	18.86	24.17	12.27	12.91	11.22	14.23
Fe <sub>2</sub> O <sub>3</sub> <sup>tot</sup>	4.51	6.11	4.39	3.53	5.16	4.50	2.38	7.13	6.94	13.18	10.36
MnO	0.08	0.11	0.08	0.07	0.09	0.08	0.05	0.14	0.13	0.20	0.17
MgO	10.60	12.54	10.36	8.59	11.56	10.34	5.23	16.54	15.90	18.00	14.42
CaO	16.54	15.51	16.65	17.80	15.76	16.35	17.77	15.48	15.58	10.54	11.71
Na <sub>2</sub> O	1.04	0.94	1.13	1.09	0.94	1.11	1.43	0.30	0.65	0.89	1.21
K <sub>2</sub> O	0.01	0.01	0.01	0.01	0.01	0.01	0.01	0.01	0.01	0.04	0.04
P <sub>2</sub> O <sub>5</sub>	b.d.	0.01	0.01	0.01	b.d.	0.01	b.d.	0.01	0.01	0.02	0.01
L.O.I.	1.03	1.29	1.27	0.68	1.00	0.94	0.85	4.37	1.93	1.78	2.80
Total	99.77	99.65	99.69	98.11	98.71	98.74	98.86	100.47	100.35	99.03	99.34
Mg#	80.72	78.53	80.79	81.26	79.98	80.37	79.69	80.52	80.33	70.88	71.27
<b>Trace elements (ppm)</b>											
Li	0.728	0.685	0.494	0.707	0.825	0.743	0.595	0.946	1.04	1.11	1.04
Sc	39.5	42.8	42.6	50.7	42.0	40.1	34.0	51.5	57.7	36.8	35.8
V	103	114	115	129	107	108	86.7	131	161	238	214
Cr	902	605	702	775	610	731	564	651	695	1190	832
Co	36.5	49.3	33.6	25.3	42.5	37.1	14.9	60.1	61.0	80.3	63.8
Ni	156	216	157	121	176	187	73.8	231.8	237.0	495.7	384.3
Cu	44.6	50.5	98.9	106	45.4	182	56.3	90.3	144	24.9	133
Zn	18.2	25.3	17.6	13.2	23.2	17.5	8.98	27.6	28.2	62.7	58.6
Ga	10.8	10.6	10.5	11.6	10.8	11.0	14.1	7.27	8.41	10.5	11.4
Rb	b.d.	b.d.	b.d.	b.d.	b.d.	b.d.	b.d.	b.d.	b.d.	0.310	0.358
Sr	179	159	155	181	152	167	214	107	114	130	162
Y	3.22	4.05	3.55	4.54	3.47	3.38	3.03	4.04	4.88	10.2	12.7
Zr*	0.994	8.94	13.91	3.97	b.d.	3.97	b.d.	17.9	17.9	21.9	27.8
Nb	b.d.	0.057	b.d.	b.d.	b.d.	0.053	0.050	b.d.	0.165	0.248	0.175
Mo	b.d.	b.d.	b.d.	b.d.	b.d.	b.d.	b.d.	b.d.	b.d.	b.d.	b.d.
Cs	0.027	0.030	0.022	0.006	0.052	0.020	0.010	0.012	0.056	0.035	0.062
Ba	b.d.	1.39	b.d.	2.14	2.64	b.d.	1.81	b.d.	1.29	11.0	9.70
La	b.d.	b.d.	b.d.	b.d.	b.d.	b.d.	0.060	b.d.	0.134	0.556	0.420
Ce	0.253	0.379	0.219	0.415	0.254	0.261	0.378	0.282	0.566	1.989	1.898
Pr	0.076	0.104	0.073	0.114	0.079	0.077	0.092	0.088	0.131	0.403	0.438
Nd	0.528	0.704	0.527	0.785	0.566	0.543	0.594	0.632	0.839	2.472	2.886
Sm	0.271	0.352	0.290	0.388	0.296	0.277	0.271	0.330	0.413	1.032	1.268
Eu	0.192	0.212	0.213	0.254	0.202	0.204	0.235	0.195	0.219	0.451	0.606
Gd	0.434	0.551	0.472	0.629	0.470	0.457	0.421	0.554	0.644	1.480	1.834
Tb	0.084	0.106	0.091	0.120	0.091	0.087	0.080	0.107	0.126	0.274	0.341
Dy	0.581	0.724	0.632	0.819	0.620	0.605	0.546	0.737	0.864	1.845	2.302
Ho	0.121	0.150	0.130	0.170	0.129	0.125	0.113	0.152	0.178	0.380	0.477
Er	0.319	0.392	0.345	0.447	0.338	0.331	0.298	0.406	0.475	1.022	1.267
Tm	0.045	0.056	0.048	0.063	0.048	0.046	0.041	0.058	0.067	0.147	0.181
Yb	0.280	0.353	0.306	0.394	0.300	0.297	0.265	0.359	0.422	0.946	1.122
Lu	0.041	0.051	0.043	0.056	0.043	0.042	0.038	0.052	0.060	0.136	0.162
Hf	0.096	0.129	0.085	0.140	0.104	0.091	0.089	0.132	0.150	0.445	0.525
Ta	b.d.	b.d.	b.d.	b.d.	b.d.	b.d.	b.d.	b.d.	0.015	0.020	0.019
Th	b.d.	b.d.	b.d.	b.d.	b.d.	0.005	0.005	0.009	0.018	0.029	0.006
Eu/Eu* <sub>N</sub>	1.71	1.47	1.75	1.56	1.65	1.74	2.12	1.38	1.29	1.11	1.21
Zr/Hf	10.34	69.30	164.13	28.38	-	43.85	-	135.16	118.96	49.13	52.98
Ce/Sm <sub>N</sub>	0.226	0.260	0.182	0.258	0.208	0.227	0.337	0.206	0.331	0.465	0.361

Abbreviations: -FeTi = dark veins without FeTi-oxides; +amph = amphibole-rich zone in epidote veins;  
halo = altered gabbro close to vein  
b.d. = below detection limit  
Normalization against chondritic values of *Sun and McDonough* [1989]  
Eu\*<sub>N</sub> = (Sm<sub>N</sub>+Gd<sub>N</sub>)/2

Table 9. (continued)

Sample	gabbroic dikes			dark veins				epidote veins			
	Wa_68A	Wa_42A	Wa_46A	Wa_47A	Wa_57A	Wa_46A -FeTi	Wa_66A -FeTi	Wa_39A	Wa_40A	Wa_43A	Wa_43B +amph
<b>Major elements (wt%)</b>											
SiO <sub>2</sub>	45.82	43.03	46.98	47.21	44.12	47.29	49.42	41.26	40.87	40.31	41.51
TiO <sub>2</sub>	2.40	1.31	1.69	1.84	1.34	0.20	0.33	0.02	0.02	0.35	1.43
Al <sub>2</sub> O <sub>3</sub>	14.49	14.19	14.31	15.17	17.22	16.93	17.80	22.76	22.53	26.05	20.84
Fe <sub>2</sub> O <sub>3</sub> <sup>tot</sup>	10.79	13.23	11.29	10.38	7.99	5.34	5.02	6.23	6.15	6.01	7.97
MnO	0.16	0.18	0.16	0.16	0.12	0.11	0.11	0.12	0.12	0.05	0.07
MgO	9.90	13.80	9.92	9.81	8.76	11.34	9.08	4.99	4.94	1.78	4.33
CaO	10.89	11.68	10.06	11.85	16.81	15.21	13.87	21.08	20.87	23.63	21.82
Na <sub>2</sub> O	2.92	1.07	2.67	1.93	0.92	1.13	2.08	0.21	0.20	0.02	0.06
K <sub>2</sub> O	0.14	0.05	0.12	0.08	0.04	0.08	0.05	b.d.	b.d.	b.d.	0.01
P <sub>2</sub> O <sub>5</sub>	0.10	0.01	0.11	0.03	0.01	0.02	0.07	0.01	0.01	0.01	0.08
L.O.I.	1.98	1.56	1.87	1.38	2.34	1.96	1.65	2.95	3.30	2.60	2.22
Total	99.00	99.60	98.85	99.37	99.13	99.03	98.91	99.03	98.41	100.20	99.74
Mg#	62.06	65.03	61.03	62.75	66.14	79.12	76.34	58.82	58.89	34.61	49.18
<b>Trace elements (ppm)</b>											
Li	0.463	0.665	0.521	1.06	3.92	2.10	2.52	14.6	3.76	0.522	0.218
Sc	51.6	36.9	38.3	39.3	46.9	36.8	31.5	3.37	0.284	6.99	18.9
V	509	426	428	438	380	110	104	82.4	22.3	208	710
Cr	382	746	399	288	512	618	532	59.6	b.d.	8.78	24.6
Co	40.3	62.4	47.5	49.3	38.5	37.8	32.2	17.3	8.05	5.06	12.9
Ni	140	307	207	181	135	174	137	66.1	31.7	26.3	59.1
Cu	59.4	34.9	320	265	366	46.0	276	5.77	6.37	4.80	5.92
Zn	50.6	59.5	54.8	78.4	25.0	21.6	26.5	15.5	9.80	5.14	11.7
Ga	15.5	14.4	15.9	14.9	13.2	10.7	13.0	20.5	20.7	22.8	25.5
Rb	0.662	0.415	0.405	0.235	0.407	0.570	0.246	b.d.	b.d.	b.d.	b.d.
Sr	191	167	146	152	229	178	156	794	567	490	430
Y	34.6	9.48	30.5	19.7	7.62	7.02	11.6	0.423	0.233	4.33	11.0
Zr*	60.6	18.9	208	57.6	20.9	22.9	60.6	b.d.	b.d.	15.9	48.7
Nb	1.50	0.300	1.72	1.56	0.434	0.424	1.30	b.d.	b.d.	0.210	1.05
Mo	b.d.	b.d.	b.d.	0.472	b.d.	b.d.	b.d.	b.d.	b.d.	b.d.	b.d.
Cs	0.012	0.080	0.023	0.011	0.014	0.057	0.017	0.009	0.006	b.d.	b.d.
Ba	25.4	8.23	26.8	17.4	7.22	4.00	15.2	b.d.	b.d.	b.d.	6.49
La	2.40	0.47	3.25	1.56	0.34	1.09	2.12	b.d.	b.d.	0.233	2.01
Ce	7.68	1.61	10.0	5.06	1.30	3.12	5.68	0.166	0.127	0.935	5.20
Pr	1.47	0.331	1.74	0.932	0.274	0.479	0.857	0.043	0.034	0.181	0.787
Nd	8.79	2.07	9.39	5.22	1.71	2.25	4.19	0.223	0.179	0.997	3.88
Sm	3.46	0.906	3.25	1.92	0.735	0.672	1.23	0.062	0.046	0.369	1.20
Eu	1.25	0.450	1.05	0.762	0.396	0.284	0.518	0.852	0.964	0.423	0.920
Gd	4.97	1.33	4.33	2.61	1.10	0.878	1.56	0.079	0.049	0.521	1.55
Tb	0.911	0.249	0.786	0.483	0.206	0.161	0.286	0.012	0.007	0.098	0.275
Dy	6.16	1.70	5.24	3.30	1.40	1.10	1.93	0.078	0.037	0.685	1.83
Ho	1.29	0.353	1.11	0.706	0.293	0.237	0.409	0.015	0.007	0.147	0.390
Er	3.47	0.949	3.03	1.97	0.785	0.681	1.17	0.040	0.017	0.417	1.08
Tm	0.494	0.134	0.447	0.297	0.112	0.106	0.178	0.006	0.002	0.064	0.161
Yb	3.13	0.865	2.91	1.98	0.719	0.717	1.19	0.034	0.014	0.423	1.07
Lu	0.443	0.124	0.424	0.294	0.103	0.110	0.179	0.005	0.002	0.063	0.160
Hf	1.37	0.402	1.38	0.692	0.362	0.246	0.239	b.d.	b.d.	0.134	0.414
Ta	0.104	0.026	0.117	0.112	0.039	0.049	0.100	0.011	0.011	0.018	0.079
Th	0.162	0.017	0.242	0.162	0.014	0.076	0.162	b.d.	b.d.	0.028	0.090
Eu/Eu* <sub>N</sub>	0.92	1.25	0.85	1.04	1.34	1.13	1.14	37.09	62.12	2.94	2.07
Zr/Hf	44.34	46.94	150.17	83.28	57.61	92.98	254.02	-	-	118.94	117.58
Ce/Sm <sub>N</sub>	0.536	0.429	0.744	0.636	0.428	1.123	1.113	0.643	0.672	0.612	1.050

Abbreviations: -FeTi = dark veins without FeTi-oxides; +amph = amphibole-rich zone in epidote veins;  
halo = altered gabbro close to vein  
b.d. = below detection limit  
Normalization against chondritic values of *Sun and McDonough* [1989]  
Eu\*<sub>N</sub> = (Sm<sub>N</sub>+Gd<sub>N</sub>)/2

Table 9. (continued)

Sample	<i>prehnite veins</i>		<i>altered gabbro</i>						<i>An bearing metagabbro</i>	
	Wa_61A	Wa_73A	Wa_43C halo	Wa_39B halo	Wa_40B halo	Wa_39C	Wa_40C	Wa_62	Wa_73B	Wa_71
<b>Major elements (wt%)</b>										
SiO <sub>2</sub>	43.03	43.17	46.36	47.45	45.60	46.45	46.61	45.59	43.87	44.42
TiO <sub>2</sub>	0.02	0.02	0.68	0.09	0.10	0.10	0.11	0.17	0.23	0.16
Al <sub>2</sub> O <sub>3</sub>	24.23	24.29	10.14	14.50	14.38	18.17	17.58	20.16	16.78	20.54
Fe <sub>2</sub> O <sub>3</sub> <sup>tot</sup>	0.31	0.21	5.35	5.29	4.51	4.72	4.52	4.25	3.54	4.26
MnO	0.02	0.02	0.11	0.12	0.11	0.09	0.09	0.07	0.07	0.07
MgO	0.54	0.53	13.79	12.71	11.80	11.76	11.77	9.02	9.89	10.61
CaO	26.66	26.99	20.57	15.03	16.92	14.46	14.37	15.67	21.16	15.47
Na <sub>2</sub> O	0.01	b.d.	0.17	1.48	0.91	1.33	1.50	1.15	0.07	1.06
K <sub>2</sub> O	b.d.	b.d.	0.01	0.01	0.01	0.01	0.01	0.02	b.d.	0.01
P <sub>2</sub> O <sub>5</sub>	0.01	b.d.	0.01	b.d.	0.01	b.d.	0.01	0.01	b.d.	b.d.
L.O.I.	4.82	4.69	2.41	3.74	4.35	3.09	3.18	3.14	4.60	3.86
Total	99.11	99.37	99.03	99.85	98.14	99.62	99.18	98.67	99.66	99.88
Mg#	75.62	81.80	82.14	81.08	82.33	81.60	82.26	79.08	83.28	81.61
<b>Trace elements (ppm)</b>										
Li	0.234	0.225	0.561	0.681	0.690	0.552	0.725	3.212	0.814	1.27
Sc	2.74	4.94	85.9	30.2	32.3	34.2	38.1	41.4	59.5	43.5
V	9.9	13.0	209	82.4	89.8	93.8	106	104	147	109
Cr	78.5	72.9	1101	566	628	640	698	645	844	851
Co	1.80	1.07	38.2	42.3	38.9	40.7	39.5	32.7	29.3	37.5
Ni	13.7	10.5	196	194	186	213	199	161	152	191
Cu	22.9	2.60	9.65	95.9	10.1	143	51.8	114.0	14.4	6.07
Zn	b.d.	b.d.	20.5	23.0	20.5	20.8	20.6	16.7	11.6	42.0
Ga	19.2	12.7	7.86	7.32	7.90	9.46	9.07	11.1	7.78	9.23
Rb	b.d.	b.d.	b.d.	b.d.	b.d.	b.d.	b.d.	b.d.	b.d.	b.d.
Sr	15.5	11.8	163	172	86.0	123	156	255	52.7	251
Y	0.573	0.588	10.0	2.39	2.50	2.67	2.95	3.66	5.27	3.63
Zr*	14.9	13.9	17.9	b.d.	14.9	b.d.	2.98	0.994	14.9	5.96
Nb	0.053	b.d.	0.139	b.d.	b.d.	b.d.	b.d.	0.052	b.d.	b.d.
Mo	b.d.	b.d.	b.d.	b.d.	b.d.	b.d.	b.d.	b.d.	b.d.	b.d.
Cs	b.d.	b.d.	b.d.	0.011	0.007	0.011	0.013	0.023	b.d.	0.013
Ba	b.d.	b.d.	3.01	b.d.	b.d.	b.d.	b.d.	6.98	b.d.	3.63
La	b.d.	b.d.	0.190	b.d.	b.d.	b.d.	b.d.	b.d.	b.d.	b.d.
Ce	0.096	b.d.	1.08	0.067	b.d.	0.069	b.d.	0.335	0.434	0.203
Pr	0.032	0.012	0.269	0.039	0.037	0.043	0.041	0.094	0.124	0.075
Nd	0.173	0.081	1.82	0.307	0.301	0.345	0.348	0.652	0.888	0.558
Sm	0.061	0.046	0.880	0.177	0.187	0.205	0.220	0.325	0.453	0.298
Eu	0.058	0.014	0.336	0.188	0.142	0.173	0.176	0.238	0.149	0.149
Gd	0.087	0.079	1.37	0.313	0.328	0.362	0.389	0.522	0.732	0.490
Tb	0.014	0.015	0.261	0.061	0.065	0.072	0.078	0.099	0.142	0.095
Dy	0.094	0.101	1.78	0.420	0.447	0.491	0.532	0.681	0.987	0.651
Ho	0.020	0.020	0.369	0.088	0.092	0.104	0.112	0.140	0.206	0.137
Er	0.050	0.053	0.978	0.233	0.246	0.270	0.294	0.372	0.550	0.364
Tm	0.008	0.007	0.136	0.033	0.034	0.038	0.041	0.052	0.078	0.050
Yb	0.049	0.044	0.865	0.204	0.220	0.236	0.257	0.325	0.482	0.314
Lu	0.007	0.006	0.123	0.030	0.031	0.034	0.037	0.047	0.071	0.046
Hf	b.d.	b.d.	0.319	b.d.	b.d.	0.050	0.052	0.111	0.169	0.102
Ta	b.d.	b.d.	0.011	b.d.	b.d.	0.016	b.d.	0.012	b.d.	b.d.
Th	0.006	b.d.	0.014	b.d.	b.d.	b.d.	b.d.	b.d.	b.d.	b.d.
Eu/Eu* <sub>N</sub>	2.45	0.70	0.93	2.42	1.74	1.93	1.82	1.76	0.79	1.19
Zr/Hf	-	-	56.01	-	-	-	57.03	8.92	87.97	58.31
Ce/Sm <sub>N</sub>	0.382	-	0.296	0.091	-	0.082	-	0.249	0.231	0.164

Abbreviations: -FeTi = dark veins without FeTi-oxides; +amph = amphibole-rich zone in epidote veins;  
halo = altered gabbro close to vein  
b.d. = below detection limit  
Normalization against chondritic values of *Sun and McDonough* [1989]  
Eu\*<sub>N</sub> = (Sm<sub>N</sub>+Gd<sub>N</sub>)/2

**Table 10.** Representative analysis of olivine from the layered gabbro and the gabbroic dikes.

	layered gabbro		gabbroic dikes	
	<i>n</i>	1σ		1σ
SiO <sub>2</sub>	300	39.08 (0.35)	97	37.53 (0.36)
TiO <sub>2</sub>		b.d.		b.d.
Al <sub>2</sub> O <sub>3</sub>		0.03 (0.10)		0.03 (0.14)
FeO		17.77 (0.51)		24.22 (1.28)
MnO		0.27 (0.06)		0.38 (0.05)
NiO		0.11 (0.03)		0.12 (0.03)
MgO		42.53 (0.58)		37.45 (1.25)
CaO		0.04 (0.02)		0.05 (0.02)
Na <sub>2</sub> O		b.d.		b.d.
K <sub>2</sub> O		b.d.		b.d.
Total		99.86 (0.59)		99.80 (0.57)
Mg#		81.01 (0.57)		73.36 (1.63)

*n* = number of analysis, 1σ = one sigma standard deviation

b.d. = below detection limit

Mg# =  $\text{Mg}^{2+}/(\text{Mg}^{2+}+\text{Fe}^{2+}) \times 100$  on a molar base

**Table 11.** Representative analysis of plagioclase from the layered gabbro, the gabbroic dikes, dark veins, altered gabbro, and An-bearing metagabbro.

core/rim Texture	layered gabbro				gabbroic dikes								
	core				core					core			
	<i>Min</i>	<i>Max</i>	<i>Mean</i>	<i>n</i> <i>1σ</i>	<i>Min</i>	<i>Max</i>	<i>Mean</i>	<i>n</i> <i>1σ</i>	<i>Min</i>	<i>Max</i>	<i>Mean</i>	<i>n</i> <i>1σ</i>	
				233				84				43	
SiO <sub>2</sub>	45.68	49.44	47.13	(0.60)	43.49	56.33	47.98	(2.22)	43.95	53.97	48.53	(2.08)	
TiO <sub>2</sub>	b.d.	0.06	b.d.		b.d.	0.06	b.d.		b.d.	0.08	0.03	(0.02)	
Al <sub>2</sub> O <sub>3</sub>	32.13	34.81	33.67	(0.49)	27.87	35.40	33.11	(1.49)	28.31	36.47	32.66	(1.97)	
FeO <sup>tot</sup>	0.27	0.80	0.47	(0.08)	0.23	1.05	0.50	(0.14)	b.d.	0.71	0.46	(0.12)	
CaO	15.69	18.73	17.21	(0.39)	10.18	19.24	16.35	(1.85)	11.80	19.70	15.98	(1.71)	
Na <sub>2</sub> O	1.14	2.72	1.92	(0.21)	0.79	5.53	2.32	(1.01)	0.54	4.91	2.60	(0.94)	
K <sub>2</sub> O	b.d.	0.08	0.02	(0.01)	b.d.	0.13	0.02	(0.02)	b.d.	0.08	0.03	(0.02)	
Total			100.44				100.31				100.31		
An	76.23	90.03	83.12	(1.88)	50.35	93.01	79.46	(9.01)	56.81	95.22	77.10	(8.34)	
Ab	9.93	23.68	16.77	(1.86)	6.92	49.46	20.41	(8.92)	4.71	42.76	22.73	(8.24)	
Or	-	0.46	0.11	(0.06)	-	0.73	0.13	(0.15)	-	0.44	0.17	(0.11)	
core/rim	rim				rim					rim			
	<i>Min</i>	<i>Max</i>	<i>Mean</i>	<i>n</i> <i>1σ</i>	<i>Min</i>	<i>Max</i>	<i>Mean</i>	<i>n</i> <i>1σ</i>	<i>Min</i>	<i>Max</i>	<i>Mean</i>	<i>n</i> <i>1σ</i>	
				111				25				21	
SiO <sub>2</sub>	44.66	49.45	46.48	(0.86)	45.22	57.25	48.28	(3.28)	45.65	53.93	48.68	(2.44)	
TiO <sub>2</sub>	b.d.	0.06	b.d.		b.d.	0.04	b.d.		b.d.	0.54	0.06	(0.11)	
Al <sub>2</sub> O <sub>3</sub>	32.26	35.45	34.07	(0.54)	27.53	35.17	33.00	(2.14)	28.12	34.70	32.13	(2.04)	
FeO <sup>tot</sup>	0.20	1.94	0.58	(0.23)	0.19	0.95	0.59	(0.21)	0.24	1.53	0.58	(0.32)	
CaO	15.52	18.83	17.66	(0.57)	9.20	18.49	16.06	(2.56)	11.50	17.79	15.57	(1.87)	
Na <sub>2</sub> O	0.90	2.64	1.62	(0.32)	0.94	6.22	2.44	(1.39)	1.51	5.03	2.73	(1.06)	
K <sub>2</sub> O	b.d.	0.04	0.01	(0.00)	b.d.	0.11	0.02	(0.02)	b.d.	0.07	0.04	(0.02)	
Total			100.51				100.43				99.97		
An	76.57	91.85	85.69	(2.82)	44.71	91.36	78.32	(12.5)	55.58	86.53	75.77	(9.37)	
Ab	8.13	23.43	14.23	(2.82)	8.55	54.67	21.56	(12.4)	13.32	44.02	24.02	(9.28)	
Or	-	0.22	0.09	(0.05)	-	0.63	0.12	(0.13)	-	0.44	0.21	(0.12)	

*n* = number of analysis, *1σ* = one sigma standard deviation

b.d. = below detection limit

Texture: *granoblastic* = anhedral/euhedral crystals, *chadacrysts* = inclusions in amphibole

An =  $\text{Ca}^{2+}/(\text{K}^{2+}+\text{Na}^{2+}+\text{Ca}^{2+}) \times 100$ ; Ab =  $\text{Na}^{2+}/(\text{K}^{2+}+\text{Na}^{2+}+\text{Ca}^{2+}) \times 100$ ; Or =  $\text{K}^{2+}/(\text{K}^{2+}+\text{Na}^{2+}+\text{Ca}^{2+}) \times 100$  on a molar base

**Table 11.** (continued)

core/rim	dark veins				altered gabbro				An-bearing metagabbro			
	core				core				core			
Texture	<i>Min</i>	<i>Max</i>	<i>Mean</i>		<i>Min</i>	<i>Max</i>	<i>Mean</i>		<i>Min</i>	<i>Max</i>	<i>Mean</i>	
<i>n</i>				1σ				1σ				1σ
SiO <sub>2</sub>	45.04	59.20	53.31	(3.99)	46.00	50.02	47.57	(0.71)	43.28	45.82	44.01	(0.39)
TiO <sub>2</sub>	b.d.	0.07	0.01	(0.02)	b.d.	0.05	b.d.		b.d.	b.d.	b.d.	
Al <sub>2</sub> O <sub>3</sub>	26.24	35.04	29.54	(2.61)	32.10	34.61	33.24	(0.47)	33.68	36.73	35.96	(0.36)
FeO <sup>tot</sup>	0.00	0.90	0.38	(0.13)	0.30	0.63	0.47	(0.07)	0.00	0.30	0.06	(0.05)
CaO	8.09	18.41	12.11	(3.16)	15.29	17.64	16.81	(0.48)	18.34	20.54	19.96	(0.33)
Na <sub>2</sub> O	0.80	7.32	4.57	(1.79)	1.59	2.99	2.09	(0.28)	0.10	1.41	0.35	(0.17)
K <sub>2</sub> O	b.d.	0.30	0.11	(0.07)	b.d.	0.04	b.d.		b.d.	0.03	b.d.	
Total			100.03				100.23				100.35	
An	37.93	92.48	59.13	(15.8)	73.76	85.55	81.56	(2.40)	87.73	99.07	96.91	(1.52)
Ab	7.43	61.33	40.21	(15.6)	14.36	26.15	18.33	(2.40)	0.93	12.18	3.06	(1.51)
Or	-	1.73	0.66	(0.42)	-	0.22	-		-	0.19	-	
core/rim	rim				rim				rim			
	<i>Min</i>	<i>Max</i>	<i>Mean</i>		<i>Min</i>	<i>Max</i>	<i>Mean</i>		<i>Min</i>	<i>Max</i>	<i>Mean</i>	
<i>n</i>				36				36				36
SiO <sub>2</sub>	52.51	58.21	55.32	(1.60)								
TiO <sub>2</sub>	b.d.	0.07	0.02	(0.02)								
Al <sub>2</sub> O <sub>3</sub>	26.42	30.25	28.05	(1.05)								
FeO <sup>tot</sup>	0.00	0.48	0.31	(0.10)								
CaO	8.31	12.64	10.44	(1.18)								
Na <sub>2</sub> O	4.49	6.81	5.59	(0.69)								
K <sub>2</sub> O	0.05	0.23	0.13	(0.03)								
Total			99.89									
An	39.90	60.66	50.47	(5.90)								
Ab	39.06	59.09	48.81	(5.81)								
Or	-	1.29	0.72	(0.21)								

*n* = number of analysis, 1σ = one sigma standard deviation

b.d. = below detection limit

Texture: *granoblastic* = anhedral/euhedral crystals, *chadacrysts* = inclusions in amphibole

An = Ca<sup>2+</sup>/(K<sup>2+</sup>+Na<sup>2+</sup>+Ca<sup>2+</sup>) x 100; Ab = Na<sup>2+</sup>/(K<sup>2+</sup>+Na<sup>2+</sup>+Ca<sup>2+</sup>) x 100 ; Or = K<sup>2+</sup>/(K<sup>2+</sup>+Na<sup>2+</sup>+Ca<sup>2+</sup>) x 100 on a molar base

**Table 12.** Representative results of clino- and orthopyroxene (wt%) from the Wadi Wariyah.

Phase core/rim	layered gabbro						gabbroic dikes						dark veins													
	clino-orthopyroxene			rim			clino-orthopyroxene			core			clino-orthopyroxene			core										
	Min	Max	Mean	1σ	Mean	Max	Min	Max	Mean	1σ	Mean	Max	Min	Max	Mean	1σ	Mean	Max	Min	Max	Mean	1σ				
<i>n</i>			212		121				60		40				80		26									
SiO <sub>2</sub>	50.46	53.40	52.09	(0.42)	50.78	54.16	52.08	(0.50)	49.66	53.41	51.93	52.20	(0.61)	53.62	55.91	52.20	52.46	(1.56)	50.07	56.07	52.46	(1.56)				
TiO <sub>2</sub>	0.19	0.54	0.41	(0.04)	0.09	0.72	0.41	(0.07)	0.12	1.27	0.61	0.33	(0.08)	0.10	0.37	0.33	0.46	(0.35)	b.d.	1.28	0.46	(0.35)				
Al <sub>2</sub> O <sub>3</sub>	0.73	3.49	3.00	(0.28)	1.11	5.72	3.03	(0.47)	0.73	3.62	2.60	1.86	(0.19)	0.76	1.45	1.86	2.56	(1.03)	0.14	3.71	2.56	(1.03)				
Cr <sub>2</sub> O <sub>3</sub>	b.d.	0.52	0.29	(0.10)	b.d.	0.58	0.29	(0.12)	b.d.	0.32	0.20	0.20	(0.07)	b.d.	0.10	0.10	0.21	(0.09)	b.d.	0.31	0.21	(0.09)				
Fe <sub>2</sub> O <sub>3</sub> <sup>#</sup>	b.d.	4.67	2.09	(0.93)	b.d.	4.08	2.05	(0.95)	0.17	4.23	1.97	1.75	(0.52)	b.d.	2.35	1.75	1.25	(1.11)	b.d.	4.03	1.25	(1.11)				
FeO	0.39	5.90	3.58	(0.93)	0.76	6.05	3.64	(1.04)	3.25	7.31	5.34	7.07	(0.89)	12.52	16.01	7.07	4.96	(1.03)	2.37	7.73	4.96	(1.03)				
MnO	0.04	0.27	0.14	(0.04)	b.d.	0.24	0.14	(0.04)	0.11	0.41	0.21	0.38	(0.06)	0.26	0.56	0.38	0.17	(0.05)	b.d.	0.34	0.17	(0.05)				
CaO	19.04	23.71	22.00	(0.86)	20.28	24.28	21.95	(0.69)	19.53	23.77	20.82	1.00	(0.25)	0.53	1.62	1.00	21.13	(1.27)	19.74	25.44	21.13	(1.27)				
MgO	15.27	18.20	16.55	(0.48)	14.39	18.13	16.55	(0.42)	13.97	16.26	16.25	16.42	(0.99)	26.13	29.45	16.42	16.67	(0.56)	14.52	16.87	16.67	(0.56)				
Na <sub>2</sub> O	0.15	0.45	0.27	(0.03)	b.d.	0.38	0.27	(0.05)	0.17	0.53	0.31	0.21	(0.01)	b.d.	0.07	0.21	0.25	(0.12)	0.06	0.55	0.25	(0.12)				
Total			100.42				100.41				100.23		99.85				100.13						100.02			
Mg#	83.17	98.67	89.25	(2.54)	83.38	97.70	89.07	(2.94)	78.06	89.53	84.95	80.39	(1.68)	74.42	80.61	80.39	86.24	(2.88)	78.52	92.28	86.24	(2.88)	71.68	77.88	84.08	(1.96)
Si	1.87	1.95	1.90		1.87	1.95	1.90		1.85	1.97	1.91	1.93		1.93	1.97	1.93	1.92		1.85	2.02	1.92		1.95	1.98	1.93	
[ <sup>VI</sup> Al]	0.03	0.13	0.10		0.05	0.13	0.10		0.03	0.15	0.09	0.06		0.03	0.06	0.06	0.08		-	0.15	0.08		0.02	0.05	0.07	
Sum	1.98	2.00	2.00		1.98	2.00	2.00		1.99	2.00	2.00	2.00		1.99	2.00	2.00	2.00		1.97	2.02	2.00		1.99	2.00	2.00	
[ <sup>IV</sup> Al]	-	0.06	0.03		-	0.12	0.03		-	0.05	0.02	0.02		-	0.02	0.02	0.03		-	0.08	0.03		-	0.02	0.03	
Ti	0.01	0.01	0.01		-	0.02	0.01		-	0.04	0.02	0.01		-	0.01	0.01	0.01		-	0.04	0.01		-	0.01	0.01	
Cr	-	0.02	0.01		-	0.02	0.01		-	0.01	0.01	-		-	0.01	0.01	0.01		-	0.01	0.01		-	-	0.01	
Fe <sup>3+</sup>	-	0.13	0.06		-	0.11	0.06		-	0.12	0.05	0.05		-	0.06	0.05	0.05		-	0.11	0.03		-	0.05	0.03	
Fe <sup>2+</sup>	0.01	0.18	0.11		0.02	0.18	0.11		0.10	0.23	0.16	0.22		0.37	0.48	0.22	0.15		0.07	0.24	0.15		0.42	0.54	0.18	
Mn	-	0.01	-		0.00	0.01	0.00		-	0.01	0.01	0.01		0.01	0.02	0.01	0.01		-	0.01	0.01		0.01	0.02	0.01	
Mg	0.84	0.99	0.90		0.79	0.98	0.90		0.78	0.90	0.89	0.90		1.41	1.55	0.90	0.91		0.80	0.92	0.91		1.37	1.48	0.93	
Ca	0.74	0.93	0.86		0.79	0.95	0.86		0.77	0.94	0.82	0.78		0.02	0.06	0.78	0.83		0.78	1.00	0.83		0.04	0.05	0.78	
Na	0.01	0.03	0.02		-	0.03	0.02		0.01	0.04	0.02	-		-	-	-	0.02		-	0.04	0.02		-	0.01	0.02	
Sum	2.00	2.02	2.00		2.00	2.02	2.00		2.00	2.01	2.00	2.00		2.00	2.01	2.00	2.00		1.96	2.03	2.00		1.99	2.01	2.00	
Endmember composition after <i>Morimoto et al.</i> [1988]																										
En	43.88	51.35	46.61		43.00	49.46	46.63		41.25	46.15	45.92	45.94		70.70	77.61	45.94	47.04		40.95	46.74	47.04		69.29	74.55	48.11	
Fs	7.38	10.63	8.85		3.48	10.15	8.89		8.51	16.55	11.60	14.26		21.19	26.89	14.26	9.89		6.61	14.73	9.89		23.05	28.38	11.32	
Wo	38.66	47.65	44.55		41.36	48.18	44.48		39.85	47.53	42.47	39.80		1.00	3.18	39.80	43.07		40.05	50.10	43.07		1.75	2.58	40.57	

*n* = number of analysis, 1σ = one sigma standard deviation

b.d. = below detection limit

<sup>#</sup>Fe<sub>2</sub>O<sub>3</sub> calculated based on stoichiometry after *Robinson* [1982]

Mg# = Mg<sup>2+</sup>/(Mg<sup>2+</sup>+Fe<sup>2+</sup>) x 100 on a molar base

Table 12. (continued).

Phase core/rim	altered gabbro				altered gabbro (halo)				highly altered gabbro				pervasively altered gabbro				prehnite veins			
	clinopyroxene core		clinopyroxene core		clinopyroxene core		clinopyroxene core		clinopyroxene core		clinopyroxene core		clinopyroxene core		clinopyroxene core		clinopyroxene core			
<i>n</i>	Min	Max	Mean	1σ	Min	Max	Mean	1σ	Min	Max	Mean	1σ	Min	Max	Mean	1σ	Min	Max	Mean	1σ
SiO <sub>2</sub>	50.48	54.85	52.71	(0.62)	51.40	54.68	52.67	(0.78)	52.23	54.22	52.52	(0.59)	51.52	53.88	52.14	(0.44)	51.48	54.96	52.76	(0.91)
TiO <sub>2</sub>	b.d.	0.52	0.37	(0.09)	b.d.	0.42	0.16	(0.10)	b.d.	0.43	0.32	(0.13)	0.21	0.65	0.58	(0.07)	b.d.	0.44	0.35	(0.14)
Al <sub>2</sub> O <sub>3</sub>	0.70	5.31	2.52	(0.50)	0.25	2.99	2.87	(0.80)	0.30	2.68	2.60	(0.67)	1.37	3.80	3.06	(0.32)	0.27	3.93	2.65	(1.06)
Cr <sub>2</sub> O <sub>3</sub>	b.d.	0.48	0.23	(0.13)	b.d.	0.59	0.17	(0.13)	0.08	0.30	0.40	(0.07)	b.d.	0.13	0.25	(0.04)	0.07	0.58	0.01	(0.12)
Fe <sub>2</sub> O <sub>3</sub> <sup>#</sup>	b.d.	4.25	1.25	(0.92)	b.d.	2.98	0.80	(0.71)	b.d.	1.01	0.81	(0.31)	b.d.	2.32	1.17	(0.55)	b.d.	2.01	0.90	(0.65)
FeO	1.16	8.23	4.57	(1.04)	1.07	7.32	5.47	(1.33)	2.41	3.94	4.20	(0.47)	3.50	5.88	4.83	(0.61)	2.97	4.93	4.29	(0.53)
MnO	b.d.	0.36	0.16	(0.05)	b.d.	0.25	0.23	(0.05)	0.06	0.20	0.13	(0.04)	0.05	0.24	0.14	(0.04)	0.04	0.18	0.15	(0.03)
CaO	19.44	25.68	21.30	(0.93)	21.07	26.30	23.29	(1.38)	22.71	24.96	23.19	(0.78)	20.51	23.62	21.43	(0.76)	22.08	25.54	22.72	(0.99)
MgO	12.37	18.01	16.89	(0.72)	14.86	17.05	14.27	(0.55)	15.99	16.73	15.64	(0.23)	15.31	17.17	16.35	(0.43)	15.22	16.60	16.15	(0.33)
Na <sub>2</sub> O	b.d.	0.44	0.24	(0.04)	0.05	0.35	0.46	(0.07)	0.09	0.27	0.24	(0.06)	0.13	0.35	0.27	(0.03)	0.07	0.43	0.23	(0.08)
Total			100.24				100.39				100.06				100.22				100.20	
Mg#	72.83	96.20	87.25	(3.07)	78.34	96.60	81.98	(3.81)	88.00	92.52	86.92	(1.38)	83.23	88.89	86.01	(1.50)	84.77	90.87	87.06	(1.57)
Si	1.87	1.98	1.92		1.90	2.00	1.94		1.92	1.99	1.93		1.90	1.98	1.91		1.89	2.00	1.93	
<sup>iv</sup> Al	0.02	0.13	0.08		-	0.10	0.06		0.01	0.08	0.07		0.02	0.10	0.09		-	0.11	0.07	
Sum	1.99	2.00	2.00		1.99	2.00	2.00		2.00	2.00	2.00		2.00	2.00	2.00		2.00	2.00	2.00	
<sup>iv</sup> Al	-	0.14	0.03		-	0.05	0.06		-	0.04	0.04		0.03	0.07	0.04		0.01	0.07	0.04	
Ti	-	0.01	0.01		-	0.01	-		-	0.01	0.01		0.01	0.02	0.02		-	0.01	0.01	
Cr	-	0.01	0.01		-	0.02	-		-	0.01	0.01		-	-	0.01		-	0.02	-	
Fe <sup>3+</sup>	-	0.12	0.03		-	0.08	0.02		-	0.03	0.02		-	0.06	0.03		-	0.06	0.02	
Fe <sup>2+</sup>	0.04	0.26	0.14		0.03	0.23	0.17		0.07	0.12	0.13		0.11	0.18	0.15		0.09	0.15	0.13	
Mn	-	0.01	-		-	0.01	0.01		-	0.01	-		-	0.01	-		-	0.01	0.00	
Mg	0.69	0.98	0.92		0.82	0.92	0.78		0.88	0.92	0.86		0.84	0.93	0.89		0.83	0.90	0.88	
Ca	0.76	1.00	0.83		0.82	1.02	0.92		0.90	0.98	0.91		0.80	0.93	0.84		0.87	1.00	0.89	
Na	-	0.03	0.02		0.00	0.03	0.03		0.01	0.02	0.02		0.01	0.02	0.02		0.01	0.03	0.02	
Sum	1.98	2.01	2.00		1.99	2.01	2.00		1.99	2.00	2.00		1.99	2.00	2.00		1.99	2.00	2.00	
Endment																				
En	35.44	50.50	47.51		42.36	47.78	41.10		45.40	46.90	44.50		43.69	48.21	46.50		42.16	46.25	45.60	
Fs	4.09	13.81	9.22		3.04	12.23	10.45		4.27	7.86	8.08		6.73	10.67	9.62		4.76	8.85	8.33	
Wo	39.18	51.63	43.27		42.80	50.91	48.45		46.54	49.78	47.42		41.35	48.27	43.88		45.57	50.64	46.07	

*n* = number of analysis, 1σ = one sigma standard deviation  
b.d. = below detection limit  
<sup>#</sup>Fe<sub>2</sub>O<sub>3</sub> calculated based on stoichiometry after Robinson [1982]  
Mg# = Mg<sup>2+</sup>/(Mg<sup>2+</sup>+Fe<sup>2+</sup>) x 100 on a molar base



**Table 13.** Representative amphibole composition (wt%) of the gabbroic dikes, dark veins, and epidote veins.

gabbroic dikes															
<i>Pargasite (VHT)</i>				<i>Hornblende (HT)</i>				<i>Actinolite (MT)</i>				<i>Cl-rich amphibole (HT)</i>			
<i>n</i>	<i>Min</i>	<i>Max</i>	<i>Mean</i>	<i>Min</i>	<i>Max</i>	<i>Mean</i>	<i>Min</i>	<i>Max</i>	<i>Mean</i>	<i>Min</i>	<i>Max</i>	<i>Mean</i>	<i>Min</i>	<i>Max</i>	<i>Mean</i>
			212 1σ			85 1σ			5 1σ			33 1σ			
SiO <sub>2</sub>	40.66	44.60	42.24 (0.82)	37.90	53.85	45.67 (2.82)	49.99	50.96	50.43 (0.34)	38.40	43.28	40.32 (1.46)			
TiO <sub>2</sub>	2.62	4.99	4.03 (0.63)	0.12	2.59	1.15 (0.73)	b.d.	0.05	0.04 (0.00)	0.17	1.04	0.55 (0.24)			
Al <sub>2</sub> O <sub>3</sub>	8.96	12.69	11.57 (0.59)	1.78	15.05	9.89 (2.43)	2.57	3.23	2.86 (0.29)	11.00	15.49	13.76 (0.99)			
Cr <sub>2</sub> O <sub>3</sub>	b.d.	0.56	0.18 (0.15)	b.d.	0.31	0.08 (0.07)	b.d.	b.d.	b.d.	b.d.	0.37	0.12 (0.08)			
FeO <sup>tot</sup>	8.95	12.61	10.60 (0.91)	8.03	18.05	10.15 (2.21)	20.41	20.76	20.54 (0.15)	10.73	18.63	14.84 (2.32)			
MnO	0.05	0.23	0.13 (0.02)	0.04	0.39	0.14 (0.06)	0.62	0.76	0.71 (0.05)	0.04	0.18	0.10 (0.02)			
MgO	12.74	16.00	14.14 (0.76)	9.12	18.51	15.79 (1.80)	9.93	10.45	10.09 (0.21)	8.33	13.96	10.91 (1.77)			
CaO	11.06	12.41	11.68 (0.26)	10.63	12.94	12.06 (0.38)	11.70	12.11	11.91 (0.17)	12.04	12.55	12.30 (0.13)			
Na <sub>2</sub> O	1.78	3.51	2.73 (0.26)	0.41	2.77	2.14 (0.54)	0.28	0.43	0.33 (0.06)	1.91	2.91	2.43 (0.23)			
K <sub>2</sub> O	0.08	0.93	0.26 (0.16)	0.03	0.67	0.18 (0.15)	0.02	0.05	0.03 (0.01)	0.15	0.76	0.43 (0.18)			
F	0.06	0.22	0.15 (0.03)	0.09	0.24	0.15 (0.02)	0.20	0.26	0.22 (0.02)	0.08	0.27	0.17 (0.03)			
Cl	0.01	0.20	0.05 (0.04)	0.01	4.70	0.53 (0.99)	0.02	0.03	0.03 (0.00)	1.62	4.88	3.25 (1.02)			
-O=F+Cl	0.03	0.13	0.08	0.05	1.16	0.18	0.09	0.11	0.10	0.41	1.21	0.80			
Total	95.54	99.00	97.69	96.00	100.13	97.74	96.66	97.69	97.12	95.65	99.28	98.39			
H <sub>2</sub> O <sub>calc</sub>	1.88	2.03	1.97	0.62	2.05	1.88	1.86	1.90	1.88	0.55	1.56	1.07			
Total <sub>calc</sub>	97.44	101.02	99.65	97.96	100.93	99.62	98.53	99.59	99.00	96.45	100.45	99.46			
Mg#	66.67	81.88	72.74 (3.22)	53.63	87.95	79.36 (7.61)	47.75	52.07	49.47 (1.63)	48.86	74.56	61.64 (7.42)			
<i>chemical formula based on 23 oxygen</i>															
Si	5.99	6.58	6.18	5.86	7.76	6.60	7.49	7.69	7.59	5.91	6.41	6.11			
<sup>IV</sup> Al	1.42	2.01	1.82	0.24	2.14	1.40	0.31	0.51	0.41	1.59	2.09	1.89			
<sup>VI</sup> Al	0.08	0.30	0.18	0.02	0.66	0.29	0.04	0.15	0.10	0.33	0.76	0.57			
Ti	0.29	0.55	0.44	0.01	0.28	0.12	-	0.01	-	0.02	0.12	0.06			
Fe <sup>2+</sup>	0.71	1.45	1.14	0.42	1.80	0.84	2.15	2.45	2.31	1.05	2.03	1.52			
Fe <sup>3+</sup>	-	0.45	0.14	0.04	0.62	0.35	0.13	0.41	0.27	0.14	0.49	0.37			
Mg	2.84	3.43	3.09	2.07	3.90	3.40	2.22	2.34	2.26	1.94	3.09	2.46			
Mn	-	0.02	-	-	0.03	0.00	0.03	0.06	0.05	-	0.02	0.01			
Fe <sup>2+</sup>	-	0.07	0.02	-	0.19	0.04	-	-	-	-	0.02	-			
Mn	-	0.03	0.01	-	0.04	0.02	0.03	0.06	0.04	-	0.02	-			
Cr	-	0.03	0.01	-	0.02	-	-	-	-	-	0.02	0.01			
Ca	1.73	1.93	1.83	1.61	2.05	1.87	1.89	1.94	1.92	1.92	2.10	2.00			
Na	0.05	0.21	0.13	-	0.17	0.07	0.03	0.04	0.04	-	0.04	0.01			
Na	0.40	0.85	0.65	0.07	0.73	0.53	0.04	0.10	0.06	0.56	0.84	0.71			
K	0.01	0.18	0.05	0.01	0.13	0.03	0.00	0.01	0.01	0.03	0.15	0.08			
Sum <sub>A-site</sub>	0.55	0.89	0.70	0.08	0.86	0.56	0.05	0.10	0.07	0.65	0.90	0.79			
Sum <sub>cations</sub>	15.55	15.84	15.69	15.08	15.88	15.56	15.05	15.10	15.07	15.65	15.90	15.80			
F	0.03	0.10	0.07	0.04	0.12	0.07	0.10	0.12	0.11	0.04	0.13	0.08			
Cl	-	0.05	0.01	-	1.24	0.13	0.01	0.01	0.01	0.41	1.29	0.84			
OH	1.85	1.96	1.92	0.65	1.95	1.80	1.87	1.90	1.89	0.57	1.54	1.08			

*n* = number of analysis, 1σ = one sigma standard deviation  
b.d. = below detection limit  
**Amphibole classification** (after *Leake et al. [1994] (Temperature scheme)*): VHT = very high temperature; HT = high temperature; MT = medium temperature  
Mg# = Mg<sup>2+</sup>/(Mg<sup>2+</sup>+Fe<sup>2+</sup>) x 100 on a molar base

**Table 13.** (continued)

Dark veins																				
	Pargasite (VHT)				Hornblende (HT)				Actinolite (MT)				Cl-rich amphibole (HT)							
<i>n</i>	Min	Max	Mean	6σ	1σ	Min	Max	Mean	240	1σ	Min	Max	Mean	22	1σ	Min	Max	Mean	10	1σ
SiO <sub>2</sub>	41.79	44.36	42.60	(0.45)		43.72	55.52	50.63	(2.58)		45.69	51.99	48.25	(1.58)		39.30	45.27	42.01	(2.59)	
TiO <sub>2</sub>	2.64	4.61	4.03	(0.45)		0.11	2.58	0.98	(0.55)		b.d.	0.09	0.06	(0.02)		0.43	1.48	0.96	(0.49)	
Al <sub>2</sub> O <sub>3</sub>	10.05	11.74	11.22	(0.31)		0.98	10.80	5.24	(2.28)		3.74	11.38	8.42	(2.06)		8.84	11.07	10.18	(0.85)	
Cr <sub>2</sub> O <sub>3</sub>	b.d.	0.18	0.04	(0.03)		b.d.	0.26	0.07	(0.06)		b.d.	0.06	0.02	(0.01)		b.d.	0.14	0.07	(0.04)	
Fe <sup>tot</sup>	10.03	12.52	11.16	(0.42)		7.40	17.41	9.98	(1.40)		6.03	11.21	8.71	(2.10)		13.64	21.60	17.48	(3.63)	
MnO	0.09	0.21	0.14	(0.02)		0.08	0.56	0.18	(0.06)		0.03	0.33	0.14	(0.08)		0.06	0.14	0.10	(0.02)	
MgO	13.26	15.69	14.06	(0.48)		14.59	20.52	17.30	(1.09)		14.45	18.88	16.92	(1.36)		7.88	13.37	10.72	(2.48)	
CaO	11.00	12.39	11.52	(0.28)		2.40	12.85	11.74	(0.92)		11.95	12.99	12.55	(0.29)		11.57	12.02	11.74	(0.14)	
Na <sub>2</sub> O	1.97	2.77	2.47	(0.18)		0.20	2.42	1.10	(0.51)		0.64	2.23	1.58	(0.46)		1.95	2.62	2.36	(0.22)	
K <sub>2</sub> O	0.11	0.74	0.28	(0.13)		0.01	0.44	0.17	(0.09)		0.04	0.21	0.11	(0.05)		0.20	0.80	0.48	(0.27)	
F	0.01	0.20	0.10	(0.06)		0.01	0.22	0.14	(0.03)		0.07	0.18	0.12	(0.02)		0.14	0.25	0.18	(0.04)	
Cl	0.03	0.13	0.07	(0.02)		b.d.	0.47	0.11	(0.10)		0.00	0.41	0.25	(0.13)		0.91	4.42	2.59	(1.60)	
-O=F+Cl	0.01	0.11	0.06			0.04	0.17	0.08			0.05	0.14	0.10			0.27	1.10	0.66		
Total	96.46	99.23	97.64			95.96	99.62	97.56			96.17	97.95	97.01			97.42	99.13	98.22		
H <sub>2</sub> O <sub>calc</sub>	1.93	2.05	1.99			1.91	2.10	2.02			1.93	2.02	1.98			0.66	1.73	1.23		
Total <sub>calc</sub>	98.44	101.22	99.63			97.97	101.71	99.57			98.10	99.91	98.99			99.09	99.91	99.44		
Mg#	67.54	80.80	72.87	(2.35)		65.70	87.10	80.19	(3.43)		73.61	91.90	83.52	(6.35)		44.39	67.80	56.79	(10.4)	
<i>chemical formula based on 23 oxygen</i>																				
Si	6.13	6.43	6.23			6.34	7.88	7.23			6.56	7.49	6.92			6.19	6.71	6.40		
<sup>IV</sup> Al	1.57	1.87	1.77			0.12	1.66	0.77			0.51	1.44	1.08			1.29	1.81	1.60		
<sup>VI</sup> Al	0.11	0.29	0.17			0.01	0.44	0.11			0.12	0.51	0.35			0.20	0.28	0.24		
Ti	0.29	0.51	0.44			0.01	0.28	0.11			-	0.01	0.01			0.05	0.17	0.11		
Fe <sup>2+</sup>	0.75	1.39	1.10			0.48	1.64	0.82			0.33	1.12	0.70			1.36	2.32	1.81		
Fe <sup>3+</sup>	0.02	0.44	0.22			0.03	0.57	0.28			0.20	0.50	0.33			0.22	0.61	0.41		
Mg	2.91	3.38	3.07			3.15	4.40	3.68			3.12	3.99	3.62			1.85	2.95	2.43		
Mn	-	0.01	0.00			-	0.01	-			-	0.02	0.00			-	0.01	-		
Fe <sup>2+</sup>	-	0.10	0.04			-	1.51	0.09			-	0.06	0.02			-	0.05	0.02		
Mn	-	0.03	0.02			-	0.07	0.02			-	0.03	0.01			-	0.02	0.01		
Cr	-	0.01	-			-	0.01	-			-	-	-			-	0.01	0.00		
Ca	1.72	1.93	1.81			0.37	1.99	1.80			1.84	2.01	1.93			1.84	1.99	1.92		
Na	0.04	0.20	0.13			0.01	0.19	0.09			-	0.08	0.04			0.00	0.10	0.04		
Na	0.48	0.63	0.57			0.01	0.56	0.21			0.14	0.59	0.40			0.49	0.78	0.66		
K	0.02	0.14	0.05			-	0.08	0.03			0.01	0.04	0.02			0.04	0.16	0.10		
Sum <sub>A-site</sub>	0.54	0.67	0.62			0.01	0.59	0.25			0.15	0.62	0.42			0.53	0.93	0.75		
Sum <sub>cations</sub>	15.54	15.67	15.62			15.01	15.59	15.25			15.15	15.62	15.42			15.53	15.93	15.75		
F	-	0.09	0.05			-	0.10	0.06			0.03	0.08	0.05			0.06	0.13	0.09		
Cl	0.01	0.03	0.02			-	0.11	0.03			-	0.10	0.06			0.23	1.18	0.68		
OH	1.88	1.99	1.94			1.83	1.95	1.91			1.85	1.95	1.89			0.69	1.71	1.23		

*n* = number of analysis, 1σ = one sigma standard deviation  
b.d. = below detection limit  
**Amphibole classification** (after Leake et al. [1994] (**Temperature scheme**)): VHT = very high temperature; HT = high temperature; MT = medium temperature  
Mg# = Mg<sup>2+</sup> / (Mg<sup>2+</sup> + Fe<sup>2+</sup>) x 100 on a molar base

**Table 13.** (continued)

Epidote veins									
	Hornblende (HT)				Actinolite (MT)				
	Min	Max	Mean	21 1σ	Min	Max	Mean	20 1σ	
<i>n</i>									
SiO <sub>2</sub>	50.32	55.26	52.11	(1.12)	52.08	58.46	54.40	(1.81)	
TiO <sub>2</sub>	0.10	1.07	0.68	(0.22)	b.d.	0.05	b.d.		
Al <sub>2</sub> O <sub>3</sub>	2.26	3.70	3.22	(0.41)	0.91	5.98	2.37	(1.48)	
Cr <sub>2</sub> O <sub>3</sub>	b.d.	0.04	b.d.		b.d.	0.09	0.02	(0.02)	
FeO <sup>tot</sup>	7.75	13.00	11.80	(1.03)	1.80	18.23	10.66	(5.58)	
MnO	0.15	0.32	0.27	(0.04)	0.04	0.19	0.12	(0.03)	
MgO	16.11	18.69	16.82	(0.51)	11.76	23.14	16.75	(3.68)	
CaO	10.83	13.03	11.49	(0.47)	12.43	13.82	13.07	(0.42)	
Na <sub>2</sub> O	0.24	0.78	0.59	(0.13)	0.01	0.97	0.23	(0.27)	
K <sub>2</sub> O	0.01	0.27	0.19	(0.05)	b.d.	0.04	b.d.		
F	0.09	0.20	0.14	(0.02)	0.04	0.19	0.12	(0.04)	
Cl	b.d.	0.21	0.16	(0.04)	b.d.	0.01	b.d.		
-O=F+Cl	0.04	0.11	0.10		0.02	0.08	0.05		
Total	95.92	98.43	97.38		96.85	98.78	97.73		
H <sub>2</sub> O <sub>calc</sub>	1.93	2.09	1.98		1.94	2.19	2.05		
Total <sub>calc</sub>	97.85	100.43	99.36		98.93	100.97	99.78		
Mg#	72.33	81.86	75.01	(1.96)	53.47	95.74	74.01	(14.0)	
<i>chemical formula based on 23 oxygen</i>									
Si	7.35	7.76	7.50		7.36	7.92	7.75		
<sup>IV</sup> Al	0.24	0.65	0.50		0.08	0.64	0.25		
<sup>VI</sup> Al	-0.02	0.16	0.04		0.04	0.36	0.15		
Ti	0.01	0.12	0.07		-	0.01	-		
Fe <sup>2+</sup>	0.87	1.21	1.06		0.20	2.26	1.24		
Fe <sup>3+</sup>	0.04	0.33	0.22		0.00	0.21	0.04		
Mg	3.46	3.91	3.61		2.60	4.67	3.54		
Mn	-	0.01	-		0.00	0.02	0.01		
Fe <sup>2+</sup>	-	0.24	0.14		-	-	-		
Mn	0.01	0.04	0.03		-	0.01	-		
Cr	-	-	-		-	0.01	-		
Ca	1.66	1.96	1.77		1.96	2.08	2.00		
Na	-	0.09	0.06		0.00	0.03	0.01		
Na	0.04	0.21	0.11		0.00	0.25	0.06		
K	0.00	0.05	0.03		0.00	0.01	0.00		
Sum <sub>A-site</sub>	0.04	0.26	0.14		0.00	0.26	0.06		
Sum <sub>cations</sub>	15.04	15.29	15.15		14.97	15.26	15.06		
F	0.04	0.09	0.06		0.02	0.09	0.05		
Cl	-	0.05	0.04		-	-	-		
OH	1.88	1.96	1.90		1.91	1.98	1.95		

*n* = number of analysis, 1σ = one sigma standard deviation

b.d. = below detection limit

**Amphibole classification** (after Leake *et al.* [1994])

**(Temperature scheme):** VHT = very high temperature; HT = high temperature;

MT = medium temperature

Mg# =  $Mg^{2+}/(Mg^{2+}+Fe^{2+}) \times 100$  on a molar base

**Table 14.** Representative composition (wt%) of magnetite and ilmenite in gabbroic dikes and dark veins from the Wadi Wariyah.

<i>n</i>	<b>Magnetite</b>						<b>Ilmenite</b>						
	gabbroic dikes			dark veins			gabbroic dikes			dark veins			
	Min	Max	Mean	Min	Max	Mean	Min	Max	Mean	Min	Max	Mean	1σ
			33			54			70			64	1σ
SiO <sub>2</sub>	b.d.	1.55	0.10 (0.27)	b.d.	0.71	0.05 (0.11)	b.d.	0.32	0.02 (0.05)	b.d.	0.24	0.02 (0.03)	
TiO <sub>2</sub>	0.23	4.04	1.10 (1.01)	0.10	4.87	1.44 (1.14)	45.94	51.94	49.67 (1.22)	45.18	51.71	49.56 (1.41)	
Al <sub>2</sub> O <sub>3</sub>	0.24	5.63	1.01 (1.10)	0.27	3.39	1.30 (0.95)	b.d.	3.90	0.09 (0.46)	b.d.	3.50	0.19 (0.53)	
Cr <sub>2</sub> O <sub>3</sub>	0.26	0.73	0.47 (0.13)	0.07	6.05	2.79 (1.59)	b.d.	0.24	0.08 (0.07)	b.d.	1.54	0.23 (0.33)	
V <sub>2</sub> O <sub>3</sub>	b.d.	3.30	1.30 (0.92)	b.d.	1.50	0.55 (0.62)	b.d.	1.53	0.90 (0.51)	b.d.	1.45	0.62 (0.58)	
Fe <sub>2</sub> O <sub>3</sub> <sup>#</sup>	57.30	68.07	64.33 (2.56)	52.33	67.49	61.50 (4.51)	2.14	12.89	6.03 (1.93)	3.03	11.62	6.01 (1.69)	
FeO	30.83	33.82	32.04 (0.91)	30.91	34.87	32.15 (0.89)	39.22	44.91	41.38 (1.30)	34.52	42.22	40.49 (1.45)	
MnO	b.d.	0.15	0.06 (0.04)	b.d.	0.36	0.04 (0.06)	0.79	3.88	1.62 (0.85)	0.74	2.44	1.50 (0.44)	
MgO	b.d.	0.75	0.14 (0.16)	b.d.	0.66	0.25 (0.21)	0.03	3.02	0.92 (0.94)	0.03	3.48	1.41 (1.10)	
CaO	b.d.	0.42	0.04 (0.08)	b.d.	0.22	0.04 (0.05)	b.d.	0.39	0.04 (0.08)	b.d.	0.29	0.05 (0.06)	
Total			100.58			100.18			100.75			100.08	
X			96.68 (2.11)			95.20 (3.07)			94.23 (1.52)			94.35 (1.30)	
<i>formula based on 4 oxygen (Magnetite) or 3 oxygen (Ilmenite)</i>													
Ti			0.03			0.04			0.94			0.93	
Al			0.05			0.06			0.00			0.01	
Cr			0.01			0.08			0.00			0.00	
Fe <sup>3+</sup>			1.85			1.76			0.11			0.11	
Fe <sup>2+</sup>			1.02			1.02			0.87			0.85	
Mn			-			-			0.03			0.03	
V			0.02			0.01			0.01			0.01	
Mg			0.01			0.01			0.03			0.05	
Ca			-			-			-			-	
Sum			3.00			3.00			2.00			2.00	

*n* = number of analysis, 1σ = one sigma standard deviation

b.d. = below detection limit

<sup>#</sup>Fe<sub>2</sub>O<sub>3</sub> calculated based on stoichiometryX = endmember composition = ilmenite: X<sub>ILM</sub>; magnetite: X<sub>UNSP</sub> based on calculation of Stormer [1984]

**Table 15.** Composition (wt%) of apatite in the dark veins from the Wadi Wariyah.

Sample	Wa_47A		Wa_77A		Wa_58A		Wa_46AA		Wa_66A	
	<i>n</i>	1σ	<i>n</i>	1σ	<i>n</i>	1σ	<i>n</i>	1σ	<i>n</i>	1σ
P <sub>2</sub> O <sub>5</sub>	40.50	(0.34)	41.08	(0.25)	41.44	(0.31)	40.74	(0.26)	41.02	(0.36)
SiO <sub>2</sub>	0.08	(0.03)	0.12	(0.04)	0.12	(0.04)	0.26	(0.09)	0.10	(0.02)
FeO <sup>#</sup>	0.05	(0.04)	0.06	(0.04)	0.05	(0.05)	0.16	(0.03)	0.11	(0.07)
MnO	0.04	(0.03)	0.02	(0.02)	0.03	(0.03)	0.04	(0.01)	0.04	(0.03)
CaO	53.94	(0.41)	55.34	(0.18)	55.03	(0.38)	55.47	(0.36)	55.05	(0.56)
Na <sub>2</sub> O	0.05	(0.02)	b.d.		b.d.		b.d.		b.d.	
F	1.08	(0.03)	0.03	(0.02)	0.04	(0.02)	0.13	(0.06)	0.43	(0.09)
Cl	3.34	(0.17)	0.87	(0.27)	1.40	(0.23)	2.03	(0.33)	1.69	(0.53)
-O=F+Cl	1.21		0.21		0.33		0.51		0.56	
Total	98.71		96.00		96.76		97.67		97.38	
H <sub>2</sub> O <sub>calc</sub>	0.37		1.52		1.39		1.18		1.12	
Total	99.08		97.52		98.15		98.85		98.50	
<i>chemical formula based on 25 oxygen</i>										
Ca	10.04		10.11		10.03		10.15		10.09	
Mn	0.01		-		-		0.01		0.01	
Fe	0.01		0.01		0.01		0.02		0.02	
Na	0.01		-		-		-		-	
P	5.96		5.93		5.97		5.89		5.94	
Si	0.01		0.02		0.02		0.04		0.02	
Sum cations	16.04		16.08		16.03		16.12		16.07	
<i>X</i> (FAp)	0.30		0.01		0.01		0.03		0.12	
<i>X</i> (ClAp)	0.49		0.13		0.20		0.29		0.25	
<i>X</i> (HAp)	0.21		0.87		0.79		0.67		0.64	

*n* = number of analysis, 1σ = one sigma standard deviation  
b.d. = below detection limit  
\*assuming Cl + F + OH = 2  
<sup>#</sup>total iron reported as FeO

**Table 16.** Representative composition (wt%) of chlorite in the epidote/prehnite veins and altered gabbros.

	epidote veins		prehnite veins		altered gabbro		highly altered gabbro		An-bearing metagabbro	
	<i>n</i>	1σ		1σ		1σ		1σ		1σ
SiO <sub>2</sub>	35	(1.24)	33	(0.13)	151	(2.60)	15	(0.04)	30	(0.46)
Al <sub>2</sub> O <sub>3</sub>	19.59	(0.52)	20.18	(0.20)	17.66	(1.94)	19.48	(0.69)	19.56	(0.78)
Fe <sub>2</sub> O <sub>3</sub>	1.40	(0.34)	1.89	(0.70)	1.83	(1.65)	1.39	(0.40)	1.17	(0.40)
FeO	9.17	(0.56)	7.57	(1.43)	8.94	(1.44)	9.62	(0.52)	9.56	(0.80)
MnO	0.13	(0.02)	0.09	(0.01)	0.11	(0.02)	0.10	(0.00)	0.10	(0.02)
MgO	26.09	(0.41)	26.46	(2.26)	26.27	(1.41)	26.04	(0.60)	26.28	(0.45)
CaO	0.25	(0.14)	0.17	(0.06)	0.26	(0.26)	0.14	(0.10)	0.12	(0.10)
Na <sub>2</sub> O	0.02	(0.01)	b.d.		0.04	(0.03)	0.02	(0.02)	b.d.	
K <sub>2</sub> O	0.02	(0.00)	b.d.		0.04	(0.06)	0.01	(0.00)	b.d.	
F	0.13	(0.00)	0.14	(0.01)	0.11	(0.05)	0.14	(0.00)	0.01	(0.01)
Cl	b.d.		b.d.		b.d.		b.d.		b.d.	
H <sub>2</sub> O <sub>calc</sub>	12.16		12.26		12.19		12.15		12.31	
Total	99.38		99.52		99.43		99.54		99.68	
O=F,Cl	0.06		0.06		0.05		0.06		0.01	
Total <sub>calc</sub>	99.32		99.46		99.38		99.48		99.67	
Mg#	83.52		86.17		83.98		82.82		83.05	
<i>chemical formula based on 28 oxygen</i>										
Si	5.94		5.96		6.25		5.95		5.93	
<sup>[IV]</sup> Al	2.06		2.04		1.75		2.05		2.07	
<sup>[VI]</sup> Al	2.48		2.60		2.34		2.46		2.44	
Fe <sup>3+</sup>	0.21		0.28		0.27		0.20		0.17	
Fe <sup>2+</sup>	1.50		1.23		1.46		1.58		1.56	
Mn	0.02		0.02		0.02		0.02		0.02	
Mg	7.62		7.67		7.68		7.60		7.65	
Ca	0.05		0.03		0.06		0.03		0.03	
Na	0.02		-		0.03		0.02		-	
K	0.01		-		0.02		0.01		-	
F	0.17		0.17		0.14		0.18		0.02	
Cl	-		-		-		-		-	
OH*	15.83		15.82		15.86		15.82		15.98	
Sum	35.92		35.86		35.89		35.91		35.90	

*n* = number of analysis, 1σ = one sigma standard deviation  
b.d. = below detection limit  
\*assuming Cl + F + OH = 16  
Mg# = Mg<sup>2+</sup>/(Mg<sup>2+</sup>+Fe<sup>2+</sup>) x 100 on a molar base

**Table 17.** Representative composition (wt%) of epidote, prehnite, and pumpellyite in the epidote/prehnite veins and altered gabbros.

core/rim	Epidote						Prehnite			Pumpellyite						
	Epidote veins			highly altered gabbro			An-bearing metagabbro			Epidote veins		Epidote veins				
	core	1 $\sigma$	rim	11	5	14	130	80	1 $\sigma$	30	1 $\sigma$					
n	53		24	1 $\sigma$												
SiO <sub>2</sub>	38.83	(0.19)	38.21	(0.40)	39.58	(0.77)	38.15	(0.17)	39.67	(0.46)	43.23	(0.31)	39.71	(3.86)		
TiO <sub>2</sub>	b.d.		0.12	(0.14)	0.04	(0.02)	0.09	(0.01)	0.02	(0.03)	0.02	(0.01)	0.04	(0.00)		
Al <sub>2</sub> O <sub>3</sub>	28.29	(0.75)	25.94	(1.36)	31.20	(0.82)	27.55	(0.79)	24.03	(0.40)	24.03	(0.40)	23.87	(0.01)		
Fe <sub>2</sub> O <sub>3</sub>	6.65	(0.96)	9.24	(1.55)	2.80	(0.36)	8.00	(1.00)	-		0.14	(0.09)	-	1.28	(0.94)	
FeO	-		-		-		-		0.06	(0.00)	0.02	(0.00)	-	-		
MnO	0.07	(0.02)	0.02	(0.01)	0.06	(0.03)	0.02	(0.02)	0.03	(0.01)	0.02	(0.00)	0.02	(0.00)	0.08	(0.05)
MgO	0.15	(0.08)	0.05	(0.08)	0.04	(0.02)	0.02	(0.02)	0.06	(0.14)	0.04	(0.03)	0.04	(0.03)	3.40	(2.28)
CaO	24.21	(0.18)	24.08	(0.28)	24.67	(0.18)	24.25	(0.17)	24.76	(0.27)	26.98	(0.19)	26.94	(0.13)	23.69	(1.34)
Na <sub>2</sub> O	b.d.		b.d.		b.d.		0.02	(0.01)	b.d.		0.08	(0.03)	0.02	(0.00)	0.07	(0.08)
F	0.06	(0.01)	0.09	(0.02)	0.02	(0.01)	0.06	(0.02)	b.d.		b.d.		b.d.		b.d.	
H <sub>2</sub> O <sub>calc</sub>	1.91		1.86		1.96		1.89		3.95		3.94		3.94		7.61	
Total	100.24		99.65		100.39		100.16		98.54		98.14		98.14		100.95	
O=F,Cl	0.03		0.04		0.01		0.03		-		-		-		-	
Total <sub>calc</sub>	100.21		99.62		100.39		100.13		98.54		98.14		98.14		100.95	
<i>chemical formula based on 12.5 oxygen</i>																
Si	3.03		2.98		3.08		2.97		6.60		6.59		6.59		6.26	
Al <sub>total</sub>	2.60		2.38		2.87		2.53		4.32		4.30		4.30		4.66	
Fe <sup>2+</sup>	-		-		-		-		0.02		0.01		0.01		0.08	
Fe <sup>3+</sup>	0.39		0.54		0.16		0.47		-		-		-		-	
Mn	-		-		-		-		-		-		-		0.01	
Mg	0.02		0.01		-		-		0.01		0.01		0.01		0.80	
Ca	2.02		2.01		2.06		2.02		4.41		4.41		4.41		4.00	
Na	-		-		-		-		0.02		0.01		0.01		0.04	
F	0.01		0.02		-		0.02		-		-		-		-	
OH*	0.99		0.98		1.00		0.98		4.00		4.00		4.00		8.00	
Sum	9.06		8.93		9.19		9.02		19.40		19.32		19.32		23.86	
X Fe	0.13		0.19		0.05		0.16		-		-		-		-	
<i>chemical formula based on 24 oxygen</i>																
<i>chemical formula based on 24.5 oxygen</i>																

n = number of analysis, 1 $\sigma$  = one sigma standard deviation

b.d. = below detection limit

X Fe = Fe<sup>3+</sup>/(Al<sup>3+</sup>+Fe<sup>3+</sup>)

Table 18. Trace element concentration (ppm) of plagioclase from the Wadi Wariyah.

Sample	core/rim	n	Sc	Ti	Co	Rb	Sr	Y	Ba	La	Ce	Pr	Nd	Sm	Eu	Gd	Tb	Dy	Ho	Er	Tm	Yb	Lu	Hf	Pb	An	ΣREE		
<b>layered gabbro</b>																													
Wa_63B	core	9	0.712 (0.169)	178 (6.41)	0.348 (0.048)	b.d.	279 (6.91)	0.135 (0.025)	3.77 (0.244)	0.112 (0.009)	0.265 (0.018)	0.037 (0.008)	0.184 (0.030)	b.d.	0.199 (0.029)	b.d.	0.009 (0.005)	b.d.	b.d.	b.d.	b.d.	b.d.	b.d.	b.d.	b.d.	b.d.	b.d.	83.16	0.81
Wa_47B	core	3	0.687 (0.456)	169 (10.4)	0.340 (0.171)	0.173 (0.243)	265 (5.63)	0.089 (0.028)	3.42 (0.882)	0.089 (0.010)	0.201 (0.003)	0.033 (0.001)	0.144 (0.018)	0.080 (0.038)	0.158 (0.042)	b.d.	b.d.	b.d.	b.d.	b.d.	b.d.	b.d.	b.d.	b.d.	0.068 (0.036)	81.33	0.71		
Wa_46B	core	4	0.513 (0.147)	165 (16.1)	0.285 (0.071)	b.d.	286 (18.7)	0.135 (0.025)	4.20 (0.709)	0.105 (0.010)	0.231 (0.006)	0.032 (0.008)	0.198 (0.064)	b.d.	0.167 (0.010)	b.d.	b.d.	0.044 (0.017)	b.d.	b.d.	b.d.	b.d.	b.d.	b.d.	0.112 (0.114)	82.36	0.78		
Wa_42B	core	4	0.644 (0.158)	210 (71.9)	0.185 (0.088)	b.d.	271 (6.28)	0.160 (0.085)	2.98 (0.284)	0.090 (0.023)	0.263 (0.045)	0.043 (0.011)	0.181 (0.036)	b.d.	0.141 (0.021)	b.d.	0.007 (0.004)	0.043 (0.026)	b.d.	b.d.	b.d.	b.d.	b.d.	b.d.	b.d.	b.d.	83.05	0.77	
<b>gabbroic dikes</b>																													
Wa_46A	core	2	2.50 (1.03)	1033 (38.7)	2.17 (1.05)	0.102 (0.058)	365 (14.5)	2.42 (1.30)	47.1 (4.47)	3.69 (0.487)	7.05 (0.304)	0.799 (0.019)	3.19 (0.212)	0.654 (0.215)	0.911 (0.048)	0.557 (0.135)	0.085 (0.057)	0.351 (0.179)	0.101 (0.047)	0.224 (0.136)	0.031 (0.008)	0.189 (0.051)	0.031 (0.018)	0.105 (0.087)	1.03 (0.062)	72.60	17.85		
Wa_46A	rim	1	5.46	1098	5.74	0.137	301	6.31	49.4	2.68	6.32	0.879	3.92	1.02	0.819	0.931	1.140	1.04	0.213	0.725	0.114	1.01	0.123	0.104	0.786	51.84	19.93		
Wa_46A	core	2	0.370 (0.282)	276 (18.8)	0.205 (0.035)	0.150 (0.066)	337 (0.091)	0.385 (0.029)	58.2 (3.49)	2.65 (0.13)	4.25 (0.049)	0.453 (0.006)	1.54 (0.014)	0.234 (0.034)	0.672 (0.016)	0.186 (0.009)	0.016 (0.01)	0.077 (0.019)	0.017 (0.000)	0.036 (0.032)	b.d.	b.d.	b.d.	b.d.	b.d.	0.869 (0.039)	51.02	10.12	
Wa_46A	core	4	0.286 (0.084)	227 (17.4)	0.479 (0.523)	b.d.	323 (32.3)	0.442 (0.054)	74.6 (6.08)	3.32 (0.29)	5.47 (0.374)	0.545 (0.049)	1.99 (0.132)	0.305 (0.072)	0.898 (0.042)	0.187 (0.019)	0.021 (0.008)	0.078 (0.036)	0.013 (0.007)	0.047 (0.025)	b.d.	b.d.	b.d.	b.d.	b.d.	0.901 (0.046)	44.08	12.87	
Wa_42A	core	3	0.603 (0.015)	229 (14.8)	1.450 (1.05)	0.152 (0.085)	354 (6.51)	0.255 (0.047)	9.77 (0.203)	0.244 (0.067)	0.62 (0.187)	0.085 (0.021)	0.39 (0.089)	0.107 (0.035)	0.395 (0.019)	0.104 (0.034)	b.d.	0.040 (0.028)	0.012 (0.003)	b.d.	b.d.	b.d.	b.d.	b.d.	b.d.	0.223 (0.036)	84.79	2.00	
Wa_42A	core	3	0.347 (0.160)	142 (16.1)	0.274 (0.043)	b.d.	394 (11.2)	0.152 (0.039)	13.3 (0.875)	0.855 (0.032)	1.40 (0.186)	0.148 (0.019)	0.54 (0.198)	0.113 (0.058)	0.442 (0.030)	0.064 (0.014)	b.d.	0.046 (0.030)	b.d.	b.d.	b.d.	b.d.	b.d.	b.d.	b.d.	0.236 (0.040)	84.79	3.60	
Wa_42A	core	3	0.372 (0.054)	162 (28.9)	0.303 (0.211)	0.102 (0.059)	378 (5.86)	0.129 (0.016)	14.4 (1.09)	0.827 (0.009)	1.46 (0.122)	0.173 (0.031)	0.69 (0.033)	0.136 (0.052)	0.450 (0.047)	0.081 (0.045)	b.d.	0.045 (0.004)	b.d.	b.d.	b.d.	b.d.	b.d.	b.d.	b.d.	0.231 (0.019)	81.00	3.86	
<b>dark vein</b>																													
Wa_47A	core	5	0.418 (0.134)	312 (34.6)	0.259 (0.066)	0.496 (0.186)	307 (14.8)	0.717 (0.049)	88.2 (45.6)	3.42 (1.22)	6.09 (1.77)	0.640 (0.152)	2.43 (0.438)	0.389 (0.082)	1.519 (0.391)	0.282 (0.024)	0.030 (0.003)	0.163 (0.046)	0.024 (0.004)	0.076 (0.022)	b.d.	b.d.	b.d.	0.008 (0.006)	b.d.	1.37 (0.301)	45.56	15.08	
Wa_47A	core	5	0.347 (0.168)	159 (20.5)	0.213 (0.082)	0.180 (0.149)	148 (7.41)	0.346 (0.080)	27.2 (10.2)	1.20 (0.484)	2.15 (0.785)	0.247 (0.069)	0.89 (0.225)	0.158 (0.048)	0.562 (0.103)	0.130 (0.007)	0.012 (0.005)	0.065 (0.015)	0.012 (0.003)	0.030 (0.010)	0.003 (0.002)	0.028 (0.009)	0.004 (0.002)	b.d.	b.d.	0.469 (0.158)	56.25	5.50	
Wa_47A	core	4	0.379 (0.109)	392 (29.4)	0.186 (0.079)	0.138 (0.138)	335 (33.8)	0.488 (0.069)	33.1 (3.31)	1.45 (0.106)	2.73 (0.141)	0.345 (0.022)	1.51 (0.108)	0.252 (0.017)	0.883 (0.040)	0.187 (0.039)	0.029 (0.007)	0.137 (0.037)	0.019 (0.003)	0.036 (0.008)	0.008 (0.003)	0.032 (0.014)	b.d.	b.d.	b.d.	0.530 (0.062)	55.37	7.61	
Wa_47A	core	4	0.445 (0.149)	403 (27.4)	0.290 (0.088)	0.138 (0.058)	296 (15.6)	0.546 (0.047)	34.8 (4.76)	1.48 (0.094)	2.79 (0.083)	0.345 (0.011)	1.49 (0.121)	0.261 (0.064)	0.829 (0.093)	0.273 (0.075)	0.025 (0.006)	0.144 (0.037)	0.018 (0.003)	0.057 (0.015)	b.d.	b.d.	b.d.	b.d.	b.d.	0.549 (0.171)	56.33	7.70	
Wa_47A	core	3	0.411 (0.058)	405 (14.2)	b.d.	0.187 (0.038)	303 (10.2)	0.429 (0.025)	42.8 (7.22)	0.800 (0.080)	1.73 (0.173)	0.338 (0.022)	1.38 (0.144)	0.235 (0.033)	0.973 (0.057)	0.123 (0.025)	0.024 (0.005)	0.079 (0.048)	0.012 (0.004)	0.038 (0.017)	b.d.	b.d.	b.d.	b.d.	b.d.	0.669 (0.157)	53.35	7.43	
<b>An-bearing metagabbro</b>																													
Wa_69	core	7	0.506 (0.241)	24 (38.1)	0.196 (0.116)	b.d.	390 (37.9)	b.d.	0.586 (0.172)	b.d.	0.017 (0.010)	b.d.	b.d.	b.d.	b.d.	b.d.	b.d.	b.d.	b.d.	b.d.	b.d.	b.d.	b.d.	b.d.	b.d.	b.d.	97.15	0.02	

n = number of analysis, 1σ = one sigma standard deviation

b.d. = below detection limit

An = corresponding An content of the analysed plagioclase







**Table 20. (continued)**

Sample	Amph	T	n	Ti	Se	Co	Ni	Rb	Sr	Y	Zr	Nb	Ba	La	Ce	Pr	Nd	Sm	Eu	Gd	Tb	Dy	Ho	Er	Tm	Yb	Lu	Hf	Ta	Pb	
<b>epidote veins</b>																															
Wa_43	Act	MT	5	501	1.13	0.493	b.d.	b.d.	270	3.77	3.56	b.d.	0.110	1.01	2.37	0.322	1.57	0.458	0.223	0.566	0.093	0.653	0.135	0.403	0.056	0.38	0.052	0.079	b.d.	0.052	
			1 $\sigma$	(217)	(0.723)	(0.161)			(44.3)	(1.93)	(1.88)		(0.059)	(0.646)	(1.65)	(0.217)	(1.06)	(0.272)	(0.081)	(0.337)	(0.045)	(0.350)	(0.077)	(0.219)	(0.025)	(0.214)	(0.028)	(0.031)		(0.056)	
<b>Cl-rich amphiboles</b>																															
Wa_42	Clamph	HT	2	7518	72.7	44.8	196	0.649	260	17.1	15.3	0.133	36.7	0.723	3.08	0.585	4.14	1.91	0.892	2.64	0.476	3.38	0.695	1.92	0.266	1.75	0.240	0.628	0.009	0.074	
			1 $\sigma$	(531)	(10.8)	(12.7)	(5.17)	(0.130)	(35)	(0.162)	(1.91)	(0.142)	(24.9)	(0.266)	(0.813)	(0.113)	(0.325)	(0.155)	(0.086)	(0.226)	(0.011)	(0.339)	(0.057)	(0.007)	(0.016)	(0.134)	(0.013)	(0.125)	(0.008)	(0.041)	
Wa_42	Clamph	HT	1	3058	5.01	60.4	236	0.607	544	2.11	b.d.	b.d.	69.3	0.488	2.01	0.446	3.47	2.13	0.859	3.58	0.640	4.44	0.911	2.47	0.401	2.40	0.322	b.d.	b.d.	b.d.	
Wa_42	Clamph	HT	2	7222	80.2	48.8	201	0.586	248	19.4	16.2	0.136	38.3	0.742	3.01	0.608	4.22	2.06	0.849	2.88	0.551	4.02	0.817	2.20	0.313	1.92	0.288	0.685	0.009	b.d.	
			1 $\sigma$	(237)	(34.9)	(7.82)	(47.4)	(0.224)	(12.7)	(9.31)	(8.65)	(0.101)	(7.98)	(0.228)	(0.806)	(0.236)	(1.93)	(0.926)	(0.327)	(1.27)	(0.202)	(2.00)	(0.345)	(0.813)	(0.116)	(0.939)	(0.116)	(0.398)	(0.005)		

n = number of analysis, 1 $\sigma$  = one sigma standard deviation

b.d. = below detection limit

**Table 21.** Trace element concentration (ppm) of epidote and prehnite from the Wadi Wariyah.

Sample	Min	n	Ti	Sr	Y	Zr	Nb	Cs	Ba	La	Ce	Pr	Nd	Sm	Eu	Tb	Dy	Ho	Er	Tm	Yb	Lu
<b>Epidote veins</b>																						
Wa_43	Epi	4	1192 (859)	551 (215)	1.45 (1.42)	1.91 (2.00)	0.022 (0.024)	b.d.	0.238 (0.077)	0.343 (0.223)	0.612 (0.416)	0.071 (0.052)	0.297 (0.261)	0.103 (0.079)	0.386 (0.185)	0.173 (0.167)	0.211 (0.202)	0.049 (0.051)	0.135 (0.122)	0.025 (0.025)	0.168 (0.154)	0.027 (0.017)
Wa_43	Epi	5	1115 (667)	570 (70)	1.41 (1.07)	6.95 (3.83)	0.011 (0.006)	b.d.	0.177 (0.077)	0.276 (0.193)	0.551 (0.363)	0.077 (0.051)	0.343 (0.252)	0.108 (0.070)	0.514 (0.289)	0.167 (0.113)	0.213 (0.160)	0.047 (0.032)	0.166 (0.129)	0.024 (0.023)	0.195 (0.164)	0.031 (0.022)
Wa_39	Epi	3	56.29 (10.40)	1005 (138)	0.07 (0.027)	b.d.	b.d.	b.d.	0.370 (0.098)	0.060 (0.011)	0.134 (0.021)	0.021 (0.001)	0.110 (0.033)	b.d.	0.543 (0.060)	b.d.	b.d.	b.d.	b.d.	b.d.	b.d.	b.d.
Wa_39	Epi	5	80.72 (43.62)	1309 (163)	0.12 (0.095)	b.d.	b.d.	b.d.	0.518 (0.191)	0.064 (0.076)	0.150 (0.158)	0.023 (0.025)	0.096 (0.081)	b.d.	1.070 (0.500)	b.d.	0.034 (0.028)	b.d.	b.d.	b.d.	b.d.	b.d.
Wa_39	Epi	5	16.16 (1.75)	14.77 (3.50)	b.d.	b.d.	b.d.	b.d.	b.d.	b.d.	b.d.	b.d.	b.d.	b.d.	b.d.	b.d.	b.d.	b.d.	b.d.	b.d.	b.d.	b.d.
Wa_39	Prh	5	35.78 (6.01)	14.72 (9.10)	b.d.	b.d.	b.d.	0.048 (0.005)	b.d.	0.005 (0.002)	b.d.	b.d.	b.d.	b.d.	b.d.	b.d.	b.d.	b.d.	b.d.	b.d.	b.d.	b.d.
Wa_43	Prh	3	23.23 (12.54)	21.89 (9.84)	0.71 (0.075)	b.d.	b.d.	b.d.	0.303 (0.201)	b.d.	b.d.	b.d.	b.d.	b.d.	b.d.	b.d.	b.d.	0.008 (0.004)	0.031 (0.015)	b.d.	b.d.	0.005 (0.001)
Wa_43	Prh	5	59.03 (6.15)	14.02 (2.46)	0.67 (0.107)	b.d.	0.016 (0.006)	b.d.	0.263 (0.109)	b.d.	b.d.	b.d.	b.d.	b.d.	b.d.	b.d.	0.036 (0.012)	0.012 (0.002)	0.065 (0.030)	0.010 (0.006)	0.061 (0.035)	0.007 (0.003)
<b>Prehnite veins</b>																						
Wa_61	Prh	11	b.d.	3.05 (2.00)	0.027 (0.026)	b.d.	b.d.	b.d.	b.d.	0.012 (0.010)	0.032 (0.036)	0.006 (0.006)	b.d.	b.d.	0.048 (0.024)	b.d.	b.d.	b.d.	b.d.	b.d.	b.d.	b.d.

$n$  = number of analysis,  $1\sigma$  = one sigma standard deviation, Mineral (Min): Epi = epidote; Prh = prehnite

b.d. = below detection limit

**Table 22.**  $^{87}\text{Sr}/^{86}\text{Sr}$ , and  $\delta^{18}\text{O}$  isotopic composition, and Rb and Sr content of whole rock samples from samples of the layered gabbro, gabbroic dikes, dark veins, epidote veins, and altered gabbros from the Wadi Wariyah. Calculated water/rock ( $W/R$ ) ratios are also listed.

Sample	Rb (ppm)	Sr (ppm)	$^{87}\text{Rb}/^{86}\text{Sr}$	$^{87}\text{Sr}/^{86}\text{Sr}$	$^{87}\text{Sr}/^{86}\text{Sr}_{\text{initial}}^{\S}$	$\delta^{18}\text{O}$ (‰)	L.O.I (%) <sup>§</sup>	$W/R^{\S}$		
								8 ppm	38 ppm	
<b>OM10_Wa_32</b>										
A	gabbroic dike	1.87	130.12	0.0404	0.70359 ± 11	0.70332	+5.8	1.78	3.0	0.6
B	layered gabbro	2.81	179.50	0.0439	0.70322 ± 12	0.70316	+5.7	1.03	1.0	0.2
<b>OM10_Wa_33</b>										
A	gabbroic dike	3.75	162.44	0.0647	0.70341 ± 14	0.70332	+7.2	2.80	1.8	0.4
<b>OM10_Wa_39</b>										
A	epidote vein	5.62	794.08	0.0199	0.70358 ± 13	0.70356	+2.0	2.95	3.1	0.7
B	altered gabbro (halo)	2.81	171.56	0.0460	0.70440 ± 13	0.70433	+2.6	3.74	8.8	1.8
C	altered gabbro	4.68	123.07	0.1068	0.70377 ± 12	0.70363	+3.1	3.09	3.5	0.7
<b>OM10_Wa_40</b>										
A	epidote vein	3.75	567.24	0.0185	0.70383 ± 10	0.70380	+2.9	3.30	4.6	1.0
B	altered gabbro (halo)	1.87	86.05	0.0611	0.70480 ± 9	0.70472	+2.9	4.35	12.7	2.7
C	altered gabbro	3.75	155.99	0.0674	0.70418 ± 13	0.70409	+2.8	3.18	6.7	1.4
<b>OM10_Wa_42</b>										
A	gabbroic dike	0.94	167.24	0.0157	0.70323 ± 9	0.70321	+5.5	1.56	1.2	0.3
B	layered gabbro	3.75	159.47	0.0659	0.70322 ± 14	0.70313	+5.5	1.29	0.8	0.2
<b>OM10_Wa_43</b>										
A	epidote vein	7.49	489.94	0.0429	0.70476 ± 12	0.70470	+1.4	2.60	12.5	2.6
B	amphibole rich	2.81	430.02	0.0183	0.70457 ± 11	0.70454	+0.9	2.22	10.8	2.3
C	altered gabbro (halo)	2.81	162.89	0.0484	0.70499 ± 12	0.70492	+0.3	2.41	15.2	3.2
<b>OM10_Wa_46</b>										
A	gabbroic dike	0.94	146.48	0.0179	0.70346 ± 13	0.70344	+5.4	1.87	2.4	0.5
<b>OM10_Wa_47</b>										
A	dark vein	1.87	151.63	0.0347	0.70333 ± 12	0.70329	+3.5	1.38	1.6	0.3
B	layered gabbro	1.87	155.22	0.0339	0.70346 ± 15	0.70341	+5.4	1.27	2.3	0.5
<b>OM10_Wa_57</b>										
A	dark vein	-	228.97	-	0.70368 ± 12	0.70368	+4.8	2.34	3.9	0.8
B	layered gabbro	4.68	180.90	0.0727	0.70347 ± 11	0.70337	+5.7	0.68	2.1	0.5
<b>OM10_Wa_61</b>										
	prehnite vein	4.68	15.47	0.8499	0.70631 ± 25	0.70516	+8.2	4.82	18.8	4.0
<b>OM10_Wa_66</b>										
A	dark vein	3.75	156.00	0.0674	0.70349 ± 13	0.70340	+5.5	1.65	2.2	0.5
B	layered gabbro	4.68	166.76	0.0788	0.70348 ± 12	0.70337	+4.9	0.94	2.1	0.4
<b>OM10_Wa_68</b>										
A	gabbroic dike	-	190.76	-	0.70400 ± 11	0.70400	+4.9	1.98	6.0	1.3
<b>OM10_Wa_71</b>										
	An-bearing metagabbro	1.87	251.24	0.0209	0.70477 ± 12	0.70474	+4.6	3.86	13.0	2.7
<b>OM10_Wa_73</b>										
A	prehnite vein	3.75	11.80	0.8914	0.70562 ± 33	0.70441	+5.0	4.69	9.5	2.0
B	highly altered gabbro	0.94	52.69	0.0499	0.70508 ± 13	0.70501	+6.2	4.60	16.5	3.5

<sup>§</sup>Initial  $^{87}\text{Sr}/^{86}\text{Sr}$  ratio calculated at 95 Ma after *Hacker et al.* [1994]

<sup>§</sup>L.O.I. is loss on ignition (in %)

<sup>§</sup> $W/R$  is water/rock ratio and it is calculated assuming a closed system. The effective  $W/R$  ratio is calculated by mass balance using the equation of *Taylor* [1977],

$$(W/R)_{\text{effective}} = [(^{87}\text{Sr}/^{86}\text{Sr}^{\text{rock}})_{\text{final}} - (^{87}\text{Sr}/^{86}\text{Sr}^{\text{rock}})_{\text{initial}}] / [(^{87}\text{Sr}/^{86}\text{Sr}^{\text{seawater}})_{\text{initial}} - (^{87}\text{Sr}/^{86}\text{Sr}^{\text{rock}})_{\text{final}}] \times (C_{\text{initial}}^{\text{rock}} / C_{\text{initial}}^{\text{rock}})$$

where  $(^{87}\text{Sr}/^{86}\text{Sr}^{\text{rock}})_{\text{final}}$  is the measured Sr isotopic ratio in the sample;  $(^{87}\text{Sr}/^{86}\text{Sr}^{\text{rock}})_{\text{fresh}}$  is taken as 0.70295 [*Lanphere et al.*, 1981];  $(^{87}\text{Sr}/^{86}\text{Sr}^{\text{seawater}})_{\text{initial}}$  is the Cretaceous seawater Sr isotopic composition (~0.70735 at 95 Ma after *Burke et al.* [1982]);  $C_{\text{initial}}^{\text{seawater}}$  is the Sr concentration of seawater and is taken as 8 ppm for today's seawater or 38 ppm for Cretaceous seawater as proposed by *Coogan et al.* [2009]; and  $C_{\text{initial}}^{\text{rock}}$  is assumed to be 160 ppm [*Kawahata et al.*, 2001].

**Table 23.** Results of the different geothermometers used to constrain the formation temperature of the gabbroic dikes, dark veins, and epidote veins.

Sample	Lithology	Amphibole*		Pyroxenes		FeTi-oxides <sup>§</sup>			Epidote <sup>1</sup>
		Range	Cl-rich	Quilf <sup>§</sup>	Al-in-cpx <sup>%</sup>	T	log fO <sub>2</sub>	ΔQFM	
Wa_02A	dv	757 - 992	583 - 751	946 ± 46	844 ± 87	548	-20.42	+1.23	-
Wa_04	gd	591 - 999	651 - 663	-	1036 ± 21	592	-20.54	-0.51	-
Wa_05A	dv	648 - 997	-	903 ± 85	828 ± 74	537	-22.54	-0.46	-
Wa_32A	gd	546 - 1000	-	-	1029 ± 41	655	-17.80	+0.29	-
Wa_33A	gd	880 - 994	-	-	990 ± 16	576	-20.74	-0.17	-
Wa_39A	epi	<480 - 492	-	-	-	-	-	-	431
Wa_40A	epi	485	-	-	-	-	-	-	467
Wa_42A	gd	658 - 985	525 - 626	912 ± 47	1035 ± 37	566	-20.88	+0.08	-
Wa_43B	epi (II)	488 - 667	-	-	-	-	-	-	421 - 587
Wa_45A	dv	721 - 752	-	-	-	-	-	-	-
Wa_46A	gd	489 - 1000	-	-	983 ± 46	566	-18.60	+2.35	-
Wa_46A	dv	481 - 706	-	-	778 ± 10	-	-	-	-
Wa_47A	dv	508 - 1000	-	-	976 ± 63	663	-16.65	+1.19	-
Wa_57A	dv	672 - 806	-	855 ± 89	851 ± 26	579	-18.72	+1.74	-
Wa_58A	dv	787 - 962	-	828 ± 122	782 ± 15	585	-19.67	+0.57	-
Wa_66A	dv	549 - 647	-	-	801 ± 30	-	-	-	-
Wa_67A	epi	-	-	-	-	-	-	-	437
Wa_68	gd	615 - 1000	-	901 ± 87	871 ± 67	614	-17.88	+1.43	-
Wa_75	epi	-	-	-	-	-	-	-	528
Wa_77A	dv	678 - 749	-	842 ± 99	793 ± 10	-	-	-	-

Abbreviations: gd = gabbroic dike, dv = dark vein, epi = epidote vein

all temperature in °C

\* Ti-in-amphibole *Ernst and Lui* [1998], standard error of the method ±40°C

§ *Andersen et al.* [1993], standard error give by Quilf

% *France et al.* [2010], standard error based on standard deviation given by compositional variation in clinopyroxene

§ *Stormer et al.* [1983], standard error not given

<sup>1</sup> *Brunsmann et al.* [2002], standard error not given

**Table 24.** Experimental conditions and newly formed phases after the experiments.

Run no. <sup>#</sup>	Temperature [°C]	Pressure [MPa]	$\Delta$ NNO	newly formed phases <sup>b</sup>
14a	860	2055	-0.03	amph, opx*
14b	860	2055	-0.03	amph, opx*
15a	900	2000	-0.23	plag, amph, opx, gl
15b	900	2000	-0.23	plag, amph, opx, apa, gl
12a <sup>s</sup>	940	2000	0.00	plag, amph, opx, gl, p-rich
13a	940	2043	-0.02	plag, amph, opx, apa, gl
13b	940	2043	-0.02	plag, amph, opx, apa, gl
16a	980	1996	-0.13	plag, ol, cpx, gl
16b	980	1996	-0.13	plag, ol, cpx, opx
17a	1020	2000	0.01	ol, cpx, gl
17b	1020	2000	0.01	plag, ol, cpx, gl

all experiments performed under water-saturated conditions

<sup>#</sup> runs marked with "a" with pure water, "b" with water + NaCl (seawater analogue)

<sup>b</sup> observed with BSE in thin section; phase abbreviations: ol (olivine), plag (An-rich plag), cpx (clinopyroxene), opx (orthopyroxene), amph (amphibole), apa (apatite), gl (glass), p-rich p-rich (phosphorus-rich melt).

\* no melt was observed in these runs implying that amph and opx was formed under subsolidus conditions

<sup>s</sup> two BSE figures from this run have been published in *Koepke et al.* [2005a]





# Appendix

## *Partial melting modelling*

The modelled melt composition during partial melting shown in Figure 34 is calculated based on the equation of in situ crystallization formulated by *Langmuir* [1989]. The equation describes the geochemical behaviour of a melt within a magma chamber, which is caused by re-injection of liquid to the solidification zone and then constantly removed due to separation. This leads to a different geochemical evolution compared to fractional or equilibrium melting. Due to the hydrous partial melting reaction of the layered gabbro can be regarded as a process, in which melt from the host rock is infrequently added to the molten part and then crystallizes within the dike/vein, the in situ crystallization may be the right choice in order to describe the trace element behaviour during hydrous partial melting of the layered gabbro. The relatively enrichment of an element concentration in the liquid ( $c_L$ ) to the initial concentration of the element in the host rock ( $c_0$ ) during in situ crystallization can be expressed by:

$$\frac{c_L}{c_0} = (M_L / M_0)^{(f(D-1)/[D(1-f)+f])} \quad (1)$$

where  $M_0$  is the initial mass of the molten gabbro and  $M_L$  is the mass of liquid added, which simplified expresses the fraction of melt remaining in the system,  $f$  is the fraction of liquid allocated to the solidification zone which is returned to the magma chamber [Rollinson, 1993]. A value of 0.8 is chosen for  $f$  in the calculation.  $D$  is the bulk rock partition coefficient for a specific element. The bulk rock partition coefficient is calculated using plagioclase and clinopyroxene partition coefficient presented by *Bédard* [2006a] (see Table A1) assuming both minerals to equally enter the liquid (“non-modal melting”).

**Table A1.** Partition coefficients for plagioclase (plag) and clinopyroxene (cpx).

Element	Plag	Cpx
Ti	0.078	0.473
K	0.252	0.004
P	0.079	0.162
Sr	2.7*	0.032
Y	0.138	0.603
Cs	0.087	0.003
Ba	1.016	0.006
La	0.358	0.028
Ce	0.339	0.059
Pr	0.316	0.116
Nd	0.289	0.115
Sm	0.237	0.259
Eu	0.55*	0.341
Gd	0.192	0.422
Tb	0.170	0.502
Dy	0.150	0.570
Ho	0.132	0.616
Er	0.117	0.640
Tm	0.104	0.644
Yb	0.094	0.635
Lu	0.085	0.617

\*Eu and Sr have been modified and taken from *Wanless et al.* [2010]

### Isotope calculations

The  $^{87}\text{Sr}/^{86}\text{Sr}$  isotope calculation for the lithologies from the Wadi Wariyah shown in Figure 32 is based on the mass balance equation for the stable isotope exchange originally formulated by *Taylor* [1977]. It estimates the relative mass, volume, or molar quantities of fluid or rock required causing the observed isotopic composition of the rock. The specific water/rock ( $W/R$ ) ratio and alteration temperature causes by the isotopic exchange between the initial and final endmember products (rock and fluid) in a simple closed system is expressed by:

$$\frac{W}{R} = \frac{\frac{^{87}\text{Sr}/^{86}\text{Sr}_r^f - ^{87}\text{Sr}/^{86}\text{Sr}_r^i}{^{87}\text{Sr}/^{86}\text{Sr}_w^i - ^{87}\text{Sr}/^{86}\text{Sr}_r^f} \cdot \frac{C_r^i}{C_w^i}}{\quad} \quad (2)$$

where  $^{87}\text{Sr}/^{86}\text{Sr}_r^f$  are the final rock  $^{87}\text{Sr}/^{86}\text{Sr}$  ratios measured in the rock and  $^{87}\text{Sr}/^{86}\text{Sr}_r^i$  are the  $^{87}\text{Sr}/^{86}\text{Sr}$  ratio for fresh igneous gabbroic rock ( $\sim 0.70295$ ) [*Lanphere et al.*, 1981];  $^{87}\text{Sr}/^{86}\text{Sr}_w^i$  is the  $^{87}\text{Sr}/^{86}\text{Sr}$  ratio of Cretaceous seawater at 95 Ma (0.70735 after *Burke et al.* [1982]).  $C_r^i$  and  $C_w^i$  are the concentrations of Sr in the rock and seawater, respectively. The initial Sr concentration in the rock is 160 ppm [*Kawahata et al.*, 2001]. For the Sr concentration of Cretaceous seawater, values of  $C_w^i = 8$  ppm (the Sr concentration of modern seawater) and  $C_w^i = 38$  ppm [*Coogan*, 2009] are used for the calculations.

The oxygen isotopic compositions of altered rocks are based on the water-rock interaction expressed by an equation formulated by *Taylor* [1974]:

$$\frac{W}{R} = \frac{\delta_r^f - \delta_r^i}{\delta_w^i - (\delta_r^f - \Delta)} \quad (3)$$

where  $W/R$  is the specific water/rock ratio in a closed system,  $\delta_r^f$  and  $\delta_r^i$  are the initial and final rock  $\delta^{18}\text{O}$  values, respectively, and  $\delta_w^i$  is the initial  $\delta^{18}\text{O}$  value of the fluid. At 50°C and 100°C, the fresh igneous gabbro ( $\delta^{18}\text{O} = +5.7\text{‰}$ ) reacts with Cretaceous seawater ( $\delta^{18}\text{O} = -1\text{‰}$ ) [*Veizer et al.*, 1999]. At 250°C and 500°C, the fresh gabbro reacts with  $^{18}\text{O}$ -enriched hydrothermal fluid (+0.5 or +2.5‰) [*Shanks*, 2001]. The gabbro-water ( $\Delta$ ) oxygen isotope fractionation is taken from *Zhao* [2003]. Due to the temperature dependence of the oxygen isotope fractionation, high temperature and low temperature hydrothermal alteration can be distinguished.

# Acknowledgments

First of all, I like to thank the German Science Foundation for giving financial support to this research (KO 1723/10-1).

A special and kindly thank goes to Prof. Dr. Jürgen Koepke who supported me with all his knowledge, patience, and who introduced me into the exciting topics of the Oman ophiolite, Mid-Ocean Ridges, and Electron microprobe. Without his assistance and effort during the last four years this thesis would not exist.

I would like to thank my committee members, Prof. Dr. Wolfgang Bach and Prof. Dr. Ulrich Heimhofer who directly agreed to take on review for this thesis.

I like to thank all people who supported me during the analytical work: Dieter Garbe-Schönberg & Ulrike Westernstoer (ICP-MS), Jasper Berndt (LA-ICP-MS), Stephan Schuth (Sr isotopes), and Adrian Boyce (Oxygen Isotopes).

Then, I like to thank all the people, who attended on two fabulous field trips exploring the Oman: Marcel Dietrich, Jürgen Koepke, Dieter-Garbe Schönberg, Harald Strauss, Tim Müller, Martin Rabe-Oeser, and Katharina Streuff.

Sincere thanks are given to all people from the Institute of Mineralogy in Hannover. It had been always a good place to go in the morning. Some special thanks are going to the people from room 137 who made every weekday not only a working day.

At last but most important I want to thank my family, my closest friends, and my gorgeous girlfriend. I'm enjoying every second with you!!!

# Curriculum vitae

Name	Paul Eric Wolff
Address	Albertstraße 12 30451 Hannover, Germany
E-Mail	paul.eric.wolff@gmail.com
Date of Birth	03.09.1983
Place of Birth	Königstein/TS

## Education

08/2010	Diploma in Geosciences (MSc equivalent), Institute of Mineralogie, Leibniz University Hannover, Germany
10/2004 - 02/2010	Postgraduates studies in Geosciences, Leibniz University Hannover, Germany
06/2003	Abitur (A-level equivalent), Gymnasium Mellendorf, Germany

# List of Publications

## Publications related to this topic

### Journals

Koepke, J., J. Berndt, I. Horn, J. Fahle, and **P. E. Wolff**, Partial melting of oceanic gabbro triggered by migrating water-rich fluids: a prime example from the Oman Ophiolite, in *Tectonic Evolution of the Oman Mountains*, edited by H. Rollinson, M. Searle, I. A. Abbasi, A. Al-Lazki and M. H. Al-Kindi, Geological Society, London, Special Publications, 392, 187-204, <http://dx.doi.org/10.1144/SP392.10>, 2014 in press.

**Wolff, P. E.**, J. Koepke, and S. Feig, The reaction mechanism of fluid-induced partial melting of gabbro in the oceanic crust, *Eur J Mineral*, 25(3), 279-298, 2013.

### Conference Abstracts

**Wolff, P. E.**, J. Koepke, J. Berndt, D. Garbe-Schönberg, S. Schuth, and A. McCaig, Multi-stage hydrothermal alteration of the lower oceanic crust – Evidences from a layered gabbro series of the Oman ophiolite (Wadi Tayin Massif), *DMG Tagung*, Universität Tübingen, 2013.

Linsler, S., T. Müller, S. Schuth, **P. E. Wolff**, J. Koepke, D. Garbe-Schönberg, and H. Strauss, Focused fluid flow zones in the Oman ophiolite (Wadi Gideah, Wadi Tayin Massif) – A key for cooling the deep crust at fast-spreading ridges, *DMG Tagung*, Universität Tübingen, 2013.

**Wolff, P. E.**, T. Müller, J. Koepke, D. Garbe-Schönberg, and H. Strauss, Petrology and geochemistry of the "Wadi Gideah" cross section in the Southern Oman ophiolite, *International Conference on the Geology of the Arabian Plate and the Oman Mountains*, Sultan Qaboos University, Muscat, Sultanate of Oman, 2012.

**Wolff, P. E.**, J. Koepke, D. Garbe-Schönberg, K. Streuff, and J. Berndt, High to low temperature hydrothermal alteration of a layered gabbro from the Wadi Wariyah (Wadi Tayin Massif, Oman ophiolite), *International Conference on the Geology of*

*the Arabian Plate and the Oman Mountains*, Sultan Qaboos University, Muscat, Sultanate of Oman, 2012.

**Wolff, P. E.**, D. Garbe-Schönberg, J. Koepke, and K. Streuff, High-temperature hydrothermal activity in the lower oceanic crust: Petrological and geochemical evidence for fluid pathways in the Oman Ophiolite, *Goldschmidt Conference Abstract*, Prag, 2011.

Koepke, J., **P. E. Wolff**, and S. Feig, Oceanic plagiogranites as products of hydrothermal activity at slow spreading ridges, *Goldschmidt Conference Abstract*, Prag, 2011.

**Wolff, P. E.**, J. Koepke, and S. Feig, Very high contents of incompatible elements in the very first melts of partially molten oceanic gabbro, *EMPG XIV Conference Abstract*, Universität Kiel, 2012.

**Wolff, P. E.**, J. Koepke, D. Garbe-Schönberg, H. Strauss, M. Dietrich, and M. Oeser, Towards a reference profile for fast-spreading oceanic crust: petrology and geochemistry of the Wadi Gideah cross section in the Southern Oman ophiolite, *DMG Tagung*, Universität Münster, 2010.

### **Publications not related to this topic**

#### **Journals**

Zhang, C., F. Holtz, J. Koepke, **P. E. Wolff**, C. Ma, and J. H. Bédard, Constraints from experimental melting of amphibolite on the depth of formation of garnet-rich restites, and implications for models of Early Archean crustal growth, *Precam Res*, 23, 206-217, 2013.

Zhang, C., F. Holtz, C. Ma, **P. E. Wolff**, and X. Li, Tracing the evolution and distribution of F and Cl in plutonic systems from volatile-bearing minerals: a case study from the Liujiawa pluton (Dabie orogen, China), *Contrib Mineral Petr*, 164(5), 859-879, 2012.

Oeser, M., H. Strauss, **P. E. Wolff**, J. Koepke, M. Peters, D. Garbe-Schönberg, and M. Dietrich, A profile of multiple sulfur isotopes through the Oman ophiolite, *Chem Geol*, 312-313, 27-46, 2010.

#### **Conference Abstracts**

Oeser, M., H. Strauss, **P. E. Wolff**, J. Koepke, M. Peters, D. Garbe-Schönberg, and M. Dietrich, Hydrothermal Alteration of the Oman Ophiolite: The Message from Multiple Sulfur Isotopes, *International Conference on the Geology of the Arabian Plate and the Oman Mountains*, Sultan Qaboos University, Muscat, Sultanate of Oman, 2012.

Oeser, M., H. Strauss, **P. E. Wolff**, J. Koepke, M. Peters, D. Garbe-Schönberg, and M. Dietrich, A profile of multiple sulfur isotopes through the Oman ophiolite, *Goldschmidt Conference Abstract*, Prag, 2011.

Eur. J. Mineral.  
2013, 25, 279–298  
Published online June 2013

Paper presented at the EMPG XIV symposium,  
Kiel, Germany (March 2012)

## The reaction mechanism of fluid-induced partial melting of gabbro in the oceanic crust

PAUL ERIC WOLFF<sup>1,\*</sup>, JÜRGEN KOEPKE<sup>1</sup> and SANDRIN T. FEIG<sup>2</sup>

<sup>1</sup> Institut für Mineralogie, Leibniz Universität Hannover, Callinstraße 3, 30167 Hannover, Germany

\*Corresponding author, e-mail: e.wolff@mineralogie.uni-hannover.de

<sup>2</sup> Central Science Laboratory, University of Tasmania, Private Bag 74, 7001 Hobart TAS, Australia

**Abstract:** Hydrous partial melting of oceanic gabbro as a consequence of fluid/rock interaction at very high temperatures is regarded as an important process for the formation of felsic lithologies within the oceanic crust. In order to investigate the principal reaction mechanism of hydrous partial melting in detail, water-saturated partial melting experiments were conducted in an internally heated pressure vessel in the temperature range 860–1020 °C and 200 MPa pressure,  $f_{O_2} \sim NNO$ , with mm-sized blocks of unmodified olivine gabbro (“microrocks”) used as a coarse-grained starting material. Although far from global equilibrium, the observed phase relations and compositional trends are as expected from a similar experimental survey designed for achieving global equilibrium, using a fine-grained powder of the same starting gabbro. The experimental results allow us to formulate a general fluid-induced reaction for hydrous partial melting of olivine gabbro as a function of temperature:

at  $T \leq 980^\circ\text{C}$ , olivine + clinopyroxene + plagioclase(I) +  $\text{H}_2\text{O} \Rightarrow$  amphibole + orthopyroxene + plagioclase(II)  
+ hydrous plagiogranitic melt;

at  $T \geq 980^\circ\text{C}$ , olivine(I) + clinopyroxene(I) + plagioclase(I) +  $\text{H}_2\text{O} \Rightarrow$  olivine (II) + clinopyroxene(II) + plagioclase(II)  
+ hydrous plagiogranitic melt.

Textural features and compositional characteristics obtained in these partial-melting experiments on microrock are in good agreement with corresponding features of late-stage assemblages in some natural oceanic gabbros from slow-spreading ridges, implying that some of the natural late-stage parageneses can be better explained as residual phases left back after a hydrous partial-melting event rather than by crystallization of a late evolved percolating melt.

One experiment performed at 940 °C produced pools of silicate melt containing droplets of a second melt strongly enriched in typical trace elements (P, Zr, Cl as proxies), which is interpreted as an effect of liquid immiscibility. The observation of unusually high concentrations of some trace elements within the first melts is in contradiction with trace-element concentrations derived from modelling using equilibrium partition coefficients. A model is implied that during the very first stage of hydrous partial melting, sub-micrometre sized phases like apatite, zircon and oxides crystallized on grain boundaries from a late-stage melt in the host gabbro may be forced into the very first melt which incorporated their trace-element inventory. A possible consequence is that the very first melts of fluid-induced partial melting of oceanic gabbro may be regarded as one possible source for the contamination of natural MORB or of corresponding felsic lithologies generated at mid-ocean ridges.

**Key-words:** experimental petrology, partial melting, oceanic gabbro, water-rock interaction, immiscible melts.

### 1. Introduction

Fluid-triggered partial melting of crustal rocks is one of the major magmatic processes on Earth. For example, the dehydration melting of amphibolite is known to be responsible for the generation of TTG rocks (tonalites, trondhjemites, and granodiorites) in the Archean (Barker, 1979), which is regarded as one important step

for the formation of the continental crust. However, in terms of the oceanic crust, it was assumed for a long time that fluid-triggered melting does not play a significant role during the formation of oceanic rocks. This point of view has changed in the last decade, when researchers observed that seawater–rock interaction in the lower oceanic crust proceeded to conditions where fluid-triggered partial melting of previously hydrothermalised sheeted dikes or